ATOMIC SCALE SIMULATION OF ACCIDENT TOLERANT FUEL MATERIALS FOR FUTURE NUCLEAR REACTORS

A Thesis Submitted to the College of
Graduate and Postdoctoral Studies
In Partial Fulfillment of the Requirements
For the Degree of Doctor of Philosophy
In the Department of Mechanical Engineering
University of Saskatchewan
Saskatoon

By
Ericmoore Elijah Jossou

Permission to use

In presenting this thesis in partial fulfillment of the requirements for a postgraduate degree from the University of Saskatchewan, I agree that the Libraries of this University may make it freely available for inspection. I further agree that permission for copying of this thesis in any manner, in whole or in part, for scholarly purposes may be granted by the professors who supervised my thesis work or, in their absence, by the Head of the Department or the Dean of the College in which my thesis work was done. It is understood that any copying or publication or use of this thesis or parts thereof for financial gain shall not be allowed without my written permission. It is also understood that due recognition shall be given to me and to the University of Saskatchewan in any scholarly use which may be made of any material in my thesis.

Requests for permission to copy or to make use of other material in this thesis in whole or part should be addressed to:

Head of the Department of Mechanical Engineering
University of Saskatchewan
57 Campus Drive
Saskatoon, Saskatchewan S7N 5A9 Canada
OR

Dean
College of Graduate and Postdoctoral Studies
University of Saskatchewan
116 Thorvaldson Building, 110 Science Place
Saskatoon, Saskatchewan S7N 5C9 Canada

Abstract

The 2011 accident at the Fukushima-Daiichi power station following the earthquake and tsunami in Japan put renewed emphasis on increasing the accident tolerance of nuclear fuels. Although the main concern in this incident was the loss of coolant and the Zr cladding reacting with water to form hydrogen, the fuel element is an integral part of any accident tolerant fuel (ATF) concept. Therefore, to license a new commercial nuclear fuel, the prediction of fuel behavior during operation becomes a necessity. This requires knowledge of its properties as a function of temperature, pressure, initial fuel microstructure and irradiation history, or more precisely the changes in microstructure due to irradiation and/or oxidation. Amongst other nuclear fuels, uranium diboride (UB_2) and uranium silicide (U_3Si_2) are considered as potential fuels for the next generation of nuclear reactors due to their high uranium density and high thermal conductivity compared to uranium dioxide (UO_2). However, the thermophysical properties and behavior of these fuels under extreme conditions are not well known, neither are they readily available in the literature. Therefore, in this thesis, density functional theory (DFT) and classical molecular dynamic (MD) simulations were used to investigate the thermophysical properties, radiation tolerance and oxidation behavior of UB_2 and U_3Si_2 as potential fuels or burnable absorbers for the next generation of nuclear reactors.

UB_2 was studied in order to understand its thermophysical properties as a function of temperature. The phonon-assisted thermal conductivity ($\boldsymbol{k_{ph}}$) exhibits large directional anisotropy with larger thermal conductivity parallel to the crystal direction. This has implications for the even dissipation of heat. The increase in thermal conductivity with temperature is justified by the electronic contribution to the thermal transport, especially at high temperatures. This shows that UB_2 is a potential ATF candidate.

In terms of radiation tolerance, Zr is more soluble in UB_2 than Xe, while uranium vacancy is the most stable solution site. Furthermore, as the concentration of Zr fission product (FP) increases, there is a contraction in the volume of UB_2, while an increase in Xe results in swelling of the fuel matrix. In terms of diffusion, the presence of an FP in the neighboring U site increases the migration of U in UB_2, making U migrate more readily than B as observed in the ideal system.

The thermophysical properties of U_3Si_2 as a possible ATF were studied and discussed considering the neutronic penalty of using a SiC cladding in a reactor. The calculated molar heat capacity and

experimental data are in reasonable agreement. Due to the anisotropy in lattice expansion, a directional dependence in the linear thermal expansion coefficient was noticed, which has also been experimentally observed. The thermal conductivity of U_3Si_2 increases with temperature due to the electronic contribution while the phonon contribution decreases with increasing temperature. A comparison of the thermal conductivity in two different crystallographic directions sheds light on the spatial anisotropy in U_3Si_2 fuel material. The inherent anisotropic thermophysical properties can be used to parametrize phase field models by incorporating anisotropic thermal conductivity and thermal expansion. This allows for a more accurate description of microstructural changes under variable temperature and irradiation conditions.

Due to the metallic nature of U_3Si_2, the oxidation mechanism is of special interest and has to be investigated. Oxidation in O_2 and H_2O was investigated using experimental and theoretical methods. The presence of oxide signatures was established from X-ray diffraction (XRD) and Raman spectroscopy after oxidation of the solid U_3Si_2 sample in oxygen. Surface oxidation of U_3Si_2 can be linked to the significant charge transfer from surface uranium ions to water and/or oxygen molecules. Detailed charge transfer and bond length analysis revealed the preferential formation of mixed oxides of U-O and Si-O on the U_3Si_2 (001) surface as well as UO_2 alone on the U_3Si_2 (110) and (111) surfaces. Formation of elongated O-O bonds (peroxo) confirmed the dissociation of molecular oxygen before U_3Si_2 oxidation. Experimental analysis by Raman spectroscopy and XRD of the oxidized U_3Si_2 samples has revealed the formation of higher uranium oxides such as UO_3 and U_3O_8.

Overall, this work serves as a step towards understanding the complex anisotropic behavior of the thermophysical properties of metallic UB_2 and U_3Si_2 considered as potential accident tolerant nuclear fuel. The calculated anisotropy of thermophysical properties can be used to parametrize phase field model and to incorporate in it anisotropic thermal conductivity and thermal expansion.

Acknowledgment

This has undoubtedly been the most exciting, emotional, and life-changing chapter of my life. When I started this phase of my life, I had no idea where it was going to take me and the kind of people I was going to meet. I want to thank everyone for making my choice to do a Ph.D. one of the best decisions of my life.

I want to thank my supervisors Prof. Jerzy Szpunar and Dr. Barbara Szpunar, for their direction and encouragement. This research would not be successful without their support. I also appreciate the support by Department of Mechanical Engineering faculty and staff members, especially the department head, Prof. Torvi and the graduate chair Prof. Chen. I also appreciate the help of the advisory committee members: Prof. Odeshi, Prof. Tse, Prof. Bugg and Prof. Zhang. My sincere thanks to my colleagues in the Advanced Materials for Clean Energy research group especially Linu Malakkal, Dotun Oladimeji, Jayangani Ranasinghe who worked with me on the ATF project.

I acknowledge financial support from the University of Saskatchewan's Dean Scholarship Award, the Department of Mechanical Engineering for the devolved scholarship and the NSERC Canada Research Chair program.

Finally, I would like to acknowledge my wife, her family, and mine for providing the love and support that helps me overcome the challenges of completing a Ph.D.

Dedication

I dedicate this thesis to God for making my dreams come to past, my lovely wife for her faith in me, my daughter for her unusual understanding as I have to be away from home for many months and to my beloved parents for their encouragement.

Table of contents

List of Figures

List of Tables

List of acronyms and their definition

AMF	Around Mean Field
ATF	Accident Tolerant Fuel
B3LYP	Becke, 3-parameter, Lee-Yang-Parr
B3PW91	Becke, 3-parameter, Perdew-Wang-91
BP	Becke-Perdew
BFGS	Broyden–Fletcher–Goldfarb–Shanno
BTE	Boltzmann Transport Equation
BZ	Brillouin Zone
CI-NEB	Climbing Image-NEB
DFT	Density Functional Theory
DFPT	Density-Functional Perturbation Theory
EAM	Embedded Atom Method
EMD	Equilibrium Molecular Dynamics
FCC	Face Center Cubic
FGR	Fission Gas Release
FLL	Fully-Localized Limit
FPs	Fission Products
FP-LAPW+lo	Full Potential Linear Augmented Plane Waves plus Local Orbitals method
GFR	Gas-cooled Fast Reactor
GGA	Generalized Gradient Approximation
GIF	Generation *IV* Forum
HCACF	Heat Current AutoCorrelation Function
HF	Hartree-Fork
K-S	Kohn-Sham
LAMMPS	Large-scale Atomic/Molecular Massively Parallel Simulator
LAO	Localized Atomic Orbital
LDA	Local Density Approximation
LFR	Lead-cooled Fast Reactor
LTEC	Linear Thermal Expansion Coefficient
LYP	Lee-Yang-Parr
MEAM	Modified Embedded Atom Method

MEP	Minimum Energy Path
MD	Molecular dynamics
MP	Monkhorst-Pack
MSR	Molten Salt Reactor
NEB	Nudged Elastic Band
NEMD	Non-Equilibrium Molecular Dynamics
NM	Non-Magnetic
NN	Nearest Neighbor
PAW	Projected Augmented Wave
PBE	Perdew-Burke-Enzerhof
PBEsol	Perdew-Burke-Enzerhof for solids
PW	Plane Wave
PW86	Perdew-Wang 86
PW91	Perdew-Wang 91
QE	Quantum Espresso
QHA	Quasi-Harmonic Approximation
RPA	Random-Phase Approximation
RPBE	Revised Perdew-Burke-Enzerhof
RTA	Relaxation Time Approximation
SFR	Sodium-cooled Fast Reactor
SIC	Self-Interaction Correction
SOC	Spin–Orbit Coupling
SP	Spin Polarization
SWCRs	Supercritical Water Reactors
TDOS	Total Density of States
US	Ultrasoft Pseudopotentials
VHTR	Very High Temperature gas-cooled Reactor

List of symbols and their definition

$v_{ext}(r)$	External potential
$n(r)$	Electron density
$F[n(r)]$	Energy density functional
$E_H[n(r)]$	Hartree energy
$T[n(r)]$	Kinetic energy functional
$E_{xc}[n(r)]$	Exchange-correlation functional
∇_i	Gradient of the potential energy on atom *i*
q_i	Charges on atom *i*
f	Embedding function
el	electrons
ph	phonons
$\omega_j(\vec{q})$	Frequency of the phonon
S	Heat current vector
Λ_{eff}	Effective mean free path
C_v	Specific heat at constant volume
v	Group velocity
E_f	Defect formation energies
μ	Chemical potential
ΔV_{rel}	Relaxation volume
k_{el}	Electronic thermal conductivity
k_{ph}	Phonon thermal conductivity
A_B	Anisotropy index of bulk modulus
A_G	Anisotropy index of shear modulus
A^U	Universal anisotropic index
B	Bulk modulus
G	Shear modulus
E	Young's modulus
θ_D	Debye temperature
v_m	Average sound velocity
v_l	Longitudinal sound velocity
v_t	Transverse sound velocity

h	Plank's constant
k	Boltzmann's constant
N_A	Avogadro's number
ρ	Density
M	Molecular weight
n	Number of atoms in a formula unit
T_m	Melting temperature
$\hbar$	Reduced Plank's constant
α_v	Volumetric thermal expansion coefficient
T	Temperature
F_o	Total free energy
B_o'	First derivative of bulk modulus
E_a	Activation energy
$N(E_F)$	Amount of electrons
E_m	Migration energy
E_F	Fermi energy level
D_o	Diffusion coefficient prefactor
Υ	Grüneisen parameter
E^{inc}	Incorporation energy
E^{sol}	Solution energy
$\widehat{H}$	Hamiltonian operator
ψ	Wave function
P	Pressure
β	Dipole moment

Chapter 1

Introduction

1.1. Overview of Chapter 1

This chapter focuses on the motivation behind this study. It also highlights the existing problem with the currently used uranium dioxide (UO_2) fuel and the need to address this problem. The overall and specific objectives of this study are also presented in this section.

1.2. Motivation

UO_2 is the primary fuel used in the existing fleet of nuclear reactors for the generation of electricity [1]. However, during in-service reactor operation, UO_2 undergoes oxidation. This oxidation generates a series of mixed-valence uranium oxides; U_4O_9/U_3O_7 and U_3O_8 whose stoichiometry depends on the temperature and oxygen partial pressure [2]. The formation of U_3O_8 from UO_2 also results in a volume increase which can potentially damage the fuel cladding in the case of direct storage of fuel elements [3]. In addition, the fission of uranium atoms occurs. This produces a wide variety of fission products (FPs) that result in defect formation as their energy is transferred to the surrounding materials. This in turn causes microstructural evolution of the fuel, which is governed by these defects [4,5]. These changes have a direct influence on the thermal conductivity, chemical stability, melting point, irradiation behavior, and cladding corrosion during fuel-cladding mechanical interaction and interaction with coolants in the case of cladding failure [6].

Furthermore, the thermal conductivity of UO_2 deteriorates rapidly with increasing stoichiometric deviation or increase in temperature [7]. This determines the temperature gradient and controls the heat transfer across the UO_2 pellet in the reactor. Therefore, after the severe accident at the Japanese Fukushima Daiichi Nuclear Power Station, caused by the 2011 earthquake and tsunamis, coupled with the poor thermal property of UO_2, improving the thermal properties of next-generation nuclear fuel became a topic of interest for national research laboratories and fuel vendors. This is because fuel with higher thermal conductivity will improve heat removal efficiency, thus lowering centerline temperatures. In the long run, detrimental temperature-dependent effects such as grain growth, pellet cracking, and FP transport will be reduced [8]. To this end, it will be of interest to enhance the thermal properties of UO_2 and/or to develop

completely new fuel forms with enhanced thermophysical properties and better response to extreme conditions such as temperature, radiation, hydriding and oxidizing environment.

1.3. Rationale for fuel selection

Next generation nuclear fuel that has enhanced thermal conductivity, higher FPs retention and more resistance to oxidation has been labelled Accident Tolerant Fuel (ATF). This is because ATFs can tolerate the loss of active cooling in the core of the reactor for a considerably longer time in the case of power loss, while maintaining or improving fuel performance during normal operation. Ott *et al.* [9] highlighted three major potential approaches for the development of ATFs:

- Improved fuel thermophysical properties and FPs retention,
- Improved cladding properties to maintain core cooling ability,
- Improved reaction kinetics with steam to minimize enthalpy input and hydrogen generation.

Hence, the focus of this thesis is to identify new fuel forms (ATFs), which address the concerns raised by Ott *et al*. [9] as highlighted above. Rather than randomly select uranium compounds for this study, potential ATFs are narrowed down based on previous work in literature. For instance, U–Si binary system (U_3Si_2, U_3Si, U_3Si_5, and USi) [10] have received historical interest as nuclear fuel for research reactors, while the borides (UB_2, UB_4 and UB_{12}) was briefly studied in the late 60's as potential nuclear fuel [11] and uranium nitride (UN) [12] only receive some attention more recently.

Furthermore, U_3Si_2, U_3Si, and U_3Si_5 have become the focus of studies in recent years due to their potential use as ATFs [13–16]. U_3Si_2 and UB_2 are considered here following the rejection of the higher density silicides such as U_3Si and U_3Si_5 based on unacceptable swelling and low melting point [15]. UN is also ruled out in this study due to its poor radiation tolerance and oxidation behavior, difficult method of fabrication, and the problem associated with handling it outside controlled atmospheres [12].

1.4. Research objectives

In view of the motivation discussed in section 1.2, the overall objective of this research is to determine the radiation tolerance, oxidation behavior, and thermophysical properties of U_3Si_2 and

UB_2 from room temperature to near the melting point in order to evaluate their potential as a fuel for advanced reactors. To realize this goal, the following specific objectives were pursued;

1. To predict the thermophysical and electronic properties of advanced fuel concepts such as uranium diboride and uranium silicide using atomistic codes within the framework of density functional theory, and classical molecular dynamics. Such properties serve as input for mesoscale methods such as phase-field for understanding fuel behavior under transient or accident conditions in the reactor.

2. To determine the effects of point defects and FPs, such as Zr and Xe, on metallic[1] fuel such as UB_2 using atomistic codes. Atomistic models of point defects and FPs can be used to develop continuum thermochemical models of point defect concentrations and FG diffusivity in the fuel matrix. Several models include the dependence of these properties on the FG content. Such thermochemical models are further used to predict fuel thermodynamic properties, such as the free energy, and to simulate FP diffusion at various temperatures.

3. To investigate the oxidation behavior of U_3Si_2 in water and oxygenated environments using a combination of experiments and *ab initio* techniques. This is important because the interaction between the surfaces of metallic nuclear fuel and oxygen can result in oxide formation and the decrease of thermal conductivity. As well, reaction with water can result in the corrosion of nuclear fuels. Hence, the reactions of U_3Si_2 with oxygen and water affect a lot of processes in the nuclear fuel cycle such as fabrication and storage of nuclear fuels, and permanent disposal of spent fuel in deep geologic repositories.

1.5. Thesis arrangement

The realization of the objectives noted above will be demonstrated in the following chapters of this manuscript-based thesis.

The thesis contains nine chapters. Chapter 1 contains the overview, motivation, rational for ATF concepts selection, and objectives of the research, while the review of relevant literature is presented in Chapter 2.

[1] Metallic fuels in this thesis are systems with no electronic band gap. They have electronic contribution to thermal conductivity and heat capacity.

Details of the computational methods used in this research study are provided in Chapter 3. These include the theory and numerical forms of the mathematical models implemented in the open source and commercially available codes used in this project.

Chapter 4 focuses on the thermophysical properties and the electronic structure of UB_2 using density functional theory. This aspect of the research work addresses the first specific objective and has been published in the *Journal of Nuclear Materials*.

In Chapter 5, the effects of point defects, and Xe and Zr fission products on the structural stability of UB_2 are discussed. This chapter fulfills the objective of determining the effects of point defects and FPs, such as Zr and Xe, on metallic fuels using atomistic codes. Research findings discussed in this chapter have been published in the *Journal of Nuclear Materials*.

Chapter 6 focuses on the anisotropic thermophysical properties of U_3Si_2 using classical molecular dynamics. The anisotropic nature of the thermal properties is highlighted. The reason for this study is to fulfil the first objective with respect to U_3Si_2. This chapter has been published in the *Journal of Nuclear Materials*.

In Chapter 7, the mechanism of U_3Si_2 corrosion by oxygen molecules is discussed. This chapter particularly addresses the third specific objective. The content of this chapter has been published in the *Journal of Physical Chemistry Chemical Physics*.

The oxidation behavior of pristine and defective U_3Si_2 in water is addressed in Chapter 8. The effect of multiple water molecules and coadsorption with oxygen atoms on the different U_3Si_2 surfaces are investigated and discussed in this chapter. The research paper has been published in *Journal of Physical Chemistry C*.

Chapter 9 provides a summary of the work done, conclusions made from the research findings, discusses ongoing work, and provides suggestions for further investigations.

Chapter two

Literature review

2.1. Overview of Chapter 2

A brief description of important concepts related to nuclear fuel is introduced in this chapter. A review of previous work available on UO_2 and some ATF concepts is provided, as well. The plausible extreme conditions that can result in fuel degradation are highlighted with respect to U_3Si_2 and UO_2 fuels. Subsequent chapters build upon this general review, and a further introduction to the specific topic of the chapters, which include critical reviews of the relevant literature.

2.2. Nuclear power

The use of fossil fuels in the generation of energy has led to the emission of carbon dioxide (CO_2) and other greenhouse gases. This implies that global warming is imminent if our present methods of energy generation are not restructured. Furthermore, as supplies of conventional fossil fuels, such as petroleum and coal, become more challenging to access, clean and renewable energy sources are needed. Nuclear energy is the only fully developed technology available that can provide relatively cheap energy, without generating harmful greenhouse gases.

Nuclear power plants use the heat generated during the fission process to heat up water to produce steam. The steam is then used to turn large turbines that generate electricity. A simple schematic of a nuclear power plant is presented in Fig. 2.1. In this design, the heat generated by fission process is removed from the reactor by the coolant in the primary loop, which is then used to generate steam in the secondary circuit. This setup prevents the transport of radioactive material from the containment building to the conventional island by separating the reactor core from the secondary loop. The steam turbines power the electrical generator. The majority of reactors are built close to a source of cool water, such as sea or a river, so that the steam can be condensed and returned to the secondary loop, although some designs use air cooling systems.

Aside from replacing coal and fossil fuel for electricity production, nuclear energy also plays a vital role in production of radioisotopes [17], and marine propulsion [18]. The first generation of nuclear power reactors around the globe were designed not only to produce electricity, but also to produce plutonium for military purposes [19].

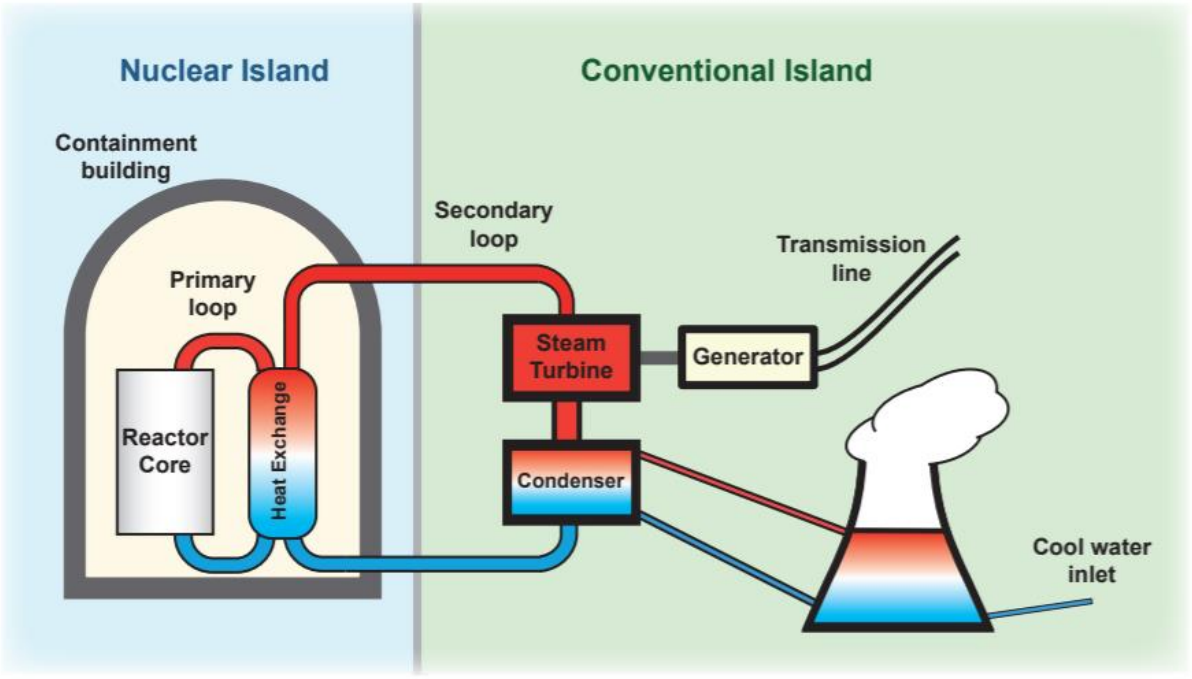

Fig. 2.1. Schematic diagram of a typical nuclear power station [20].

2.2.1. Nuclear reaction

The heat for boiling water to run the turbines comes from nuclear reactions, which occur when there is a splitting of the nuclei of atoms (fission) or a combination of small nuclei which form more massive atoms (fusion). A typical fission reaction is illustrated in Fig. 2.2.

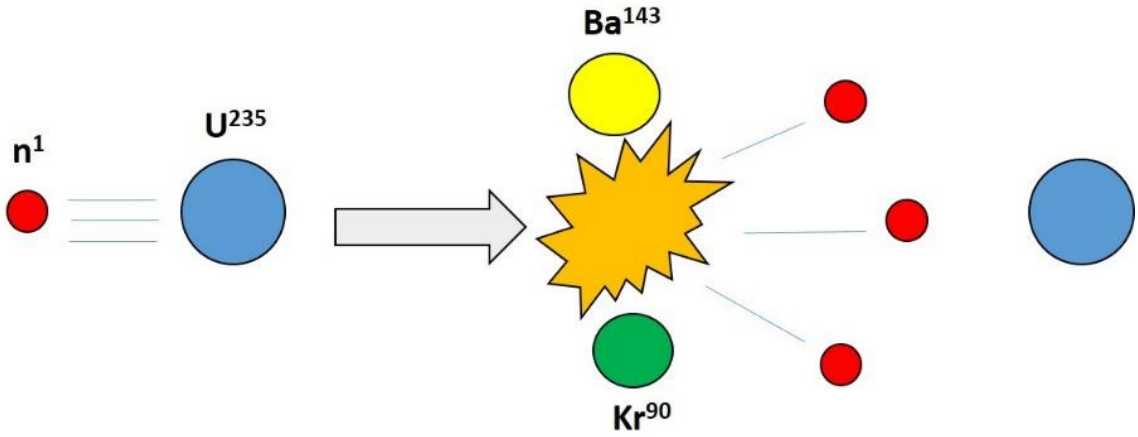

Fig. 2.2. Neutron absorption by a U^{235} nucleus fissions to form two fission products (e.g. Kr^{90} and Ba^{143}) and several high velocity neutrons. For a chain reaction to occur one of these neutrons must fission a second U^{235} nucleus.

During the fission reaction, the parent element fragments into a bimodal distribution of elements whose atomic masses are approximately half that of the fragmented uranium, as shown in Fig. 2.2. Nuclear energy generation is due to the difference in mass, which is because the combined mass of the fragmented nuclei is less than that of the fissile species (mass deficit). The mass deficit is then equated to the binding energy by Einstein's famous equation, $E = \Delta mc^2$ where 'c' is the speed of light [21]. The energy is released as thermal or kinetic energy, and electromagnetic radiation [22]. Fig. 2.3 shows the binding energy of nuclei as a function of their atomic number.

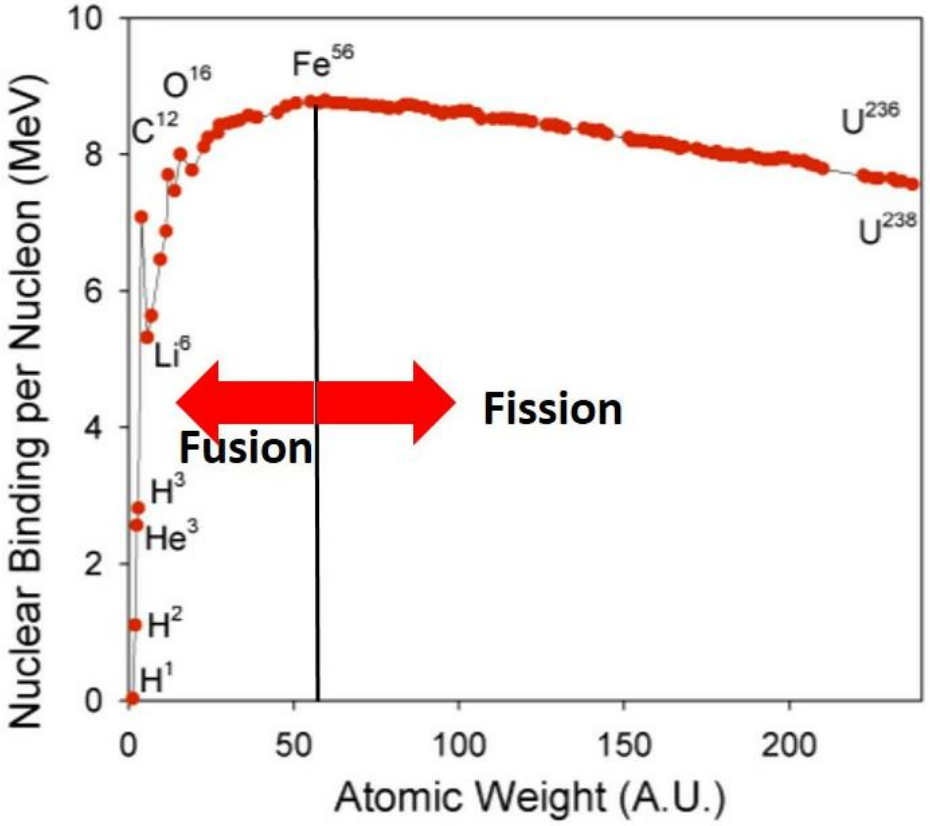

Fig. 2.3. Binding energy per nucleon as a function of atomic weight (A.U.) of isotopes. Arrows represent fission and fusion respectively. Adapted from Ref. [23].

Even though nuclear reaction can be spontaneous, introducing a neutron can result in transmutation of the nucleus, thereby increasing the probability of the occurrence of the fission reaction. The neutron produced from the fission process usually initiates another fission process, such that a fission chain reaction is sustained [24]. The chain reaction, in turn, leads to the formation of a cascade of FPs. The types and yield of FPs generated are dependent on the neutron energy spectrum, available fissile isotopes, type of reactor, and burn up or the amount of fission [25]. Fig.

2.4 shows the distribution of FPs generated in percentage yield, as a function of atomic mass of FPs [26]. The accommodation and distribution of fission products in the fuel varies between reactors.

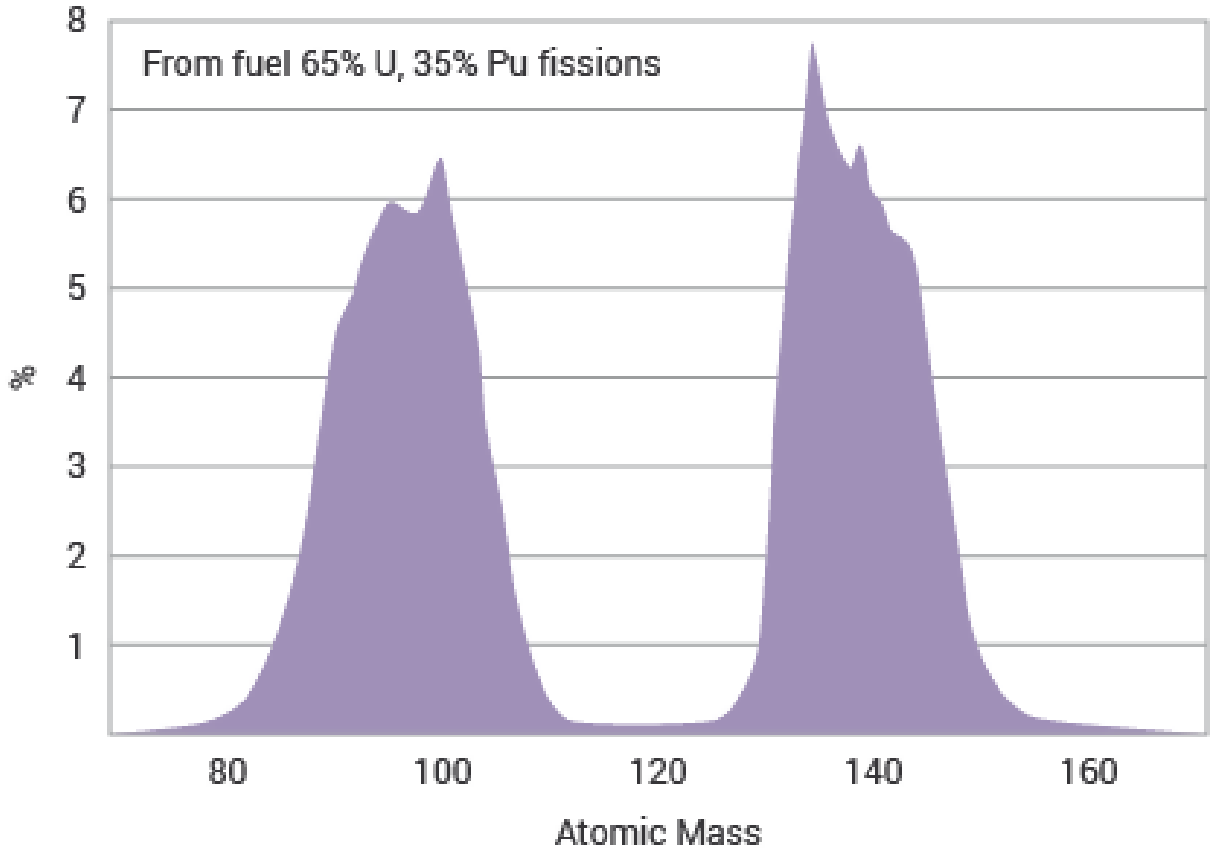

Fig. 2.4. Distribution of Fission Product across the periodic table. Adapted from Ref. [27].

2.3. Generation of nuclear reactors

Since the design and deployment of the first commercial nuclear reactor in the 1950s [28], there has been a consistent technological advancement of nuclear reactors with each stage of improvement referred to as a ‘Generation.' Currently, three generations of nuclear power systems, i.e., Generations I, II, and III, are used around the world. Because generation III+ are believed to be within the current state-of-the-art, fundamental research on nuclear reactors is focused on advanced reactors commonly called Generation IV [29]. They are expected to improve actinide waste management, economics, safety, reliability, and resistance to proliferation. Beyond the reactor design, new fuel forms are proposed for the operation of these advanced reactors. Fig. 2.5 shows the evolution in Generations and their main representatives throughout the decades.

In 2000, a group of countries formed the Generation IV forum (GIF) with the purpose of developing the research necessary to test the feasibility and performance of Generation IV nuclear systems, and to make them available for industrial use by 2030 [29]. After a thorough review of about 100 design concepts in 2002, GIF members selected six systems for further research and development.

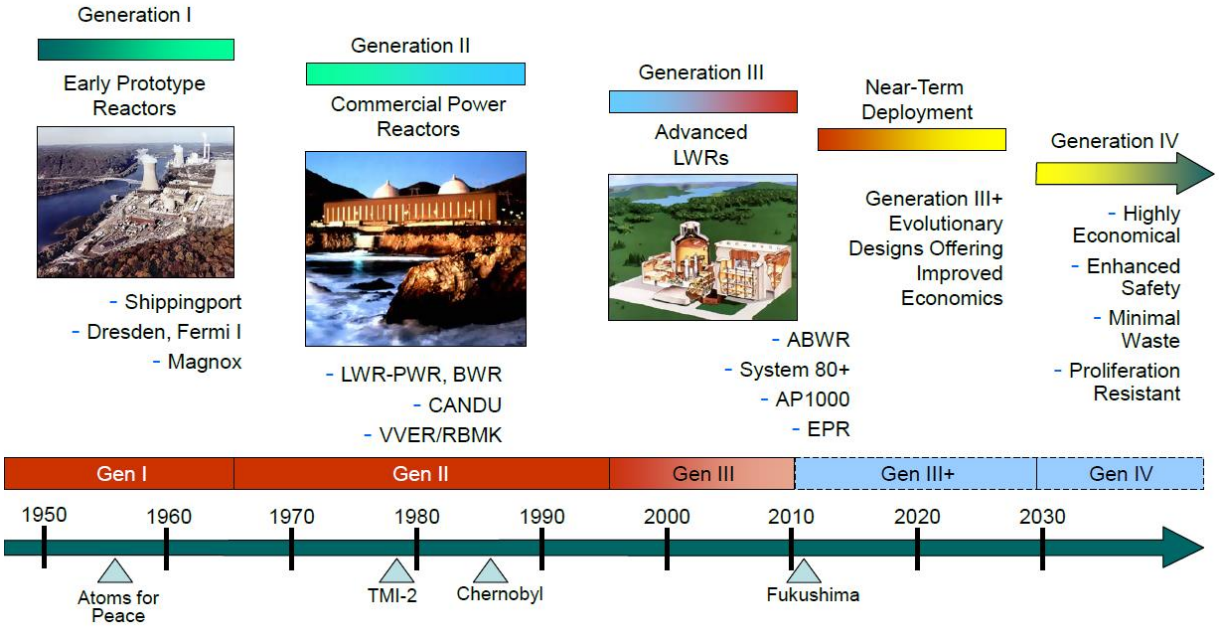

Fig. 2.5. Generation of nuclear reactors since the inception of the nuclear age [30].

The six systems are Sodium-cooled Fast Reactor (SFR), Lead-cooled Fast Reactor (LFR), Gas-cooled Fast Reactor (GFR), Supercritical Water-cooled Reactor (SCWR), Very High Temperature gas-cooled Reactor (VHTR), and the Molten Salt Reactor (MSR). The coolants to be used in these reactors include water (SCWR), helium (GFR and VHTR), sodium (SFR), lead or lead-bismuth (LFR), and fluoride salts (MSR) [31]. Table 2.1 summarizes the technical features of the six Gen IV systems.

As a member of the GIF, Canada is focused on the development of the SCWR given her experience with the CANada Deuterium Uranium (CANDU) reactor. The SCWR system features two fuel cycle options. The first option is an open cycle with a thermal neutron spectrum reactor, while the second option is a closed cycle with a fast-neutron spectrum reactor and fuel reprocessing capability. The two variants operate as a water-cooled reactor above the thermodynamic critical point of water (22.1 MPa, 374°C) thereby achieve a thermal efficiency of ~44% [27].

Table 2.1. Approximate operating environment for Gen IV systems. They are rated in terms of safety, proliferation resistance, and physical protection [32].

Reactor type	Coolant Inlet Temp (°C)	Coolant Outlet Temp (°C)	Maximum Dose (dpa*)	Pressure (MPa)	Coolant
SCWR	290	500	15–67	25	Water
VHTR	600	1000	1–10	7	Helium
SFR	370	550	200	0.1	Sodium
LFR	600	800	200	0.1	Lead
GFR	450	850	200	7	Helium/SC CO_2
MSR	700	1000	200	0.1	Molten salt

*dpa is a displacement per atom and refers to a unit that radiation material scientists used to normalize radiation damage across different reactor types. For one dpa, on average each atom has been knocked out of its lattice site once.

The actualization of the fast-spectrum option is dependent on the successful development of suitable materials that can withstand the harsh environment prevalent in the reactor. In either variant of the SCWR, the model plant is expected to provide about 1700-MWe power, at an operating pressure of 25 MPa, and a reactor outlet temperature of 550°C.

The fact that SCWRs are water reactors, they share the steam explosion and radioactive steam release hazards of BWRs and LWRs as well as the need for extremely expensive heavy-duty pressure vessels, pipes, valves, and pumps as shown in Fig. 2.6. These shared problems are inherently more severe for SCWRs due to operation at higher temperatures [33]. Therefore, safety features similar to the BWR are added to the SCWR design.

Due to the low density of the supercritical water, an additional moderator is added to thermalize the core in the case of a thermal type reactor. It is important to note that the balance of plant is considerably simplified, because the coolant does not change phase in the reactor.

The SCWR system is highly economical compared to other concepts, because of the high thermal efficiency and simple plant design. The fast-spectrum is ranked highly with respect to sustainability due to the possibility of actinide recycling. The SCWR is also well rated in terms of safety, proliferation resistance, and physical protection.

The SCWR system is primarily designed for electricity production, with an option for efficient fuel management. Based on the technological readiness and the milestones achieved so far in materials compatibility research, the SCWR system is estimated to come online in 2025 [29]. Table

2.2 lists the 14 GIF members, the ten active members that signed the Framework Agreement, and the systems on which these members are working, as of 2018.

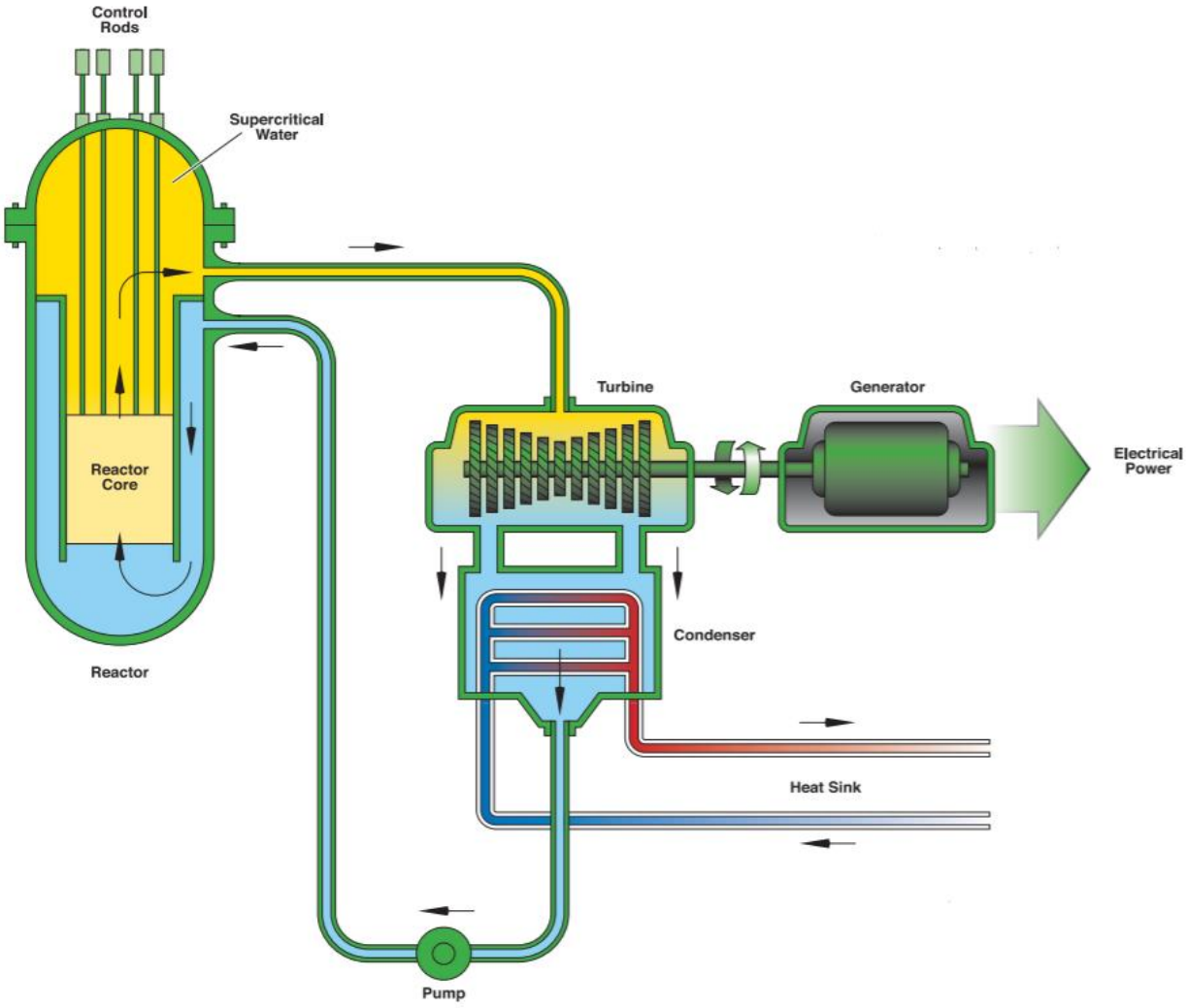

Fig. 2.6. Schematic of Supercritical Water Reactor [29].

Table 2.2. The involvement of GIF members in Gen IV systems R&D as of 2018 is presented in Table 1. [34].

GIF member	Implementing agency	Generation IV reactors					
		GFR	SCWR	SFR	VHTR	LFR	MSR
Argentina							
Australia	Australian Nuclear Science and Technology (ANSTO)				×		×
Brazil							
Canada	Department of Natural Resources (NRCan)		×				
China	China Atomic Energy Authority (CAEA) Ministry of Science and Technology (MOST)		×	×	×		
Euroatom	European Commission's Joint Research Centre (JRC)	×	×	×	×	×	×
France	Commissariat à l'énergie atomique et aux énergies alternatives (CEA)	×		×	×		×
Japan	Agency for Natural Resources and Energy (ANRE) Japan Atomic Energy Agency (JAEA)	×	×	×	×	×	
Korea	Ministry of Science, ICT and Future Planning (MSIP) Korea Nuclear International Cooperation Foundation (KONICOF)			×	×	×	
Russia	State Atomic Energy Corporation "ROSATOM" (ROSATOM)		×	×		×	×
South Africa	Department of Energy (DoE)						
Switzerland	Paul Scherrer Institute (PSI)				×		×
United Kingdom							
United States	Department of Energy (DOE)			×	×		×

2.4. Nuclear fuel

Fissile isotopes of an element are required for the occurrence of a fission reaction. The most used fissile isotope is the U^{235}, but in nature, uranium consists of two isotopes of interest: ^{235}U (0.72 atomic %), which is fissile, and ^{238}U (99.27 atomic %), which is fertile. The CANDU reactor which

uses deuterium as a moderator, runs on unenriched, natural uranium as its fuel, while most Light Water Reactors (LWRs) and Advanced Gas-cooled Reactors (AGRs) use uranium fuel enriched 3 to 5% ^{235}U as a low-enriched uranium (LEU) fuel. Some research reactors use highly enriched uranium (HEU) with >20% ^{235}U. However**,** international efforts have substituted LEU fuel in most of these research reactors. Some radioisotope production also uses HEU as target material for neutrons, and this is being phased out in favor of LEU [35].

Due to the metallic nature of uranium, it has high thermal conductivity which is desirable for efficient heat dissipation, but the low melting point of 1405 K [36,37] and the structural phase transitions from orthorhombic to tetragonal at 935 K and tetragonal to body-centered cubic at 1045 K [37,38], limits its use at high temperatures typical of commercial reactors. This informs the development of uranium-plutonium-zirconium (U-Pu-Zr) alloys which are considered to be one of the most promising metallic fuels. The addition of Zr in U-Pu matrix was sought to increase the melting temperature of U-Pu alloys and to enhance the compatibility between the fuel and stainless-steel cladding by suppressing the interdiffusion of fuel and cladding constituents during steady-state reactor operations. However, their deployment in reactors has been slowed down by the limited understanding of the irradiation behavior of U-Pu-Zr transmutation fuels [39]. Hence, uranium metals are processed to produce UO_2 which is a ceramic material with a high melting point of 3500 K and is used in most LWRs [40].

2.4.1. Currently used fuel: UO_2

UO_2 is the primary fuel used in the nuclear power industry today. There are about 450 commercial nuclear power reactors around the world as of September 2019, while about 50 are at different stages of completion [41]. Most of these reactors are of the LWRs, AGRs, or the CANDU reactor types, and they are fueled with sintered pellets of UO_2 containing natural or slightly enriched uranium. UO_2 powder is a ceramic fuel, which is usually processed by sintering to improve its mechanical properties. During sintering, the following significant changes commonly occur: an increase in grain size, changes in pore shape, pore size, and pore number.

A significant drawback in the continuous use of UO_2 is the low thermal conductivity, which is further degraded due to irradiation damage at high temperatures. The Schematic (Fig. 2.7) represents an irradiated UO_2 fuel at the microscopic scale. Fig. 2.7 (a) depicts the grain boundary structure of the UO_2 fuel with the most important radiation-induced features such as dislocation

lines and loops, gas inclusions, metallic precipitates, and grain restructuring due to high burn-up. Fig. 2.7 (b–d) is the Scanning Electron Microscopy (SEM) images showing the microstructure of UO_2 after irradiation. Where Fig. (b) is the UO_2 fuel after exposure to radiation at high temperature, (c) shows interconnected gas bubbles at grain boundaries, and (d) represents the fuel pellet after restructuring. Fig. 2.7 (e–g) are Transmission Electron Microscopy (TEM) images showing dislocation lines. Fig. 2.7 (e) shows the formation of small intragranular gas bubbles uniformly aligned along fission tracks, while (f) represents the accumulation of metallic precipitates, and (g) are grains in the high burn-up structure region after restructuring [42].

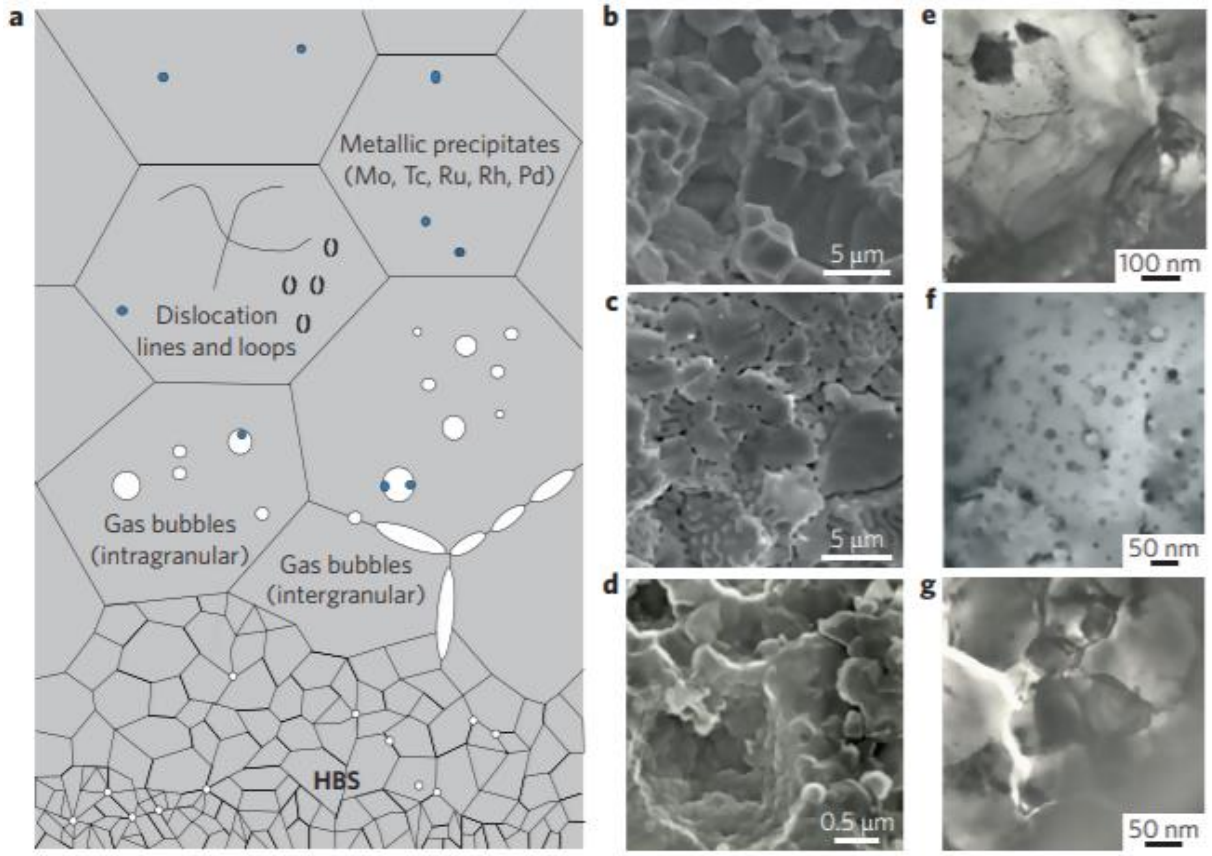

Fig. 2.7. Some parameters affecting thermal conductivity of UO_2 fuel pellet. Figure reproduced with permission from Nature materials [42].

As discussed earlier, a range of FPs are generated during fission process when the reactor is in operation. These FPs are either soluble or insoluble in the UO_2 lattice. FPs are collected into representative groups that exhibit similar chemical and physical behaviors in irradiated fuel as shown in Table 2.3. The FPs may be distributed among several phases, depending on the temperature, pressure, and composition of the fuel after burnup.

The state of the FPs determine their behavior in nuclear fuel materials. In the case of fission gases (FGs) such as Xe, Kr and He which are produced during fission events, they move in a ballistic manner along the lattice and come to a rest after the energy has been dissipated to the surrounding material. It is important to note that fission gas release occurs within fuel matrix in three stages:

Table 2.3. Chemical state of fission products in irradiated UO_2 fuel [26].

Fission products[a]	Chemical state	% of fission yield[b]
Xe, Kr, Br, I (Cs, Rb, Te)	Volatile or gaseous product	13+ (12)
Cs, Rb, Ba, Zr, Nb, Te (Mo, Sr)	Oxide precipitate	30 +(15)
Mo, Tc, Ru, Rh, Pd, Ag, Cd, In, Sn, Sb (Tc)	Metallic precipitate	27 +(1)
Sr, Y, La, Ce, Pr, Nd, Pm, Sm, Nb (Zr, Ba, Te)	Products in solid solution	30 +(19)

a. Brackets indicate elements that exhibit the possibility of an alternative chemical state.

b. For a 3.2% enriched PWR fuel rod at 2.9% burn-up. The bracketed Figures correspond to the bracketed elements in column 1.

1. Transport of gas atoms through the bulk of the grain,

2. Grain face bubble nucleation, growth, and interconnection with grain edge bubbles,

3. Transport of gas through interconnected grain edge tunnels to free surfaces for release.

If initiated near the grain boundaries, FGs may come to rest at the grain boundary instead of in the fuel lattice as observed in UO_2 [43]. If the FG becomes immobile within the fuel crystal, subsequent fission events may cause crystal damage and species re-location may result in further migration of the gas atom to the grain boundary [44].

2.4.2. Evolutionary fuel concepts

The near-term evolutionary fuel concepts consist of minor modifications to the standard UO_2–Zicarloy fuel rod materials to provide enhanced accident tolerance. The use of oxide additives such as Cr_2O_3 and Al_2O_3 in UO_2 is considered to be an attractive technical and economical solution. This technology might be able to reduce lengthy approval time for new fuel design, because it uses existing infrastructure, experience, and expertise. Therefore, evolutionary concepts can be deployed in a shorter time frame [45–47].

For instance, to combat the issue of FGR, fuel vendors, such as AREVA, have focused on the manufacturing of UO_2-Cr_2O_3 composite fuel due to the fact that Cr_2O_3 promotes the formation of

larger grain sizes in UO_2 fuel which enhances FG retention. A combination of experimental observation and multiscale simulation was used by Che and co-workers [48] to assess the enhanced safety associated with chromia-doped fuel compared to the standard UO_2 fuel in LWRs. Predictions from BISON indicated that the fuel rod with Cr_2O_3-doped UO_2 was subject to a lower FGR and resulted in reduced volumetric expansion, less radioactive gas release upon fuel rod failure, and delayed fuel rod rupture compared to the fuel rod with standard UO_2.

Similarly, Westinghouse has developed a Al_2O_3-Cr_2O_3 doped UO_2 pellet (also referred to as ADOPT: Advanced DOped Pellet Technology) [49]. The additives facilitate densification and diffusion during sintering, which results in about 0.5% higher density within a shorter sintering time and nearly five times larger grains, compared with standard UO_2 fuel. While improving the desired properties, the amount of chromium has been kept low to minimize the parasitic neutron absorption. On the other hand, aluminum has a minimal cross-section for thermal neutrons similar to that of Zr. Hence, the use of Al_2O_3 with Cr_2O_3 to improve the grain size growth in UO_2. The properties of the Al_2O_3-Cr_2O_3-doped pellets are very similar to pellets with just Cr_2O_3 dopant, and the addition of Al_2O_3 can be viewed as a way to lower the total amount of Cr_2O_3 dopant [45].

2.4.3. Revolutionary fuel concepts: Accident tolerant fuel

The nuclear accident at Fukushima in March 2011, motivated fuel vendors, in collaboration with national and international regulatory agencies, to consider an alternative fuel-clad system that can withstand the loss of coolant for a considerably longer time in the case of an accident. The alternate fuel-clad system must maintain high safety and reliability during regular operation, and it would be preferable if significant changes to the present design of the current reactor are not required [9]. Such fuel is expected to have higher thermal conductivity, reduced centerline temperature during operation, reduced reactions with cladding, and reduced probability for melting. The cladding is also expected to reduce vulnerability to fracture and have an increased resistance to thermal shock and melting.

This calls for a paradigm shift toward new fuel forms that can withstand severe accidents such as station blackout (SBO) and loss of coolant accident (LOCA) for a considerable period. Any solution deployment will involve the coupling of fuel and clad with minimal chemical interaction. Hence, the approach adopted is a gradual transition from a traditional UO_2-Zircalloy system to a more advanced fuel-cladding forms, as illustrated in Fig. 2.8 [50].

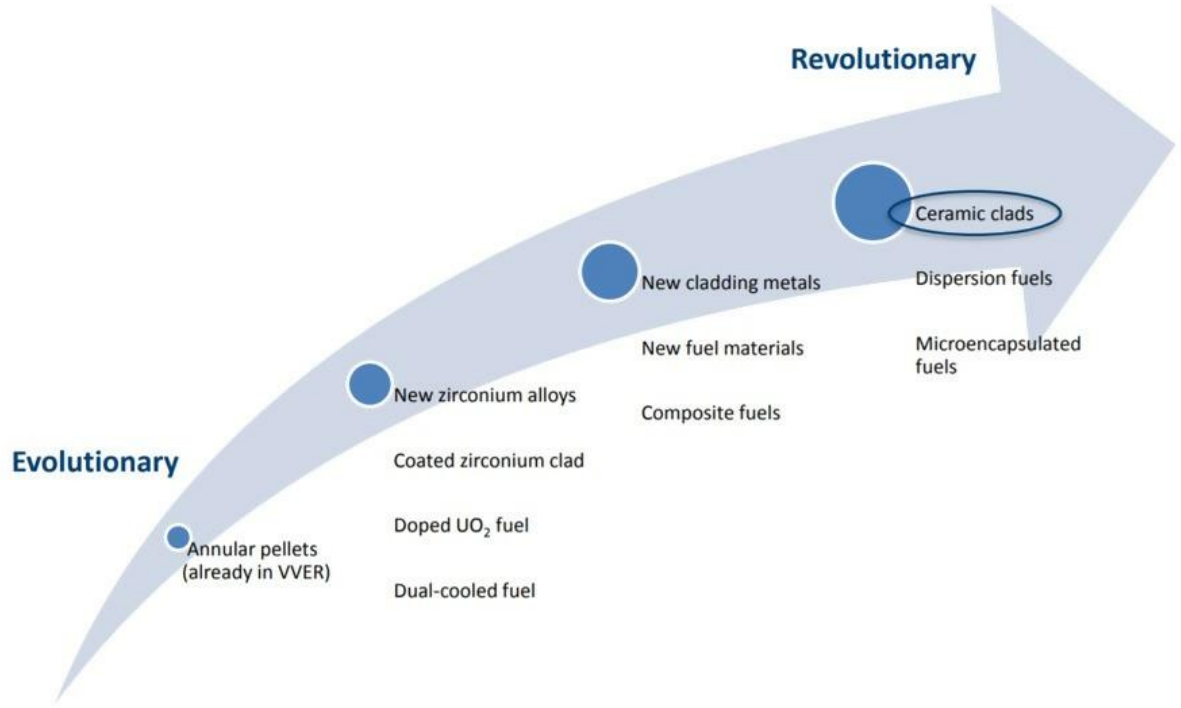

Fig. 2.8. Schematic showing transition from evolutionary to revolutionary fuel concepts [50].

Revolutionary fuel concepts include the addition of ceramic (SiO_2, BeO, SiC, diamond) or metallic (Mo, Cr) additive materials into UO_2 pellets. Encapsulated fuel such as UO_2 encapsulated in a Mo microcell and materials with high fissile density (silicides, borides, and carbides) are also considered to be revolutionary according to Nuclear Energy Agency (NEA) classification [51]. Recent developments in the area of UO_2-Mo micro-cell composite, uranium silicides and uranium borides are further discussed below due to their potential use as ATFs.

2.4.3.1. UO_2-Mo micro-cell composite as ATF

In a previous study, Kim *et al*. [8] studied the properties of UO_2-Mo micro-cell composites, which are produced by conventional powder processing and sintering techniques. During fabrication, a mixture of UO_2 and Mo powder was pressed to form green pellets, which were then sintered at an elevated temperature at which the Mo for the micro-cell's wall formed a liquid phase, thereby penetrating through grain boundaries and enveloping the UO_2 grains to make the designed metallic micro-cell. Cr can also be used in place of Mo as metallic cell wall materials because of the relatively high melting temperature, high thermal conductivity, and manageable neutron absorption cross section. The schematic of the design concept is shown in Fig. 2.9.

The thermal conductivity of a micro-cell UO_2-Mo pellet is significantly increased compared to that of the UO_2 pellet. Furthermore, the thermal conductivity of the UO_2-Mo pellet with continuous Mo channels is much higher than that of the simple UO_2-Mo pellet with disconnected Mo particles according to Kim *et al*. [52]. They showed that the increase in thermal conductivity is proportional to the Mo metal volumetric fraction and is slightly affected by the cell size and cell wall thickness. It is confirmed that the continuous Mo micro-cell works as a heat conducting channel in the pellet.

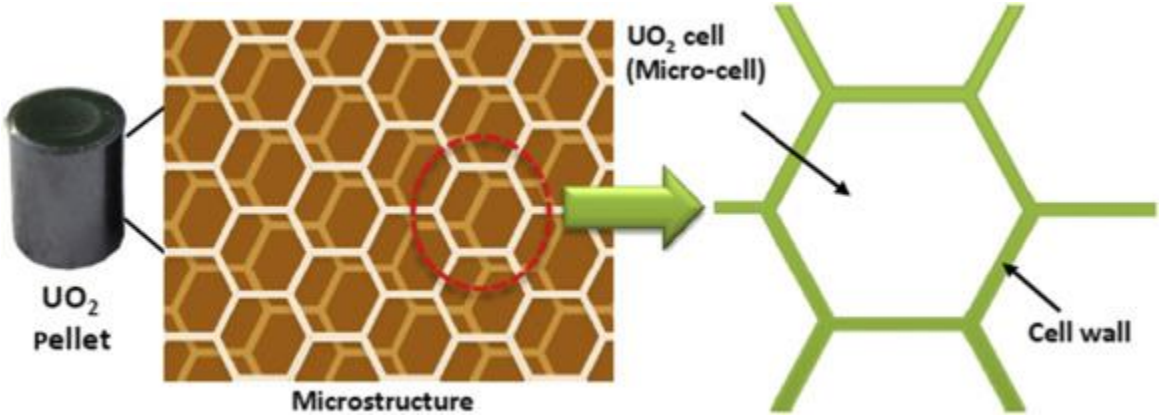

Fig. 2.9. Conceptual schematic representation of a microcell UO_2 pellet [8].

A more recent out-of-pile test was conducted to evaluate the thermophysical properties and fuel behavior of 5 vol% Mo microcell UO_2 pellet under the normal operating conditions and accident conditions. The results clearly show a 100% increase in the thermal conductivity at 1000 ^oC. On the other hand, the linear thermal expansion coefficient of the Mo metallic microcell UO_2 pellet decreased with an increasing Mo content which is due to the lower thermal expansion coefficient of Mo compared to UO_2. Under the transient conditions, it is expected that the mechanical stress on the cladding due to pellet expansion can be reduced by this feature of the metallic microcell pellet [52].

Irradiation testing of UO_2-Mo microcell pellets is currently ongoing at above ~12,000 MWd/mtU and is proceeding to reach a higher burnup. This will be followed by further testing of the thermophysical properties of the radiated pellets. However, preliminary analysis of the online measurement data of the fuel centerline temperature of irradiated microcell UO_2 pellet exhibited a temperature that was remarkably lower than the reference UO_2 fuel, typically ~20% lower [52].

2.4.3.2. Uranium Silicides as an ATF

Research activities in the last few years have also been focused on determining thermophysical properties, developing an economical processing route, understanding the oxidation behavior, determining radiation tolerances, and understanding pellet-cladding interactions of various metallic ATF concepts [13,53–57].

For instance, White *et al*. prepared buttons of U-Si binary alloys, such as U_3Si_2, U_3Si, U_3Si_5, and USi, by arc-melting uranium feedstock with silicon. For each of the U-Si binary alloys, thermophysical properties were determined. Their work clearly shows that the increase in the thermal properties is due to the presence of electronic contribution. A follow up work by Antonio *et al*. [58] further showed that the thermal conductivity of U_3Si_2 is ~8.5 W/m-K at room temperature and the electronic part dominates heat transport above 300 K, with ~2 W/mK contribution from phonons in the low temperature regime. However, the contribution from phonon-phonon scattering at high temperatures is lacking in their study. This is investigated at an atomic scale in Chapter 6.

Aside from the use of arc-melting for synthesizing U_3Si_2, Lopes *et al*. [59] investigated the possibility of using spark plasma sintering (SPS) techniques to prepare U_3Si_2 pellets. The results showed that pellets of U_3Si_2 with high density (>95% Theoretical Density) can be obtained with an SPS in the temperature range of 1200 –1300 ^oC in a shorter time compared to the arc-melting method. However, scalability of SPS for mass production of U_3Si_2 pellets need to be developed.

Work has also been done on the incorporation of a burnable absorber into U_3Si_2. For example, Turner *et al*. [60] investigated three different methods of mixing gadolinium with uranium silicide in order to determine the potential for its use as a burnable poison with U_3Si_2. However, formation of a ternary U-Si-C phase suggests that an alternative method of burnable poison introduction will be required.

Due to the tetragonal crystal structure of U_3Si_2, the thermophysical properties are expected to be anisotropic [61]. This was confirmed in recent study by Obbard *et al*. [62] who investigated the anisotropic nature of the lattice expansion using an *in-situ* neutron diffraction method. Their result showed an onset of anisotropy in the thermal expansion above 1000 ^oC with a reduced expansion in the a-axis and an increased expansion in the c-axis. This is supported by the previously observed anomalies in the thermal expansion at this temperature by White *et al*. [13]. However, anisotropy

in the thermal conductivity has not been studied, which accounts for part of my work in Chapter 6 of this thesis.

Besides the experimental work on U_3Si_2, there have been a number of computational investigations towards understanding the thermophysical properties, electronic structure, and defects behavior of U_3Si_2 as an ATF.

Wang *et al*. [63] predicted the structural, elastic, and electronic structure properties of U_3Si_2 using the density functional theory (DFT) with a Hubbard U correction of 4.0 eV. They also predicted the formation energy of a uranium vacancy defect to be the lowest compared to the silicon vacancy. In a follow up study, Noordhoek *et al*. [64] using a U value of 1.5 eV predicted the elastic, electronic, and vibrational properties of U_3Si_2. They further predicted new stable structures of binary U-Si compounds using an evolutionary algorithm code. Finally, they observed that the generalized gradient approximation (GGA) and GGA + spin orbit coupling description of U_3Si_2 is not stable on the convex hull. Meanwhile, they also predicted the ferromagnetic phase of U_3Si_2 to be the most stable in contradiction to current experimental results.

Aside from the thermophysical properties of nuclear fuel materials, defects behavior plays a critical factor in the life cycle of nuclear fuels. Work by Middleburgh *et al*. [66] using the density functional theory and thermochemical analysis, assessed the stability of U_3Si_2 with respect to non-stoichiometry reactions in both the hypo- and hyper-stoichiometric regimes. They observed that the degree of non-stoichiometry in U_3Si_2 is much smaller than in UO_2 and at most reaches a few percent at high temperature. They concluded that non-stoichiometry will affect the performance of U_3Si_2 due to the formation of a non-stoichiometric $U_3Si_{2\pm x}$ phase or precipitation of a second U-Si phase.

In a separate study, Andersson *et al*. [67] investigated the self-diffusion of U, Si, and Xe in U_3Si_2 using DFT +U. Due to the tetragonal structure of U_3Si_2, the diffusion coefficients differ in the a-b plane and along the c axis of the crystal structure. They observed that U self-diffusion is fast in the a-b plane through an interstitial mechanism. Meanwhile Xe is predicted to preferentially occupy U (2a site) vacancies under all thermodynamic conditions. The fastest Xe diffusion mechanisms are predicted to be assisted by a second vacancy, either a U (2a site) vacancy along the c-axis or a Si vacancy in the a-b plane of the U_3Si_2 structure. In comparison to UO_2, the self-diffusion rates

in U_3Si_2 are faster than U diffusion in UO_2, and the rate of the U interstitial mechanism is even faster than that of O diffusion in UO_2.

Due to the possible formation of a secondary U-Si phase, Lopes *et al*. [68] evaluated the stability of the U_5Si_4 phase investigated earlier by Middleburgh *et al*. [66]. They predicted a hexagonal P6/mmm U_5Si_4 structure using an evolutionary algorithm code. However, phonon calculations reveal that this structure is dynamically unstable. This together with the observation of the existence of a stable isostructural ternary $U_{20}Si_{16}C_3$ (P6/mmm) phase implies that U_5Si_4 could be stabilized by oxygen or carbon. This justifies the exclusion of a U_5Si_4 phase from the phases of U-Si explored in their future studies.

In order to further provide data for the development of a U_3Si_2 fuel, Beeler *et al*. [69] developed a semi-empirical modified Embedded-Atom Method (MEAM) potential to aid multiscale simulations of U-Si systems. The potential is fitted to the formation energy, defect energies, and structural properties of U_3Si_2. The primary phase of interest (U_3Si_2) is well described over a wide temperature range and displays good behavior under irradiation and with free surfaces. The potential can also describe a variety of U-Si phases across the composition spectrum. This potential is used in Chapter 6 of this thesis for calculating the thermophysical properties of U_3Si_2.

2.4.3.3. Uranium borides as an ATF or burnable absorber

As mentioned earlier, the uranium borides (UB_2, UB_4, and UB_{12}) are also of interest in the development ATFs. Unlike the U–Si alloys, few works have been done on the borides. For instance, Flotow *et al*. [11] synthesized and measured the heat capacity of UB_2. They also determined the entropy, enthalpy and Gibbs energy of formation. The relatively high value for the coefficient of the linear term of the heat capacity indicates that uranium diboride is a good electrical conductor. This fact, is supported by the electronic structure calculation by Matar *et al*. [70] which shows a metallic character based on the electronic density of states (DOS) and the crystal orbital overlap populations (COOP) analysis.

More recently, after part of the work that is presented here was published in peer reviewed journal [71], Burr *et al*. [72] investigated the stability, diffusivity and clustering behavior of defects in UB_2 in light of the potential application as a burnable absorber in the nuclear fuel. They clearly showed the anisotropic behavior of the diffusion process which is absent in the work presented in this

thesis. They proceeded to explain the limiting effect of the anisotropic migration of defects (both interstitials and vacancies) on the radiation tolerance of UB_2.

In a CALPHAD analysis, Noordhoek *et al*. [65] studied the thermodynamic stability of UB_2 as a composite fuel. They showed that at equilibrium, the formation of UO_2-UB_2 composite results in a reduction of UO_2 to hypostoichiometric UO_{2-x}. The extent of hypostoichiometry is influenced by the type of uranium boride secondary phase. The thermal conductivity of the composite decreases with the departure from stoichiometry. However, they noticed that the effect is small with small deviations and reduces at high temperatures.

Meanwhile, the CALPHAD analysis of U_3Si_2-UB_2 showed the possible formation of a third phase which can be present as a minor component of the composite. In the case of UN-UB_2 composite, the authors observe the presence of UN and UB_2, and uranium metal in the nitrogen-poor region, while nitrogen rich regime consists of UN, UB_2 and BN [65].

To further the development of boride fuel, Guo *et al*. [73] synthesized uranium tetraboride (UB_4) by boro-carbothermal reduction of UO_2 using B_4C and carbon as combined reduction agents in an argon environment. They showed that the oxidation of UB_4 in air started at 500 ^oC; which means there was better oxidation resistance than other basic uranium nuclear fuels (such as UO_2 and UC, UN, and U_3Si_2). This has an implication on safe handling when used as a nuclear fuel or burnable absorber.

Overall preliminary work on the silicides and borides suggest their possible use as an ATF. However, recent outcomes of irradiation behavior under LWR conditions [74,75], cladding compatibility [76–78], behavior under accident conditions [79–81], and economic considerations [50,51,82] have helped stakeholders to focus on U_3Si_2 rather than the other U–Si binary alloys [55,83]. Meanwhile data on the thermophysical properties of the borides is lacking. This accounts for part of my work in Chapter 4 of this thesis.

2.5. Thermophysical properties of nuclear fuel

Improving upon the thermophysical properties of UO_2 is a primary focus of any alternative LWR fuel. This is because the poor thermal conductivity of UO_2 drives steep thermal gradients and high centerline temperatures during reactor startup and operation [84]. Hence, improvements in the thermal conductivity of the fuel will limit thermally-induced stresses, which is otherwise responsible for pellet cracking. Lower temperatures throughout the fuel pellet will also reduce

diffusion, and thereby retard species transport and in-pile restructuring. All of these evolutions contribute to operational uncertainty [85].

In Table 2.4, some of the important thermophysical properties to look out for in an ATF are presented for several prospective fuels.

Table 2.4. Various Thermophysical Properties of ATF Fuels [86]. The properties reported here are density (ρ), Uranium density (U-ρ), Thermal conductivity (k), and Melting point.

Properties	UO_2	U	U-7Mo	UN	UC	U_3Si	U_3Si_2	UB_2	UH_3
ρ (g/cm^3)	10.97	19.1	17.7	14.32	13.63	15.4	12.2	12.7	10.95
U-ρ ($atoms/nm^3$)	24.47	48.33	43.5	34.2	32.8	37.5	28.6	29.5	27.4
k at 25°C (W/mK)	8.7	27.5	28	54	25	15	8.5	~63	~15
Melting point (°C)	2865	1132	1150	2800	2790	930*	1662	2430	–

*Peritectic temperature

Therefore, in selecting an ATF, the thermal conductivity stands out in importance for fuel performance. A plot showing the thermal conductivities of selected leading ATF candidates compared to reference UO_2 fuel can be seen in Fig. 2.10. For instance, the thermal conductivity of U_3Si_2 increases with temperature, which implies possible reduction in peak centerline temperatures [79].

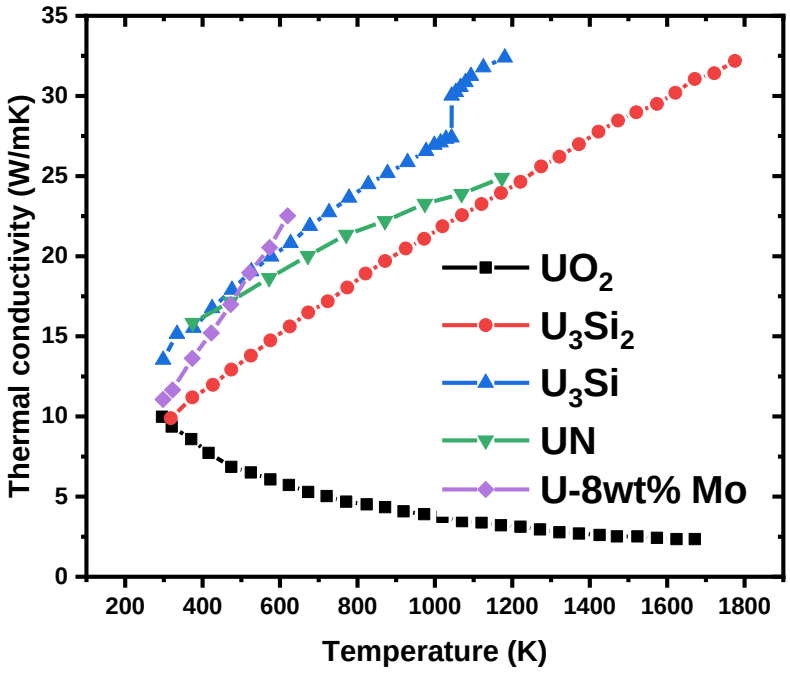

Fig. 2.10. Thermal conductivities of fuels of interest as a function of temperature. Fuels are reference UO_2 [87], U_3Si_2 [13], U_3Si [14], UN [88] and U-8wt% Mo [89].

Additional property affecting fuel temperature distributions is the specific heat capacity, which determines the amount of stored energy in the fuel system. A plot of specific capacity as a function of temperature is presented in Fig. 2.11. It is clear that the ATFs have higher specific heat capacity compared to UO_2. The combination of these parameters play a leading role in nuclear reactor dynamics and the performance of the system during transient conditions.

These properties are primarily affected by radiation and other prevalent reactor condition during operation. For instance, gaseous fission products released from the fuel pellets to the gap during reactor operation can degrade the thermophysical properties of the fuel.

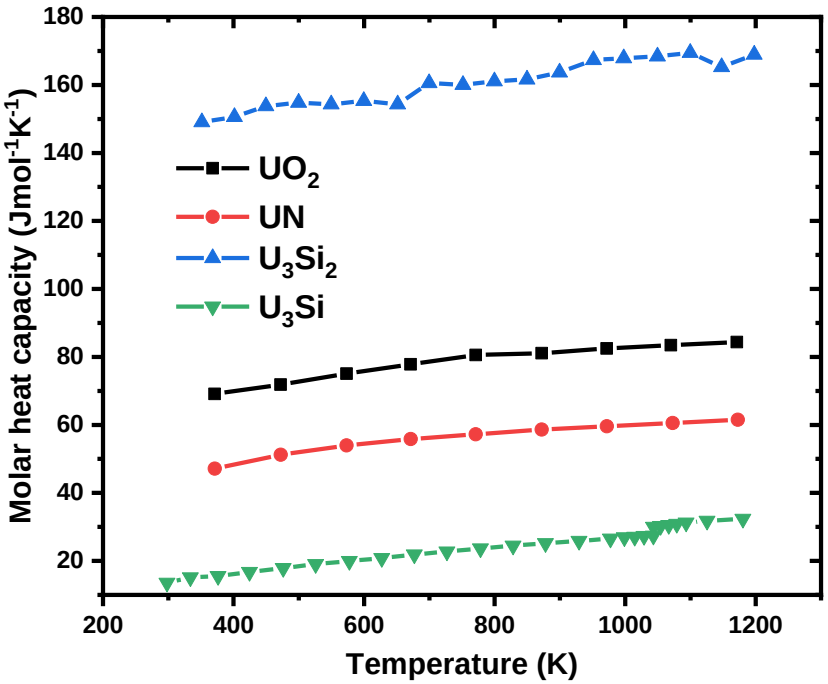

Fig. 2.11 Specific Heat and stored excess enthalpy of fuels as a function of temperature. Fuels are reference UO_2 [90], UN [91], U_3Si_2 [13], and U_3Si [14].

2.6. Fuel behavior under reactor conditions

Understanding the behavior of fuels and cladding materials during the operation of nuclear reactors is a necessary step towards improving the economics and safety of nuclear power. Generation IV reactors pose greater challenges because of a more extreme condition at which they are expected to operate (Table 2.1). Therefore, it is important to be able to predict and understand changes in the performance of the reactor and the fuel pellets during their operation in a set of extreme conditions, such as ionizing and energetic radiation, coupled with high temperature and pressure,

while in contact with chemically challenging environments that leads to fuel corrosion. There have been attempts in the nuclear fuel community to understand the effect of radiation, pressure, and oxidizing environments on different fuel forms.

2.6.1. Impact of radiation on U_3Si_2 Fuel

In terms of radiation damage as it relates to ATF concepts, Miao *et al*. [53] investigated the microstructural evolution of U_3Si_2 irradiated by 84 MeV Xe ions at 300, 450, and 600 ^oC, respectively. U_3Si_2 was found to decompose into a Si-enriched nanocrystalline USi matrix phase and a U-enriched amorphous inclusion phase at 450 ^oC once the radiation dose reached ~150 dpa. TEM images showed the existence of an oxidation layer after irradiation under the 10^{-5} Pa vacuum alongside the formation of intragranular Xe bubbles with bimodal size distribution within the Xe deposition region of the sample. This is consistent with rate theory simulations of fission gas behavior in U_3Si_2 reported for LWRs under steady state operation scenarios [80].

Further studies showed that U_3Si_2 is easily amorphized by 1.5 MeV Kr^{2+} irradiation at a low dose of 0.32 ± 0.02 dpa at room temperature [10] while a more recent systematic investigation of the irradiation parameters by Yao *et al*. [54] established the critical temperatures for amorphization to be 540 K and 580 K for 1 MeV Ar^{2+} and Kr^{2+}, respectively. A dependence on ion mass and energy is identified in which the critical amorphization temperature increases for ions with lower energy and heavier ion mass.

Asides the impact of heavy ions such as Kr and Xe, neutron irradiation play a significant role on damage accumulation in nuclear fuels [92]. Therefore in a recent study, Marquez *et al*. [93] developed a mesoscale model for predicting the formation of subgrains in nuclear fuels under neutron irradiation. The prediction from this model was compared with experimental observation from subdivided rim of UO_2 at high burnup, which validate the model application. They concluded based on analysis of U_3Si_2 data that, the main driver for swelling in U_3Si_2 would be fission gas accumulation at crystalline grain boundaries which stem from diffusion of FPs to grain boundary which act as trap sites. This result is consistent with the outcome of a separate model which includes components for intra-granular and grain-boundary behavior of FGs [94].

Finally, the need to close existing fuel cycle is an attractive option that account for possible blending of U_3Si_2 with spent fuel stored under geological repository [95,96]. To assess the behavior of U_3Si_2 under geological repository conditions, the kinetics of γ-radiation and $H_2O_2^-$

induced oxidative dissolution was studied by Maier and coworker [97]. The irradiation experiments show that the surface area normalized radiation chemical yields for uranium dissolution for U_3Si_2 and UO_2 in HCO_3^- solution differ by a factor of 5–10 in favor of UO_2. This difference can largely be attributed to the difference in dissolution yield.

The relative stability of U_3Si_2 under repository conditions compared to UO_2 has implication for future storage of U_3Si_2 spent fuel or blending with UO_2 spent fuel which have radiolytic oxidants that are capable of oxidizing U(IV) to the much more soluble U(VI) and thereby enhance the release of radionuclides from the fuel matrix [98].

2.6.2. Oxidation and hydriding behavior of U_3Si_2 Fuel

Another important extreme condition of concern is the harsh corrosive environment which impacts the phase transformation that occurs in the fuel due to oxidation or hydriding. Initial assessment of the oxidation behavior of U–Si alloys in oxygen environment was investigated by Wood *et al*. [53] using thermogravimetric technique. The oxidation kinetics of U_3Si_2, USi, and U_3Si_5 both below and above the breakaway oxidation onset follows the well-defined oxidation dynamics of U oxidation. U_3Si_2 and USi display later onsets of breakaway oxidation compared to U_3Si_5. The breakaway oxidation and pulverization occurred at a temperature comparable to UO_2 during air oxidation. In a complementary work by Yan *et al*. [99], the oxidation process of U_3Si_2 was studied by in-situ x-ray photoelectron microscopy (XPS) analysis. Beside the formation of UO_2 observed in thermogravimetric analysis, they inferred that uranium silicate might form when oxygen exposure increases. Similar behavior and breakaway trends are observed in a steam environment [55,57].

The need to improve the oxidation resistance of U_3Si_2 becomes important given the highly oxidizing environment prevalent in LWRs. Therefore, Sooby-Wood *et al*. [100] investigated the potential use of Al to improve the oxidation resistance of U_3Si_2. Thermogravimetric data acquired indicates that increasing amounts of Al in U_3Si_2 further delays the onset of breakaway oxidation, providing enhanced oxidation resistance in air. They also observed the formation of Al_2O_3 after annealing in air at 500 ^oC. However, the possibility of Al_2O_3 serving as passivation layer was not establish in this study.

Asides the concerns with oxidation, hydrogen adsorption can significantly influence the integrity of nuclear fuel material given the possibility of the interaction with steam. It is well known that

hydrogen absorption of a material usually lead to an expansion of the unit cell [101]. In fact, it is one of the causes of embrittlement in pipeline steels [102] and could cause degradation in zircalloy cladding [103] as well. Therefore, in a hydrogen adsorption experiment, Maskova *et al*. [104] observed that the hydrogenation of U_3Si_2 leads to the formation of a hydride with ~1.8 H/f.u. This result is consistent with density functional theory calculations by Middleburgh *et al*. [105]. Furthermore, the reaction with hydrogen, yields ~10% volume expansion and proceeds at very low H pressure.

In summary, the results of the studies outline here demonstrate that preferential oxidation of U will dominate the response of the U-Si compounds investigated under oxidizing conditions and the oxidation of Si will not occur before the formation of UO_2. However, a fundamental understanding of the formation mechanism of surface oxides in these new fuel forms is lacking. Therefore, this work is an attempt to provide an atomic-level explanation of how oxidation occurs in U_3Si_2.

Chapter 3

Computational methods

3.1. Overview of Chapter 3

The techniques that have been used in this thesis and the methodology used to predict specific material behaviors are outlined in this chapter. A historical overview of density functional theory (DFT) is provided. Detailed explanations of DFT and DFT + U at various levels of approximation are briefly reviewed. The theory and numerical implementation of Molecular Dynamics (MD) are discussed.

3.2. Introduction to materials modelling methods

The interactions of electrons and nuclei ultimately determine the properties of materials. Therefore, electronic structure calculations at the level of DFT [106] and atomistic simulation at the level of MD [107] provide the necessary tools for predicting materials properties and behavior under different conditions. DFT is used to solve electronic structure problems in condensed matter physics. In many cases, the results predicted from DFT agree quite well with the experimental results and observations [108]. Classical MD, on the other hand, requires empirically fitted potential, but can be used to study larger systems at a finite temperature using today's computational resources.

3.3. Density Functional Theory

DFT is formulated base on two theorems postulated by Hohenberg-Kohn [109] and the Kohn-Sham (K-S) equations [110]. It is presently the most widely used method to compute the total energy, and electronic structure of solids, where the only variable used is the ground state electron density $n(r)$ of the system, rather than the many electron wave-functions. A detail formalism of the method is discussed next.

3.3.1. Many-body problem

Materials are well described as quantum mechanical systems made up of nuclei that are surrounded by a cloud of electrons. The non-relativistic time-independent Schrödinger Equation describes the quantum state of a matter.

$$\hat{H}\psi = E\psi, \tag{3.1}$$

where $\hat{H}$ is the Hamiltonian operator, E is the energy of eigenstate ψ, and the unknown function ψ is the wave function the calculation of which uniquely determines all the observable properties of the system. When specialized to interacting atoms in space, the Hamiltonian can be written (in atomic units) as follows:

$$\hat{H} = -\frac{\hbar^2}{2m_e}\sum_i \nabla_i^2 - \sum_{i,I}\frac{Z_I e^2}{|r_i - R_I|} + \frac{1}{2}\sum_{i\neq j}\frac{e^2}{|r_i - r_j|} - \frac{\hbar^2}{2M_I}\sum_I \nabla_I^2 + \sum_{I\neq J}\frac{Z_I Z_J e^2}{|R_I - R_J|}, \tag{3.2}$$

where m_e is the mass of electrons and M_I is the mass of the nuclei. Equation 3.2 has five terms, which are the kinetic energy of electrons, the electron-nuclei interactions, the electron-electron interactions, the kinetic energy of nuclei, and the interactions between nuclei and nuclei, respectively. Such a many-body problem can only be solved numerically for a very small system. Since electrons have much shorter relaxation time that ions, the Born-Oppenheimer approximation is commonly used to decouple the movement of the nuclei from the electrons [111]. This approximation is based on the difference in mass between the nuclei and the electrons. To put this in perspective, the lightest nucleus, the hydrogen atom, is actually 1,836 times heavier than an electron. Furthermore DFT, as described in the next section, provides an enormous simplification to the many-body equation 3.2, reducing it to two-body Coulomb terms the exchange-correlation, which is a functional of the local electron density only.

3.3.2. Hohenberg-Kohn method

The many-electron wavefunction is a function of 3N variables and, due to the complexity, in 1964 Hohenberg and Kohn formulated two theories that reduced the energy of a many-body system to electron density evaluation [109]. The proofs of these theorems are outside the scope of this thesis. Interested readers are referred to review papers [112–116] and several textbooks [117] that provide mathematical proofs of these theorems. The two theorems are stated as follows:

Theorem 1*: For any system of interacting particles in an external potential* $v_{ext}(r)$*, the potential* $v_{ext}(r)$*, is determined uniquely, except for a constant, by the ground state particle density* $n_o(r)$*.*

Theorem 2*: A universal functional for the energy E* [$n(r)$] *in terms of the density* $n(r)$ *can be defined valid for any external potential* $v_{ext}(r)$*, and for any particular* $v_{ext}(r)$*, the ground state energy of the system is the global minimum value of this functional, and the density* $n(r)$ *that minimizes the functional is the exact ground state density* $n_o(r)$*.*

Hohenberg-Kohn theorem reduces the N-body problem to solving for the electron density n(r), such that the functional E[n(r)] is minimized. Unfortunately, the solution is intractable since the exact solution of the functional is unknown [117].

3.3.3. The Kohn-Sham variational equations

In 1965, Kohn and Sham reformulated the many-body problem in order to find an analytical solution for it. The Kohn-Sham equations assume the exact ground state density can be represented by the ground state electron density of a non-interacting auxiliary system. The auxiliary Hamiltonian is chosen to have the usual kinetic operator and an effective local potential. They then wrote the energy density functional $F[n(r)]$ as:

$$F[n(r)] = T[n(r)] + E_H[n(r)] + E_{xc}[n(r)], \tag{3.3}$$

The first term, $T[n(r)]$, corresponds to the kinetic energy functional for a fictitious system of non-interacting electrons producing the same density as $n(r)$.

$$T[n(r)] = 2\sum_{i=1}^{N} \int n(r)\left(-\frac{\hbar^2}{2m}\right)\nabla^2 n(r)dr, \tag{3.4}$$

The second term, $E_H[n(r)]$, is the Hartree energy, which is due to Coulombic interactions:

$$E_H[n(r)] = \frac{1}{2}\int\int \frac{n(r)n(r')}{|r-r'|}drdr', \tag{3.5}$$

The last term, $E_{xc}[n(r)]$, called the exchange-correlation functional, is a correction term, which accounts for all the many-body effects missing in $F[n(r)]$. The functional form of the correction term $E_{xc}[n(r)]$ is unknown and must be approximated. Therefore, reasonable approximations, such as local density approximation (LDA) [110] and generalized gradient approximation (GGA) [118], are required to solve the equations.

3.3.4. Exchange-correlation functional

This exchange-correlation functional, E_{xc}, accounts for all the physics that was lost when a non-interacting system was assumed. The self-interaction is accounted for in the exchange correlation component, and the correlation piece of the functional must adequately handle all nonlinear effects of the electron correlation. The form of $E_{xc}[n(r)]$ is not known, so for Kohn-Sham DFT to be a useful method, E_{xc} must be approximated. Many kinds of methods are used to evaluate this term: LDA, GGA, hybrid functionals, and exact exchange, which are discussed below in detail.

There has been a lot of work in the development of functionals for estimating the energy associated with the exchange-correlation. The exchange-correlation provides a physical description of the density of electrons around the nucleus of an ion. The LDA offers a simple way to make this approximation. The LDA uses only the electron density, ***n(r)***, at a spatial point ***r*** to determine the exchange-correlation energy at that point. The uniform electron gas of the same density is taken to be the exchange-correlation energy density. The exchange part of the functional is defined as the exact expression derived for a homogeneous electron gas [56].

$$E_{xc}^{LDA}[n(r)] = \int n(r)\varepsilon_{xc}^{hom}\, n(r)dr, \tag{3.6}$$

For a homogeneous electron gas, the exchange energy becomes:

$$\varepsilon_{xc}^{hom} = \frac{-e^2}{4\pi\varepsilon}\frac{3}{4}\left(\frac{3n}{\pi}\right)^{1/3}, \tag{3.7}$$

The LDA does not consider the exchange correlation energy due to the inhomogeneities in the system. As a consequence, the GGA [119,120] was formalized to account for this. The GGA is an attempt to correct the deficiency of the LDA by adding the gradient of the electron density, $|\nabla n(r)|$, as an independent variable.

$$E_{xc}^{GGA}[n(r)] = \int n(r)\varepsilon_{xc}\,(n, |\nabla n|)dr, \tag{3.8}$$

The gradient introduces non-locality into the description of the exchange and the correlation. This can improve the functional's performance significantly by helping to account for fast varying changes in the electron density that are not well described by the LDA. Several approximations of the gradient have been implemented, and all of them give better results for geometries, vibrational frequencies, charge densities, and binding energies than LDA. However, its computational cost is higher. The main reason for using GGA is to decrease binding energies, which are overestimated by LDA. Some implemented functionals are: Perdew-Wang 86 (PW86) [121], Perdew-Wang 91 (PW91) [122], Becke-Perdew (BP) [123], Lee-Yang-Parr (LYP) [124], Perdew-Burke-Enzerhof (PBE) [118], Revised Perdew-Burke-Enzerhof (RPBE) [125], and Perdew-Burke-Enzerhof for solids (PBEsol) [126]. Often, these functionals contain experimental parameters to adjust the energy of a series of atoms. In this thesis, all the calculations are carried out with the GGA-PBEsol and GGA in the *Wu-Cohen* (GGA-WC) functional [127], which tend to be excellent functionals for the description of chemical bonds of solids. In some cases, other functionals have been tested for comparison.

Even with the improvement in GGA, some chemical characteristics are still poorly described. For instance, GGA underestimates bandgap of semiconductors, while the results are overestimated in Hartree-Fork (HF) calculation. Intuitively, Becke *et al*. [123] mixed a portion of the exact exchange from HF with the exchange and correlation from DFT to improve the unknown part of the exchange-correlation. This makes this method become a hybrid of DFT and HF. One of the most commonly used versions of hybrid functionals among quantum chemists are B3LYP (Becke, 3-parameter, Lee-Yang-Parr) and B3PW91 (Becke, 3-parameter, Perdew-Wang-91) [128]. The definition of the exchange-correlation energy is given by:

$$E_{xc}^{hybrid} = E_{xc}^{LDA} + a_0(E_x^{HF} - E_{xc}^{DFA}) + a_x E_x^{Becke} + a_c E_c, \tag{3.9}$$

with coefficients that are empirically adjusted to fit atomic and molecular data. DFA denotes an LDA or GGA functional. The hybrid functionals work exceptionally well for atoms and molecules, but some numerical issues come up for solid state calculations, where periodic conditions are required.

3.3.5. Periodic boundaries and Bloch's theorem

The eternal potential acting on the electron in solid state crystals must have the same periodicity as the crystal lattice. The potential $u(r)$ is therefore a periodic function with the period equal to the period of the corresponding Bravais lattice:

$$u(r) = u(r + R) \tag{3.10}$$

where R are the vectors which belong to the Bravais lattice. Based on the work of Hohenberg and Kohn [109], if the potential is periodic, then the electron density is also periodic. Hence:

$$\rho\,(r) = \rho\,(r + R), \tag{3.11}$$

The electron density is given by

$$\rho\,(r) = \sum_i |\psi_i(r)|^2, \tag{3.12}$$

This means the magnitude of the wavefunction must also retain the lattice periodicity. However, the wavefunction's phase are not, periodic. This implies that there are infinite number of wavefunction that satisfy Equation 3.11. Hence, the set of Kohn-Sham equations to be solved is intractable. This problem is circumvented by applying Bloch's theorem to the periodic system as follows:

$$\psi_k(r) = u(r)e^{ik.r}, \tag{3.13}$$

Such that

$$\psi(r) = \int \psi_k(r)d^3k, \tag{3.14}$$

And therefore

$$\psi(r) = \int |\psi_k(r)|^2 d^3k, \tag{3.15}$$

Where u(r) is a function with the same periodicity as the simulation cell and k is a vector which denote the position in in reciprocal space. This means that $e^{ik.r}$ is an arbitrary phase factor which scales the periodic function u(r) in the neighboring unit cells:

$$\psi_k(r+R) = u(r+R)e^{ik.(r+R)}, \tag{3.16a}$$

$$= u(r)e^{ik.r}e^{ik.R}, \tag{3.16b}$$

$$= \psi_k(r)e^{ik.R}, \tag{3.16c}$$

The periodicity in the reciprocal space (k space) means that we only need to consider k vectors within a portion of the reciprocal space called the Brillouin zone. Also the need to integrate over all the possible k vectors when constructing the electron density is eliminated since the wavefunction change slowly as we vary k. Hence, we can approximate the integral with a summation:

$$\psi(r) \approx \sum_k \psi_k(r), \tag{3.17}$$

For each k vector, there is a discrete set of eigenstates that leads to the formation of energy bands. Properties such as the total energy and density of states are calculated by integration over the sample k points in the Brillouin zone. The number of sample k points that are required in order to obtain converged results depends on nature of the materials as well as the properties under consideration.

3.3.6. Basis sets for the wave functions

To solve the Schrödinger equations computationally in an efficient manner, it is common to transform the differential single-particle Schrödinger equations into a linear eigenvalue problem by expanding the Kohn-Sham wave functions using a basis set. Since crystalline structures have periodicity, one can apply periodic boundary conditions and use a plane wave (PW) basis sets for the expansion of the valence orbitals and charge densities.

Basis superposition errors are also avoided if PW are chosen to be orthogonal across the system. In principle, the basis set should be complete enough to represent any wave-function, but this requires an infinite number of PWs and, in practice, the functions are truncated at the kinetic energy that sufficiently converges the total energy calculation. The results presented in this thesis are carried out using the QE code, which employs a plane-wave basis set.

According to Bloch theorem [128], translational symmetry can be used to reduce the infinite number of the one-electron wave-functions, when computing the number of electrons in the unit cell. The plane wave function ($e^{ik.r}$) is a linear combination of the periodic basic function ($u_i(r)$). Then, the one-electron wave-functions can be expressed as the product of a periodic part and a wave-like part as expressed in Equations 3.18a–b:

$$u_i(r) = \sum_G c_{i,G} e^{iG.r}, \tag{3.18a}$$

$$\psi_i(r) = e^{ik.r} u_i(r) = \sum_G c_{i,k+G} e^{ik+G.r}, \tag{3.18b}$$

where the electronic wave function is the sum of the plane waves at each k-point in the first Brillouin zone (BZ) and $c_{i,k+G}$ are the coefficients of the plane waves. The K-S equations in the reciprocal space become:

$$\sum_{G'} \left(\frac{\hbar^2}{2m} |k+G|^2 \delta_{GG'} + V_{ion}(G-G') + V_H(G-G') + V_{xc}(G-G') \right) c_{i,k+G'} = \epsilon_i c_{i,k+G'}, \tag{3.19}$$

The electronic wave function is represented as an expansion of plane waves that involves the convergence of the kinetic energy cut-off ($E_{cut} = \frac{\hbar^2}{2m}|k+G|^2$), which comes from the kinetic term in the K-S equations. The E_{cut} limits the maximum length of the G vectors leading to a finite basis set. Poor truncation of the plane waves expansion would result in the kinetic energy being less than the E_{cut}, which in turn introduces an error in the computed total energy. The flowchart in Fig. 3.1 shows how an actual calculation can be performed to determine the ground state energy, forces, stress, and so on. A numerical procedure is implemented in the DFT codes to update the n and V_{eff} until self-consistency is achieved successively.

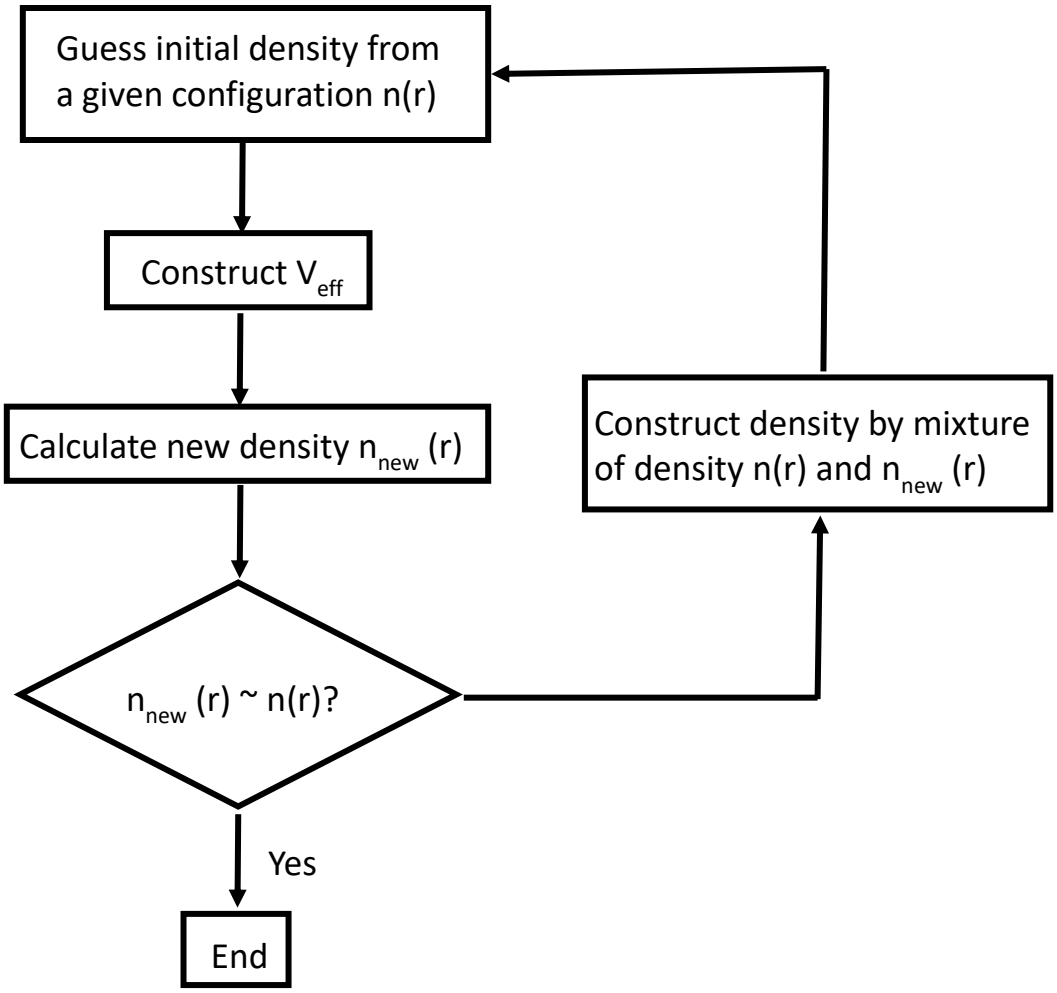

Fig. 3.1. A flowchart illustrating the procedure in the self-consistent calculations using DFT with PW basis set.

3.3.7. Pseudopotentials

Even within the Kohn-Sham formalism, the computational cost of the simulations is strongly dependent on the number of electrons in the system. This is because the tightly bound core orbitals, and the highly oscillatory nature of the valence electrons, demand a high value of E_{cut}, and hence the number of plane-waves to be used to describe the electronic wave functions [129] accurately. This accounts for the use of the frozen-core electron approximation called pseudopotential, where core electrons are calculated in a reference configuration and remain invariable in the calculations. Then, the wave-functions for valence electrons are substituted by pseudo-wave-functions, which reproduce the energy levels obtained by an all-electron calculation.

Pseudopotentials are different from the all-electron wave-functions, because in the inner zone, near the nucleus, they are designed not to have any node. This substantially decreases the number of

plane-waves required. Fig. 3.2 shows how pseudopotentials and the pseudo wavefunctions that are produced by them differ from the all-electron type potential and wavefunction. Fig. 3.2 further indicates the importance of using a sensible cut-off radius to create the pseudopotential. Pseudopotentials do two things: remove core electrons and modify the core region of the valence electrons' wavefunctions. There are different kinds of pseudopotential such as ultrasoft pseudopotentials (US) [130,131] or norm-conserving pseudopotentials [132], which are the ones used in the present thesis.

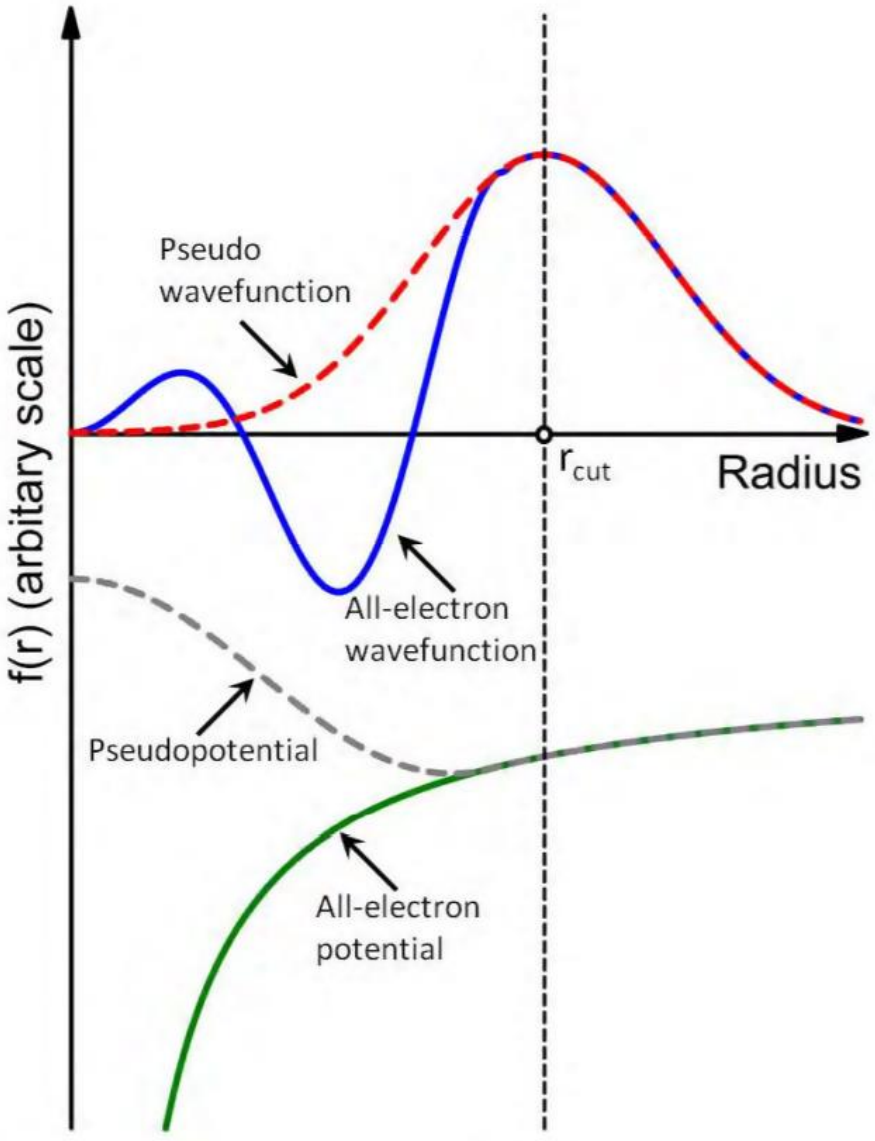

Fig. 3.2. Diagram illustrating the difference between the all-electron potential and wavefunctions with the pseudopotential and wave-function. The cut-off radius for the pseudopotential is shown. Figure adapted from "sketch pseudopotential" by Wolfram Quester. Original uploader was wquester at en.wikipedia [133].

3.3.8. Limitations of DFT

In general, DFT is remarkably successful in determining a wide range of properties of the materials. However, there are certain limitations to the method. Standard DFT methods often perform poorly in describing the electronic and magnetic properties of strongly correlated materials, *i.e.* materials with delocalized *d*- and *f*-electrons [134]. This limitation is revealed for example in U_3Si_2 which is unstable when treated with DFT due to the presence of delocalized *f* electrons [58]. Several methods exist to better treat the correlations of *5f* electrons: the self-interaction correction (SIC) method, the DFT+U method, hybrid functionals, and the DFT + dynamical mean-field theory (DMFT) method. In this thesis, the DFT + U method is used to treat the delocalized 5*f* electrons in the uranium orbital of U_3Si_2. The +U stabilizes the structure of U_3Si_2 by splitting or localizing the U 5*f* electrons as shown by Andersson *et al*. [135].

3.3.9. The DFT+U method

One method of correcting the strong intra-atomic electronic correlations is by adopting the DFT+U approach, which adds an on-site Coulomb repulsion to the DFT Hamiltonian. Different formulations of the DFT+U approximation have been devised [134,136], but whichever form is taken, the main concept is to correct the LDA or GGA with a mean-field Hubbard-like term designed to improve the description of the electron correlations relating to the on-site Coulomb repulsions. The corrective term is only applied to the correlated orbitals (*d* or *f)*, and the total energy functional takes the following form:

$$E_{DFT+U}[n(r)] = E_{DFT}[n(r)] + E_U\left[n_m^{I,\sigma}\right] - E_{dc}[n^{I,\sigma}], \tag{3.20}$$

where the E_{DFT} is the LDA or GGA energy term as in equation 3.20, the electron density, and $n_m^{I,\sigma}$ is the atomic-orbital occupations with spin σ for the correlated atom *I*. E_U is usually expressed as follows:

$$E_U[n(r)] = \frac{1}{2}\sum_{\{m\},I,\sigma}\left[< m,m''|V_{ee}|m',m''' > n_{mm'}^{I,\sigma}, n_{m''m'''}^{I,-\sigma} + (< m,m''|V_{ee}|m',m''' > - < m,m''|V_{ee}|m'',m' >)n_{mm'}^{I,\sigma}n_{m''m'''}^{I,\sigma}\right], \tag{3.21}$$

In equation (3.21) the V_{ee} integrals represents the electron-electron interactions computed on the wave functions of the localized basis set (e.g. d or f atomic states) that are labeled by the index m.

This can be further expressed as a function of the screened on-site Coulomb and exchange parameters U and J respectively [137]:

$$U = \frac{1}{(2l+1)^2}\sum_{m,m'} < m, m' | V_{ee} | m, m' >, \quad 3.22$$

$$J = \frac{1}{2l(2l+1)}\sum_{m \neq m', m'} < m, m' | V_{ee} | m, m' >, \quad 3.23$$

E_{dc} is the "double counting term," i.e., a mean-field evaluation of the Hubbard term removing the same amount of Coulomb repulsion from the DFT part of the Hamiltonian. E_{dc} can be assessed using the Around Mean Field scheme [138] or the Fully-Localized Limit scheme [139], which is better adapted for strongly correlated materials [140]. There exist two formulations of the DFT+U approach. In Dudarev's approach [136], only the difference $(U - J)$ refer to as effective Hubbard U comes into play in the energy functional, whereas in Liechtenstein's formulation [134], both parameters separately come into use. Hence either the value of the difference $(U - J)$ or both U and J parameters have to be chosen. The DFT + U value can be chosen by fitting DFT predictions to experimental observables or based on an analysis of experimental spectroscopic data. Such an approach requiring parameter adjustment can thus be seen as a phenomenological many-body correction. There, however, exist methods based on a linear response approach [141] or on the Random-Phase Approximation [142] to calculate the interaction parameters U and J entering the DFT+U functional from first-principles. However, commonly effective Hubbard U is used as implemented in Quantum ESPRESSO code [143].

3.4. Classical Molecular Dynamics (MD) simulation

Classical Molecular Dynamics (MD) is a modelling and simulation technique used to investigate the structural evolution, dynamics, and thermodynamics properties of materials. MD is based on the idea of solving Newton's law of motion, which is given as:

$$F_i = m_i a_i = m_i \frac{d^2 r_i}{dt^2}, \quad (3.24)$$

where, F_i is the force acting on an atom *I*, m_i is the mass of atom *i*, and a_i is the acceleration of atom *i*. By assigning kinetic energy to the system, MD allows the atomic trajectories to be sampled. The force acting on the atom can be defined with reference to gradient (∇_i) of the potential energy U of the atom as:

$$F_i = -\nabla_i \mathrm{U}\,(r_1, r_2, \ldots\ldots, r_N) = -\nabla_i \mathrm{U}\,(r^N), \tag{3.25}$$

where the gradient is taken with respect to the coordinates on atom *i*, and can be stated as:

$$-\nabla_i \mathrm{U}\,(r^N) = \frac{\partial \mathrm{U}\,(r^N)}{\partial x_i}\hat{x} + \frac{\partial \mathrm{U}\,(r^N)}{\partial y_i}\hat{y} + \frac{\partial \mathrm{U}\,(r^N)}{\partial z_i}\hat{z}, \tag{3.26}$$

To describe the interaction between atoms, an appropriate interatomic potential (described in 3.5) is needed. For different types of materials, the potentials that have been used to describe the system may take different forms.

3.4.1. Numerical integration scheme

The integration scheme of Newton's equation of motion is an integral part of the MD simulations. Integration schemes such as velocity Verlet [144] and fifth order gear predictor – corrector [145] are commonly used to solve Newton's equation numerically. The Verlet algorithm is implemented in the MD code used in this work. This is because it is simple yet robust, while not perfect it is quite adequate for many purposes. The velocity Verlet approach uses the Taylor series expansion to approximate the positions, velocities, and the accelerations of the interacting atoms in a system by splitting a second order differential equation into two first order differential equations. Taylor expansion of (i) $r_i(t+\delta t)$ about $r_i(t)$ and (ii) $v_i(t+\delta t)$ about $v_i(t)$ gives the equations 3.27 and 3.28:

$$v_i(t+\delta t) = v_i(t) + a_i(t), \tag{3.27}$$

$$r_i(t+\delta t) = r_i(t) + v_i(t)\delta t + \frac{1}{2}a_i(t)\delta t^2, \tag{3.28}$$

The beginning of the Verlet algorithm is equation (3.28), which gives the position of atom i forward in time from t, i.e., at $t+\delta t$. The position backward in time is from the same equation by substituting $-\delta t$ with$+\delta t$:

$$r_i(t-\delta t) = r_i(t) - v_i(t)\delta t + \frac{1}{2}a_i(t)\delta t^2, \tag{3.29}$$

Combining Equation (3.28) and (3.29) gives:

$$r_i(t+\delta t) = 2r_i(t) - r_i(t-\delta t) + a_i(t)\delta t^2, \tag{3.30}$$

Using Taylor expansion and since all other terms are known, equations 3.27 and 3.28 can then be expressed by the velocity Verlet algorithm as:

$$r_i(t+\delta t) = r_i(t) + v_i(t)\delta t + \frac{1}{2m}F_i(t)\delta t^2, \tag{3.31}$$

$$v_i(t+\delta t) = v_i(t) + \frac{1}{2}(F_i(t) + F_i(t+\delta t))\delta t, \tag{3.32}$$

The positions at $t + \delta t$ depend only on quantities that are evaluated at t. By repeatedly solving the velocity Verlet equations, the evolution of the system with time can be determined.

Although the processing power of computers is always increasing, the size of the system that can be simulated is still limited compared to real life materials system. Whether limited by memory or time considerations, the number of atoms in a MD system is small in comparison to Avogadro's number. For instance, the systems used in this thesis contain atoms ranging from 10^3–10^4 atoms, without resorting to large parallel machines, this number of particles is approaching the upper limit of what can be studied in a reasonable period with a modern computer. As such, the MD simulations presented here are limited to nanometer sized systems and nanosecond timescales. Underlying these system constraints is the need to keep the δt to only 1 or 2 femtoseconds to provide a reliable solution to equation 3.24.

Due to the system size used in the MD simulations, some issues arise when simulating bulk properties of materials. For instance, given the small size of atoms in the simulation cell, they have more atoms at the surface compared to macroscopic systems, which contain billions of atoms. To correct this problem, periodic boundaries are used as illustrated in Fig. 3.3. Periodic boundary conditions make it look like the simulation cell is being embedded in an infinite bulk material.

This is achieved by surrounding the primary simulation cell by images of itself. Whatever happens to atoms in the primary cell, also takes place in the image cells. Any atom crossing a periodic boundary is wrapped around to appear at the other side of the cell. For instance, in fractional coordinates, when an atom crosses the boundary at x = 1, it would appear at x = 0. As this work considered bulk materials, periodic boundary conditions were employed for all MD and DFT calculations respectively.

MD simulation gives the position and velocity of atoms that make up the system under consideration. Statistical mechanics provide a link between measurable, observable quantities such as temperature and atomic scale properties. This is achieved through the use of thermodynamics, which represents all possible positions and momenta of a system that have a set of common

extensive quantities. Extensive quantities are the independent thermodynamic variables of a system, from which all other quantities can be deduced.

In a typical MD simulation, the number of atoms (N) in a volume (V) is fixed irrespective of the state of the system. Furthermore, the energy (E) of the system is conserved, making the system to be in the so called NVE microcanonical ensemble (constant number of atoms, volume, and energy).

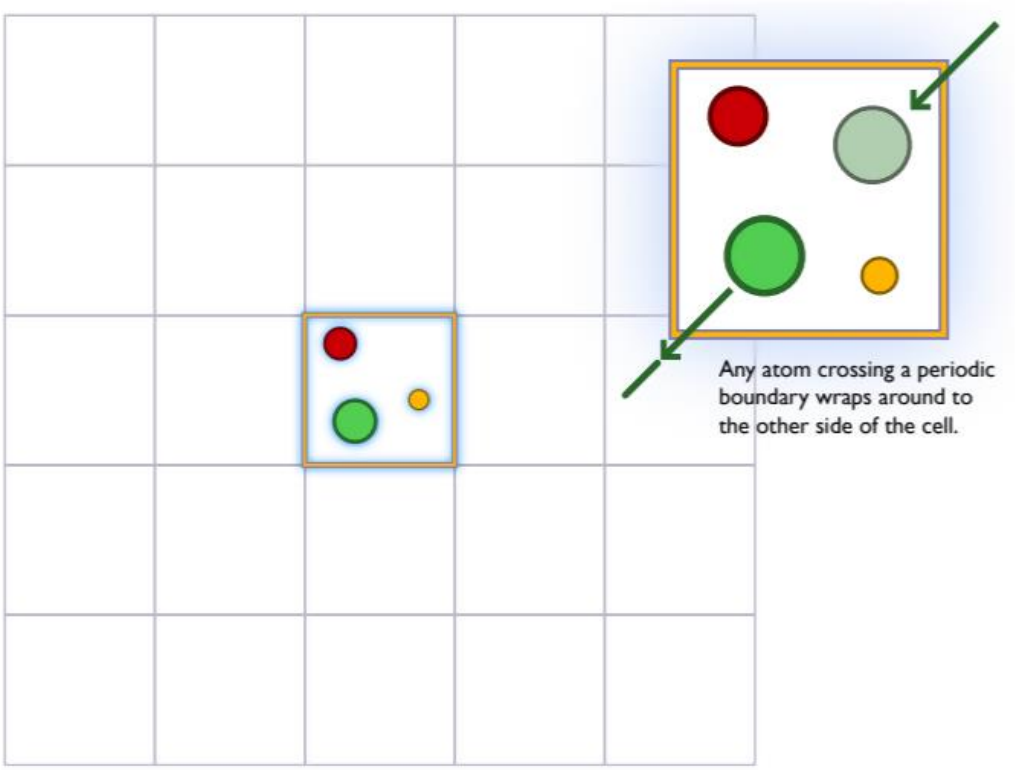

Fig. 3.3. Schematic demonstration of periodic boundary conditions in two dimensions. The central simulation cell is surrounded by images of itself tessellated in space.

Thermodynamic quantities such as pressure and temperature can also be calculated, as well. Similarly, NVT is a canonical ensemble, and NPT is an isothermal-isobaric ensemble. These are the most widely used ensembles in MD simulations and have been employed in the current study. Besides, there are other types of ensembles, such as grand canonical ensemble, in which the total number of the atoms (N) in the system can be changed, while a fixed uniform chemical potential has to be maintained.

3.5. Empirical potential description of crystalline solids

The predictive power of MD simulations lies in the accurate description of the interatomic forces between the atoms by a potential set. Physically, there are many different types of interatomic bonding. Covalent, ionic, and metallic bonding are considered to be primary bonding types, while van der Waals and hydrogen bonding are considered to be secondary bonding types. Specific interatomic potentials, U, describe these bonding types. For ionic systems, such as UO_2, one of the most widely used potentials is the Buckingham potential combined with Coulombic interactions, 4-range Buckingham, Buckingham-Morse, or tabulated potential forms [146]. The Buckingham potential is expressed as:

$$U_{Buck}(r_{ij}) = A_{ij} exp\left(\frac{-r_{ij}}{\rho_{ij}}\right) - \left(\frac{C_{ij}}{r_{ij}^6}\right), \tag{3.33a}$$

where A_{ij}, ρ_{ij}, and C_{ij} are the empirical parameters that are fitted to the system, and r_{ij} is the separation between the two ions *i* and *j*. The first term in equation 3.33a is a repulsive interaction, which decreases exponentially with an increase in distance between atoms *i* and *j*. The second term is an attractive contribution due to dipole interactions.

$$E_{Coulomb} = \frac{1}{2}\sum_{i=1}^{N}\sum_{j\neq i,1}^{N}\frac{q_i q_j}{r_{ij}}, \tag{3.34b}$$

where N denotes the total number of ions in the system, and q_i and q_j are the charges on atom *i* and *j* respectively. The r^{-1} dependence makes the sum conditionally convergent. The summation of the Coulombic term over the system can be carried out using either Ewald sum [145] or direct sum [147].

The Embedded Atom Method (EAM) is used to describe metallic systems as the pair-potential scheme omits a crucial piece of the physics of metallic bonding [148]. The energy of the system can be expressed as follows:

$$U_{ij} = \sum_i F(\bar{\rho}_i) + \frac{1}{2}\sum_i \sum_{i\neq j} \emptyset(r_{ij}), \tag{3.35}$$

$$\bar{\rho}_i = \sum_{j\neq i} \rho_j^a(r_{ij}), \tag{3.36}$$

where *F* (embedding function) is the energy required to embed an atom *i* in the combined electron density $\bar{\rho}_i$ which is contributed from each of its neighboring atoms j by an amount $\rho_j^a(r_{ij})$, while $\emptyset(r_{ij})$ is the pair potential function representing the energy in bond *ij*, which is due to the short-

range electrostatic interaction between atoms, and r_{ij} is the distance between an atom and its neighbor for that bond.

The EAM potential is further modified to account for angular dependent interactions by the addition of the electron density term. The total energy U_{ij} of the modified embedded atom method (MEAM) [149] is similar to equation 3.35, except that electron density captures the angular dependent as follows [150]:

$$\bar{\rho}_i = \sum_{j\neq i} \rho_j^a(r_{ij}) + \sum_{jk}[a_j^1\, a_k^1 cos\theta_{jik} - a_j^2 a_k^2(1 - 3cos^2\theta_{jik})]\rho_j^a(R_{ij})\rho_k^a(R_{ik}), \qquad (3.37)$$

The second term is the angularly dependent term, introduced to augment $\overline{\rho}_i$. Where the atomic density ρ_j^a depends on the type of atom j, θ_{jik} is the angle between atoms $j, i, and\ k$ with atom i and the central atom, and the $a_i^{1,2}$ are constants depending on the atom type i. The angular dependent term must decrease in magnitude as either bond length of the three atoms i, j or i, k increases.

3.6. Phonon and electronic thermal conductivity

The thermal conductivity of nuclear fuel pellets is an important thermophysical property in nuclear reactors. It is argued in the literature that the high thermal conductivity of metallic systems is mainly contributed by the electrons (*el*) while the phonon (*ph*) contribution is small, and hence neglected in some cases [151]. However, work on uranium diboride (UB_2), which is a metallic system, showed significant phonon contribution [71]. This implies the scattering centers that contribute to thermal conductivity depends on the nature of the material. Phonon scattering occurs in three phonon interactions, which result from anharmonicities in the interatomic potential. The other phonon scattering center, which contributes to thermal conductivity, includes impurities, grain boundaries, or local distortions of the lattice. The total thermal conductivity of metallic nuclear fuel is determined by the combination of the contribution to the thermal conductivity both from electronic and phonon transport as follows:

$$k_{total} = k_{el} + k_{ph}, \qquad (3.38)$$

Where k_{el} is the electronic contribution to the thermal conductivity, is calculated by utilizing the Boltzmann transport theory (BTE) and the relaxation time approximation (RTA), as implemented in the BoltzTraP code [152] from which we can obtain σ/τ while k_{ph} is the phonon contribution to thermal conductivity. This can be calculated by solving the Boltzmann Transport Equation

(BTE) or using the Non-Equilibrium Molecular Dynamics (NEMD) and the Equilibrium Molecular Dynamics (EMD) methods.

3.6.1. Electronic thermal conductivity

The electronic thermal conductivity (k_{el}) at a given temperature T, can be calculated from electrical conductivity tensor (σ) of a material using Wiedemann-Franz law [151]:

$$k_{el} = \sigma LT, \tag{3.39}$$

where L is the Lorenz number which equals $L = 2.44 \times 10^{-8}$ W Ω K^{-2}.

The electron-electron contribution to electrical resistivity (ρ_{el-el}) which is related to σ_{el-el} can be obtained using the equation 3.40:

$$\rho_{el-el} = \frac{1}{\sigma_{el-el}} = \frac{1}{\frac{\sigma}{\tau}\tau_{el-el}}, \tag{3.40}$$

where τ_{el-el} is the electronic relaxation time for electron-electron scattering, τ is the total electronic relaxation time and $\frac{\sigma}{\tau}$ is calculated using the Semi-Classical Boltzmann Theory with the relaxation time approximation and the rigid band approximation as implemented in the BoltzTraP code [152] . The full tensor of σ is calculated from the conductivity distributions:

$$\sigma\ (T;\mu) = \frac{1}{V}\int \sigma_{\alpha\beta}(\epsilon)\left[-\frac{\partial f_{\mu}(T;\varepsilon)}{\partial \varepsilon}\right] d\varepsilon, \tag{3.41}$$

Where *f* is the Fermi-Dirac distribution function, ε is the band energy, μ is the Fermi level, α, β are tensors mode and $\sigma_{\alpha\beta}(\epsilon)$ is defined as:

$$\sigma_{\alpha\beta}(\epsilon) = \frac{1}{N}\sum_{i,k} \sigma_{\alpha\beta}(i,k)\frac{\delta(\varepsilon-\varepsilon_{i,k})}{d\varepsilon}, \tag{3.42}$$

Where k is a set of k-points elements in reciprocal space, N is the number of k-points sampled, *i* is the band index and $\sigma_{\alpha\beta}(i,k)$ is given by:

$$\sigma_{\alpha\beta}(i,k) = e^2\tau_{i,k}v_{\alpha}(i,k)v_{\beta}(i,k), \tag{3.43}$$

where e is the elementary charge and v_{α} is the group velocity of the electrons.

3.6.2. Thermal Conductivity from BTE

A microscopic model of the phonon assisted thermal conduction in materials was formulated by Peierls in 1929 [153]. The so called BTE for phonons captures the effect of three phonon scattering. This makes it challenging to solve due to the inelastic nature of the scattering process. Therefore, over the decades, there has been the development of several numerical methods for solving the BTE to model phonon transport.

For instance, Joshi and Majumdar developed an equation for phonon radiative transfer that employed average phonon properties [154]. Chen used a Ballistic Diffusive equation for phonon transport, where phonons are defined as transporting in either ballistic or diffusive regimes [155], while Narumanchi *et al*. employed the finite volume method to solve the BTE for thermal transport modelling in electronic devices using mode-dependent phonon properties [156].

Omini and Sparavigna pioneered a more robust iterative solution in the 1990s [157]. The drawback of this method is the use of interatomic potential to obtain the interatomic forces to arrive at an exact solution of the phonon BTE. A fully predictive approach with the interatomic forces determined from first principles is implemented in the SHENGBTE code [158].

Here the heat current or the amount of heat transported by the phonon in branch *j* of the dispersion relation with a wave vector $\vec{\boldsymbol{q}}$ can be taken as the energy of the phonon times its group velocity:

$$\vec{J}_j^p(\vec{q}) = \hbar\omega_j(\vec{q})\vec{v}_j(\vec{q}) \,, \tag{3.44}$$

where $\omega_j(\vec{q})$ in equation 3.29 is the frequency of the phonon. If there are $f_j(\vec{q},\omega)$ phonons in the phonon branch j, the total heat flow per unit volume due to all the phonons in the crystal is given by equation 3.45:

$$\vec{\boldsymbol{J}}_j^p(\vec{q}) = \frac{1}{V}\sum_{j,\vec{\boldsymbol{q}}}\ \hbar\omega_j(\vec{\boldsymbol{q}})\vec{v}_j(\vec{\boldsymbol{q}})\, f_j(\vec{\boldsymbol{q}},\omega), \tag{3.45}$$

where *V* denotes the volume of the unit cell of the system.

At thermal equilibrium, phonon distribution $f^0(\vec{\boldsymbol{q}},\omega)$ is given by the Bose-Einstein statistics, which is $f^0(\vec{\boldsymbol{q}},\omega) = \left[\exp\left(\frac{\hbar\omega_j(\vec{\boldsymbol{q}})}{k_BT}\right) - 1\right]^{-1}$. This distribution deviates from f_j^0, when the system is not in equilibrium. The Boltzmann transport equation describes the statistical behavior of this deviation from the equilibrium state under the thermal gradient of ∇T. Boltzmann transport theory

assumes that the diffusion causes the rate of change of phonons in a small volume due the thermal gradient, as well as, scattering arising from allowed processes. In a steady state, there must be no net change of the number of phonons in the considered small volume of the system. Hence, the rate of change of the distribution function due to the diffusion needs to be canceled by the rate of scattering as stated in equation 3.46:

$$\frac{df_j(\vec{q},\omega)}{\partial t}|_{steady} = \frac{df_j(\vec{q},\omega)}{\partial t}|_{diffusion} + \frac{df_j(\vec{q},\omega)}{\partial t}|_{scattering} = 0, \tag{3.46}$$

where $\frac{df_j(\vec{q},\omega)}{\partial t}|_{diffusion}$ is due to diffusion or motion of the phonon and can be expressed as equation 3.47:

$$\frac{df_j(\vec{q},\omega)}{\partial t}|_{diffusion} = -\frac{\partial}{\partial t}\left[\vec{\nabla} f_j(\vec{q},\omega).\boldsymbol{v}_j(\vec{q})\right], \tag{3.47}$$

The scattering term comes from the different processes, such as phonon – phonon interaction and phonon interaction with impurities. This can be further expressed by equation 3.48:

$$\frac{df_j(\vec{q},\omega)}{\partial t}|_{scattering} = \vec{\nabla}T.\vec{v}_j(\vec{q})\frac{df_j(\vec{q},\omega)}{\partial t}, \tag{3.48}$$

Applying the relaxation time approximation (RTA) to solve the BTE, it is assumed that the relaxation time is $\tau_j(\vec{q},\omega)$. This means that the scattering rate can be recast as follows:

$$\frac{df_j(\vec{q},\omega)}{\partial t}|_{scattering} = \frac{f_j(\vec{q},\omega)-f^0(\vec{q},\omega)}{\tau_j(\vec{q},\omega)}, \tag{3.49}$$

$$f_j(\vec{q},\omega) = f^0(\omega) + g_j(\vec{q},\omega), \tag{3.50}$$

For computational expediency, $\frac{df_j(\vec{q},\omega)}{\partial t}|_{scattering}$ can be expanded as linear dependent of the first order of ∇T. Hence, $g_j(\vec{q},\omega)$ can be rewritten as follows:

$$g_j(\vec{q},\omega) = -\boldsymbol{F}.\vec{\nabla}T\frac{df_0}{dT}, \tag{3.51}$$

$$\boldsymbol{F} = \boldsymbol{\tau_\lambda^0}(\vec{\boldsymbol{v}} + \boldsymbol{\Delta_\lambda}), \tag{3.52}$$

where $\boldsymbol{\tau_\lambda^0}$ is the relaxation time within RTA and $\boldsymbol{\Delta_\lambda}$ is a measure of how much is the deviation of heat current from RTA.

The generated heat current is related to the thermal gradient through Fourier's Law. If the thermal gradient is in the direction β, then the effective thermal current across a surface in the direction α is given by the equation 3.53. The proportionality constant being defined as the thermal conductivity tensor.

$$J_\alpha^p = -\sum_\beta k_{\alpha\beta}(\nabla T)^\beta, \tag{3.53}$$

By comparing equation 3.45 and 3.53, $k_l^{\alpha\beta}$ can be obtained in terms of $\boldsymbol{F}$ as follows:

$$k_{ph}^{\alpha\beta} = \frac{1}{k_B T^2 VN}\sum_{j,q} f^0(f^0+1)(\hbar\omega)^2 \vec{\boldsymbol{v}}^\alpha \boldsymbol{F}^\beta, \tag{3.54}$$

In the approach implemented in ShengBTE, equation 3.36 is solved iteratively starting with a zeroth-order approximation $\boldsymbol{F}_\lambda^0 = \tau_\lambda^0 v_\lambda$. The stopping criterion is that the relative change in the conductivity tensor calculated using equation 3.54, as measured using the Hilbert–Schmidt norm, is less than a configurable parameter with a default value of 10^{-5} W/mK. Taking the value calculated at the zeroth iteration is equivalent to using the RTA solution. It is important to note that the iterative process can have a large impact on the results when studying materials with high k_{ph}, such as diamond, where normal three-phonon processes play an important role, as the RTA deals with normal processes as resistive [159]. However, in systems like Si and Ge, where the Umklapp scattering is dominant, iterating to convergence typically adds less than 10% to the thermal conductivity at room temperature, when compared to the RTA result [160].

3.6.3. Thermal conductivity from EMD simulation

In equilibrium molecular dynamics simulations, we use the fluctuation-dissipation theorem from linear response theory to provide the connection between the energy dissipation in irreversible processes and the thermal fluctuations in equilibrium [161]. The net flow of heat in a solid, given by the heat current vector *J*, fluctuates around zero at equilibrium. In the EMD method, the thermal conductivity is related to how long it takes for these fluctuations to relax to equilibrium. In the case of an isotropic material, the conductivity is defined by equation 3.56 [161,162]:

$$k_{ph} = \frac{1}{K_B V T^2}\int_0^\infty \langle S_\alpha(\mathrm{t}) S_\alpha(0)\rangle \mathrm{dt}, \qquad \alpha = x, y \text{ or } z \text{ direction} \tag{3.56}$$

where V represents the volume of the simulation cell, K_B is the Boltzmann constant, t is time, T is temperature, and $\langle S_\alpha(t) S_\alpha(0)\rangle$ is the ensemble average of S_α in the α-direction, usually called the

heat current autocorrelation function (HCACF). In crystals where the fluctuations have long life times (i.e., the mean free path of phonons is large), the HCACF decays slowly. The thermal conductivity is related to the integral of the HCACF and is accordingly large. In materials such as amorphous solids, where the mean free path of phonons is small, thermal fluctuations are quickly damped leading to a small integral of the HCACF and a low thermal conductivity [163]. S_α denotes the heat current in the α-direction, which can be computed by equation 3.57 [164]:

$$S_\alpha = \frac{1}{V}\left[\sum_i E_i v_{i,\alpha} + \frac{1}{2}\sum_{i,j}(F_{ij} \cdot v_i) r_{ij}\right], \tag{3.57}$$

where E_i and v_i are the total energy and velocity of atom i, respectively, F_{ij} is the force exerted by atom j on atom i, and r_{ij} is the instantaneous and equilibrium interatomic separation vectors between atoms i and j.

Due to finite size effect in the EMD method, the thermal conductivity will depend on the size of the simulation cell if there are not enough phonon modes to accurately reproduce the phonon-phonon scattering in the associated bulk material. This effect can be removed by increasing the simulation cell size until the thermal conductivity reaches a size-independent value.

3.6.4. Thermal conductivity from NEMD

Non-equilibrium molecular dynamics, also known as the direct method, extract the thermal conductivity from the Fourier's law. In this method, one needs to impose a one-dimensional temperature gradient (Δa) on a simulation cell by giving room for kinetic energy exchange between the heat source and sink, and measure the resulting heat flux, J_z. The phonon thermal conductivity, k_{ph}, is computed then computed using equation 3.58:

$$k_{ph} = -\frac{J_z}{\Delta a}, \tag{3.58}$$

where the heat flux, J_z is given by equation 3.59:

$$J_z = \frac{KE_z}{2tL_xL_y}, \tag{3.59}$$

KE_z is the amount of transferred kinetic energy calculated over all exchanges during the simulation time t in the z-direction. L_x and L_y are the supercell lengths of the area through which the heat is transferred. The temperature gradient, Δa, is given by equation 3.60:

$$\Delta a = \frac{\Delta \mathrm{T}}{\Delta L_z}, \tag{3.60}$$

where T is the temperature in Kelvin and L_z is the length of the supercell in the *z*-direction.

In the NEMD method, the system is first allowed to reach a steady state, after which long simulations are conducted in order to obtain correct statistical measurements. The NEMD approach is often the method of choice for studies of nanomaterials, while for bulk thermal conductivity, particularly high-conductivity materials, the equilibrium method is typically preferred due to less severe size effects [165].

In NEMD simulations, finite-size effects arise when the length of the simulation cell L is not significantly longer than the phonon mean free path. This is understood to be a result of scattering that occurs at the interfaces with the heat source and sink. As a result, the system size limits the phonon mean free path. To eliminate the size effect, Schelling *et al*. [166] proposed a method based on the Matthiessen's rule to determine the effective mean free path Λ_{eff}, when L ~ Λ_∞, where Λ_∞ is the mean free path for an infinite system. The following relation gives the effective mean free path:

$$\frac{1}{\Lambda_{eff}} = \frac{1}{\Lambda_\infty} + \frac{4}{L}, \tag{3.61}$$

The factor of 4 in equation 3.61 occurs because as phonons move along the length of the simulation box from the heat source to the sink, its average distance after the previous scattering event should be L/4. From kinetic theory, the thermal conductivity is given as $k = \frac{1}{3} C_v v \Lambda$, where C_v and v are the specific heat and the phonon group velocity. Combing with equation 3.31, the effective thermal conductivity is obtained in equation 3.62:

$$\frac{1}{k_{eff}} = \frac{1}{k_\infty} + \frac{12}{C_v v L}, \tag{3.62}$$

Equation 3.62 suggests that a plot of 1/κ vs 1/L should be linear and that the thermal conductivity of an infinite system can be obtained by extrapolating to 1/L = 0. Fig. 3.4 shows the examples of

using equation 3.62 to extract the thermal conductivity with infinite sizes for silicon and diamond. Good linear fits found in these cases imply the successful application of equation 3.62.

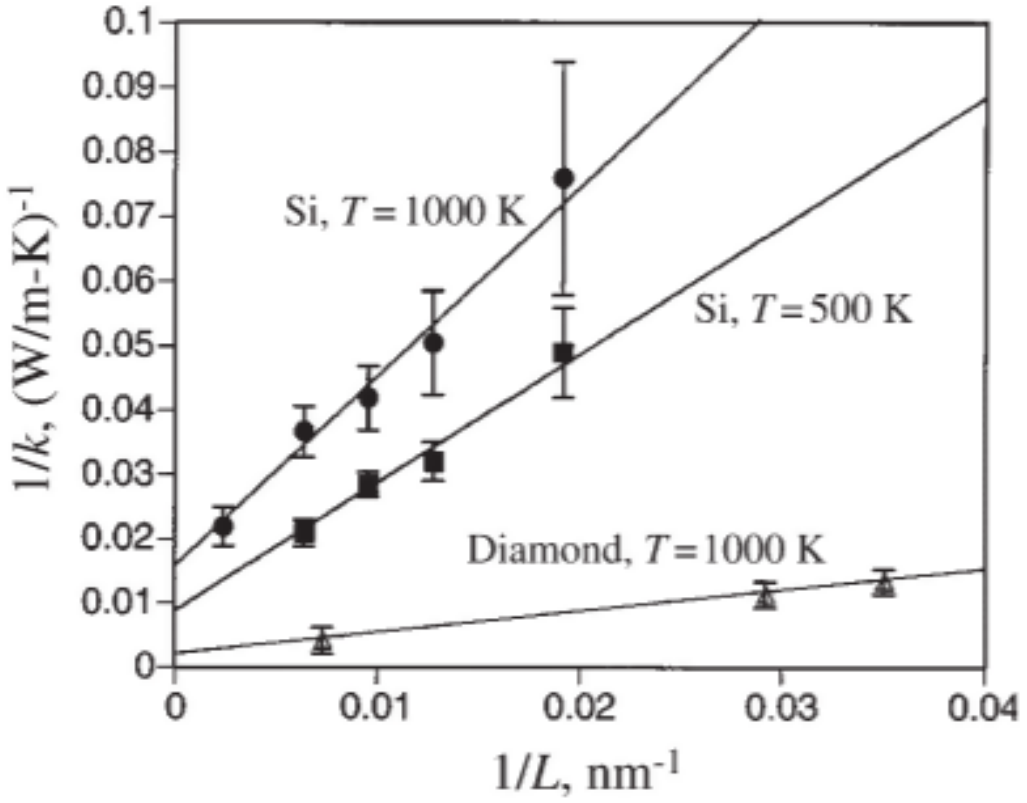

Fig. 3.4. System size dependence of thermal conductivity for silicon and diamond. From Schelling *et al*. [166]. Copyright (2002), with permission from American Physical Society.

3.7. Elastic constants

Elastic constants describe the behavior of crystals as a function of elastic deformations. Elastic properties are related to mechanical and thermal properties such as specific heat, thermal expansion, Debye temperature, melting point, and Grüneisen parameter. They also give information about the anisotropic character of bonding in crystals.

Elastic constants are obtained by computing the second order derivatives of the total energy with respect to the distortion parameter [167,168]. This calculation is very sensitive to data point selection, due to numerical inaccuracies around the minimum of total energy vs. atomic displacements. Each C_{ij} was derived *via* the second-order Taylor expansion of the total energy with respect to the applied distortion, equation 3.63:

$$C_{ij} = \frac{1}{V_o}\frac{\partial^2 E}{\partial \varepsilon_i \partial \varepsilon_j} \quad 3.63$$

where E is the total energy of the strained cell, ε is the component of the applied strain, and V_o is the equilibrium unit cell volume.

In hexagonal systems such as UB_2, there are only five independent elastic constants Ref. [15]. They can be determined by imposing strains, either individually or in combination, along specific crystallographic directions. There are only five independent elastic constants for hexagonal crystal, which are C_{11}, C_{33}, C_{44}, C_{12} and C_{13}. C_{66} can be determined by the symmetry relationship:

$$C_{66} = \frac{1}{2}(C_{11} - C_{12}), \quad (3.64)$$

For hexagonal and tetragonal crystalline structures, the well-known Born criteria [169] must be satisfied for mechanical stability:

$$C_{11} > 0, C_{44} > 0, C_{11} > |C_{12}| \text{ and } (C_{11} + C_{12})C_{33} - 2C_{13}^2 > 0, \quad (3.65)$$

Results from elastic constants calculated can be used to determine the theoretical polycrystalline bulk modulus B and shear modulus G based on the approximations of Voigt [170], Reuss [171] and Hill [172]. Hill showed that the Voigt and Reuss methods resulted in the upper and lower bounds of the isotropic elastic modulus respectively. Therefore, estimation of the bulk and shear moduli is calculated as the arithmetic mean of both values. For a hexagonal crystal like UB_2, the Voigt bound of B and G can be estimated as follows:

$$B_V = \frac{1}{9}[2(C_{11} + C_{12}) + C_{33} + 4C_{13}, \quad (3.66)$$

$$G_V = \frac{1}{30}(M + 12C_{44} + C_{66}), \quad (3.67)$$

The Reuss bounds [29], the moduli are given by:

$$B_R = \frac{C^2}{M}, \quad (3.68)$$

$$G_R = \frac{5}{2}\frac{C^2 C_{44} C_{66}}{3B_V C_{44} C_{66} + C^2(C_{44} + C_{66})}, \quad (3.69)$$

$$M = C_{11} + C_{12} + 2C_{33} - 4C_{13}, \quad (3.70)$$

$$C^2 = (C_{11} + C_{12})C_{33} - 2C_{13}^2 \quad (3.71)$$

The bulk and shear modulus are computed in the Hill empirical average using equations (3.72) and (3.73):

$$B_H = \frac{1}{2}(B_V + B_R), \quad (3.72)$$

$$G_H = \frac{1}{2}(G_V + G_R), \quad (3.73)$$

Furthermore, Young's modulus E and Poisson's ratio *v* can be estimated as:

$$\mathrm{E} = \frac{9B_H G_H}{3B_H + G_H}, \quad (3.74)$$

$$\sigma = \frac{3B_H - 2G_H}{2(3B_H + G_H)}, \quad (3.75)$$

Elastic anisotropy of crystals reflects a different character of bonding in various directions; this has an important implication because it influences various physical properties of materials. It can be described either through; the universal anisotropic index A^U proposed by Ranganathan and Ostioja-Starzeweski [173] for crystals with any symmetry defined by:

$$A^U = 5\frac{G_V}{G_R} + \frac{B_V}{B_R} - 6 \geq 0, \quad (3.76)$$

or through the percentage anisotropy indexes of bulk and shear moduli (A_B and A_G), proposed by Chung and Buesen [174], defined as follows:

$$A_B = \frac{B_V - B_R}{B_V + B_R}, \quad (3.77)$$

$$A_G = \frac{G_V - G_R}{G_V + G_R}, \quad (3.78)$$

3.7.1. Debye temperature and sound velocities

Debye temperature (θ_D) is a critical parameter which reflects the strength of bond in a solid-state material. In this work, semi-empirical formulae were used to estimate the Debye temperatures of UB_2 and U_3Si_2 by using the elastic constants, the average sound velocity (v_m), the longitudinal

sound velocity (v_l) and the transverse sound velocity (v_t). The Debye temperature is related to the average sound velocity as follows [175]:

$$\theta_D = \frac{h}{k}\left[\frac{3n}{4\pi}\left(\frac{N_A\rho}{M}\right)\right]^{\frac{1}{3}} v_m, \tag{3.79}$$

The average sound velocity in polycrystalline materials is given as [176]:

$$v_m = \left[\frac{1}{3}\left(\frac{2}{v_t^3} + \frac{1}{v_l^3}\right)\right]^{\frac{1}{-3}}, \tag{3.80}$$

v_l and v_t can be expressed in terms of polycrystalline bulk (B) and shear (G) moduli [177]:

$$v_t = \left(\frac{G}{\rho}\right)^{\frac{1}{2}}, \tag{3.81}$$

$$v_l = \left(\frac{3B+4G}{3\rho}\right)^{\frac{1}{2}}, \tag{3.82}$$

In the above expressions, h and k are Plank's and Boltzmann's constants; N_A is Avogadro's number; ρ is the density; M is the molecular weight; and n is the number of atoms in a formula unit.

3.8. Thermodynamic properties with quasi-harmonic approximation

The quasi-harmonic approximation is an extension of the harmonic method, in which the local potentials are described by harmonic wells, but their minima are not clamped to the ground state lattice positions. In the framework of quasi-harmonic approximation (QHA), volume dependence of various thermodynamic properties can be captured by calculating the phonon frequencies at different volumes around the equilibrium volume. In QHA, anharmonicity is included in an indirect way through the volume dependence of phonon spectrum. Described below are the thermodynamic properties derived from phonons using QHA.

3.8.1. Thermal Expansion

The Helmholtz free energy at volume $V(T)$ and temperature T is a sum of the electronic energy ($E(V(T), T)$ and vibrational energy $F_{vib}(V(T), T$ for a given volume $V(T)$ and temperature (T):

$$F(V(T), T) = E(V(T)) + F_{vib}(V(T), T) \tag{3.83}$$

The electronic entropy is not accounted for in this thesis. The vibrational Helmholtz free energy is calculated by evaluating the phonon density of states at different volumes and integrating the energy of phonons ($\hbar\omega$) over the density of states ($\rho(\omega)$) and weighing it by the temperature-dependent Boltzmann factor as described before [178]:

$$F_{ph}(V(T),T) = k_B T \int_{\omega_{min}}^{\omega_{max}} \rho(\omega)\ \ln\left[2\sinh\left(\frac{\hbar\omega}{2k_B T}\right)\right] d\omega \tag{3.84}$$

where k_B is the Boltzmann constant. The equilibrium volume at each temperature was calculated by fitting the free energy to the Birch-Murnaghan equation of state [179]:

$$F(V(T),T) = F_0(T) + \frac{B_0(T)V(T)}{B_0'(T)}\left[\frac{\left(\frac{V_0(T)}{V(T)}\right)^{B_o'(T)}}{B_0'(T)-1} + 1\right] - \frac{B_0(T)V_0(T)}{B_0'(T)-1} \tag{3.85}$$

where $F_0(T)$, $B_0(T)$, and $B_o'(T)$ are the values of the total free energy, bulk modulus and the first derivative of bulk modulus, for the equilibrium primitive unit cell volume $V_0(T)$ respectively at the temperature T. The expression to calculate the volumetric thermal expansion coefficient (α_V) at constant pressure (P) is given by equation (3.86).

$$\alpha_V(T)_p = \frac{1}{V_o(T)}\left(\frac{\partial V_o(T)}{\partial T}\right)_p \tag{3.86}$$

3.8.2. Heat Capacity and entropy

The specific heat capacity at constant volume (C_V) and entropy (S) are calculated using equations (3.87) and (3.88) for fixed volume and constant pressure, respectively.

$$C_V(T) = N_A k_B \int_{\omega_{min}}^{\omega_{max}} \frac{\left(\frac{\hbar\omega}{k_B T}\right)^2 e^{\left(\frac{\hbar\omega}{k_B T}\right)}}{\left[e^{\left(\frac{\hbar\omega}{k_B T}\right)} - 1\right]^2} \rho(\omega) d\omega \tag{3.87}$$

$$S = -k_B \int_0^{\infty} \rho(\omega)\left(ln\left(1 - e^{-\frac{\hbar\omega}{k_B T}}\right) + \frac{\hbar\omega}{k_B T\left(1 - e^{-\frac{\hbar\omega}{k_B T}}\right)}\right) d\omega \tag{3.88}$$

where N_A is Avogadro's number, k_B is the Boltzmann constant and $\rho(\omega)$ is the density of states of phonons (with $\hbar\omega$ energy) per primitive unit cell.

3.9. Surface modelling

Different surfaces can be created from the bulk crystal structure by cutting along different crystallographic planes. The interaction of a surface with molecules in the gaseous or liquid phase could alter the surface chemistry. Atoms at the surface commonly tend to have lower coordination than those in the bulk system. Due to changes in the coordination of surface atoms and the presence of dangling bonds in some cases, the surface may need reconstruction or geometry relaxation to attain equilibrium.

Two common models used in surface simulations include the cluster model and the periodic slab model. The cluster model treats the surface as a small isolated cluster of atoms one facet of which has the same symmetry and atomic arrangement as the crystal surface intended for study. In a periodic slab model, periodicity in two lateral directions generates exposed surfaces with vacuum on either side of the slab, as shown in Fig. 3.5. Two important things should be kept in mind when using the periodic slab model. The vacuum thickness should be large enough to avoid surfaces of consecutive slabs from interacting with each other, and the thickness of the slab should also be thick enough to prevent interaction between the two surfaces of one slab. One could "freeze" one end of the slab usually at the bottom to mimic the bulk, while the atoms at the topmost layers are allowed to relax unconstrainedly. This is denoted by relaxed and fixed atoms in Fig. 3.5. This approach permits the simulation of a single surface and allows more choice in complex surfaces.

The different low-index surfaces investigated in this thesis were created from the optimized bulk materials, using the METADISE code [180]. This does not only consider periodicity in the plane direction, but also provides the different atomic layer stacking resulting in a zero dipole moment (β) perpendicular to the surface plane, as is required for a realistic surface model description [181].

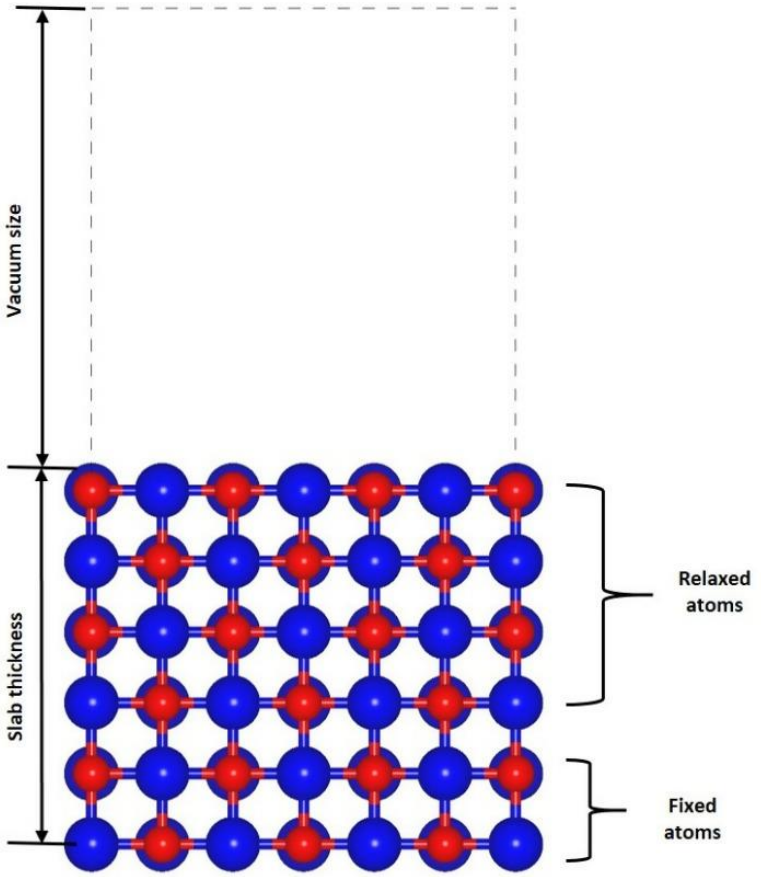

Fig. 3.5. Representation of a periodic slab model showing a slab constructed with six atomic layers thickness and a vacuum region.

In this model, the crystal is represented by a stack of planes perpendicular to the surface. The dipole model, which is the classification of surface based on electrostatic criteria, was introduced by Tasker [120] who considers the crystal as a stack of planes, where three possibilities can arise as illustrated in Fig. 3.6. In type I, each plane has an overall zero charge, because it is composed of anions and cations in stoichiometric ratio thereby making it to be non-dipolar. Whereas, in type II, the stacking nature of three symmetrically charged planes cancels out the dipole moment perpendicular to the surface. In type I and II, there is no need for reconstruction of the surface, because the repeat unit, which is non-dipolar, is perpendicular to the surface. However, in type III surfaces, the alternating charged planes stacked in a sequence produces a dipole moment perpendicular to the surface. However, the surface can be reconstructed to have a zero dipole moment perpendicular to the surface by moving half of the ions with similar charge from the top to the bottom of the slab.

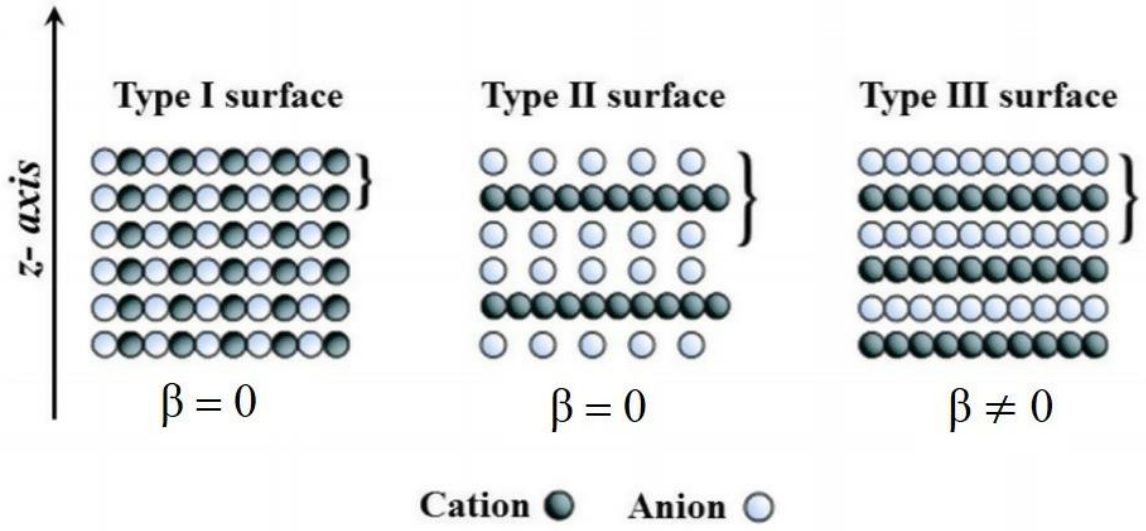

Fig. 3.6. Surfaces classification according to Tasker [181]: (a) Type I, each plane contains an equal number of cations and anions (the net dipole moment is zero; β = 0); (b) Type II, each plane is charged, but there is no net dipole moment perpendicular to the surface (β = 0); (c) Type III, includes charged planes and a dipole moment normal to the surface (β ≠ 0).

3.9.1. Surface stabilities

The surface stability is an important property of the surface, because it influences the reactivity. Generally, the less stable surfaces tend to be more reactive towards adsorbing species than the more stable ones. The free surface energy of a given plane is a measure of the stability of a particular surface, where a small, positive value indicates a stable surface. Using the periodic slab model containing slabs with two surfaces, the surface energy (γ) of the U_3Si_2 surfaces were determined according to equation 3.89:

$$\gamma_r = \frac{E_{slab}^{relaxed} - nE_{bulk}}{2A}, \quad (3.89)$$

In this Equation, $E_{slab}^{relaxed}$ is the slab energy with all atomic coordinates relaxed unconstrainedly; nE_{bulk} is the energy of an equal number (n) of bulk U_3Si_2 formula unit; A is the area of the slab surface; and the factor of 2 reflects the fact that there are two surfaces for each slab.

3.9.2. Surface adsorption

Atoms and molecules interact with surfaces with forces originating either from the van der Waals interactions or from the hybridization of their orbitals with those of the atoms of the substrate [182]. Depending on which contribution dominates, we speak of physiosorption or of

chemisorption. These are limiting cases since hybridization is always present at small enough adsorption distances, even for adsorbed rare gases.

Physiosorption is based on the van der Waals interactions between the adsorbate and the substrate and also between the adsorbed molecules. The adsorption energy depends on the number of atoms involved in the interaction. The geometrical structure and electronic properties of the physisorbed molecule or atom, and also of the surface are essentially preserved. At the most a slight deformation may take place. A physisorbed molecule can spontaneously leave the surface after a certain amount of time.

Chemisorption on the other hand occurs when there is the formation of a chemical (often covalent) bond between the adsorbate and surface. Binding energies are typically of several eV. Compared to physiosorption, the geometrical structure and electronic characteristics of the chemisorbed molecule or atom are strongly perturbed. The hybridized orbitals formed are often characterized by charge transfer from the substrate to adsorbate and vice versa. The surface structure is also typically not preserved in chemisorption, as the surface atoms usually undergo relaxation in order to minimize their energy.

Oxidation of surfaces depend on how rapidly chemisorption occurs and the strength of the chemisorption bond. If the bond is too weak, the oxidizing molecule may desorb prior to reacting and if strong enough, the release of the product and regeneration of the site may be retarded.

When atoms or molecules adsorb at surfaces, energy is released due to bond formation. The energy released is called adsorption, E_{ads}, which is a function of coverage and distribution of the adsorbates at the surface. Considering an oxygen molecule, (O_2), adsorbed on U_3Si_2 surface, the adsorption energy is calculated using the expression:

$$E_{ads} = E_{surface+O_2} - (E_{surface} + E_{O_2}), \tag{3.90}$$

where $E_{surface+O_2}$ is the total energy of the substrate-adsorbate system in the equilibrium state, $E_{surface}$ and E_{O_2} are the total energies of the substrate with clean surface and the free O_2 molecule in the spin triplet state respectively. By this definition, a negative adsorption energy indicates exothermic reaction and favorable adsorption. The total energy of an isolated molecule can be obtained in cubic box of size large enough (> 10 Å) to minimize lateral interactions in neighboring cells.

There is also possibility of co-adsorption of two or more molecules on a surface. For instance co-adsorption energies between the H_2O and O on the U_3Si_2 surface is calculated as follows:

$$E_{co-ads} = E_{surface+(H_2O+O)} - (E_{surface} + E_{H_2O} + 1/2E_{O_2}), \quad (3.91)$$

Where E_{H_2O}, E_{O_2}, $E_{surface}$, and $E_{surface+(H_2O+O)}$ are the total energy for the free molecule of water, molecular oxygen, the clean U_3Si_2 surface, and the co-adsorbed (H_2O+O) + U_3Si_2 surface systems, respectively.

3.10. Defect energies and defect volumes

In a broader term, defect energetics are simply the energy difference between a perfect crystal supercell and one that contains the defect or defect cluster expressed as equation 3.92:

$$E_f = E_d - E_p \pm \sum_X \mu(X), \quad (3.92)$$

where E_d and E_p are the total energies of the defective and perfect simulation cells, and $\mu(X)$ is the chemical potential of all species *X* that are added or removed from the perfect crystal to form the defect. Equation 3.92 is only valid for non-charged defects.

Since the systems under investigation are metallic, the chemical potential μ is simply calculated as the DFT energy per atom of the ground-state crystalline phases of uranium, boron, silicon and zirconium namely the low temperature α phase uranium crystal (orthorhombic), silicon crystal (diamond structure), boron in the α-rhombohedral with 12 atoms per unit cell and zirconium with hexagonal closed packed structure. Specific defects formation energies are calculated using the following expressions:

Formation energy of a vacancy is the energy cost of creating a vacancy. This is given by

$$E_F^{VacX} = E^{N-1} - E^N + \mu(X), \quad (3.93)$$

where E^N is the energy of the supercell without defects, E^{N-1} is the energy of the supercell with a vacancy and $\mu(X)$ is the chemical potential calculated as the total energy per atom of the ground-state structure.

The Fission product (FP) **incorporation energy** $E_{inc}\,(FP)$ is defined as the energy required to incorporate a FP in a preexisting point defect site. It gives important information about the behavior of defects in defective system. It is expressed as follows

$$E_{inc}\,(FP) = E_{def}\big(FP_{trap}\big) - E_{def}\big(V_{trap}\big), \tag{3.94}$$

where $E_{def}\big(FP_{trap}\big)$ is the defect energy of the FP located on a trap site and $E_{def}\big(V_{trap}\big)$ is the defect energy of the preexisting trap site. The chemical potential of Xe is the total energy of an isolated gas atom, and that Zr is total energy of Zr with hexagonal closed packed structure.

The solution energy (E_{sol}) is the sum of the incorporation energy $E_{inc}\,(FP)$ and the energy require to create the trap site. For example, if the trap site is a vacancy site, then E_{sol} is given by equation 3.95:

$$E_{sol} = E_{inc}\,(FP) + E_F^{VacX}, \tag{3.95}$$

The antisite formation energy (E_f^A) is the energy cost of atoms swapping position in the lattice

$$E_f^A = E_A^N - E^N, \tag{3.96}$$

where E_A^N is the energy of the supercell with the antisite pair.

The relaxation volume (ΔV_{rel}) of a defect is defined as the difference in volume between a supercell containing the defect (V_d) and the perfect supercell (V_p):

$$\Delta V_{rel} = V_d - V_p, \tag{3.97}$$

When calculating ΔV, mass action is not considered; in other words, the number and types of atoms between the defective and perfect cell do not have to be the same. This allows for comparison of defects involving different species. A related quantity often found in the literature is the defect formation volume (ΔV_{for}), wherein the number of atoms involved in the volumetric change is conserved:

$$\Delta V_{for} = V_d - \frac{N_d}{N_p} V_p, \tag{3.98}$$

where N_p and N_d are the number of atoms in the perfect and defective simulation cell, respectively. However, the defect formation volume is only correctly defined for intrinsic defects of elemental solids [183], as the reference volume of an isolated extrinsic atom is not a strictly defined quantity.

The formation energy of a compound is defined as the difference between the cohesive energies of the compound and its constitutive elements. For example, in the case of UB_2, it decomposed as follows:

$$\alpha\text{-U (solid)} + 2\text{B (solid)} \longrightarrow UB_2$$

This yielded the following equation for formation energy per atom:

$$E^f_{(U_aB_b)} = \frac{E(U_aB_b) - aE(U) - bE(B)}{a+b}, \tag{3.99}$$

where a and b are the number of uranium and boron atoms in the unit cell of UB_2 respectively. E (U) is the energy per U atom in the ground state structure and E (B) is the energy per B atom.

Chapter 4

A first principles study of the electronic structure, elastic and thermal properties of UB_2

4.1. Overview of Chapter 4

The possible use of Uranium diboride (UB_2) as a fuel in a nuclear reactor requires knowledge of its thermophysical properties as a function of temperature. This study was initiated to provide data on the thermal properties and electronic structure of UB_2. These properties can be used by the nuclear fuel modeling and simulation community to parametrize performance codes, thereby providing the necessary tools for fuel performance evaluation under normal and accident conditions.

This chapter is presented as manuscript #1 (A first principles study of the electronic structure, elastic and thermal properties of UB_2). My contributions to this paper include a review of relevant literature, design and carrying out of the required simulation, analysis of results and preparation of the manuscript. My supervisors, Prof. Jerzy Szpunar and Dr. Barbara Szpunar, reviewed the paper before it was submitted for publication. The manuscript was submitted for publication after implementing their suggestions. To avoid repetition of information provided in Chapter 3 of this thesis, the equation for calculation of k_{ph} has been removed from this chapter. The copyright permission to use the manuscript in this thesis was obtained from the publishers and it is provided in APPENDIX E.

The manuscript was published in 2017 in *Journal of Nuclear Materials*:

- E. Jossou, L. Malakkal, B. Szpunar, D. Oladimeji, J.A. Szpunar, A first principles study of the electronic structure, elastic and thermal properties of UB_2, J. Nucl. Mater. 490 (2017) 41–48. doi:10.1016/j.jnucmat.2017.04.006.

A first principles study of the electronic structure, elastic and thermal properties of UB_2

Ericmoore Jossou[1], Linu Malakkal[1], Barbara Szpunar[2], Dotun Oladimeji[2], Jerzy A. Szpunar[1]

[1]*Department of Mechanical Engineering, College of Engineering, University of Saskatchewan, 57 Campus Drive, Saskatoon, S7N 5A9, Saskatchewan, Canada.*
[2]*Department of Physics and Engineering Physics, College of Art and Science, University of Saskatchewan, 116 Science Place, Saskatoon, S7N 5E2, Saskatchewan, Canada*

4.2. Abstract

Uranium diboride (UB_2) has been widely utilized for refractory use and is a proposed material for Accident Tolerant Fuel (ATF) due to its high thermal conductivity. However, the applicability of UB_2 towards high temperature usage in a nuclear reactor requires investigation of the thermomechanical properties, but recent studies have failed in highlighting applicable properties. In this work, an in-depth theoretical outlook of the structural and thermophysical properties of UB_2, including but not limited to elastic, electronic and thermal transport properties, is presented. These calculations were performed within the framework of Density Functional Theory (DFT) + U approach, using Quantum ESPRESSO (QE) code considering the addition of Coulomb correlations on the uranium atom. The phonon spectra and elastic constant analysis show the dynamic and mechanical stability of UB_2 structure, respectively. The electronic structure of UB_2 was investigated using full potential linear augmented plane waves plus local orbitals method (FP-LAPW+lo), as implemented in WIEN2k code. The absence of a band gap in the total and partial density of states confirms the metallic nature while the valence electron density plot reveals the presence of covalent bonds between adjacent B–B atoms. The phonon-assisted thermal conductivity ($\boldsymbol{k_{ph}}$) was predicted by solving Boltzmann transport equation (BTE) using ShengBTE code. The second-order harmonic and third-order anharmonic interatomic force constants required as input to ShengBTE were calculated using Density-functional perturbation theory (DFPT). However, the electronic thermal conductivity ($\boldsymbol{k_{el}}$) was predicted using Wiedemann-Franz law as implemented in Boltztrap code. In addition, the sound velocity along 'a' and 'c' axes exhibit high anisotropy, which accounts for the anisotropic thermal conductivity of UB_2.

Keywords: *Uranium diboride; Boltzmann transport equation; thermal conductivity; electronic structure.*

4.3. Introduction

Uranium dioxide (UO_2) is the standard U-bearing compound of choice for commercial nuclear reactors due to its high melting point, thermal stability and chemical stability. In the wake of the tragic nuclear accident at Fukushima, there is a renewed interest in the design of safer fuel for Generation IV nuclear reactors. In comparison to the present ceramic oxide fuels, the metallic UB_2 fuel has superior thermophysical properties, including high thermal conductivity and a comparable melting point. Moreover, UB_2 has higher uranium density, which could provide reactor performance gains at constant enrichment, or be used to offset a neutronic penalty incurred by replacement of zirconium cladding (low neutron cross section) with a more oxidation-resistant option [184].

Until now, only a limited experimental investigation to characterize the behavior of UB_2 has been available. For instance, Dancausse *et al.* [185] investigated the behavior of UB_2 under pressure with no structural transformation up to 50.3 GPa. The authors observed the relative contraction in lattice parameters $\Delta a/a_o$ and $\Delta c/c_o$ between the ambient and highest pressure to be 6.5% and 3.9%, respectively.

Matar *et al.* [70] investigated the electronic structure of a series of binary uranium boride compounds, including UB_2, within the framework of the density functional theory (DFT) in which the effects of exchange and correlation were treated within the local spin density approximation (LSDA). The results of the partial crystal orbital overlap population (PCOOP) showed that the U–U interaction contributed relatively less to chemical bonding within the lattice, while U–B and B–B interactions were very pronounced and similar. The effect of the on-site Coulomb force due to the 5*f* electron was not accounted for; however, this has been covered in our present studies.

To gain insight into the thermal properties of UB_2, which is necessary for the evaluation of safety and lifetime of UB_2 fuel, theoretical calculations must be performed for this compound. It is well known that the elastic properties are essential in understanding the macroscopic properties of a material because they relate to various fundamental solid state and thermodynamic properties.

Therefore, in this work, *ab initio* techniques are deployed to determine the structural, elastic, electronic and thermal properties of UB_2. Subsequently, by analyzing the elastic and electronic properties, its bonding character is also examined. Since, this system is ionic and non-magnetic (NM) like any other AlB_2-type hexagonal structure [186], the inclusion of spin polarization (SP)

or spin–orbit coupling (SOC) has no influences on the structural and elastic properties of the compound. With this in mind, all the results in this work are presented for NM cases.

4.4. Computational details

Density functional theory (DFT) [109] calculations of structural and elastic properties of UB_2 were performed with Quantum ESPRESSO (QE) code [143] which also implement quasi-harmonic approximation (QHA) within density functional perturbation theory (DFPT) [187] and a plane-wave-pseudopotential framework to calculate the lattice dynamics and thermodynamic properties. An interface to QE, qe-nipy-advanced [188] method, developed in our group was also used for this investigation. The exchange-correlation functional within the generalized gradient approximation (GGA) for solids (PBEsol) [126] and ultrasoft pseudopotentials was employed to represent the interaction between the valence electron and the ionic core.

Due to the onsite Coulomb repulsion among the localized U *5f* electrons, the Hubbard (DFT + U) approximation was utilized to estimate the strong correlation effect [136]. The total energy convergence of the hexagonal structure was obtained using a kinetic energy cut off of 70 Ry and the Brillouin zone (BZ) integration over a Monkhorst–Pack of 8×8×6 mesh. The dynamical matrices for phonon density of states were calculated on a mesh of 5×5×3 q-points in the irreducible BZ while QHA [189] was used to predict the thermodynamic properties such as the thermal expansion, heat capacity at constant volume and entropy.

The electrical conductivity was calculated using the BoltzTraP code [152] and the electronic structure calculated by QE for a vast number of k points mesh of 20×20×16. In contrast to uranium nitride (UN), which has been studied extensively [88], there are no experimental data on the resistivity of UB_2 that would allow us to evaluate the relaxation time of the electrons. Hence, a derived correlation of the relaxation time of electrons for UN with the scaling factor equal to the atomic density ratio of UN to UB_2 (0.718), was used:

$$\tau(T) = 0.718(1.50 \times 10^{-22}T^2 - 8.64 \times 10^{-19}T + 4.13 \times 10^{-15})s, \qquad (4.1)$$

The electronic conductivity ($\boldsymbol{k_{el}}$) was then estimated by the Wiedemann–Franz law for the temperatures between 300 K and melting point, where $\boldsymbol{k_{el}} = L\sigma T$ (the Lorentz number (L) is $2.45 \times 10^8\ V^2K^{-2}$, σ is electrical conductivity in Sm^{-1} and T is the temperature in Kelvin) [151], while the phonon-assisted thermal conductivity ($\boldsymbol{k_{ph}}$) was predicted by solving the

Boltzmann transport equation (BTE) using the ShengBTE solver code [158]. The three-phonon scattering matrix elements were obtained from the harmonic and anharmonic interatomic force constants (IFCs) using DFPT and DFT as implemented in QE code. In the approach implemented in ShengBTE, equation 3.54 was iteratively solved starting with a zeroth-order approximation. The stopping criterion was such that the relative change in the calculated conductivity tensor was less than a configurable parameter. Stopping at the zeroth iteration is equivalent to operating under the RTA.

We used a 4×4×4 supercell to calculate the third-order IFCs for solving BTE while force cut off distance was set such that the interaction range was up to the five nearest neighbors. A mesh of 5×5×3 q-points was used to calculate the second-order IFCs needed to compute the $\boldsymbol{k_{ph}}$ of UB_2. Once the harmonic second order and the third-order anharmonic IFCs were calculated, $\boldsymbol{k_{ph}}$ of UB_2 was then calculated by solving the BTE as implemented in the ShengBTE package. The q-space grid of 15×15×12 was used for solving the BTE, as this grid size was found to give well converged lattice thermal conductivity ($\boldsymbol{k_{ph}}$) values for UB_2.

The electronic structure of UB_2 was computed using the full-potential linearized augmented plane wave plus local orbitals (FPLAPW+ lo) method [190] in the framework of the DFT as implemented in the Wien2k code [191]. The atomic sphere radii, R_{MT} was set to 2.4 a.u and 1.8 a.u for U and B, respectively. The basis sets cut-off parameters for well-converged calculations was set to $R_{MT}.K_{max} = 9, G_{max} = 25Ry^{1/2}$, and $L_{max} = 9.5$ for a Fourier expansion of the changing density. Structural optimization was done by fitting the data to a Birch-Murnaghan equation of state [179].

The implementation of GGA + U is rotationally invariant, hence $U_{eff} = (\mathrm{U} - \mathrm{J})$ was used, where J was set to zero. Usually, the value of U_{eff} may be obtained from spectroscopy data which are not available for UB_2. The U value could also be calculated self-consistently [141]. In that case, the Hubbard U is based on a linear response approach that allows the parameters entering the DFT + U correction to be fixed in close relationship with the behavior of the system under consideration. However, in this thesis the value of U is treated as a semi-empirical parameter which is obtained by fitting the calculated lattice parameter to experimental value [192]. The U_{eff} of 2.00 eV was used in the electronic structure calculations.

4.5. Results and discussion

4.5.1. Ground-state structural and elastic properties

UB_2 has the AlB_2-type hexagonal structure with one formula unit per cell and belongs to the space group of *P6/mmm* (191).The structure is characterized by a 2-dimensional boron network with U and B hexagonal layers stacked perpendicular to the c-axis at 0 and ½ [185]. Fig. 4.1 is schematic of the crystalline unit cell. X-ray crystallography data has shown that one uranium atom occupies 1a Wyckoff site (0,0,0) and two boron atoms occupy 2d Wyckoff sites (1/3,2/3,1/2) [193]. The ground states (0 K) property of the structure was obtained by minimizing the total energy with respect to the lattice parameters ('a' and 'c').

The stable crystalline structural properties was calculated by the DFT + U scheme as adopted in the studies of many other uranium nuclear fuels, such as UO_2 [194], UN [195] and U_3Si_2 [63]. The U value used in this work was determined by testing different U values to predict the lattice parameter of UB_2 [192], and it was found that a value of $U_{eff} = 2.0\ eV$ gives lattice parameters which agrees well with experimental values determined at room temperature (See Fig. A.4.1. in Appendix A). It is well known that GGA+U may lead to a metastable state, but recently Noordhoek *et al.* [64] investigated a series of U-Si alloys and showed that the effect of local minimum was quite small. This gave some confidence to trust the results of this work since the technique involved in determining a global electronic minimum is computationally expensive.

The calculated lattice parameters along with the values from the experiment are listed in Table 4.1. The comparison of the calculated value with the experimental data reported by Beckman *et al.* [196] suggests that the lattice parameter predicted by this work is in excellent agreement. The calculated bond lengths of $d_{B-B} = 2.694$ Å and $d_{U-B} = 1.811$ Å are in good agreement with the values 2.69 Å and 1.81 Å, respectively, determined by Beckman *et al.* [196].

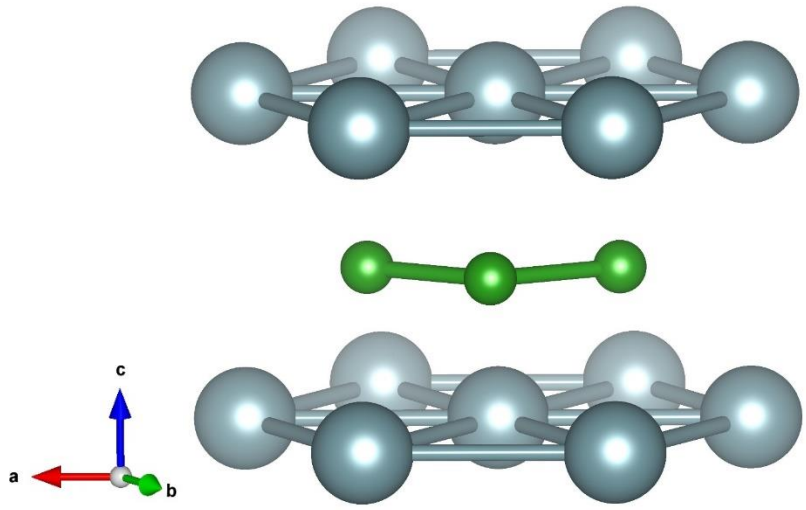

Fig. 4.1. Crystal structure of uranium diboride (UB_2) showing the unit cell. (Color scheme: U= grey and B= green).

Table 4.1. Structural properties of UB_2 calculated in this work using GGA+U with $U_{eff} = 2.00\ eV$.

Type of Calculation	a	c	c/a	V	B	B´
GGA [This work]	3.114	3.981	1.278	33.43	231.3	3.64
GGA + U [This work]	3.139	3.994	1.272	34.08	225.9	3.75
Expt. [196]	3.136	3.988	1.272	33.97	–	–

The calculated results for the elastic constants are shown in Table 4.2. UB_2 is mechanically stable since all its elastic constants fulfill Born stability criteria as stated in equation 3.65. It is well known that C_{11} and C_{33} determine the stiffness-to-uniaxial strains along the crystallographic 'a' and 'c' axes respectively. The other elastic constants, C_{12}, C_{13}, C_{44} and C_{66}, are related to shear deformation.

Results from elastic constants calculated are used to determine the theoretical polycrystalline bulk modulus B and shear modulus G using equations 3.66–3.73 while the Young's modulus E and Poisson's ratio *v* are estimated using equations 3.74 and 3.75 respectively.

Table 4.2. Elastic constants C_{ij} (GPa) for UB_2. Results presented are for the GGA and GGA + U. The U parameter is 2.00 eV.

Type of Calculation	C_{11}	C_{33}	C_{44}	C_{12}	C_{13}	C_{66}
GGA	341.93	502.92	104.92	161.08	280.39	90.43
GGA + U	339.25	505.26	93.99	173.75	292.55	82.75

The ratio of bulk modulus to shear modulus, B/G, for polycrystalline can be used to determine brittleness or ductility of the material. Even though B and G are elastic properties, Pugh [197] established a relationship between elasticity and plasticity of metals. It must be noted that Pugh's approach is entirely empirical but provides a quick way of estimating the ductility of materials. According to Pugh [197], a value greater than 1.75 implies ductility and a lower value is indicative of the brittleness of the material. The B/G of UB_2 calculated with GGA (2.29) and GGA + U (3.29) implies that it is ductile in nature.

Further conclusion can be drawn in regard to the ductile nature of UB_2 on the basis of its Poisson ratio[2]. It is important to note that any relationship drawn between ductility and Poisson ratio would seem at first non-intuitive as the Poisson ratio is established within the elastic domain while ductility and brittleness describe material response within the plastic domain. However, recent empirical work has establish a correlation between brittle–ductile transformations related to a change in the Poisson ratio [198]. In this case, the value of 0.36 means that UB_2 is ductile since the critical value which separates ductility from brittleness is 0.26 [199].

Elastic anisotropy of UB_2 is determined using the universal anisotropic index A^U as given by equation 3.76 and through the percentage anisotropy indexes of bulk and shear moduli (A_B and A_G) using equations 3.77 and 3.78 respectively.

Table 4.3. Calculated bulk and shear moduli B and G, Young's modulus E in GPa, the Poisson's ratio σ, and the anisotropic indexes of UB_2 using GGA+U with $U_{eff} = 2.00\ eV$.

Type of Calculation	B	G	B/G	E	σ	A^U	A_B	A_G
GGA[3]	269.74	92.35	2.92	248.67	0.35	0.04	0.08	0.01
GGA + U	274.65	83.55	3.29	227.57	0.36	0.08	0.09	0.01

The Voigt and Reuss approximation of the Bulk moduli should give the same value for B and G for isotropic systems. Consequently, deviations from zero indicate anisotropy. The result of the anisotropic index A^U suggests that UB_2 is elastically anisotropic. This fact is further corroborated by the percentage anisotropy, both in shear A_G and compression A_B, which are greater than zero,

[2] Poisson ratio is the ratio of transverse contraction (or expansion) strain to longitudinal extension strain in the direction of stretching force.

[3] The values reported here are different from the values published in the Journal of Nuclear Materials because there was a transfer error during manuscript preparation. Hence, the corrected values are provided here.

as shown in Table 4.3. It is also noted that the obtained percentage anisotropy in A_B is greater than A_G, suggesting that UB_2 is more anisotropic in compressibility.

4.5.2. Debye temperature and sound velocities

Debye temperature (θ_D) of UB_2 is calculated using equation 3.79. In order to compute θ_D, the mean velocity is calculated using equation 3.80. The calculated results are presented in Table 4.4. The estimated value of θ_D is ~393 K (GGA) which is comparable to experimental value of 394±17 K by Flotow *et al*. [11] while 383 K (GGA+U) is underestimated by ~7% (upper limit) or overestimated by ~1% (lower limit) in comparison to the experimental result. The melting temperature was also estimated with a semi-empirical equation, given as [200]:

$$T_m = 553 + 5.91(C_{11}), \tag{4.2}$$

The calculated value of 2830.97 K is reasonably close to the experimental value of 2658 K [201] as shown in Table 4.4 below.

Table 4.4. Theoretical sound velocities (m/s), Debye and melting temperatures (K) of UB_2 using GGA + U with $U_{eff} = 2.00\ eV$.

Type of Calculation	v_l	v_t	v_m	θ_D	T_M
GGA	5560.02	2631.79	2961.21	392.67	2846.81
GGA + U	5513.40	2564.86	2888.35	383.00	2830.97

4.5.3. Electronic structure

To further understand the bonding characteristics of the UB_2 structure, the total Density of States (TDOS) and partial DOS (PDOS) of UB_2 were calculated using the all-electron, full-potential linearized augmented plane wave plus local orbitals (FP-LAPW+lo) code, in the WIEN2k implementation. We use WIEN2k as a means to explore any possible effects of semi-core electrons on bonding [191]. Moreover, it also highlights the band character thus making it possible to obtain information about the hybridization of the orbitals in the band structure plot. To account for discrepancy that may arise from the use of a U_{eff} value derived from the QE code, we optimized the volume in WIEN2k using the U_{eff} derived from QE (See Fig. A.4.2 in Appendix A). The volume is underestimated by ~2% in comparison to the QE result.

The result of Fig. 4.2a shows that UB_2 is metallic with the energy band crossing the Fermi level. In Fig. 4.2b, below the Fermi energy level (valence band), there is a significant hybridization of the uranium *d* and *f* states with the boron 2*p* states in the UB_2 compound which means that there is charge transfer between U and B atoms. This is an indication of the formation of ionic bonds between adjacent U and B atoms. Also, the contribution of 5*f* electrons in uranium are pronounced at the Fermi energy level which suggests that they may be responsible for the electron conduction in UB_2.

This observation is further corroborated by the band character plots of the band structure which shows dominance of the U 5*f* bands in the conduction band as illustrated in Fig. 4.3a. Significant distortion in the spherical charge distribution around the boron atoms compared to the uranium atoms, as shown in Fig. 4.3b, was also observed. Between the adjacent boron atoms, there is a subtle charge density bridge, attributed to the slight covalent character in the B–B bonds.

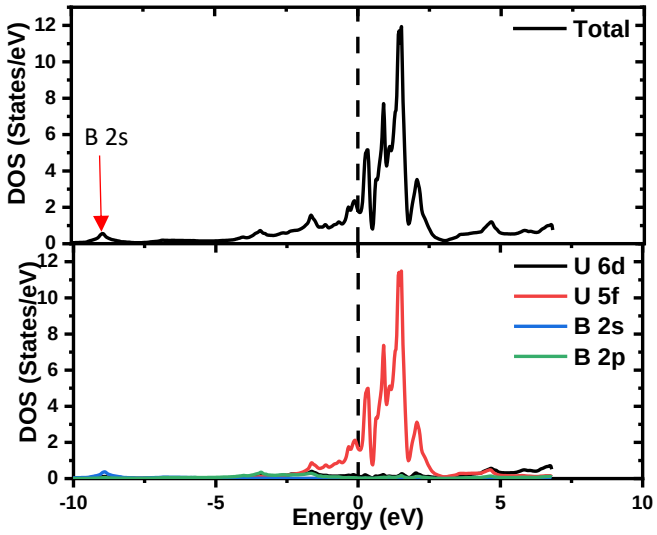

Fig. 4.2. The total and partial density of states for UB_2. The DOS are calculated at the optimized geometry for the given density functional and magnetic ordering. The Fermi energy level is 0.0 eV and is represented using the dashed line. The sharp feature the conduction band is due to the B 2s orbital.

Furthermore, based on the charge distribution of UB_2 shown in Fig. 4.3b, the charge density around the U atom is higher than B due to the presence of more valence electrons. Therefore, the electron distribution of U atoms exhibits a spherical shape, which may be an indication of the lack of covalent bonds on U atoms. This fact is supported by the PCOOP analysis by Martar *et al.* [70].

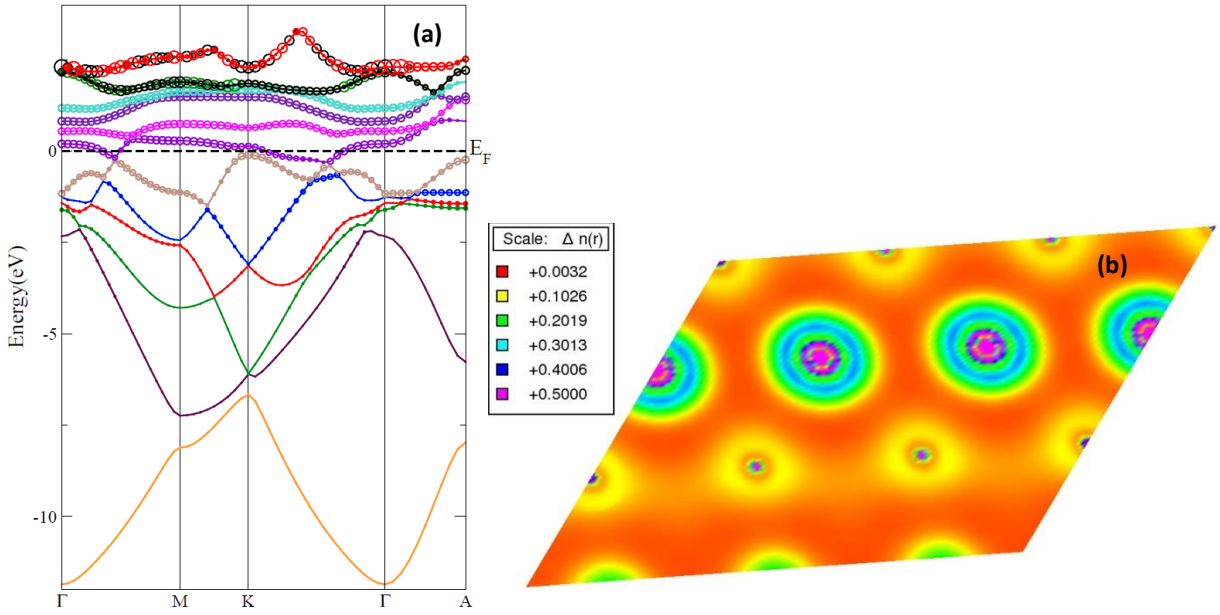

Fig. 4.3. (a) The band structure of UB_2 (b) Valence charge density distribution plot computed in the basal plane. Charge density distribution for the atoms are labeled accordingly, and the electron density scale presented.

Our calculations show that GGA exchange–correlation potentials without the on-site interactions between 5*f* electrons gives a good description of the structural properties of UB_2 in comparison to the available experimental data. Therefore, GGA was mainly used for the following study of phonons and thermodynamic properties of UB_2 due to computational cost of DFPT + U calculation within QE.

4.5.4. Phonon dispersion relation

The phonon frequency of crystalline structures is one of the fundamental aspects when considering the phase stability, phase transformations and the thermodynamics of these materials. The absence of imaginary frequencies (negative frequencies in the Fig. 4.4) in phonon dispersion curve and the phonon density of states give an indication that the structure is dynamically stable. The phonon dispersion of UB_2 consists of 9 branches: 3 acoustic and 6 optic. Fig. 4.4a shows the phonon spectrum of UB_2 along the high symmetry paths Γ-M-K-Γ-A-L-H of the hexagonal BZ.

The phonon density of the state in Fig. 4.4a-b is apparently separated by U and B due to the significant difference in masses of the constituent atoms and stiffness of the bonding between the atoms. The low frequency (below 180 cm^{-1}) is dominated by the heavier U atom because the acoustic modes originate mainly from heavy elements, while above 180 cm^{-1}, the optical phonon

modes are due to the boron atoms. Our simulated lattice dynamic calculations can serve as a reference for future experiments.

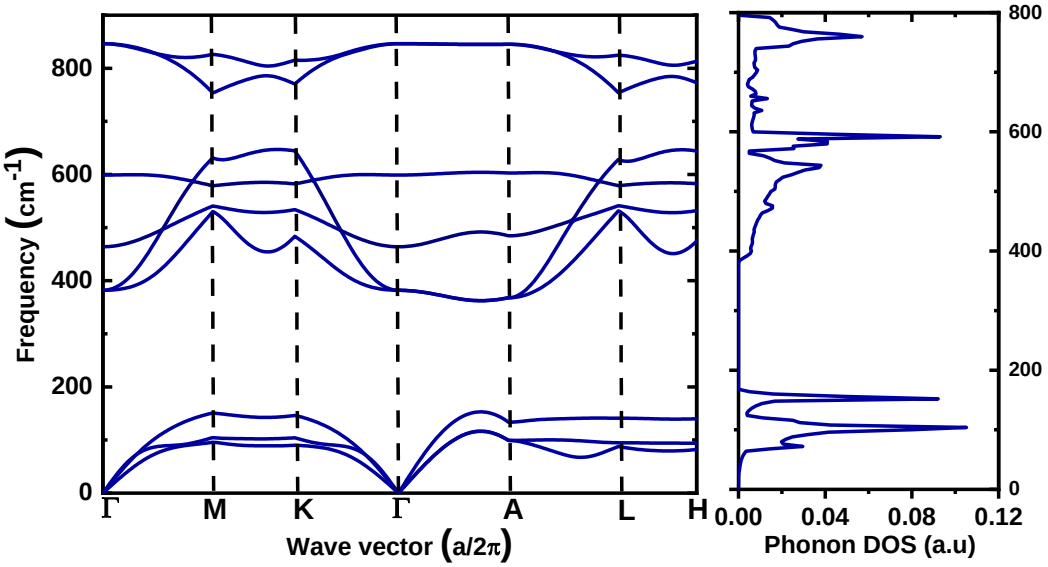

Fig. 4.4. Calculated phonon dispersion curves and total phonon density of states of UB_2.

4.5.5. Thermodynamic properties

The contribution of lattice vibration of thermodynamics properties of UB_2 was calculated. The Helmholtz free energy at volume *V (T)* and temperature *T* is approximated using equation 3.83.

The volumetric thermal expansion is an important design parameter for high-temperature structural applications. It originates from the anharmonicity of the interatomic potential and can be related to the intrinsic energy of the solid, just like the specific heat and the thermal conductivity. Most solids expand on heating owing to the anharmonicity of the chemical bond. Therefore, the volumetric thermal expansion is calculation using QHA derived model in equation 3.86.

In Fig. 4.5a, the volume as a function of the temperature is presented while the inset shows the coefficient volumetric thermal expansion. Unfortunately, there is no experimental data for comparison.

The temperature dependence of heat capacity at constant volume, C_v, is plotted in Fig. 4.5b. We observed that the C_v rapidly increases with the increase in temperature and is proportional to T^3 at low temperature, whereas it tends to a constant value at a high temperature, following the Dulong-Petit law, showing that all of our calculations are reliable.

The entropy (S) of a material can be estimated from thermodynamics relations such that $S = -(\frac{dF}{dT})_V$. The entropy of UB_2 as a function of temperature up to T_m was calculated, as shown in Fig. 4.5c. This work only includes Quasiharmonic lattice vibrational contribution, and entropy is expected to be underestimated at a temperature above θ_D where thermal electronic contribution becomes important.

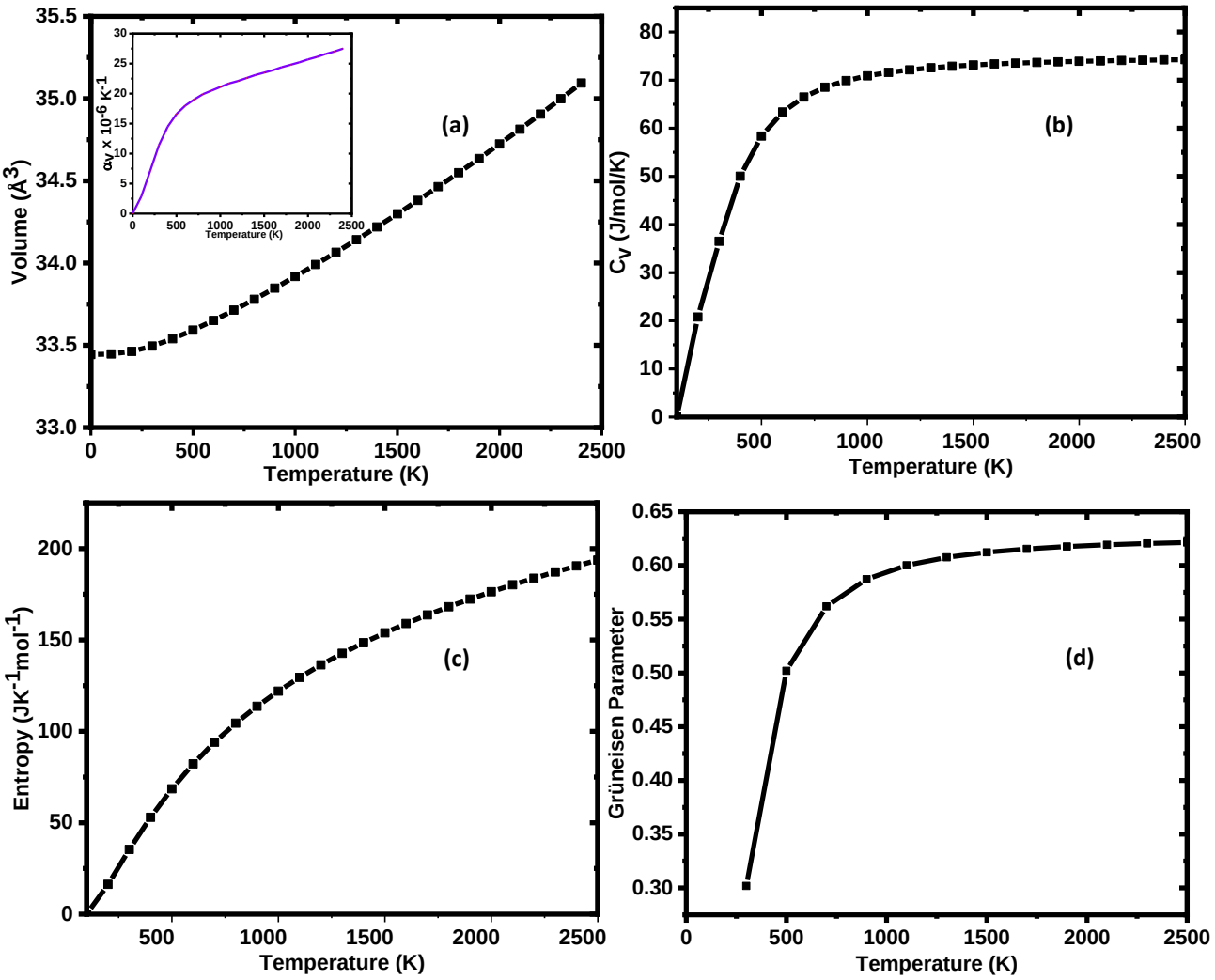

Fig. 4.5. (a) Comparison of change in volume as a function of temperature. Inset of Fig. 4.5a shows the volume thermal expansion by quasi-harmonic approximation (QHA). Calculated (b) heat capacity (c) lattice assisted entropy (d) Grüneisen parameters of UB_2 as function of temperature.

The Grüneisen parameter Υ, which reflect the anharmonicity of various phonon modes, is closely related to the thermal expansion of materials. Υ are positive in most materials accounting for the

thermal expansion. Fig. 4.5d implies there is no possibility of negative thermal expansion at any temperature regime in UB_2 due to the absence of negative value in Grüneisen parameters [202].

4.5.6. Thermal Conductivity

The thermal conductivity of nuclear fuel is an important property as it determines its surface and centerline temperature during operation and its maximum allowable rate of direct heating. Even though UB_2 is metallic, we calculated both the $\boldsymbol{k_{ph}}$, which is due to phonon–phonon (*ph–ph*) scattering at $T< \theta_D$, and the $\boldsymbol{k_{el}}$, which is due to electron–electron (*el–el*) and electron-phonon (*el–ph*) scatterings, respectively, at $T > \theta_D$. It is well known that *el–el* interaction dominates thermal and electrical transport in metallic systems while phonons play a critical role since the electron transport is limited by *el–ph* scattering at intermediate and high temperatures [203].

The total thermal conductivity ($\boldsymbol{k_{total}}$) was estimated by adding $\boldsymbol{k_{ph}}$ and $\boldsymbol{k_{el}}$. The value of $\boldsymbol{k_{ph}}$ for a material can be calculated in several ways [204] that include relaxation time approximation (RTA) [205], Callaway model [206], Slack model [207] and by solving BTE. In this work, $\boldsymbol{k_{ph}}$ was calculated using BTE. In 2014, Li *et al.* [158] developed a software package (ShengBTE) for computing the $\boldsymbol{k_{ph}}$ of crystalline bulk materials based on a full iterative solution to the BTE.

In Fig. 4.6a, a combined plot of $\boldsymbol{k_{ph}}$, $\boldsymbol{k_{el}}$ and $\boldsymbol{k_{total}}$, is presented. $\boldsymbol{k_{total}}$ decreases in the temperature range of 300-500 K which suggests that phonon-phonon scattering is dominant in this temperature regime; this is justified by the calculated θ_D of ~ 400 K. As discussed above, due to the absence of data, electron relaxation time for UB_2 was calculated using a derived correlation for UN (equation 4.1). *el–el* and *el–ph* scattering are accounted for since the data used are from experiments where the various interactions are not decoupled. A significant electronic contribution to the total thermal conductivity was observed. Although further experimental data is needed to confirm the relaxation time assumption, a large electronic thermal conductivity is expected due to the presence of uranium 5*f* electrons, which are strongly hybridized with 3*p* electrons of the boron atoms below the Fermi energy, as shown in Fig. 4.2 and 4.3.

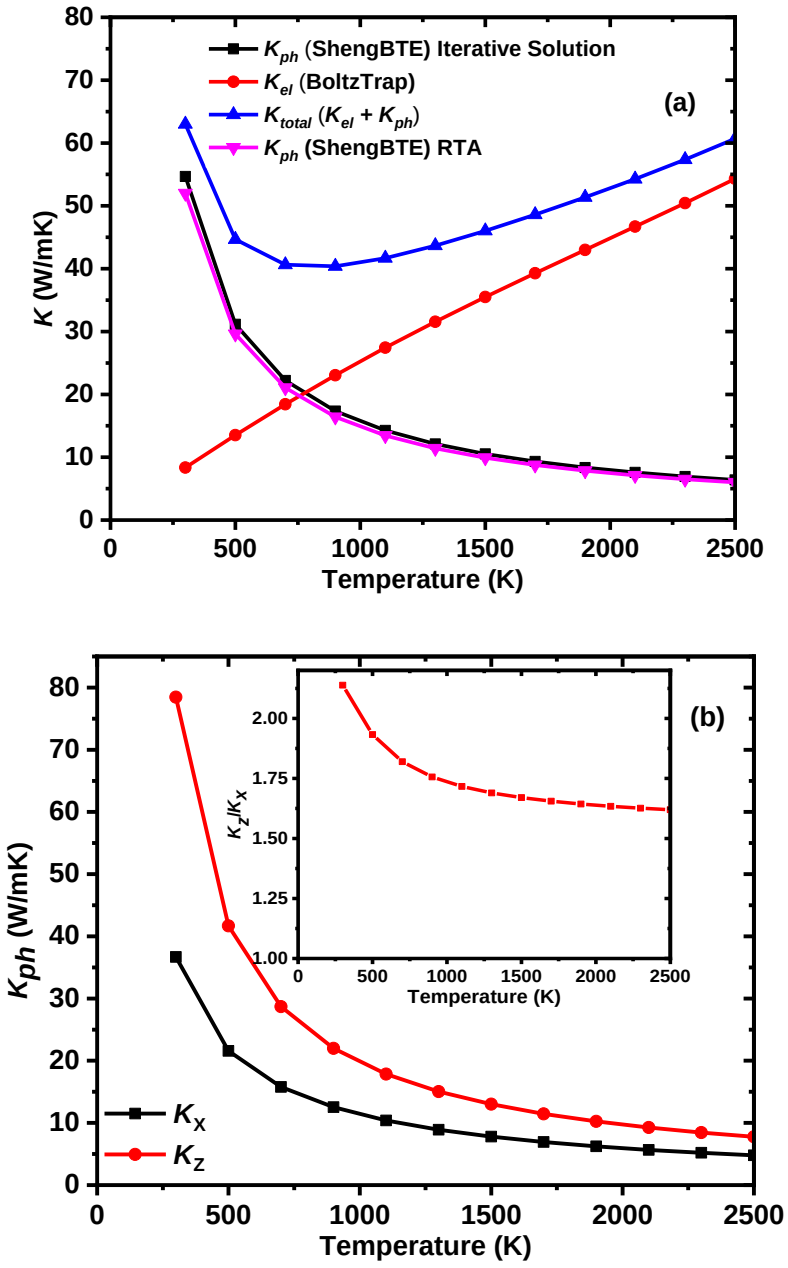

Fig. 4.6. (a) k_{ph} of UB_2 obtained by solving BTE iteratively and using Relaxation Time Approximation (RTA). k_{total} with electronic contribution estimated by Wiedemann-Franz law (b) anisotropy in k_{ph} of UB_2.

The lattice thermal conductivity k_{ph} from RTA at 300 K is 52.00 W/mK, and this magnitude is 4.9% lower than the result from the iterative solution presented in Fig. 3.6a. This implies that UB_2 has strong Umklapp scattering; and in such a case, the RTA can give a reasonable result.

Fig. 4.6b shows the calculated anisotropy in the k_{ph} value of UB_2 and the inset shows the k_z/k_x (k_x and k_z are the thermal conductivity in the *x* and *z* crystallographic directions) variation as a function of temperature. The lattice thermal conductivity exhibits significant directional anisotropy with the ratio of k_z to k_x ranging between 2.14 at 300 K and 1.61 at 2500 K. This implies that anisotropy in the phonon assisted thermal conductivity decreases as temperature increases.

This anisotropy occurs due to differences in group velocity, anharmonicity and scattering phase space along the different directions [208]. The longitudinal sound velocity (v_l) and the transverse sound velocity (v_t) are primarily harmonic parameters, while their ratio v_l/v_t is an anharmonic quantity which depends on the ratio between the axial and shear rigidities of interatomic bonds [209]. It was found that the value of v_l/v_t was 2.06 which is close to the ratio of k_z to k_x at room temperature. This means that the strong anisotropy in the k_{ph} should be ascribed to its anisotropic sound velocities amongst other factors that have not been explored in this work. It is important to state here that, anisotropy in the electronic thermal conductivity is not considered in this analysis.

At lower temperatures, the effect of isotopic scattering is not significant, but as temperature increases, typically above the Debye temperature, the enhancement of thermal conductivity in isotopically enriched sample ranges between 2.2% and 7.3%. This observation agrees with the fact that isotopic scattering is enhanced by the high-frequency phonons [163].

4.6. Conclusions

In this work, DFT technique has been deployed in studying the ground state properties, electronic structure and thermal transport properties of UB_2. The dynamic and structural stabilities were determined from the phonon dispersion relation and elastic constants respectively. The Poisson's ratio and B/G were calculated which show that UB_2 is ionic and ductile in nature. Furthermore, the bonding character has been elucidated from the electronic structure calculations, which highlights the metallic nature and the nature of the covalent bond between adjacent boron atoms. The anisotropic thermal conductivity of UB_2 was calculated as well as its variation in k_z/k_x ratio as a function of temperature. Also, it was shown that the sound velocity along 'a' and 'c' axes exhibit strong anisotropy, which results in the anisotropic thermal conductivity of UB_2. The trend of results within this study show that UB_2 is a potential candidate for metallic nuclear fuel, but it needs further computational and experimental work to better understand its behavior at extreme conditions (including but not limited to temperature, pressure and radiation).

Chapter 5

First-principles study of defects and fission product behavior in uranium diboride

5.1. Overview of Chapter 5

In this chapter, the results of the investigation of the effect of point defects and fission products such as Xe and Zr on the structural stability of UB_2 is presented. The structural changes in UB_2 when doped with Xe and Zr are compared. The energetics and the diffusion pathways for the migration of FPs are also discussed. The mechanism of Zr secondary phase precipitation was determined based on the thermodynamic stability of the solution product (zirconium diboride).

This chapter is presented as manuscript #2 (First-principles study of defects and fission product behavior in uranium diboride). My contributions to this paper include a review of the relevant literature, materials modelling and simulation, analysis and discussion of results and preparation of the manuscript. The manuscript was reviewed by my supervisors, Prof. Jerzy Szpunar and Dr. Barbara Szpunar, and their comments were addressed before submission for publication. The copyright permission to use the manuscript in this thesis was obtained from the publishers and it is provided in APPENDIX E. Our sincere gratitude goes to Dr. Pérez Daroca for meaningful discussion and kind assistance in setting up Nudge Elastic Band and Bader charge analysis within Quantum ESPRESSO module.

The manuscript was published in 2017 in *Journal of Nuclear Materials*:

- E. Jossou, D. Oladimeji, L. Malakkal, S. Middleburgh, B. Szpunar, J. Szpunar, First-principles study of defects and fission product behavior in uranium diboride, J. Nucl. Mater. 494 (2017) 147–156. doi:10.1016/j.jnucmat.2017.07.027.

First-principles study of defects and fission product behavior in uranium diboride

Ericmoore Jossou[1],Dotun Oladimeji[2], Linu Malakkal[1] , Simon Middleburgh[3],

Barbara Szpunar[2], Jerzy Szpunar[1]

[1]*Department of Mechanical Engineering, College of Engineering, University of Saskatchewan, 57 Campus Drive, Saskatoon, S7N 5A9, Saskatchewan, Canada*

[2]*Department of Physics and Engineering Physics, College of Art and Science, University of Saskatchewan, 116 Science Place, Saskatoon, S7N 5E2, Saskatchewan, Canada*
[3]*Westinghouse Electric Sweden, SE-721 63 Västerås, Sweden*

5.2. Abstract

A Systematic study of defects and incorporation of xenon (Xe) and zirconium (Zr) fission products in uranium diboride (UB_2) has been investigated using density functional theory (DFT) calculations as implemented in Quantum ESPRESSO code. The incorporation and solution energies show that both FPs (Xe and Zr) are most stable in U vacancies with Zr being more stable than Xe. A volume expansion is observed as the concentration of Xe increases in the fuel matrix, while Zr incorporation leads to a contraction. Bader charge analysis is used to establish the formation of Zr–B ionic/covalent bonds due to large electron transfer observed, while there is only a weak electronic interaction between Xe and the UB_2 lattice. Finally, using climbing-image nudged elastic band calculation, we find that the energy barrier of U diffusion in UB_2 is 0.08 eV higher than B migration.

Keywords: *Uranium diboride; nuclear fuel; electronic structure; density functional theory; fission product.*

5.3. Introduction

In the wake of the nuclear accident that occurred at Fukushima in 2011, the drive to improve upon uranium oxide, the standard nuclear fuel coupled with zirconium cladding, became evident. In light of this, there is now a large international research effort towards the development of Accident Tolerant Fuel (ATF) concepts for the current fleet of light water reactors and Generation IV nuclear reactors. The uranium density and thermophysical properties of uranium diboride (UB_2) and the silicides, especially U_3Si_2, make them attractive fuel materials both from an economic and safety perspective as potential replacement for UO_2 [1]. UB_2 has a high uranium density of 11.6 g/cm^3 compared to UO_2 which has a density of 9.7 g/cm^3 [210].

An important issue in the development of a new nuclear fuel concept is the understanding of the effects of fission products on the performance of the fuel during irradiation [211–216]. Therefore, the aim of this paper is to investigate the behavior of point defects and incorporation energy of fission products (FPs) such as xenon (Xe) and zirconium (Zr) in UB_2. Point defects, such as vacancies, antisites and interstitials, are also studied because they can significantly modify the thermomechanical properties of materials. The stability of FPs in UB_2 solid solutions is critical for evaluating its performance as a potential replacement for UO_2 nuclear fuel. To date, there have been a series of theoretical investigation to study the roles of FPs such as helium, xenon, krypton, zirconium, and effect of oxygen in UO_2, UC, ThN, and ThC, amongst others [9–11].

In 2013, J. Lian *et al*. studied the stability of Zr in bulk UO_2 by using density functional theory. They showed that Zr prefers to occupy a uranium site compared to the oxygen site. Their results further reveal that Zr and ZrO_2 precipitates are insoluble in UO_2 [220] which supports the observation of Zr containing gray phases in UO_2 [221].

Besides first principles studies of the electronic structure of UB_2 [70], pressure-induced phase transition experiment carried out using a synchrotron-based X-ray [185], and more recently defect evolution in UB_2 by Burr *et al*. [72], and conference presentation on Xe and Zr behavior in UB_2 [222], otherwise, there appear to be few defects work on UB_2 compare. Middleburgh *et al*. [176] investigated the incorporation energies, solution energies and diffusion pathways of helium and lithium in ZrB_2; a material with a crystal structure similar to UB_2.

Due to the high thermal conductivity of metallic fuels, there has been a lot of focus on materials such as uranium mononitride (UN) and uranium silicides [7, 17–19]. For instance, the incorporation and diffusion of Xe in UN were studied by Zhang *et al*. They showed that the diffusion of Xe in UN prefers to occur through U vacancy sites. Also, the incorporation energies of Xe in five different sites was calculated. Their results suggested that Xe prefers to occupy vacancy clusters with the largest steric space [223].

In this work, the behavior of Xe and Zr in UB_2 was systematically studied using first principles approach. In fission processes, one of the most abundant products is Xe, while Zr may originate from either fission events or Zr/ZrO_2 from cladding materials due to the solid phase diffusion at the fuel/cladding materials interface in nuclear reactors [220]. The formation energy of intrinsic

point defects was calculated and analyzed. The incorporation and solution energy of Zr and Xe in UB_2 were subsequently determined and discussed. The influence of Xe and Zr defects at different concentrations on the volume and electronic structure of the UB_2 system was modelled. Finally, the migration and activation energies of vacancy-assisted self-diffusion of B and U in UB_2 crystal is presented. This was compared with the migration of Xe around U vacancy.

5.4. Computational details

In this study, the behavior of Xe and Zr in UB_2 was investigated using the Quantum ESPRESSO plan-wave pseudopotential code [143] within the framework of density functional theory (DFT) [224]. The exchange-correlation functional potential is described by the generalized gradient approximation (GGA) in the Perdew-Burke-Ernzerhof (GGA-PBE) formulation. All of our calculations used the norm-conserving PBEsol (pseudopotentials functional for solids) pseudopotential [225] where these potentials treat $6d^1\ 5f^3\ 7s^1$ as valence electrons for U and $2s^2\ 2p^1$ as valence electrons for B. Due to the onsite Coulomb repulsion among the localized U 5*f* electrons, we used the Hubbard (DFT + U) approximation to account for the strong correlation effect [226]. As described in our previous work, the Hubbard U parameter for UB_2 was determined to be 2.0 eV [227].

DFT with GGA or GGA + U approximation does not consider van der Waals interaction, which is a major component of the binding properties of inert gases. However, previous work gave reliable trends for the incorporation energies of Xe, He and Kr in UN [185], He in iron [186] and, more recently, He in thorium carbide [187].

The Brillouin zone was sampled by an 8×8×6 k-point mesh using the Monkhorst-Pack (MP) scheme [228] and a 1360 eV energy cut off was used. Point defects and impurities calculations permitted the atomic positions and the cell size and shape to vary using the conjugate gradient method within the Broyden–Fletcher–Goldfarb–Shanno (BFGS) algorithm until residual Hellmann–Feynman force [229] on each relaxed atom are less than 0.02 eV/Å while for volume optimization, a 0.01 GPa threshold was used. A Methfessel-Paxton smearing [230] width of 0.27 eV (0.02 Ry) was used to integrate the bands at the Fermi level.

The convergence of defect formation energies was checked by considering supercells which are repeated unit of the 3-atom hexagonal cell with the following repetition configuration: 2×2×2 (24 atoms), 3×3×2 (54 atoms) and 3×3×3 (81 atoms) to understand the impact of image interactions

due to the periodic boundary conditions applied in this methodology [218]. A 3×3×3 supercell containing 81 atoms was used for defect energy calculations as this was judged to be adequate to provide useful values given the computational constraints. Visualization of the structures was obtained using the Vesta programme [231,232] and XCrySDen [233].

The Nudged Elastic Band (NEB) method [234] was used within the Quantum ESPRESSO code to find the minimum energy path (MEP) between an initial and final transition state. The MEP was found by constructing a set of intermediate images replica of the system between the initial and final state. An optimization of the band, involving the minimization of the force acting on the images, brings the band to the MEP. An improvement of this method is the climbing image NEB (CI-NEB) [235]. The migration energies, E_m of vacancy assisted diffusion of Xe, U and B atoms within bulk UB_2 was calculated within the NEB formalism and after a few iterations the image with the highest energy was identified. The CI-NEB scheme was then used to find the final converged MEP.

5.5. Results and discussion

5.5.1. Stability of point defects

Uranium diboride (space group *P6/mmm*) is used as a refractory material due to its high thermal conductivity, but currently it also being considered as a potential candidate for development of ATFs. The calculated ground state lattice parameters of UB_2 are a=b=3.139 Å and c=3.994 Å, and they are in good agreement with the experimental values of a=b= 3.136 Å and c=3.988Å [196]. The structure is characterized by a 2-dimensional boron network with U and B hexagonal layers stacked perpendicular to the c-axis at 0 and ½ [70]. Fig. 5.1 provides a schematic of the UB_2 unit-cell. X-ray crystallography data has shown that one uranium atom occupies 1*a* Wyckoff site (0, 0, 0) and two boron atoms occupy 2*d* Wyckoff sites (1/3, 2/3, 1/2). UB_2 shares similar positions (multiplicity and Wyckoff letter), symmetry and coordinates with ZrB_2 since they both have the AlB_2-type hexagonal structure [14, 39-40].

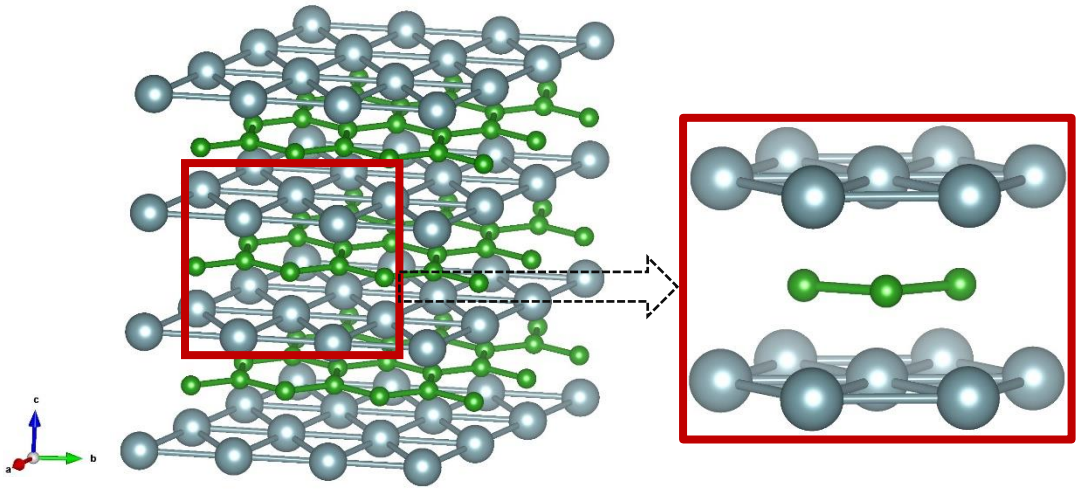

Fig. 5.1. Crystal structure of uranium diboride (UB_2) showing the unit cell with the full hexagonal structure in the primitive unit cell highlighted from a 3× 3 × 3 supercell. (Color scheme: U = grey, and B = green).

Four types of point defects, including uranium vacancy, boron vacancy, Schottky trivacancy and uranium-boron antisite pair are shown in Table 5.1 As both the uranium and boron have one symmetrically distinct site, atoms in the hexagonal sublattice were randomly selected for defect calculations while taking into account the displacement of the nearest neighbor (NN) atoms.

Table 5.1. Volume changes relative to perfect UB_2 crystal and the formation energies (E^f) of four different types of point defects. The formation energy of UB_2 is calculated to be –3.28 eV/atom.

Defect type	Notation	Coordinates	E^f (eV/atom)	ΔV/V (%)
Uranium vacancy	V_U	U(1/3, 1/3,0)	8.96	–0.61
Boron vacancy	V_B	B(0.5556, 0.4444,0.1667)	5.40	–0.16
Schottky Trivacancy	$(V_U: 2V_B)$	U(2/3, 1/3, 0) B(0.2222, 0.7778, 0.1667) B(0.5556, 0.4444, 0.8333)	14.57	–0.92
Antisite pair	$(B_U: U_B)$	B(1/3, 2/3, 1/3) U(0.7778, 0.5556, 0.5000)	5.52	–2.03

The formation energy of a B vacancy, which is 5.40 eV, is more stable compared to U vacancy (8.96 eV). The changes in the volume of UB_2 in the presence of point defects is also shown in Table 5.1. The results show a contraction in volume for the vacancies considered, while antisite defect, which is formed by the exchange of a U and a B in neighboring site, results in the swelling of the UB_2 structure. The formation energy of 5.52 eV suggests that the creation of antisites is highly unstable, and hence may not exist in UB_2. This can be attributed to the significant difference in atomic radius and electronegativity of U and B atoms, respectively.

The calculated total density of states (DOS) of UB_2 without defects and with U and B vacancies is presented in Fig. 5.2. There is no significant difference among the defective structures due to the

small fraction of defects. This is similar to the TDOS of defective ThC presented in Ref. [238]. The inset shows the charge density of a defect-free UB_2 in the (100) plane and a diffuse electron density exit between the B–B atoms.

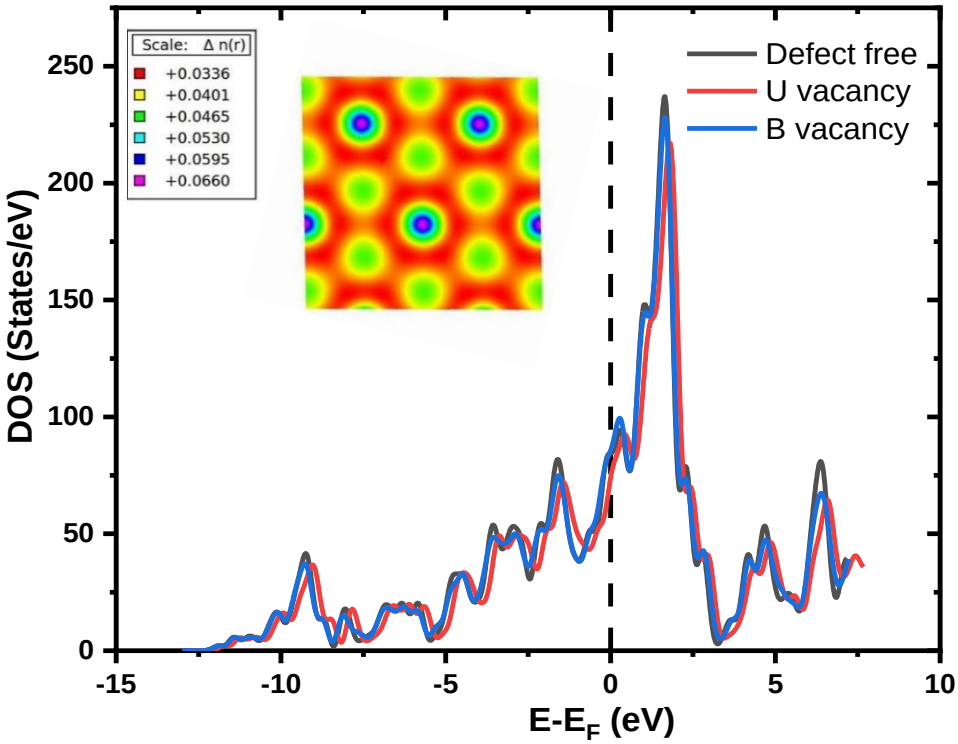

Fig. 5.2. Calculated total density of states of UB_2 for a defect-free structure containing 81 atoms and with U and B vacancies. The inset shows the electron density of defect-free structure. The Fermi energy level is not set to zero here as it does not affect the interpretation of the results herein.

It is important to point out here that, the electronic DOS discussed in this Chapter appear to have some different features from the one in Chapter 4. Similar differences were observed by Topsakal *et al* while comparing density of states from QE and WIEN2k for rare-earth nitrides. They, opined that such disagreement might be due to placement of *f* electrons in the core region or failure of generated norm-conserving pseudopotential in the trivalent ionic state [239]. The former might be the case here.

5.5.2. Stability of fission products

In this section, the calculated incorporation energies of Zr and Xe at different sites in UB_2 is computed and the values are reported in Table 5.2. The lowest incorporation energy in Table 5.2 is the U vacancy site, which means that a U vacancy is the most stable solution site for Zr among the defects considered. This is comparable with previous work on UO_2 [201] where Zr and Ba FPs are more stable in the U vacancy sites. Lan *et al*. suggest that the preferential substitution of Zr for

the U atom can be attributed to the +4 charge state on both U and Zr [174]. Although, the UB_2 system is less ionic compared to UO_2, hence, the stability of Zr in a U vacancy site is likely due to the chemical and steric similarities between Zr and U. The positive incorporation energies of Xe at the different sites implies that it is insoluble and prefers to form bubbles or segregate from the UB_2 structure.

Table 5.2. Incorporation Energies E^{inc} (eV), displacement of the first nearest neighboring (NN) atoms of zirconium and xenon ΔR nn (Å) and Bader charge of Z (Z=Zr, Xe) in a $3 \times 3 \times 3$ supercell of UB_2 for different insertion site.

	Z= Zr			Z= Xe		
Type	E^{inc} (eV)	ΔR nn (Å)	ΔQ(Z) (|e|)	E^{inc} (eV)	ΔR nn (Å)	ΔQ(Z) (|e|)
V_U	–14.48	–0.053	2.306	4.21	0.030	0.494
V_B	–3.29	–0.024	1.167	6.67	–0.006	1.142
I_Z	–4.88	–0.316	1.186	12.24	–0.185	1.324

The charge density distribution due to Zr and Xe incorporation was calculated to determine the nature of bonding between the FPs and boron atoms. The atomic charges for each atom were calculated using the Bader topological method [240]. The net charge transfer due to Xe in a pre-existing uranium configuration is 0.494|e|, compared to 2.306|e| for Zr as shown in Table 5.2. This implies a weak electrostatic interaction between Xe and neighboring atoms due to its filled electronic shell, while a Zr-B bond is formed between the Zr and B atoms with U_{vac} having the most electron transfer, which is due to a covalent or ionic character. There is an increase in charge transfer from Xe in the following order: $V_U > V_B > Xe_i$. The reverse is the case for Zr incorporation. The increase in electron transfer from Xe can be associated with polarization of its charge density due to the increased steric space in the interstitial position.

Defect formation usually leads to perturbation of crystal structures. Table 5.2 shows that U and B vacancies induce small inward displacement of -0.053 Å and -0.024 Å respectively, with respect to the first nearest neighbor (NN). A small displacement of atoms less than 0.06 Å appears in the immediate vicinity of the defects and its effect is negligible beyond the first NN shell; hence the volumetric change due to defects incorporation in UB_2 is small.

The incorporation energy does not account for the formation energy of vacancies since it is not sensitive to the concentration of insertion sites of the FPs [241]. Therefore, the solution energy as a function of FP concentration was calculated. Here, one, two, three and four substitutional Zr and Xe defects in a $3 \times 3 \times 3$ supercell was considered, which are equivalent to 3.70, 7.41, 11.11 and

14.81 mol. % respectively. The molar concentration is defined as the ratio of Zr or Xe FP defects to U sites in the UB_2 lattice. A uranium site was randomly selected for the first FP, as shown in Fig. 5.3b, while neighboring U sites were subsequently selected for FP insertion. The dopant-dopant distance ranges from 3.12 to Å 12.34 Å. In Table 5.3, the solution energy of Zr and Xe at different U sites for different concentrations are presented. UB_2 supercells with the FPs are displayed in Fig. 5.3.

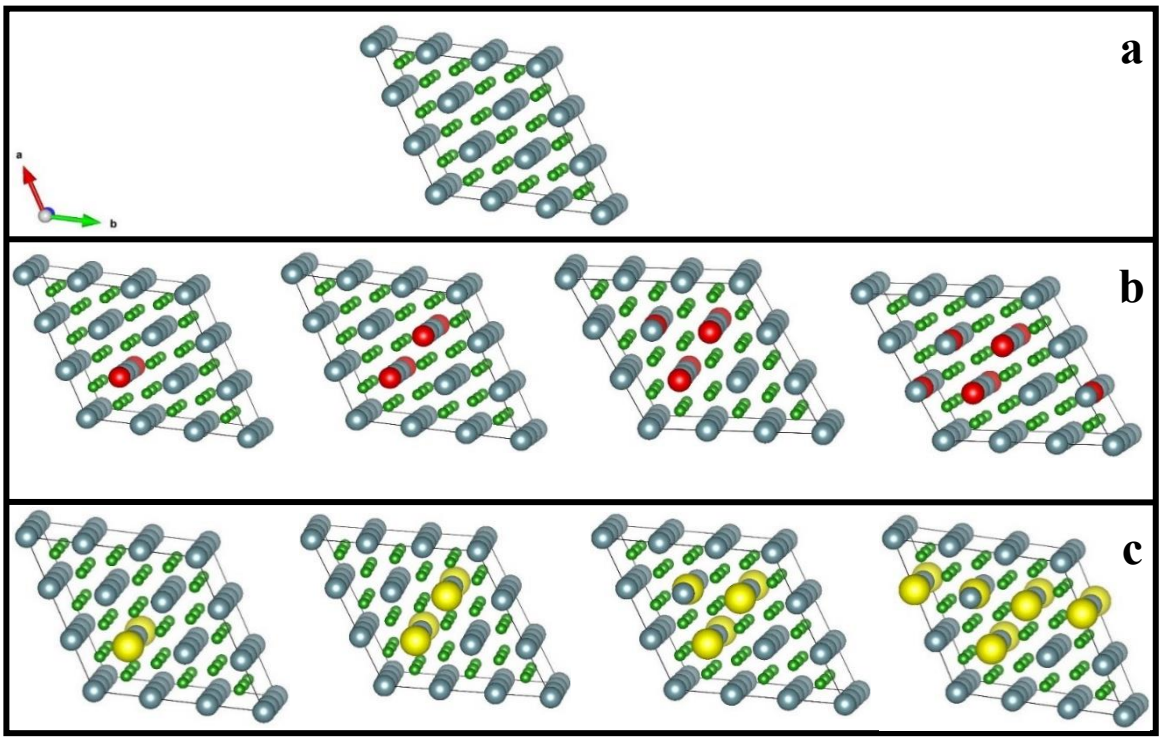

Fig. 5.3. Schematic drawing of defective structure for different concentrations. Panel a shows defect free, uranium and boron vacancies respectively in the structure. Panel b and c correspond to the concentration of 3.70 – 14.81 mol. % Xe or Zr. Color scheme: U= grey, B= green, Xe= yellow, Zr= red).

The energies in Table 5.3 represents the energy per defective atom. The incorporation and solution energy of Xe in U pre-existing site are positive. This means that incorporation of a Xe atom into UB_2 is energetically unfavorable to different degree depending on the concentration of Xe, while in the case of Zr FP both the incorporation and solution energies are favorable (negative), which indicates that Zr atoms occupy a U vacancy site in the UB_2 matrix. Overall, DFT calculations predict Zr to be soluble in UB_2 while Xe is insoluble. This is in agreement with previous studies where the behavior of Zr, Ba and Xe as FPs in UO_2, UC and UN fuel matrix was investigated [218,242,243].

Table 5.3. Formation energy E^f, incorporation energy E^{inc}, solution energy E^{sol} per atom respectively, volume change ΔV/V, and Bader charge ΔQ (Z) (Z=Zr, Xe) of defective UB_2 at different concentration[4].

Z=Zr					
Conc. (mol. %)	E^f (eV)	E^{inc} (eV)	E^{sol} (eV)	ΔV/V (%)	ΔQ(Z) |e|
3.70	8.96	–14.48	–6.19	–0.11	2.306
7.41	8.97	–13.65	–4.68	–0.37	2.286
11.11	8.89	–13.72	–4.83	–0.60	2.269
14.81	8.78	–13.05	–4.27	–0.81	2.125

Z=Xe					
Conc. (mol. %)	E^f (eV)	E^{inc} (eV)	E^{sol} (eV)	ΔV/V (%)	ΔQ(Z) |e|
3.70	8.96	4.21	13.17	0.67	0.494
7.41	8.97	3.27	12.24	1.53	0.484
11.11	8.89	3.07	11.96	2.70	0.433
14.81	8.78	2.99	11.77	4.92	0.413

FPs can contribute to an increase in the fuel volume, commonly referred to as fission product swelling [221]. This leads to chemical as well as mechanical interactions between the fuel pellets and the metallic cladding material, constituting the first barrier against the release of radioactive FP into the environment. Therefore, in this work, the influence of FP concentration on the supercell volume of UB_2 is investigated as shown in Table 5.3.

Fig. 5.4 is a plot of the supercell volume as a function of the FPs concentration. The volume continues to increase (swelling) as the concentration of the Xe FP increases while there is volume decrease (contraction) as the concentration of Zr increases. The volume change in UO_2 due to Zr was compared to that of UB_2 and the comparison shows that for a corresponding Zr concentration, there is more contraction in UO_2 than UB_2 [220]. Furthermore, a linear relationship is observed as the UO_2 and UB_2 are each doped with Xe. As well, UO_2 is more prone to swelling than UB_2 at the same concentration, which becomes more noticeable as the concentration of Xe increases [244]. Previous studies on UO_2 attributes these structural changes to the nucleation of Xe gas bubbles (gaseous swelling) and insoluble precipitate formation (solid swelling) [245].

A closer look at Table 5.3 shows that at Xe concentration of 3.70% corresponds to a volume change of 0.67 and 4.92 at Xe concentration of 14.81%. This variation is due to the larger atomic radius

[4] The average, minimum and median of the energy of incorporation and solution energies is presented in Appendix B as Table B.5.1. The average, minimum and median is not representative of the data. Hence, one must refer to each individual data point.

of the Xe atom (2.16 Å) when compared to the U atom (1.86 Å). The Xe atoms induced strain on the nearest B site, causing the B atom to move outward when Xe occupies a pre-existing U atom site. The same explanation holds for Zr FPs in the reverse.

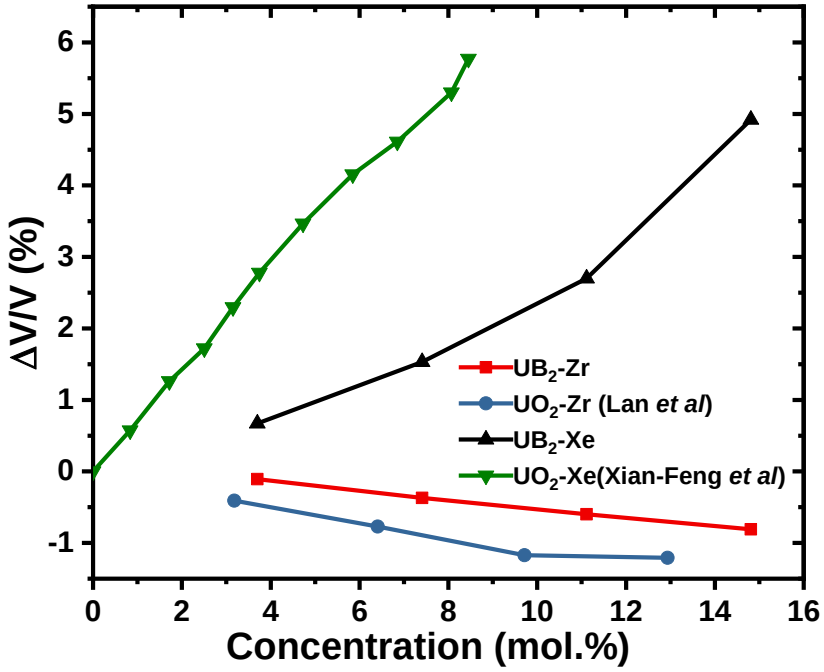

Fig. 5.4. The concentration influence of substitutional Zr and Xe defects on the unit cell volume of UB_2. The experimental data were obtained from Refs. [214, 238].

The Bader charge analysis on Zr–doped UB_2 shows a net transfer of ~2.23|e| from the Zr atom to the B atom at all FP concentrations. This implies the formation of a Zr–B bond which is further corroborated by the partial density of state (DOS) in Fig. 5.6a-d**.** The overlying or hybridization of the Zr 4*d* orbital and B 2*p* orbital in the energy range of –12.5 to 7.5 eV is responsible for the Zr-B bond formation. As the concentration of Zr increases, there is no appreciable change in the electronic structure of the material, unlike UO_2 which transform from semiconducting to a metallic system due to increased concentration of Zr [220]. The total DOS remains unchanged as shown Fig. 5.5a after the solution of a substitutional Zr defect in the UB_2 matrix.

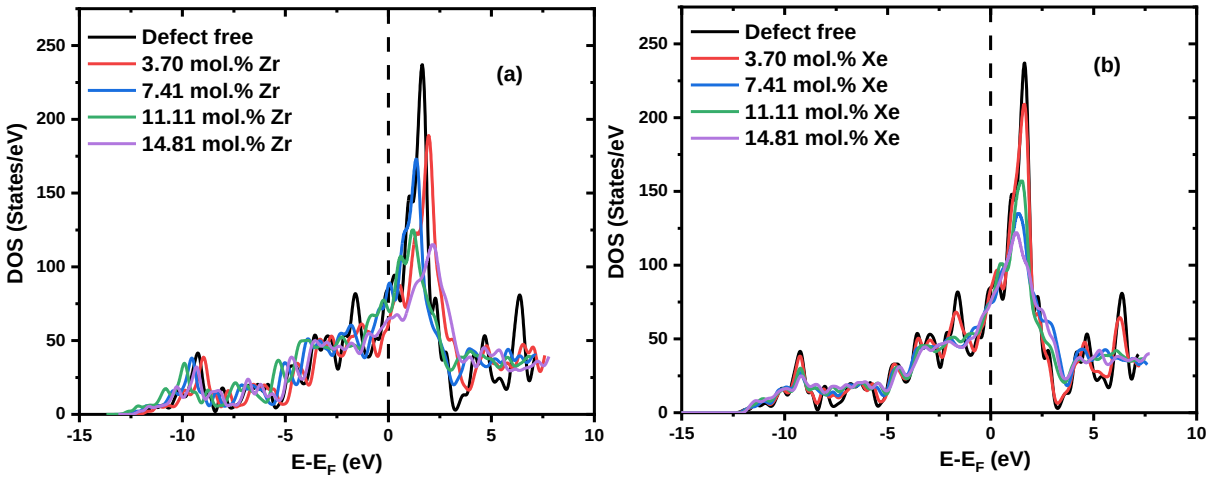

Fig. 5.5. The calculated total density of states of UB_2 doped with 3.70 mol. % - 14.81 mol.% (a) zirconium and (b) xenon respectively.

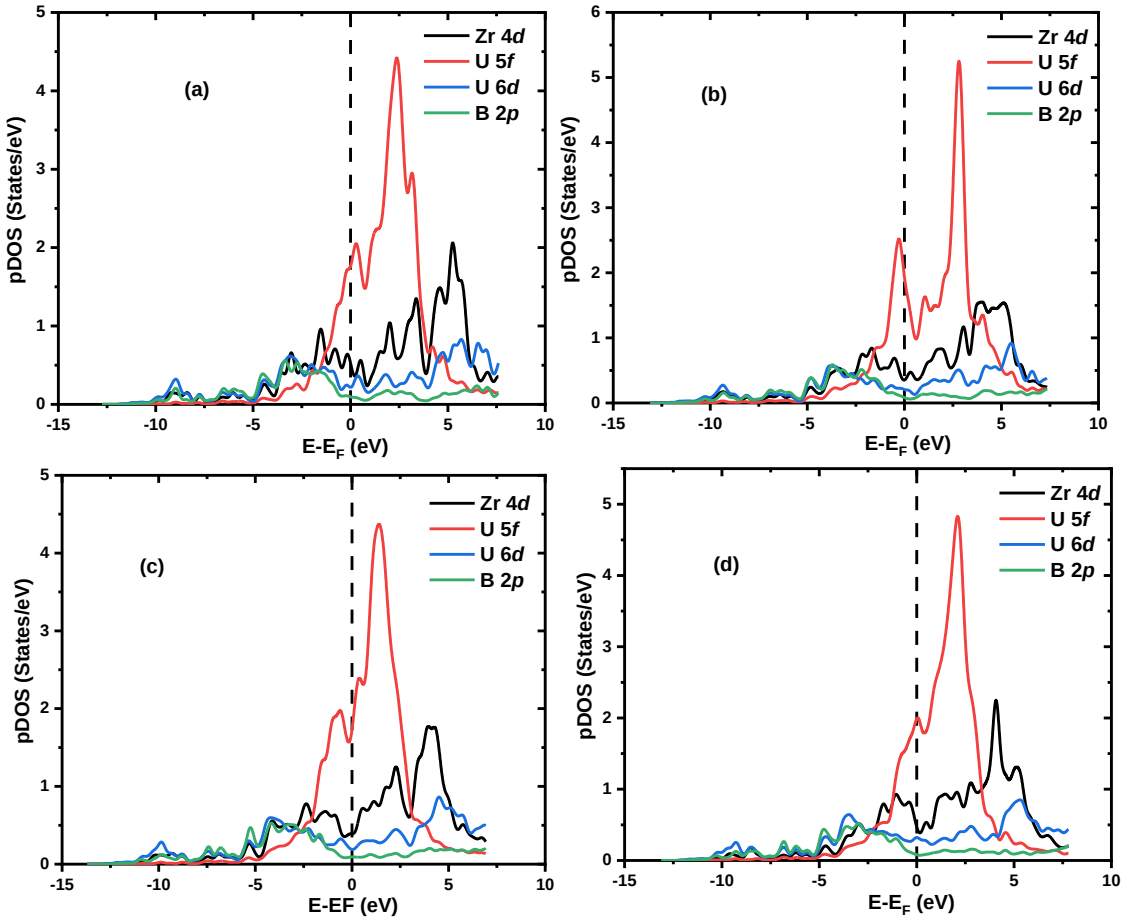

Fig. 5.6. Projected DOS of defective UB_2: (a-d) for Zr-doped UB_2; (e-h) for Xe-doped UB_2.

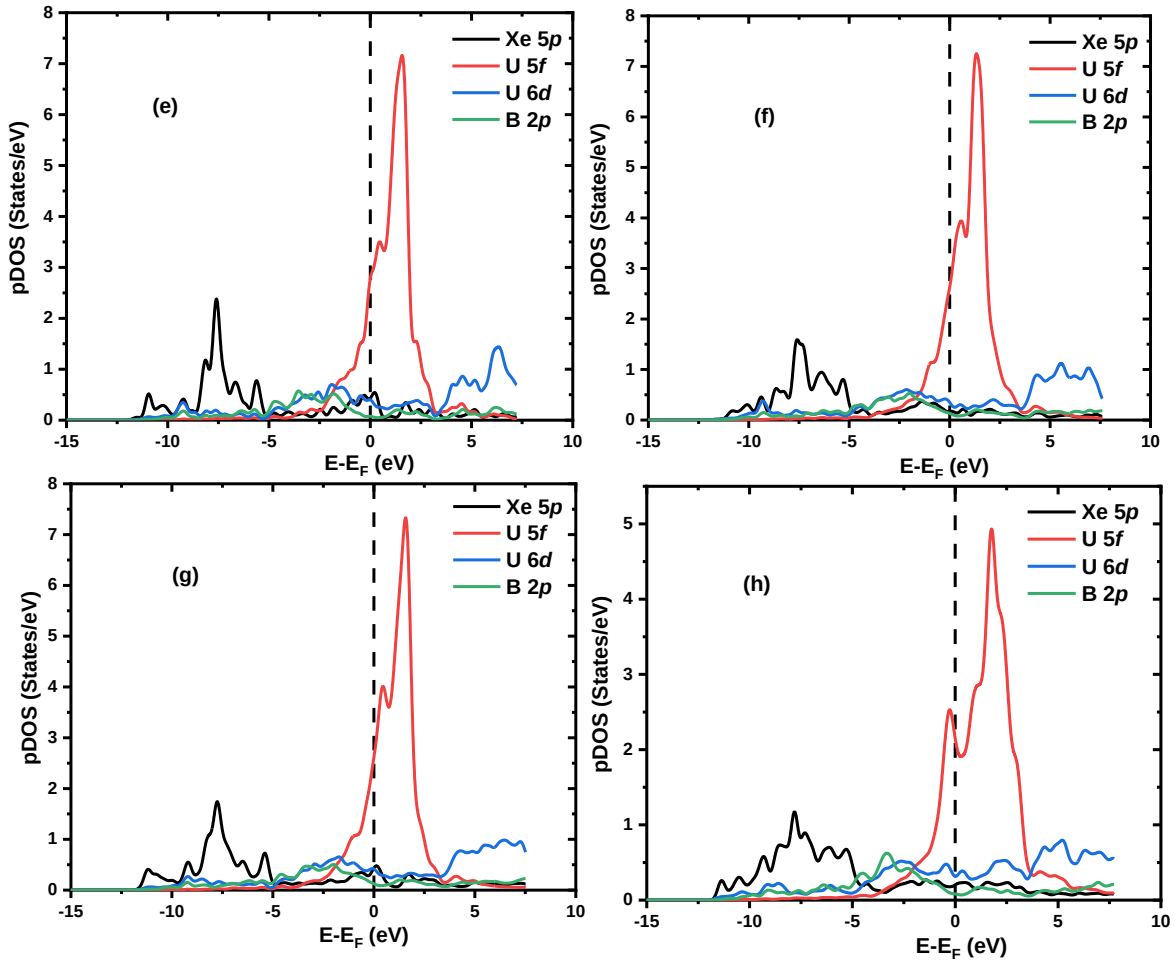

Fig. 5.6. Projected DOS of defective UB_2: (a-d) for Zr-doped UB_2; (e-h) for Xe-doped UB_2.

In the case of Xe, from Table 5.3, there is a moderate net charge transfer ranging from 0.413 to 0.494 |e| from Xe to B which means there is a weak electronic interaction between Xe and B as a result of the filled electronic shell of the Xe. This interaction reduces as Xe concentration increases.

5.5.3. Stability of Zr precipitates

Zr is soluble in UB_2 but it can also precipitate out of solution in a more stable secondary phase. In this work, the behavior of Zr and ZrB_2 in UB_2 as a secondary phase is investigated. The crystal structures are displayed in Fig. 5.6. The space groups of the two phases under consideration are α-Zr metal (P63/*mmc*) and ZrB_2 (*P6/mmm*). The solution energy of ZrB_2 is defined as the difference between the solution energy sum of a Zr and two B atoms at their most favorable insertion sites and the formation energy of ZrB_2.

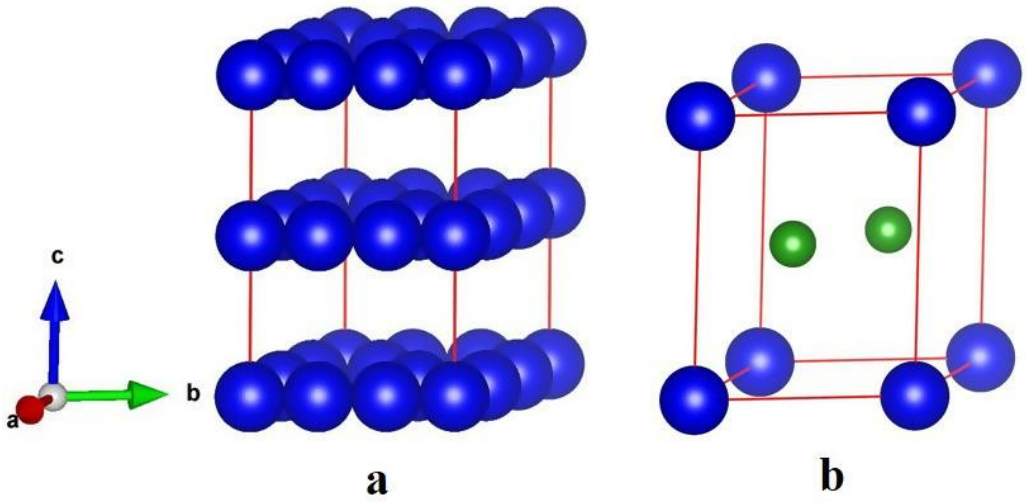

Fig. 5.7. Crystal structures of Zr metal (a) and ZrB_2 (b). Color scheme: Zr= blue and B= green.

The solution of ZrB_2 into the UB_2 matrix can be estimated by the following reaction:

$$ZrB_2 \text{ (solid)} + U_U \longrightarrow Zr_U + UB_2 \text{ (solid)}$$

The solution energy of ZrB_2 in UB_2 can be calculated as follows:

$$E^{sol}_{ZrB_2} = E^{sol}_{Zr \in U} + E^{f}_{ZrB_2} - E^{f}_{UB_2}, \tag{5.1}$$

where $E^{f}_{ZrB_2}$ and $E^{f}_{UB_2}$ are the formation of ZrB_2 and UB_2 respectively. A positive solution energy means that ZrB_2 is insoluble in the UB_2 matrix.

The formation energies of ZrB_2 and the hexagonal close packed (HCP) Zr metal are –6.88 eV per ZrB_2 formula unit and –6.54 eV per Zr atom. Table 5.4 shows that the calculated solution energies of Zr metal and ZrB_2 precipitates in UB_2 are -8.17 and –2.23 eV respectively. In comparison to ZrB_2, Zr is approximately 4 times more soluble in UB_2 fuel matrix. This result suggests that Zr and ZrB_2 are soluble in the UB_2 fuel matrix. It is interesting to note that the solution energy of Zr in interstitial position is 2.10 eV which suggests that the Zr atoms prefer to occupy the U vacancy site.

Table 5.4. Formation energy and solution energy of Zr precipitates in UB_2.

Type	Zr metal	ZrB_2
E^f (eV)	–6.54	–6.88
E^{sol} (eV)	–8.17	–2.23

5.5.4. Self-diffusion of B and U in UB_2

The vacancy-mediated diffusion of U and B in the UB_2 crystal lattice was also studied. The diffusion pathways considered in this study include vacancy migration to one of the NN atoms of the same species. Calculation of the diffusion coefficient of U and B vacancies was done using the Arrhenius equation [246]:

$$D = D_o \exp(-E_a/K_bT), \quad 5.2a$$

$$E_a = E_f + E_m, \quad 5.2b$$

where E_a is the activation energy, E_f is the formation energy and E_m is the migration energy. D_o is a prefactor, which can be expressed as $D_o = (nd^2/2\alpha)\upsilon$, where n is the number of equivalent jumps, d is the hop-distance between two jump minima, α is the dimension, υ is attempt frequency (which is given by Vineyard equation $\nu = (\Pi_j^N \upsilon_j)/(\Pi_i^{N-1}\upsilon_i^*)$ [246,247]) υ_j and υ_i^* are the initial and transition states frequencies of the eigen modes respectively and N is the vibrational degree of freedom.

In Fig. 5.8a-b, four images of the diffusion pathways are shown respectively for B and U vacancy-assisted migration. Nudged Elastic Band (NEB) calculations were implemented using these migration paths and the energy of migration E_m calculated are listed in Table 5.5. The corresponding E_a were calculated using equation 5.2b.

A plot of how the energy changes with the image number is found in Fig. 5.9. We have calculated the migration energies for U and B vacancies. There are a couple of different vacancy mechanisms because of the symmetry of the UB_2 crystal structure; in particular, diffusion may occur along the c axis or in the basal plane. Some of the basal plane mechanisms may also have c components. The reaction profile in Fig. 5.9a show the migration of a U atom into a neighboring pre-existing vacancy site. We also considered the effect of local defect structure on the migration energy of the uranium atom as shown by Fig.8c. In the case where the NN species are boron and uranium atoms

respectively, the migration energy is 2.69 eV but varies from 2.41-2.48 eV when the NN U atom is replaced by Xe and Zr atoms, as shown in the Fig. 5.9a.

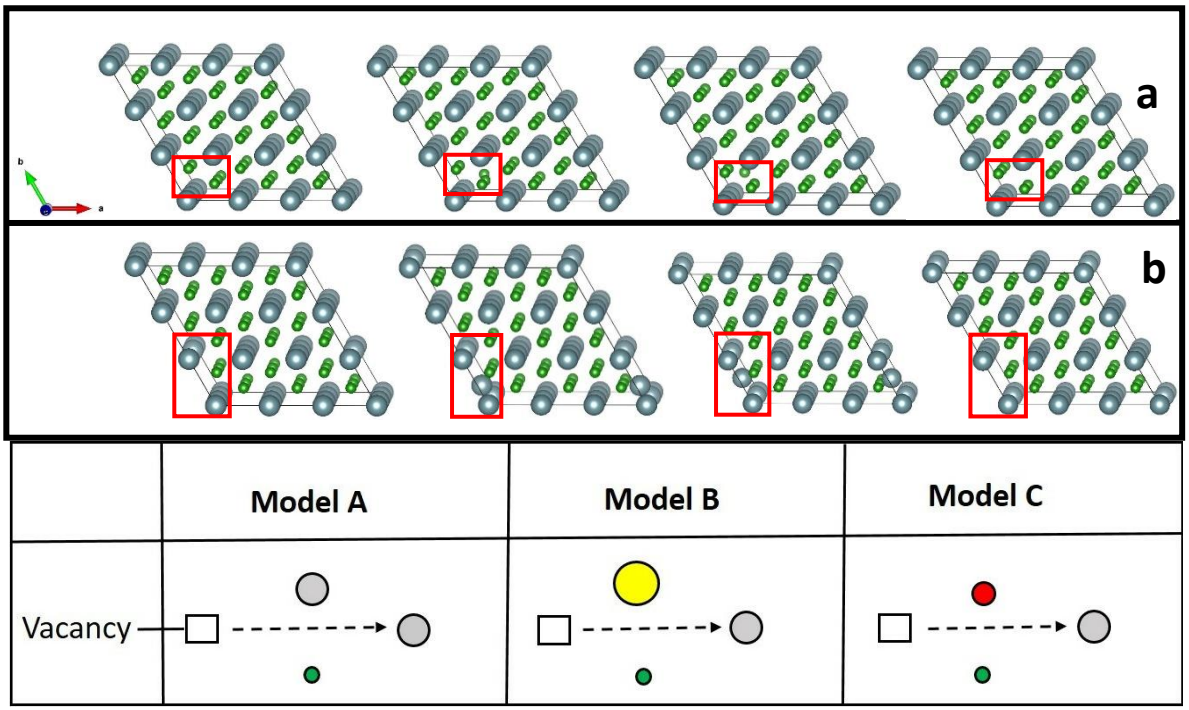

Fig. 5.8. Vacancy-assisted migration of (a) boron (b) uranium along the basal plane of the UB_2 crystal. Color scheme: B= green and U= grey. Directions of migration are highlighted in red (c) Model A, B and C with different defect configurations surrounding the migration path. (Color scheme: U= grey, B= green, Xe= yellow, Zr= red).

Table 5.5. Self-diffusion and Xe migration energies in UB_2 along the basal planes.

Diffusion pathways	E_f (eV)	E_m(eV)	E_a (eV)
U-vacancy assisted U migration	8.96	2.69	11.65
U-migration around Xe	8.96	2.41	11.37
U-migration around Zr	8.96	2.48	11.44
B-vacancy assisted B migration	5.40	1.98	7.38

The mobility of boron to the nearest boron vacancy site in the basal plane requires a migration energy of 1.98 eV as shown in Fig. 5.9d. It must be noted that the after publication of this work, Burr *et al*. [72] computed the vacancy assisted migration energy for the c-plane. Their result clearly establish that U and B vacancy diffusion is anisotropic nature. They also pointed out the fact that diffusion in the basal plane is orders of magnitude faster than the c-axis.

Diffusion of Xe involves the migration of Xe from one lattice site to another, which is governed by the concentration of mobile clusters, i.e. the concentration of vacancies bounded to the Xe trap

site during vacancy formation. The diffusion of Xe incorporated into a pre-existing U vacancy site with a NN U vacancy was investigated. In comparison to migration of U and B, Xe atoms diffuse slower through the fuel matrix as reflected by a E_m value of 6.05 eV in Fig.5.9c. This can probably be attributed to the size of the Xe atom and the fact that it is insoluble in the crystal of UB_2.

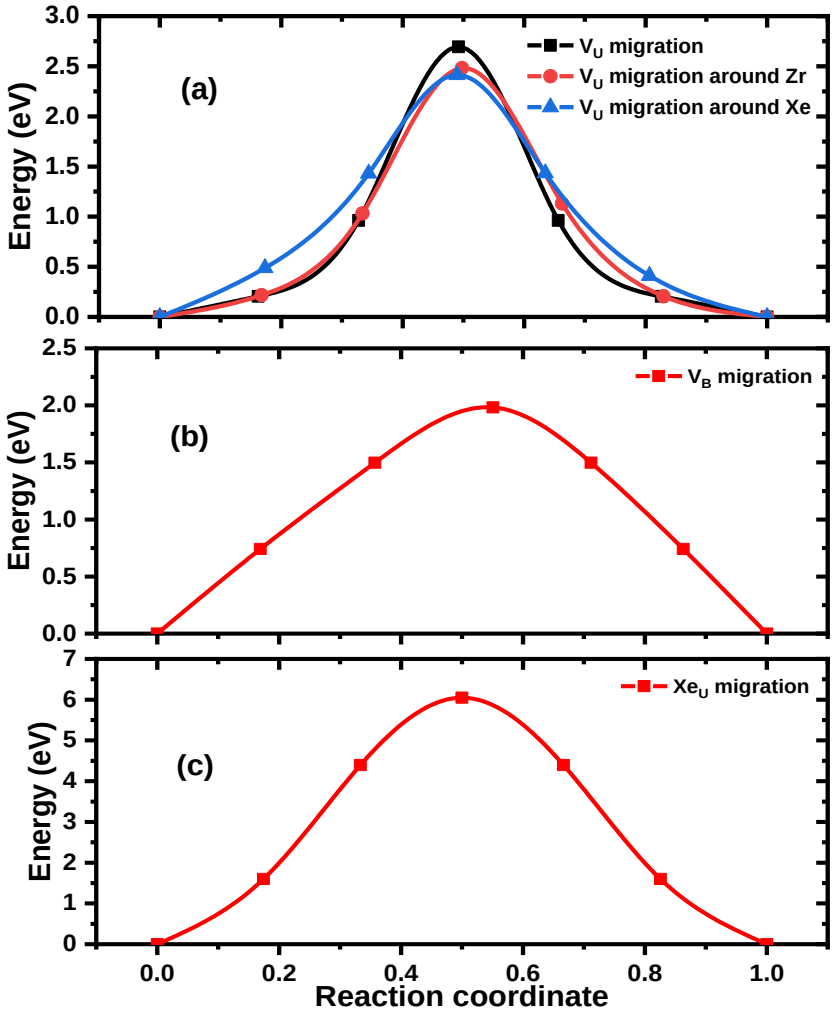

Fig. 5.9a-c. Calculated activation barriers for (a) U-vacancy assisted U migration, U-migration around Xe and U-migration around Xe (b) B-vacancy assisted B migration (c) U-vacancy assisted Xe migration.

In Fig. 5.10 the diffusion coefficients as a function of temperature for the migration of U and B atoms through different migration pathways considered are presented. The result obtained for U diffusion through a vacancy in a Xe doped UB_2 is very close to an undoped matrix, suggesting that the presence of a neighboring Xe atoms has minimal influence on the diffusion of U into a vacancy. It was also observed that the diffusion coefficient (express as Log[D/D0]) for B defects are more significant compared to the result obtained for U migration.

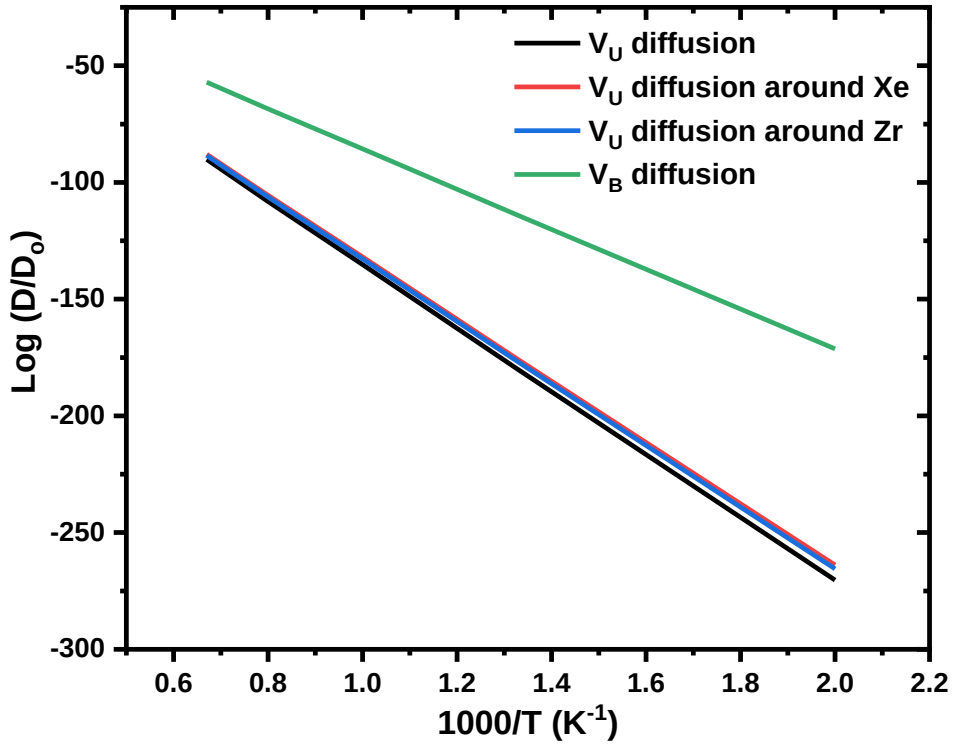

Fig. 5.10. Diffusion coefficients (express as Log(D/D_0)) as a function of temperature for diffusion of U and B atoms through vacancy paths.

5.6. Conclusions

We have investigated through these theoretical studies the incorporation and solutions energies of Zr and Xe in UB_2. It was found that Zr is more soluble in UB_2 than Xe within the GGA framework. The electron density of state of the defective fuel matrix was calculated and unlike UO_2 that transition from semiconducting to metallic, UB_2 maintains its metallic properties as impurity concentration was increased. The same holds true for the point defects considered in this work. Furthermore, as the concentration of Zr FP increased, there was a contraction in the volume of UB_2 while the increase in Xe resulted in swelling of the fuel matrix. This difference in perturbation of the crystal structure is due to the difference in the atomic radius of the FPs. The presence of Xe or Zr in neighboring U sites does not impact the migration of U in UB_2 in any significant way. The obtained results provide a fundamental understanding in regard to effect of fission products on the volume change in UB_2 matrix and the vacancy mediated diffusion behavior of fission products in UB_2 at an atomic level and can guild future experiments.

Chapter 6

Anisotropic thermophysical properties of U_3Si_2 fuel: An atomic scale study

6.1. Overview of Chapter 6

The overall goal of this research is to screen high-density uranium compounds toward the identification of ATFs for the next generation of nuclear reactors. The thermophysical properties serve as a key parameter in the selection of an ATF. Therefore, in this chapter, the thermal conductivity, heat capacity, and thermal expansion of U_3Si_2 from room temperature to near the melting point was calculated. Due to the metallic nature of U_3Si_2, it becomes essential to also determine the thermal conductivity contribution not only from phonons but also from the electrons. Evaluation of both contributions could not be obtained from Laser Flash experiments and had to be calculated. The equilibrium and non-equilibrium methods, as implemented in the molecular dynamics code LAMMPS for this calculation, were used.

The current chapter is presented as manuscript #3 (Anisotropic thermophysical properties of U_3Si_2 fuel: an atomic scale study). The simulations and analysis were carried out by Ericmoore Jossou with assistance from Dr. Md. Jahidur Rahman and Dotun Oladimeji. The manuscript in its entirety was written by Ericmoore and supervised by Dr. Barbara Szpunar and Prof. Jerzy Szpunar. The MEAM potential fitting and parameterization was performed by Dr. Benjamin Beeler of Idaho National Laboratory, USA. We gratefully acknowledge Dr. Edward Obbard for providing us with experimentally measured lattice parameters from his recent study. To avoid repetition of information provided in Chapter 3 of this thesis, the equations for calculation of some ground state properties have been removed from this chapter. The copyright permission to use the manuscript in this thesis was obtained from the publishers and it is provided in APPENDIX E.

The manuscript was published in 2019 in *Journal of Nuclear Materials*:

- E. Jossou, M. J. Rahman, D. Oladimeji, B. Beeler, B. Szpunar, J. Szpunar, Anisotropic thermophysical properties of U_3Si_2 fuel: An atomic scale study, J. Nucl. Mater. 521 (2019) 1–12. doi:https://doi.org/10.1016/j.jnucmat.2019.04.033.

Anisotropic thermophysical properties of u_3si_2 fuel: an atomic scale study

Ericmoore Jossou[1], Md. Jahidur Rahman[1], Dotun Oladimeji[2], Benjamin Beeler[3], Barbara Szpunar[2], Jerzy Szpunar[1]

[1]Department of Mechanical Engineering, College of Engineering, University of Saskatchewan, 57 Campus Drive, Saskatoon, S7N 5A9, Saskatchewan, Canada.
[2]Department of Physics and Engineering Physics, College of Art and Science, University of Saskatchewan, 116 Science Place, Saskatoon, S7N 5E2, Saskatchewan, Canada.
[3]Idaho National Laboratory, Idaho Falls, ID, 83415, USA.

6.2. Abstract

Due to renewed interest in uranium silicide compounds as a candidate for nuclear reactor fuels, there is a need for extensive investigations of their thermophysical properties as a function of temperature. In this work, we calculate the thermophysical properties of the U_3Si_2 compound within the framework of molecular dynamics (MD) using a semi-empirical modified Embedded-Atom Method (MEAM) potential and density functional theory (DFT). Thermal expansion, thermal conductivity, heat capacity, and elastic properties are presented as a function of temperature from 300 to 1800 K. The thermal conductivity of U_3Si_2 increases with temperature due to the electronic contribution while the phonon contribution decreases with increasing temperature. The phonon contribution to the thermal conductivity at 300 K is estimated at 2.03 W/mK and 1.41 W/mK using non-equilibrium molecular dynamics (NEMD) and equilibrium molecular dynamics (EMD), respectively. The electronic contribution is estimated to be 8.56 W/mK using the semi-classical Boltzmann transport theory at 300 K. Furthermore, we compared the thermal conductivity in two different crystallographic directions to shed light on the spatial anisotropy using NEMD and EMD methods. The inherent anisotropic thermophysical properties can be used to parametrize phase field models to incorporate anisotropic thermal conductivity and thermal expansion, allowing for a more accurate description of microstructural evolution under variable temperature and irradiation conditions.

Keywords: *Uranium silicide; Anisotropy; molecular dynamics; thermophysical; MEAM.*

6.3. Introduction

Uranium dioxide (UO_2) is the standard fuel in today's Light Water Reactors (LWRs). The nuclear accident at Fukushima in 2011 provided motivation for fuel vendors, in collaboration with national and international regulatory agencies, to consider an alternative fuel that can withstand the loss of coolant for a considerably longer time in the case of an accident. Alternate fuel types must maintain high safety and reliability during normal operation, and it would be preferable if major changes to the present design of the LWRs are not required [1,248].

Binary uranium-silicon compounds such as U_3Si_2 have attracted a lot of attention as a nuclear fuel material because of some more favorable characteristics when compared to UO_2. For instance, U_3Si_2 has a higher thermal conductivity and higher fissile material density [13] but lower melting point and reduced oxidation resistance compared to UO_2. The enhanced heat removal capabilities make uranium silicide fuel a promising potential fuel for generation *IV* reactors. However, until recently there has been limited study on the thermal properties of uranium silicide [58] compared to properties such as oxidation behavior [249,250], structural information [251,252], and radiation resistance [213,253].

According to experiments [251,252], U_3Si_2 has a tetragonal crystal structure (space group 127) with U occupying *2a* and *4h* Wyckoff positions while Si occupies the *4g* site as shown in Fig. 6.1. Using a particle swarming optimization code, Noordhoek *et al*., predicted a new U_3Si_2 phase with space group number 2 which has not been experimentally synthesized [64].

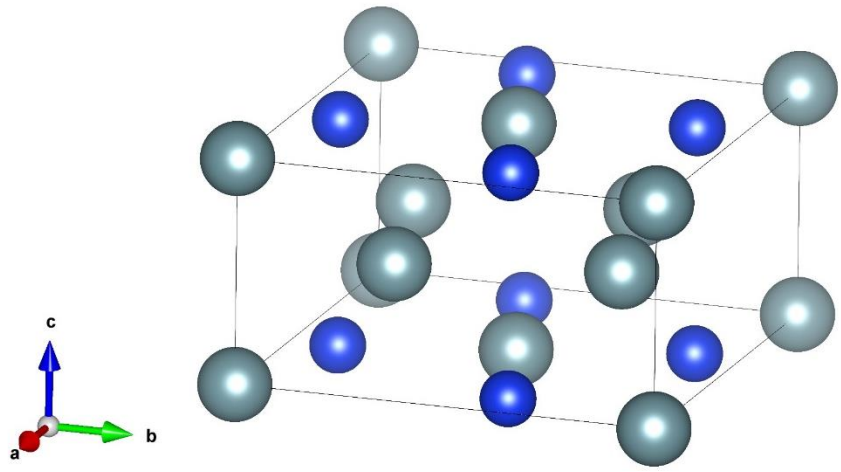

Fig. 6.1. Unit cell of ordered uranium silicide containing 2 formula units of U_3Si_2 (10 atoms). (Color scheme: U=grey, Si=blue).

Due to the growing interest in Accident Tolerant Fuels (ATFs) in the last few years, some work has been conducted on U-Si alloys focused on U_3Si_2. Density functional theory (DFT) calculations by Noordhoek *et al.* provided detailed data on the electronic structure [64] and work by Middleburgh *et al.* modeled the formation energies of point defects [66]. White *et al*. developed a feasible powder metallurgy method of preparation and measured the thermophysical properties of U_3Si_2 [13].

More recently, Obbard *et al.* used *in-situ* neutron diffraction to collect the temperature dependence of lattice parameters and the lattice thermal expansion coefficient was calculated. They observed anisotropy in lattice expansion at ~1000 ^oC, corroborating the dilatometry measurement of White *et al*. [3, 14] .

Our recent work within the framework of DFT explores the mechanism of oxidation from an atomistic perspective [254], while work by Sooby-Wood *et al*., experimentally showed the oxidation kinetics in the presence of air and steam [55,57]. Furthermore, Sooby-Wood *et al*., investigated the possibility of reducing oxidation by alloying of U_3Si_2 with aluminium, exploring formation of an Al_2O_3 passivation layer for preventing further oxidation [100].

Recent *in-situ* TEM observation of Xe ion irradiated U_3Si_2 indicates that, at normal reactor operation conditions, uranium silicide is stable and no radiation-induced amorphization was reported [56]. In a similar experiment using Kr ions, Miao *et al*. noticed that U_3Si_2 is oxidized forming a mixture of nanocrystalline UO_2 and a Si-enriched amorphous phase, raising concern for radiation assisted corrosion issues [213].

Beyond the properties of pristine U_3Si_2, it is essential to understand the underlying behavior in an extreme environment typical for a nuclear reactor. The radiation-induced defects and fission products in nuclear reactor fuel result in microstructural changes which in turn alters the fuel's thermophysical properties [255]. This has a significant effect on the thermal conductivity which decreases as radiation dose increases due to the contribution from phonon scattering. Such behavior is difficult to determine from experiment due to the limitation and cost of irradiation experiments. Therefore, Beeler *et al*. developed a MEAM potential to model the formation of point defects, and calculated formation energy and thermophysical properties of U_3Si_2 [69]. The interatomic potential reported in Beeler's paper will be used in this work to calculate various thermophysical properties of U_3Si_2.

The thermophysical properties such as specific heat, the coefficient of thermal expansion, density and the thermal conductivity of the fuel as a function of temperature are important and must be known in order to effectively model and predict fuel behavior under normal and unusual irradiation conditions. In this work, we calculated these properties for pristine U_3Si_2 under normal conditions and evaluate the results obtained by comparing them with the experimental data available in the existing literature.

6.4. Computational details

6.4.1. Phonon assisted thermal conductivity calculation

Molecular Dynamics (MD) simulations, employing a set of interatomic potentials for U_3Si_2 derived previously by Beeler *et al*. [69] are adopted in the Large-scale Atomic/Molecular Massively Parallel Simulator (LAMMPS) [256]. In the proposed model the potential energy E_i, of an atom *i* with respect to all other atoms has two components which are: (I) a pair potential description of each system and (II) an angular dependent many-body embedding function contribution. The embedding function is the energy required to embed atom *i* into a system with a background electron density. The detailed formalism of the modified many-body embedded atom method (MEAM) is well described in references [149,257].

The phonon assisted thermal conductivity (k_{ph}) of a material must account for several scattering mechanisms which include isotopic scattering, point defect scattering, three-phonon scattering and grain boundary scattering to name just a few. The value of k_{ph} can be calculated in different ways [258] including the relaxation time approximation [205], Callaway model [206], Slack model [258], Non-Equilibrium Molecular Dynamics (NEMD) [258], Equilibrium Molecular Dynamics (EMD) with Green-Kubo formalism [161,162] and by solving Boltzmann transport equation iteratively [157]. However, the computational cost of using some of these techniques especially, the Lattice dynamics based methods, is a major concern. Therefore, in this work, we calculated k_{ph} using the MD-based methods and the electronic thermal conductivity (k_{el}) was approximated using the *Wiedemann–Franz law* relationship [151]. The calculation of k_{ph} was done using both EMD and NEMD methods for comparison.

6.4.1.1. Equilibrium molecular dynamics simulation

In the EMD approach, the Green-Kubo method relates the equilibrium fluctuations of the heat current vector, S, to the thermal conductivity tensor via the fluctuation-dissipation theorem. Hence, the thermal conductivity is calculated using equations 3.56 and 3.57.

The EMD simulations were performed using the LAMMPS code [256]. The starting structures of size $14 \times 14 \times 16$ were first run for 4,000,000 time steps using an isothermal-isobaric (NPT) ensemble to allow the volume to expand using a Nosé-Hoover thermostat and barostat with a damping time of 0.1 ps and 0.5 ps respectively at zero external pressure, and then equilibrated under a constant volume and energy ensemble (NVE) for 4,000,000 time steps at temperatures of interest. A time step of 0.25 fs was deemed suitable to maintain energy conservation. To avoid statistical noise during heat flux collection, NVE was run for an additional 2,000,000 time steps. Correlation functions were evaluated from the heat current time series. The converged value of the HCACF integral is averaged in computing the thermal conductivity following the method reported by Sellan *et al*. [259]. Hence, the thermal conductivity was averaged between 950 to 1250 ps (see Fig. C.6.1 in Appendix C).

6.4.1.2. Non-equilibrium molecular dynamics simulation

In the NEMD simulations, the systems were initially equilibrated using an NPT ensemble with a Nosé-Hoover thermostat and barostat with a damping time of 0.1 ps and 0.5 ps respectively at zero external pressure. These structures are equilibrated until the potential energy and system volume reached a stable value at 1.75 ns. This is visually confirmed by a quick plot of total energy and volume against simulation time (see Fig. C.6.2 in Appendix C). Once equilibration is achieved, another 0.25 ns were simulated in order to get the average values of the lattice parameter and enthalpy of the system.

Following NPT equilibration, the NVE ensemble is used over a period of 0.25 fs, during which the Müller-Plathe approach is used [260]. In the NEMD method [261], kinetic energy can be transferred between atoms from one region of the supercell to another. Here, we used a rectangular supercell (slab) of five different lengths including 100, 125, 150 and175 unit cells in the x and z direction respectively. The supercell is split into several bins with a constant heat flux J_z, generated by heat exchange of atoms between the hot and cold region, respectively, as shown by the

schematic illustration in Fig. 6.2 (inset). The temperature gradient, Δa, is established between the two extreme temperatures due to the kinetic energy exchange. Eventually, a steady state in thermal gradient is reached where J_z is equal and opposite to the kinetic energy exchange so that the temperature profile remains constant. In Fig. 6.2 (main), a steady state temperature distribution, along the direction of heat transfer, is plotted for the largest system (5 × 5 × 175 unit cells) studied with the cold region at both ends and the hot region at the middle of U_3Si_2. This shows that the temperature at the center of the supercell is higher than that at the edge. The slope of the profile is the temperature gradient of the system, Δa. Temperature control can be simulated by addition or subtraction of the non-translational kinetic energies in the heat bath such that momentum is conserved.

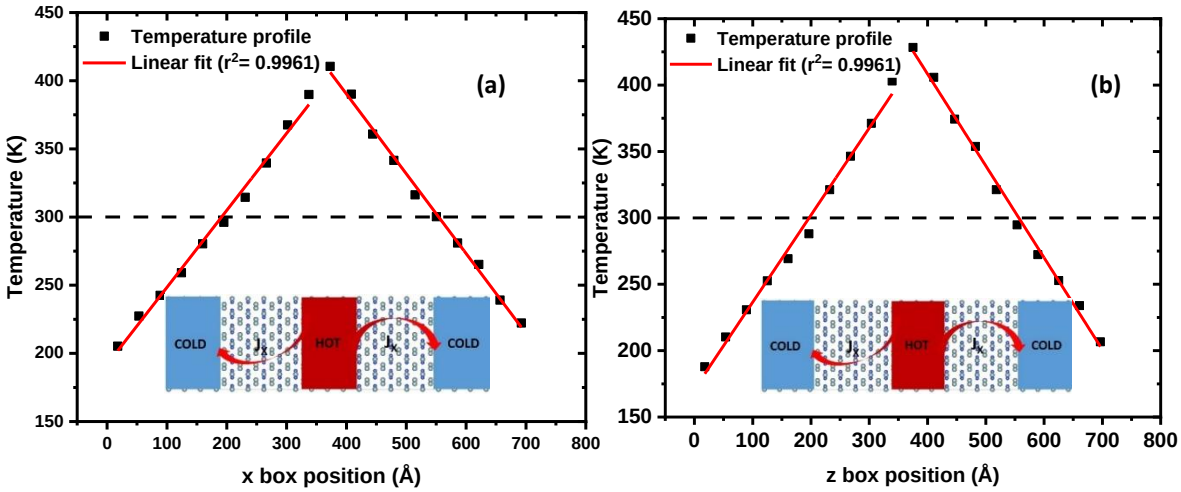

Fig. 6.2. A steady-state temperature profile for a (a) 175 × 5 × 10 (b) 5 × 5 × 175 unit cell system with the cold region at both ends and the hot region at the middle of U_3Si_2. The inset is a schematic illustration of the NEMD simulation setup used to study thermal conductivity of U_3Si_2. (Color scheme: U=grey, Si=blue).

Due to the spatial difference in the *x* and *z* directions of tetragonal U_3Si_2 structure, we expect difference in phonon transport in both directions. To investigate the spatial anisotropy in k_{ph}, we applied the same methods discussed above to the *x* direction of the crystal.

6.4.2. Electronic thermal conductivity calculation

The electronic thermal conductivity is calculated based on equations 6.5–6.8, the full tensor of σ is calculated using $\tau_{i,k}$ and the electronic band structure data is calculated within the framework

of DFT as implemented in the Quantum ESPRESSO code [143]. The exchange and correlation effects were described by the generalized gradient approximation (GGA) in the *Wu-Cohen* (GGA-WC) formulation [127]. The norm-conserving *Wu-Cohen* (WC) pseudopotentials (where these potentials treat $6d^1\ 5f^3\ 7s^1$ as valence electrons for U and $3s^2\ 3p^6$ as valence electrons for Si) was used in this calculation. The choice of the GGA-WC is because it is able to predict the binding energy of U_3Si_2 with non-magnetic ordering which is more stable than the ferromagnetic phase in agreement with experimental observation [252] and our earlier calculations [262] using CASTEP code and the same functional [263]. An earlier DFT (GGA/PBE) calculation performed by Noordhoek *et al.* predicted a ferromagnetic phase [64].

The strong on-site Coulomb repulsion among the localized uranium 5*f* electrons is described by the DFT + *U* formalism formulated by Liechtenstein *et al.* [264]. The Hubbard U parameter of 1.5 eV was utilized in this work in line with an earlier valued reported by Noordhoek *et al.* [64]. The Fermi surface effects were treated by the smearing technique of Methfessel-Paxton [230], using a smearing parameter of 0.02 Ry (0.27 eV). An energy threshold defining self-consistency of the electron density was set to 10^{-8} eV and a beta mixing factor of 0.3. Brillouin zone integration was performed using $20 \times 20 \times 24$ Monkhorst-Pack [265] k-point grids centred at the Γ point and a 120 Ry energy cut off was used. Structural relaxation was carried out to minimize the energy using the conjugate gradient method within the Broyden-Fletcher-Goldfarb-Shanno (BFGS) algorithm [266], until the magnitude of the residual Hellmann-Feyman force on each relaxed atom reached 0.01 eV $Å^{-1}$.

6.5. Results and discussion

6.5.1. Lattice parameter and thermal expansion

As a preliminary step, we calculate the lattice parameter '*a*' and '*c*' as a function of temperature. Not only is it required for all simulations, but also the thermal expansion coefficient α is a simple characteristic that depends directly on the anharmonic terms in the potential. Therefore, it gives a quick indication of how appropriate the interatomic potential is for studying thermal conductivity. The total energies, lattice parameters and volumes were determined by averaging over the last 0.25 ns of the NPT MD equilibrations. The linear thermal expansion coefficient (LTEC) and volumetric thermal expansion are then given by the relationship respectively:

$$\alpha_p = \frac{1}{l}\left(\frac{\partial l}{\partial T}\right)_p, \quad (6.1a)$$

$$\alpha_v = \frac{1}{v}\left(\frac{\partial v}{\partial T}\right)_p, \quad (6.1b)$$

where l is the lattice parameter in x and z direction while v is volume. The derivative of the lattice parameter with respect to temperature, $\frac{\partial l}{\partial T}$ and $\frac{\partial v}{\partial T}$ were calculated by fitting a straight line to the lattice parameters and volume respectively at a specific temperature, T, and the points within $T \pm 15$ K on either side (See Fig. C.6.3 in Appendix C for detailed plots from which lattice gradients are extrapolated) in order to reduce numerical fluctuations. The calculated lattice parameters *a*, *c* and cell volume at 0 K are presented in Table 6.1. There is a variation between our MD results and previous DFT + U and experimental measurements. For instance, a comparison with DFT + U calculations from Noordhoek *et al.* showed that *a* is underestimated by ~2.1 % and *c* overestimated by ~4 %.

Table 6.1. Structural properties (lattice parameter a, c (Å) and volume (Å^3)) of U_3Si_2 calculated at 0 K using MEAM U-Si potential and compared to DFT + U calculations as well as experiment. The uncertainty in the MD results is the deviation over the averaged value from the last 0.25 ns of the simulation.

	a	c	Volume/atom	c/a
This work (MD)	7.078±0.002	4.064±0.002	20.355±0.003	0.574±0.0002
Noordhoek (DFT+U) *et al*. [11]	7.230	3.891	20.339	0.538
Jossou (DFT+U) *et al.* [254]	7.210	3.860	20.066	0.535
Zachariasen (Expt.) [251]	7.315	3.893	20.831	0.532
Obbard (Expt.) *et al.* [62]	7.324	3.882	20.832	0.530

The average lattice parameters *a*, *c* and cell volume *v* as a function of temperature obtained from the MD simulation for U_3Si_2 are shown in Fig. 6.3a–c. Experimental values are also plotted in the range from 298 K to 1872 K [14]. The lattice parameter *a* and cell volume *v* are underestimated while *c* is overestimated but it is clear that the MD results follow the experimental trend. Some disagreement with experiment is understandable since the interatomic potential model was not fitted to this data. In Fig. 6.3a–c the behavior of the lattice parameters and cell volume can be seen to be almost linear in the range of 298-1800 K. Finally, Fig. 6.3d–f shows thermal strain $\Delta l/l_0$ as a function of temperature where l is lattice parameters *a*, *c* and cell volume *v* for U_3Si_2 structure. There is a subtle change in the thermal gradient at temperature points which marks the onset of

change in the LTEC calculated for U_3Si_2 in Fig. 6.4. The variation in the calculated LTEC values compared to experimental data is predictable as the individual components of the thermal expansion are underestimated, especially after ~500 K.

We compared the LTEC computed from the volumetric strain, $\Delta v/v$ (LTEC = $\alpha_v/3$ and α_v is the volumetric thermal expansion) with experimental measurements and the previous MD result. A fairly good agreement is observed between the data calculated here and the work of Loch *et al*. [267] and Shimizu [268] especially at temperatures above 900 K, while underestimation is noticed in comparison to the recent measurement by White *et al*. [13] and Taylor *et al*. [269]. The average LTEC from 300 to 1200 K is 11.81× 10^{-6} K^{-1}, in excellent agreement with the result of Beeler *et al.* [69].

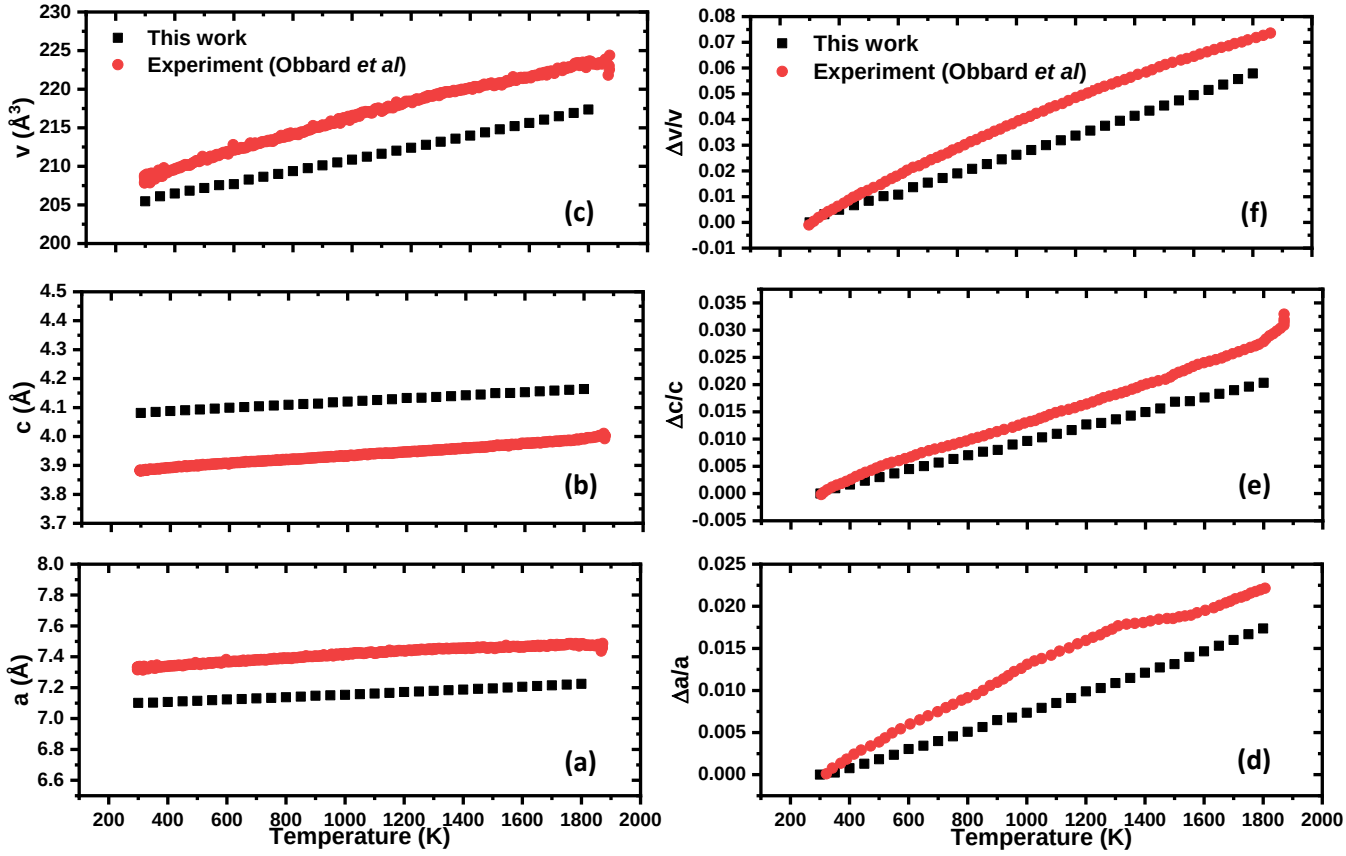

Fig. 6.3. (a–c) Shows variation of lattice parameter and cell volume (d–f) Thermal strain in lattice parameters and in cell volume as a function of temperature. The experimental lattice constants and lattice strain data were obtained from Ref. [62]. Each data point is averaged from the last 0.25 ns of the simulation. The error bars from the standard deviation are too small to see.

Beeler *et al.* [69] calculated an average LTEC but did not report unique *a*/*c* expansion coefficients. Additionally, this work utilizes a more refined temperature sampling, which allows for a more intricate analysis of the nature of anisotropic thermal expansion. This work is performed in order to compare with the experimental results from Obbard *et al.* [62]. We looked at the directional dependence of LTEC and it is interesting to note that the there is an overlap between the α_a and α_c component at 1500 K. Unlike the work of Obbard *et al*., there is no distinct transition point in the data reported here.

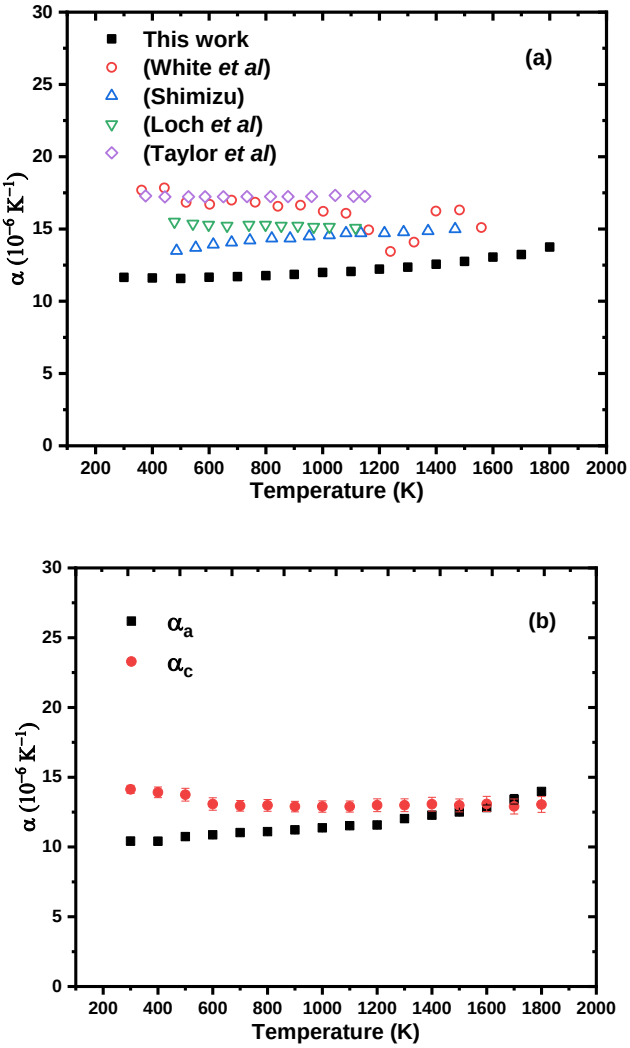

Fig. 6.4. (a) Linear thermal expansion coefficients of U_3Si_2 calculated from volumetric strain (b) anisotropy in linear thermal expansion coefficient in *a* and *c* direction as a function of temperature. The experimental linear thermal expansion coefficient data were obtained from Refs. [13, 267-269]. Each data point is averaged from the last 0.25 ns of the simulation. The error bars from the standard deviation are too small to see in the LTEC calculated from volumetric strain.

The difference in the results might be due to the nature of the MEAM potential since it was not developed for calculating thermophysical properties [69]. It is also well known that thermal expansion can be made up of lattice, electronic, magnetic and vacancy/interstitial components, depending upon the material and temperature range. The MD model does not account for all of these factors, and the electronic contribution could be especially important given the metallic nature of U_3Si_2 [270].

To further investigate the observed anisotropy, we compute the *c*/*a* ratio which is a measure of the tetragonality of the structure. The change in *c*/*a* with temperature is important, because it has a direct influence on the evolution of the LTEC. However, in this work the non-uniform expansion of the *a* and *c* lattice parameters is not captured by the *c*/*a* ratio as it remains constant across the whole temperature range as shown in Fig. 6.5, which in turn results in the anisotropic nature of the LTEC in U_3Si_2. The *c*/*a* ratio is higher in our calculation but nonetheless follows the experimental trend.

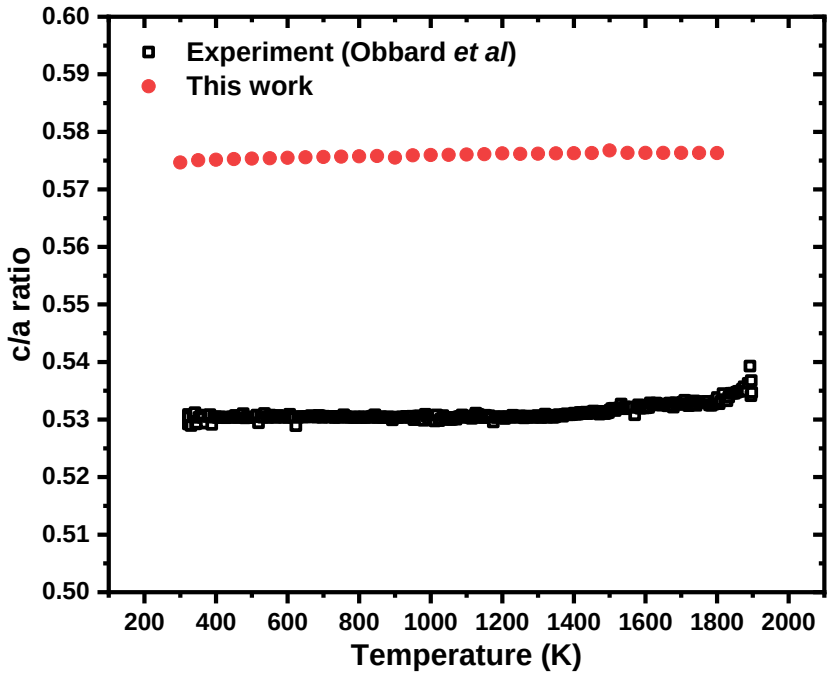

Fig. 6.5. The temperature dependence of the *c*/*a* ratio of U_3Si_2. The experimental *c*/*a* data were derived from Ref. [62]. Each data point is averaged from the last 0.25 ns of the simulation. The error bars from the standard deviation are too small to see.

6.5.2. Enthalpy and specific heat

In this work we determine the enthalpy increment (increase in enthalpy with respect to standard temperature and pressure as a function of temperature, using the relationship $H(T) - H(298K)$. Just like the lattice parameter, the enthalpy increment increases approximately linearly with temperature as shown in Fig. 6.6a. The first derivative of the enthalpy increment with respect to temperature is used to calculate the specific heat capacity at constant pressure due to phonon scattering, C_{ph}, (including both harmonic and anharmonic contributions) using the following relationship,

$$C_{ph} = \frac{1}{n}\left(\frac{\partial H}{\partial T}\right)_p, \tag{6.2a}$$

where n is the number of moles. The first derivative of the enthalpy was calculated by fitting a straight line to the enthalpy (see Fig. C.6.4 in Appendix C material for detailed plots from which enthalpy gradients are extrapolated) at a given temperature T and the data at T±15 K on either side. The molar heat capacity of a metal is the summation of the dilatational, harmonic and anharmonic lattice (phonon), and electronic terms. The total molar heat capacity, C_p is estimated by addition of the C_{ph} and the electronic heat capacity, C_{el} given by:

$$C_{el}(T) = \gamma T, \tag{6.2b}$$

where γ is the electronic specific heat coefficient (estimated to be 13.2 mJ/mol-K^2 from DFT+U calculations [271]) and T is the temperature in Kelvin.

The calculated C_{ph} values agree with the Dulong Petit Law value above the Debye temperature of U_3Si_2 which is ~200 K [58]. The sum of C_{ph} and C_{el} components of heat capacity give the total heat capacity, C_p, shown in Fig. 6.6b. The C_{el} is smaller compared to the C_{ph}. However, it is significant as shown by recent measurement by Antonio *et al* [58].

In comparison to previous work, our result agrees with recent experimental data by White *et al* [272] at high temperature (~1200 K and above) and the result of Knacke *et al* [273] from 1300 K. The difference at temperature < 1200 K might be due to the fact that dilatational term is not accounted for in MD simulation. The result is consistent with work by Beeler *et al* who determined

C_{ph} at 400 K to be 134 J/mol-K [69] meanwhile our result is underestimated by ~13% in comparison to recently measured value by Antonio *et al* at 300 K as 149 J/mol-K [58].

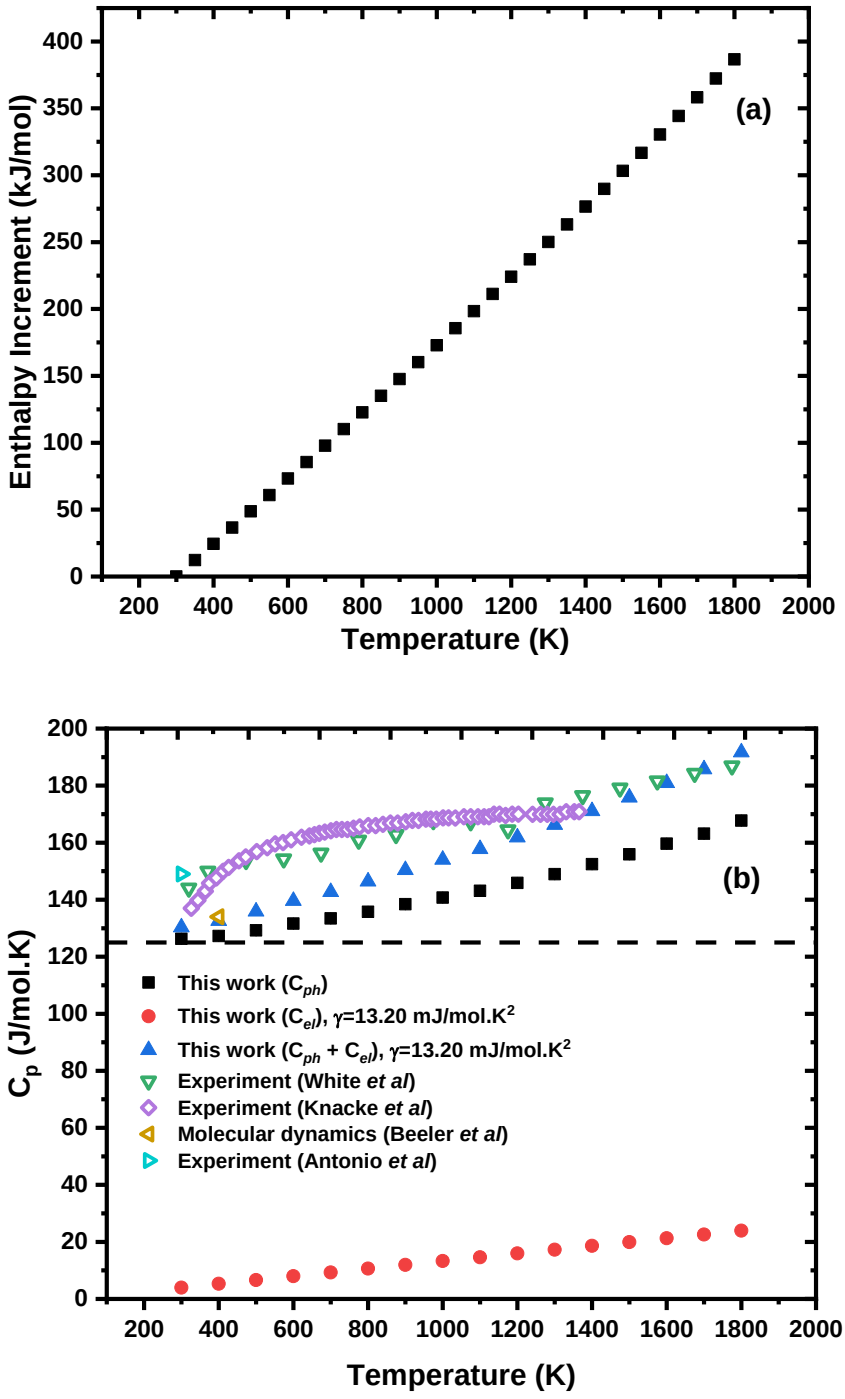

Fig. 6.6. (a) The change in enthalpy relative to the enthalpy at 300 K (b) molar heat capacity at constant pressure as a function of temperature. The experimental heat capacity at constant pressure data were obtained from Refs. [58, 69, 272-273]. Each data point is averaged from the last 0.25 ns of the simulation. The error bars from the standard deviation are too small to see.

6.5.3. Elastic constants

Elasticity describes the physical and internal changes of solid material under the application of stress and strain. The elastic coefficients and moduli can be also linked to the atomic bonding, deformation characteristics and mechanical and structural stability. To investigate the mechanical stability of the intermetallic U_3Si_2, we estimated the elastic constants at 0 K by applying strain in the appropriate directions of the supercell. A triclinic box was used in order to allow the box to change its shape accordingly to the imposed strain. After the energy minimization of the lattice, the stress tensor was computed in order to obtain the elastic constants. The elastic constants at finite temperature (300 K) are determined using the structure optimized at 300 K with the appropriate lattice parameter. The simulations are carried out in an isothermal condition, where a thermostat is applied to maintain the desired temperature in the system so that the temperature remains constant [274]. Temperatures considered here allow for comparison with DFT results (0 K) and experimental data at 300 K. The calculated elastic constants of a single crystal of U_3Si_2 are listed in Table 6.2 along with the reported values from DFT calculations [63,64,271] and experiment [275]. For tetragonal symmetry, there are six independent elastic constants, that is, C_{11}, C_{12}, C_{13}, C_{33}, C_{44} and C_{66}. The calculated elastic constants of U_3Si_2 fulfil the Born criteria for mechanical stability [276]. Therefore, it can be said that U_3Si_2 is mechanically stable at ambient conditions.

While DFT calculations are more physically rigorous than the MEAM model used here, they are more accurate than MD simulations. The bulk and shear moduli here are estimated using the Hill's model which is an average of the Voigt and Reuss bounds [172] while Beeler *et al.* used only the Voigt bound, hence the difference in bulk modulus. As shown in Table 6.2, there is a general softening in the elastic constant as we increased the temperature from 0 to 300 K, and a look at the experimental measurements which are done at room temperature shows that Young's modulus is overestimated in our MD calculation by ~15–20% at 300 K, while comparison with DFT shows that our result is underestimated by ~3–17% [271]. There are various deviations in the calculated Bulk moduli in comparison to the measured values of 68.3 and 64.3 GPa, which are from the different sets of U_3Si_2 samples prepared at Los Alamos National Laboratory [275]. It is also important to mention that theoretical calculations assume a single crystal during simulations while experimental measurements were conducted on polycrystalline U_3Si_2 samples with the possible presence of porosity, grain boundaries and microcracks, which might account for the general

overestimation in DFT and MD data. The external defects can significantly reduce the magnitude of the elastic properties [274].

The elastic and thermophysical properties of solids are related through the Debye model. Furthermore, the Debye temperature, θ_D is related to many physical properties such as specific heat, elastic constants, and melting point, T_m [277]. The calculated elastic constants can be used to estimate the T_m of solids based on a correlation derived by Fine *et al*. [200] from studying many cubic, hexagonal and tetragonal metals. Their correlation is based on the assumption that there is a relationship between the elastic constants and the melting points of materials as observed in tungsten and sodium metal while commonly used MD methods such as moving interface method is based on the assumption that solid-liquid liquid phase of materials coexistence at the onset of melting [278]. It must be noted here that the correlation was originally used for metals but has been extended to other materials of tetragonal structure according to Mehl *et al*. [279]. The Fine *et al*. correlation for tetragonal structure is given by:

$$T_m = 354K + 4.50K/GPa\left(\frac{2C11+C33}{3}\right) \pm 300, \tag{6.3}$$

Using equations 3.79–3.82 derived in Chapter 3, the polycrystalline properties of U_3Si_2 are calculated and are presented in Table 6.3. These results are also compared to recent DFT result from Wang *et al*. [63]. The calculated value of the T_m from data at 0 K and 300 K are 1224.99 ± 300 and 1198.40 ± 300 K, respectively. Furthermore, DFT work by Szpunar *et al.* reports T_m for paramagnetic and ferromagnetic U_3Si_2 phases as 1796 and 1250 K respectively [280]. This method of estimation significantly under predicts the melting point compared to the experimental value of 1938 K [281] and the MD result of 1775 K [282]. This relation provides a quick method for estimating the T_m using the elastic constants calculated in this work. The calculated value of the Debye temperature of U_3Si_2 agrees well with the reported theoretical value of 280.92 K [63]. It is overpredicted by approximately 76 (81) K in comparison to a recent experimental measurement of 200 K [58].

6.5.4. Thermal conductivity

6.5.4.1. Phonon contribution to the thermal conductivity

The total thermal conductivity of metallic nuclear fuel is determined by the combination of the contribution to the thermal conductivity both from electrons and phonon transport using equation 3.28. The k_{el} is the electronic contribution to the thermal conductivity that is calculated below using the Wiedemann-Franz law [151]. We have calculated the k_{ph} of U_3Si_2 at temperatures from 300 to 1500 K by both the NEMD and the EMD methods. The size of the supercell has a considerable effect on the thermal conductivity calculated using both methods. Therefore, rigorous convergence testing for a finite simulation cell size was carried out for the two methods.

In the EMD approach, the convergence of k_{ph} with respect to the HCACF integral and finite simulation cell size are key sensitivity tests that are needed to achieve converged values of thermal conductivity. The HCACF integral is directly proportional to the thermal conductivity (see equation 3.56). Convergence in HCACF is achieved by varying the correlation length (truncation time) until it has decayed to zero. The normalized HCACF (Fig. 6.7a) at 300 and 1200 K and its integral (Fig. 6.7b) at 300 K is presented Fig. 6.7. The HCACF integral converged after 0.90 ns, hence we specify the converged value of the HCACF integral by averaging its value between times of 0.95 and 1.25 ns (the shaded region of Fig. 6.7b). The number of phonons needed to capture the *ph–ph* scattering in the bulk material is dependent on the simulation cell size.

This effect is reduced by increasing the simulation cell length until the thermal conductivity reaches a size independent value. In this work, we investigated system sizes of $8 \times 8 \times 10$, $10 \times 10 \times 12$, $12 \times 12 \times 14$, $14 \times 14 \times 16$, $16 \times 16 \times 18$ and $18 \times 18 \times 20$ (12000, 20160, 31360, 46080 and 64800 atoms, respectively) all at a temperature of 300 K. These systems correspond to lengths L_z of 4.68, 5.46, 6.24, 7.02 and 7.80 nm respectively.

Table 6.2. Elastic constants (GPa) and elastic moduli (GPa) of U_3Si_2 at 0 and 300 K. Experimental U_3Si_2 specimens labelled a= set A (samples1 – 5) and b= set B (samples 6 – 7) were prepared from different feedstocks [275]. Beeler *et al*. [69] used only the Voigt bound in estimation of the bulk modulus while the Hill's average of the Voigt and Reuss bounds is used in this work.

	C_{11}	C_{33}	C_{12}	C_{13}	C_{44}	C_{66}	G	B	E	ν
MEAM at 0K (This work)	210.2	160.2	178.9	65.8	103.1	35.4	51.1	126.7	135.1	0.3
MEAM at 0K [69]	210.2	160.2	178.9	65.8	103.1	35.4		134	–	–
DFT at 0K [64]	149.0	139.0	49.0	48.0	63.0	46.0	53.0	81.0	130.0	0.2
DFT at 0K [63]	167.3	205.3	45.6	50.3	67.5	74.1	67.7	92.0	163.1	0.2
DFT at 0K [271]	155.0	142.0	47.0	50.0	65.0	46.0	57.0	83.0	139.0	0.2
MEAM at 300K (This work)	208.6	145.8	144.9	67.0	91.0	47.1	60.0	118.7	154.0	0.3
Experiment [275]	137.9	–	–	–	53.8	–	–	68.3±0.5[a]	130.4±0.5[a]	0.182±0.003[a]
								64.3±0.3[b]	122.9±2.4[b]	0.179±0.007[b]

Table 6.3. Theoretical sound velocities (m/s), Debye and melting temperatures (K) of U_3Si_2 predicted using the elastic properties at 0 and 300 K. Fine *et al*. [200] included a margin of error ($\pm$300 K) in their correlation which is included in this thesis.

Temperature (K)	V_l (m/s)	V_t (m/s)	V_m (m/s)	θ_D (K)	T_m (K)
MEAM at 0	4174.17	2295.05	2558.19	276.19	1224.99 $\pm$300
MEAM at 300	4125.83	2338.76	2600.55	280.76	1198.40 $\pm$300
DFT at 0 [63]	3865.04	2355.32	2601.53	280.92	1163.75 $\pm$300
Expt. [281]	–	–	–	200 [58]	1938 [281]
MD [69]	–	–	–	–	1775 [69]

In Fig. 6.7b we show the computed thermal conductivity obtained by direct integration for 1.25 ns of the HCACF for different choices of simulation cell. We see that the 12000 atom (3.90 nm) system results in the lower value of 0.73 W/mK, compared to the simulations in a larger system size of 64800 atoms (7.80 nm). It is apparent from Fig. 6.7b that the results for k_{ph} are converged by 31360 atoms (6.24 nm) with a value of 1.41 W/mK. However, we used the simulation cell with 46080 atoms (7.02 nm) for all calculations incase the first convergence point is off trend. (See Appendix C (Fig. C.6.1) for convergence of HCACF with respect to supercell size and the dependence of k_{ph} on collection time (t) calculated for cell sizes of $8 \times 8 \times 10$, $14 \times 14 \times 16$, $16 \times 16 \times 18$ and $18 \times 18 \times 20$. The same finite size convergence tests have been used in a previous work [283].

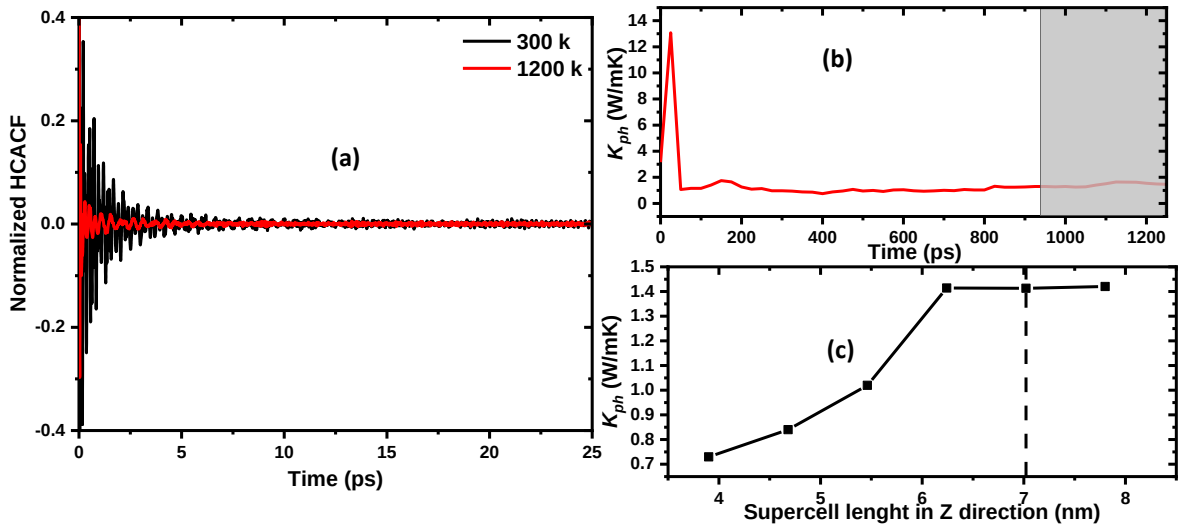

Fig. 6.7. (a) Normalized heat current autocorrelation function at 300 and 1200 K respectively (b) its integral for U_3Si_2 at 300 K. The HCACFs are normalized by their initial values. The shaded region in the (b) indicates the time range over which the HCACF integral is averaged to predict the phonon assisted thermal conductivity k_{ph}. Note that the time scale of the inset is 50 times that of the body (c) Thermal conductivity plotted against lateral simulation box dimensions at 300 K. Results converged at supercell length of 6.24 nm.

In the NEMD, it has been shown in the previous study that the finite size of the system can limit phonon mean free path, hence underestimating the thermal conductivity. Furthermore, it is well known that the supercell dimension in the L_x and L_y directions (perpendicular to heat flux) have a small effect on the thermal conductivity, but changes along the L_z (direction of heat flux) are more

significant [283]. Therefore, we estimated the minimum L_z used in the NEMD simulation with the relationship derived by Sellan *et al*. [259]:

$$k_{\infty}^{max} = \frac{L_z K_B (v_L + 2v_T)}{18a^2 c}, \tag{6.4}$$

where k_{∞}^{max} is the maximum k_{ph} that can be accurately predicted by linear extrapolation with a minimum L_z used in the NEMD simulation, K_B is Boltzmann constant, v_L and v_T are the longitudinal and transverse velocities, respectively, from Table 6.3 while *a* and *c* are the simulation cell parameters at 300 K. As a rule of thumb, the minimum L_z is increased until $k_{\infty}^{max} \sim k_{ph}$ predicted by linear extrapolation approach or equation 3.58. A quick check shows that the results are converged at an L_z of 100 unit cells, which is a necessary condition for accurate k_{ph} prediction within the NEMD formalism. The same L_z supercell sizes are applied to the *x* direction, since the size of L_x has a minimal effect on the thermal conductivity values.

The linear relationship between $1/k$ and $1/L$ is well described in Ref. [261] and plotted in Fig.6. 8 for the perfect U_3Si_2 structure as a function of temperature. Supercell sizes of $5 \times 5 \times 100$, $5 \times 5 \times 125$, $5 \times 5 \times 150$, and $5 \times 5 \times 175$ unit cells with heat flow in the *z* direction. Due to the spatial anisotropy in the *x* and *z* direction, a simulation system containing $100 \times 5 \times 10$, $125 \times 5 \times 10$, $150 \times 5 \times 10$, and $175 \times 5 \times 10$ unit cells were used for heat exchange in the *x* direction as well. The y-intercept is used to determine the thermal conductivity of the bulk U_3Si_2 as shown in Fig. 6.8a-b. The data points at 1500 K deviate slightly from linearity due to statistical noise which accounts for the unusual increase in k_{ph} at 1500 K.

Having computed the thermal conductivity of U_3Si_2 using the NEMD and the EMD method, we are now in a position to directly compare the results. For the NEMD at 300 K, extrapolation to $1/L_z = 0$ yields a value of k_{ph} of 2.37 and 1.37 W/mK (crystallographically averaged k_{ph} is 2.04 W/mK) in the *x* and *z* directions respectively while the EMD method gives a result of 1.50 and 1.23 W/mK (crystallographically averaged k_{ph} is 1.41 W/mK) for a $14 \times 14 \times 16$ system at 300 K in the *x* and *z* directions, respectively.

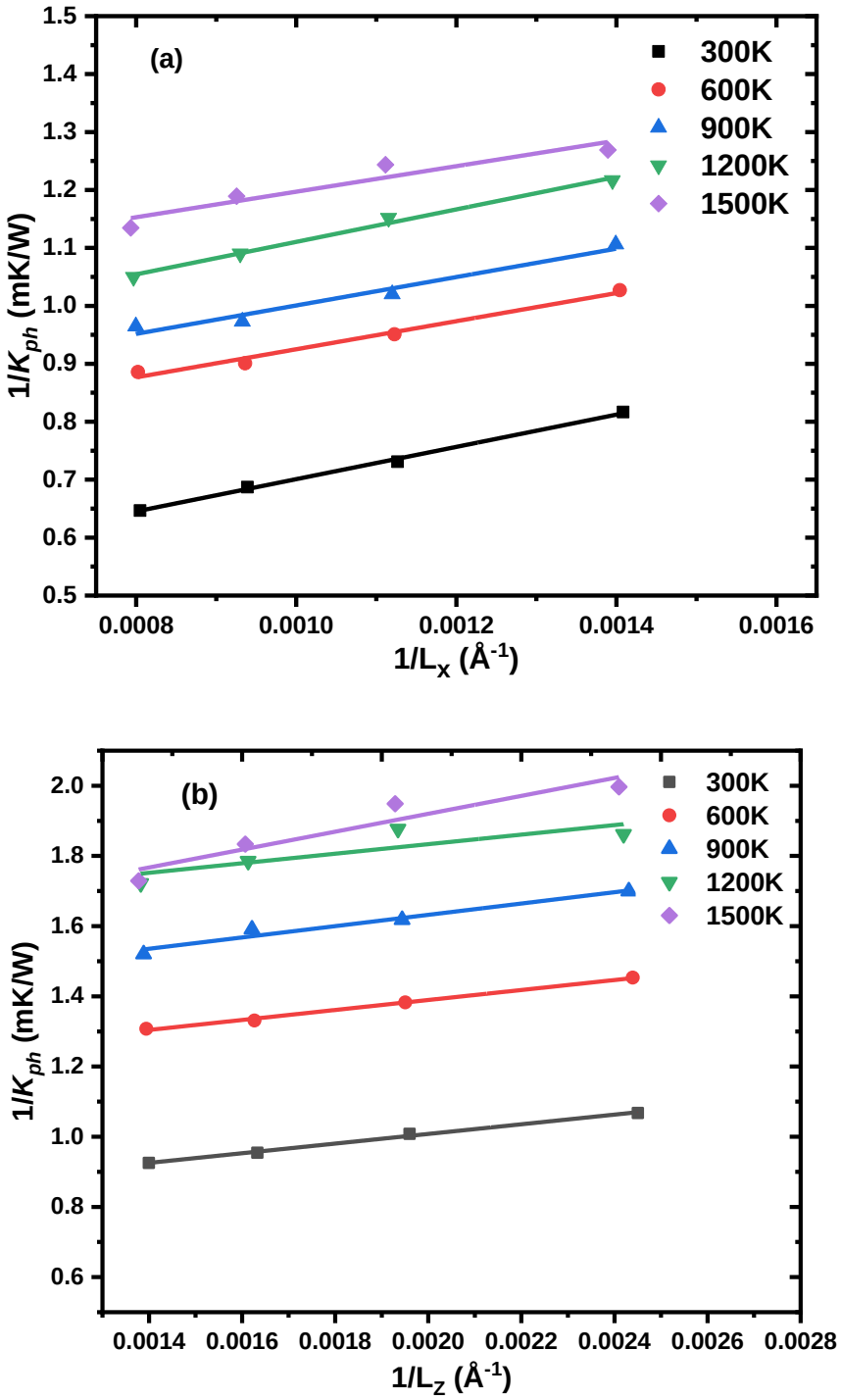

Fig. 6.8. The variation of the reciprocal of thermal conductivity as a function of the reciprocal of supercell length for perfect U_3Si_2 at a range of temperatures in (a) *x* (b) *z* directions respectively. The y-intercept indicates the reciprocal of bulk thermal conductivity.

The predicted thermal conductivities from the two methods are plotted against temperature from 300 –1500 K in Fig. 6.9a. In the temperature range of study, it is reasonable to think that Umklapp process (phonon-phonon interactions) dominates; hence k_{ph} should decrease like 1/T which is not obvious from the calculated values of Fig. 6.9a.

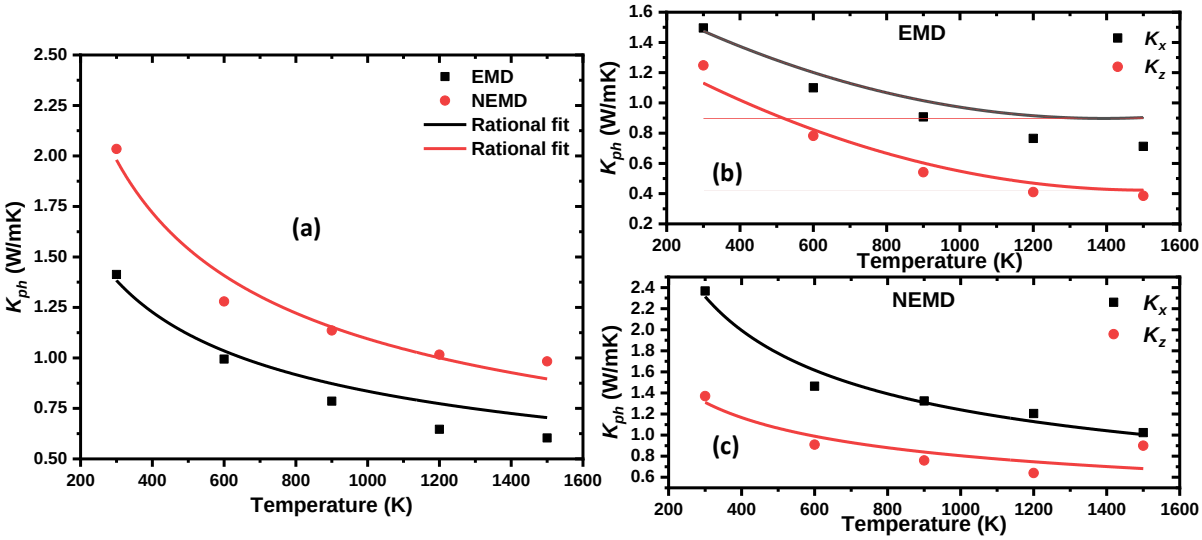

Fig. 6.9. (a) The directionally averaged k_{ph} of U_3Si_2 (b–c) spatial anisotropy in k_{ph} using EMD and NEMD approach over the temperature range of 300 to 1500 K.

These values were therefore fitted with a function of the form *c*/T + *k* to highlight the 1/T dependence.

Unlike the Boltzmann Transport Equation (Lattice dynamics and MD) prediction methods, there are no major assumptions inherent to the EMD and NEMD methods other than the choice of the interatomic potential and the damping parameters, which are consistent here. The predicted thermal conductivity values from the EMD are lower compared to NEMD results but generally within about ~18–30%. Our MD results compare reasonably well with recent work by Antonio *et al.*, who predicted a k_{ph} from 0 – 350 K, with a value of 1.99 W/mK at 300 K, which is higher by ~29% compared to our EMD (1.41 W/mK) while in excellent agreement with NEMD (2.03 W/mK) results, respectively [58]. Previous work by others have found that EMD and NEMD thermal conductivity predictions are consistent [283,284] except when there is significant contribution of low frequency or long mean free path phonons to k_{ph} of the materials [259]. This accounts for the difference in the result from the methods used in this study. It is also important to note that the many-body MEAM potential used here is not developed with a special focus on thermal properties of U_3Si_2.

We further explored the directional dependence of k_{ph} as presented in Fig. 6.9b-c, which shows the variation in k_x and k_z as a function of temperature in both methods. The k_{ph} exhibits significant directional anisotropy. In order to track the trend, we fitted the data to a quadratic equation which points to a moderate decrease in k_z/k_x from 0.83 at 300 K and 0.54 at 1500 K in the EMD data. NEMD results also follow similar trend except at 1500 K due to the unusual increase in the thermal conductivity which can be ascribed to thermal fluctuations. To reduce the effect of thermal fluctuation, we computed thermal conductivity at 1200 and 1500 K by averaging 3 independent simulations with values of 0.67±0.04 W/mK at 1200 K and 0.76±0.07 W/mK at 1500 K.

The anisotropic behavior may be attributed to differences in group velocity, anharmonicity, and scattering phase space along the different directions [285]. It is well known that the longitudinal sound velocity (v_l) and the transverse sound velocity (v_t) are primarily harmonic parameters while their ratio v_l/v_t is an anharmonic quantity which depends on the ratio between the axial and shear rigidities of interatomic bonds [209]. We find that the value of v_l/v_t is 1.76 which is a deviation from unity (isotropic behavior). This implies that the anisotropy in the k_{ph} of U_3Si_2 should be ascribed to its anisotropic sound velocities amongst other factors that have not been explored in this work.

In metallic system like U_3Si_2, it has been shown that at the low temperature i.e. $T \ll \theta_D$, only phonon scattering, *ph–ph*, plays a role in the thermal conductivity calculation [151,286] while in the $T \gg \theta_D$ regime, *el–el* interaction is the main contribution, hence it is not surprising to have low k_{ph} at 300 K given the fact that the θ_D has been determined to be ~281 K from our MD simulation and ~200 K from experiment [58]. Low k_{ph} contribution means that as temperature increases, degradation in phonon-based thermal conductivity is not a big concern in U_3Si_2 fuel, since k_{el} is the dominant component of k_{total} and increases with increasing temperature.

6.5.4.2. Incorporation of the electronic contribution to the total thermal conductivity

The electronic contribution to thermal conductivity is a consequence of the electrons presence at the Fermi energy. It is evident from both the band structure and partial density of states (PDOS) as shown in Fig. 6.10 that U_3Si_2 is metallic with the bands crossing the Fermi level (0 eV in Fig.

6.10). It can be seen in the PDOS that the conduction band is composed of a significant number of uranium 5*f* and a small number of 6*d* states, respectively. The U atoms act as the charge carriers and the 5*f* electrons as conduction electrons as observed in the region around the Fermi energy which is predominantly the uranium *f* electrons.

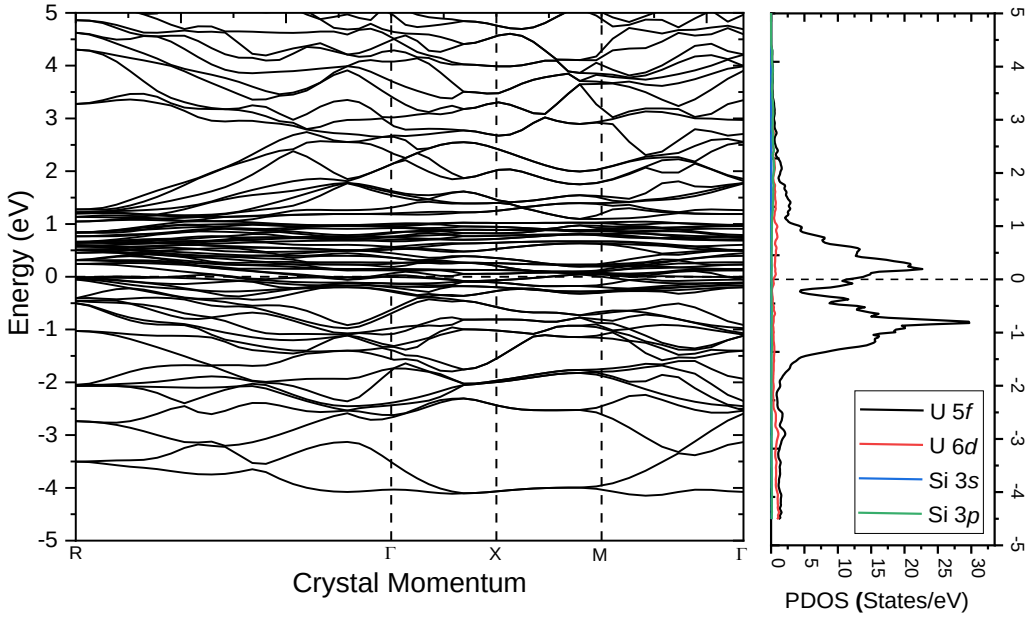

Fig. 6.10. Band structure and the total density of state of bulk U_3Si_2.

A closer look at the band structure further corroborates our observation of appreciable band overlap between valence and conduction states, which is responsible for the metallic nature of U_3Si_2. The significant amount of electrons at the Fermi level implies that the electronic contribution to the heat capacity and thermal conductivity of U_3Si_2 is mainly due to the dominant U 5*f* bands at the Fermi energy level.

In the calculation of k_{el}, the value σ/τ is determined from equation 6.8. Fig. 6.11a is a plot of σ/τ of electrons along different crystallographic directions in U_3Si_2 over the temperature range of 300 to 1500 K. We observed that overall, the value σ/τ shows a very weak temperature dependence with a 10% change over the entire range of 300 to 1500 K. A plot of the crystallographically averaged k_{el} along with the individual *x* and *z* components is shown in Fig. 6.11b. Our result slightly overestimates k_{el} in comparison to recent work by Srinivasu *et al.* [287]. This is not surprising since they used electrical resistivity data from Miyadai *et al.* [288] which is different from the value reported by Shimizu which is used in this work. Ranasinghe *et al.* [289] used the value from Shimizu, but the k_{el} is slightly lower compared to this work due to the fact that

temperature dependent values of τ are used in the calculations. They assumed that the correlation of τ(T) for UN ($\tau(T)_{UN}$) and U_3Si_2 have similar forms which is the basis for scaling the coefficient of $\tau(T)_{UN}$ for U_3Si_2. This assumption is not made in this work, and thus we have used a temperature independent τ in the calculations of k_{el}.

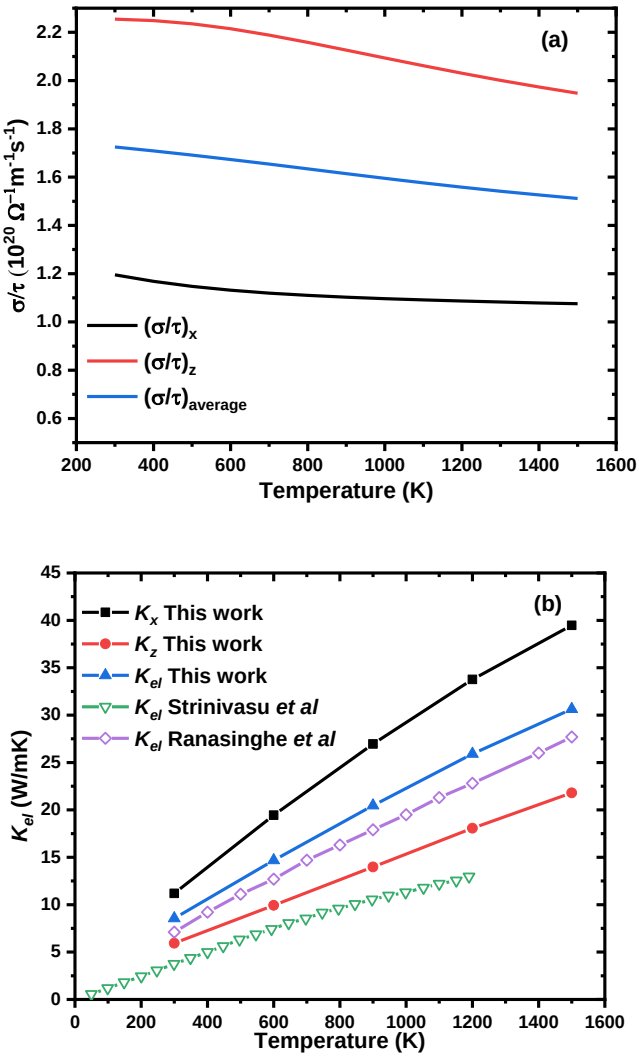

Fig. 6.11. (a) Plot of σ/τ of electrons in U_3Si_2 (b) directional dependence k_{el} over the temperature range of 300 to 1500 K. The theoretical thermal conductivity data were obtained from Refs. [287, 289].

A comparison between k_{ph} and k_{el} (Fig. 6.12a) clearly shows that the phonon thermal conductivity is relatively small compared to the electron thermal conductivity and its contribution at high temperature would be insignificant. Excellent agreement is observed for k_{total} values from 300 K to 1000 K compared to recent theoretical [290] and experimental [13] data as shown in Fig. 6.12b.

Slight deviation becomes present once temperatures exceed 500 K, with our predictions overestimating the value of k_{total}.

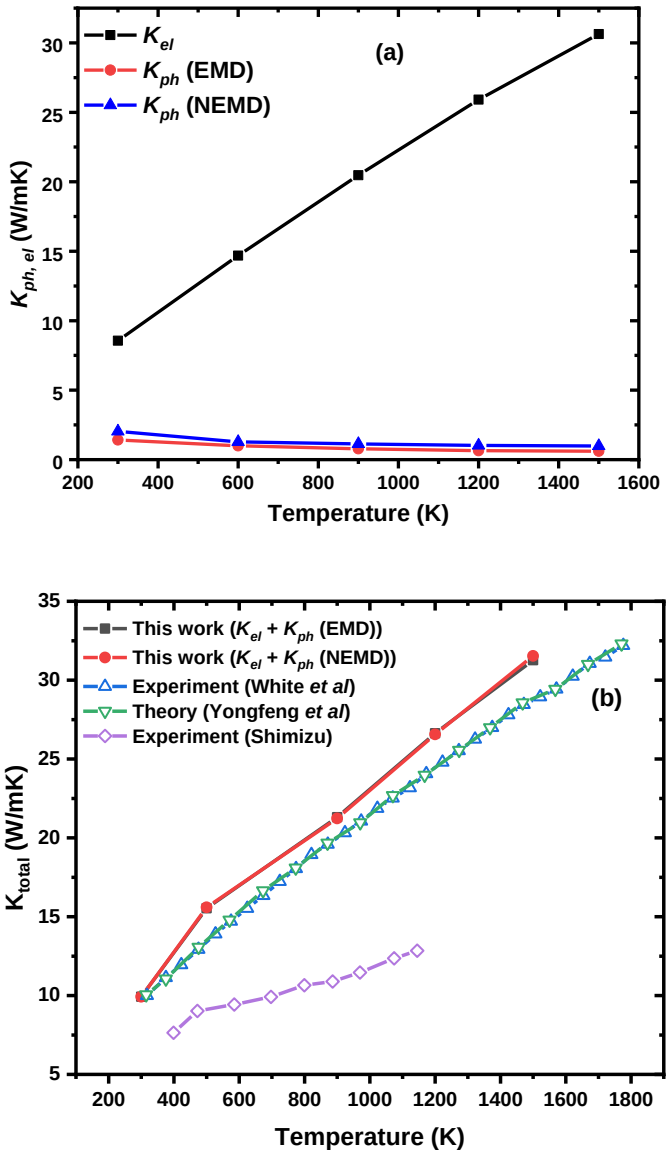

Fig. 6.12. (a) Comparison of $k_{ph,\ el}$ and (b) k_{total} over the temperature range of 300 to 1500 K. The experimental and theoretical thermal conductivity data were obtained from Refs. [13, 290, 268].

Similar trends have been reported for the thermal conductivity values of α-uranium where a similar method was used [291]. Furthermore, values reported by Shimizu are lower compared to our data which might be due to the defects in the structure and method of measurement [39].

To further explain the difference in Shimizu's data in comparison with recent works, we note that defects such as point defects, impurities, porosities and dislocations can significantly decrease the thermal conductivity of metallic systems such α-U, U_3Si_2 due to their influence on both the phonon and electronic component of the thermal conductivity [70].

6.6. Conclusions

In summary, we have performed a systematic atomistic study to investigate the anisotropic, temperature-dependent thermophysical properties of U_3Si_2 using a MEAM interatomic potential and first principles calculations. Based on the equilibrated structure of U_3Si_2, we obtain the values of thermal expansion coefficient, bulk modulus, and heat capacities at different temperatures, which are in good agreement with corresponding experimental measurements. A comparison of calculated molar heat capacity with experimental data also shows reasonable agreement with experiments.

Due to the anisotropy in lattice expansion with temperature, we noticed a directional dependence in the linear thermal expansion coefficient which has also been experimentally observed. The agreement between our calculations and experiments emphasizes the validity of our methods and model, and the effectiveness of the MD method employed in this work.

In addition, we also calculated the phonon assisted thermal conductivity of U_3Si_2. Both the EMD (Green–Kubo) and the direct (NEMD) methods have been utilized to determine the phonon-based thermal conductivity. Both methods were also used for all predictions of the directional dependence of k_{ph} in U_3Si_2.

It is important to note that each method has its own strengths and limitations. Both methods exhibit finite-size effects. These are much more severe in the NEMD method due to the presence of real interfaces at the heat source and sink. In the use of EMD it is sometimes difficult to obtain a converged value of the HCACF due to divergence. Such behavior has been observed in complex unit-cell (superlattice) [292], disordered materials and molecular chains [293]. To ensure the accuracy of the methods, we used the convergence scheme proposed by Sellan *et al.* [259]. Hence, EMD and NEMD gives results that are complementary in nature.

The electronic thermal conductivity was determined from first principles band structure calculations and the Wiedemann-Franz law. The electronic contribution to the thermal

conductivity in U_3Si_2 was confirmed to be the predominant component at temperatures of interest. Unlike other metallic fuel such as UB_2 where there is significant k_{ph} [71], U_3Si_2 has a k_{ph} less than 2 W/mK, which means that above the Debye temperature, the thermal transport is mainly driven by k_{el} which increases with temperature. Therefore, 'k_{ph} drag' on the k_{total} at reactor's operating temperature is insignificant compared to UB_2. The results also indicate an anisotropic behavior of the thermal conductivity in the *x* and *z* directions, in that the thermal conductivity is much higher in the *z* direction than in the *x* direction. The total thermal conductivity calculated is slightly higher than the recent experimental data by White *et al.* [13], but generally shows excellent agreement across the entire temperature range.

Overall, this work serves as a first step towards understanding the complex anisotropic behavior of the thermophysical properties of metallic U_3Si_2 nuclear fuel. The calculated anisotropic thermophysical properties can be used to parametrize phase field models to incorporate anisotropic thermal conductivity and thermal expansion, allowing for more accurate description of microstructural evolution under variable temperature and irradiation conditions or in continuum models to understand how the thermal gradient and the centerline temperature evolve during normal operation and accident conditions.

Chapter 7

Oxidation behavior of U_3Si_2: Experimental and first principles investigation

7.1. Overview of Chapter 7

In this chapter, density functional theory and experimental study are used to determine the thermodynamic stability and the oxides formed during the interactions between U_3Si_2-O_2 interfaces. The observations in this study could justify the need to control the texture of U_3Si_2 during powder metallurgy preparation to aid the formation of a passivating oxide layer during the process of corrosion.

This chapter is presented as manuscript #4 (E. Jossou, U. Eduok, N.Y. Dzade, B. Szpunar, J.A. Szpunar, Oxidation behavior of U_3Si_2: an experimental and first principles investigation, Phys. Chem. Chem. Phys. 20 (2018) 4708–4720. doi:10.1039/C7CP07154J). My contributions to this paper include a review of relevant literature, design and carrying out of the required simulation, analysis of results and preparation of the manuscript. My supervisors; Prof. Jerzy Szpunar and Dr. Barbara Szpunar reviewed the paper before it was submitted for publication. The manuscript was submitted for publication after implementing their suggestions. To avoid repetition of information provided in Chapter 6 of this thesis, the crystal description of the U_3Si_2 have been removed from this chapter. The copyright permission to use the manuscript in this thesis was obtained from the publishers and it is provided in APPENDIX E. Dr. Andrew Nelson from Los Alamos National Laboratory provided the sample used for this study.

The manuscript was published in 2018 in Journal of *Physical Chemistry Chemical Physics*:

- E. Jossou, U. Eduok, N.Y. Dzade, B. Szpunar, J.A. Szpunar, Oxidation behavior of U_3Si_2: an experimental and first principles investigation, Phys. Chem. Chem. Phys. 20 (2018) 4708–4720. doi:10.1039/C7CP07154J.

Oxidation behavior of U_3Si_2: Experimental and first principles investigation

Ericmoore Jossou[1], Ubong Eduok[1], Nelson Y. Dzade[2], Barbara Szpunar[3], Jerzy A. Szpunar[1]

[1]*Department of Mechanical Engineering, College of Engineering, University of Saskatchewan, 57 Campus Drive, Saskatoon, S7N 5A9, Saskatchewan,* Canada.

[2]*Department of Earth Sciences, Utrecht University, Princetonplein 9, 3584 CC, Utrecht, The Netherlands.*

[3]*Department of Physics and Engineering Physics, College of Art and Science, University of Saskatchewan, 116 Science Place, Saskatoon, S7N 5E2, Saskatchewan,* Canada.

7.2. Abstract

Uranium-containing metallic systems such as U_3Si_2 are potential Accident Tolerant Fuel (ATF) for Light Water Reactors (LWRs) and the next generation of nuclear reactors. Its oxidation behavior, especially in oxygen and water-enriched environments, plays a critical role in determining its applicability in commercial reactors. In this work, we have investigated the oxidative behavior of U_3Si_2 experimentally and by theoretical computation. The appearance of oxide signatures has been established from X-ray diffraction (XRD) and Raman spectroscopic techniques after oxidation of the solid U_3Si_2 sample in synthetic air (oxygen and nitrogen). We have also studied the changes in electronic structure as well as the energetics of oxygen interactions on U_3Si_2 surfaces using first principles calculations in the Density Functional Theory (DFT) formalism. Detailed charge transfer and bond length analyses revealed the preferential formation of a mixed oxides of UO_2 and SiO_2 on the U_3Si_2 (001) surface as well as UO_2 alone on the U_3Si_2 (110) and (111) surfaces. Formation of peroxo (O_2^{2-}) state confirmed the dissociation of molecular oxygen before U_3Si_2 oxidation. Core experimental analyses of the oxidized U_3Si_2 samples have revealed the formation of higher oxides from Raman spectroscopy and XRD techniques. This work is introduced to further a better understanding of the oxidation of U-Si metallic fuel compounds.

Keywords: *Uranium Silicide; Nuclear fuel; Oxidation; Oxides; Density Functional Theory.*

7.3. Introduction

Uranium silicides have attracted significant scientific interest in recent times owing to their potential as a replacement for uranium dioxide (UO_2) fuel in commercial light water reactors (LWRs), and by extension can be used in supercritical water reactors (SCWRs). Due to its high thermal conductivity which increases with temperature, high uranium density (11.3 g-U/cm^3) and irradiation behavior, uranium sequisilicide (U_3Si_2) has become a material of interest for generation *IV* nuclear reactors [10,13,51,53,56]. U-Si compounds and metallic fuels in general, however, easily get oxidized when in contact with oxygen and water, making them difficult to characterize [253].

Furthermore, as a nuclear fuel for commercial reactors, there is a minimum performance requirement in the presence of oxygen, water enriched environment, radiation and temperature. This has prompted the need to rigorously investigate the thermal properties and oxidation behavior of U_3Si_2 in water and oxygenated environment using both experimental and theoretical techniques.

Earlier investigations of the oxidation behavior of U_3Si_2 (alongside USi and U_3Si_5) between room temperature to 1000^{o}C reveals that UO_2 is preferentially formed [250] which inhibit the formation of a passivating SiO_2 layer that is expected to serve as protective barrier in the UN–U_3Si_2 composite [184]. This inference was reached based on thermodynamics argument and we posit further investigation of this behavior from atomistic perspective with the aim of providing fundamental understanding of oxidation of U_3Si_2 fuel material.

Previous theoretical calculations of the surface properties and compositions of actinide-bearing compounds have been focused extensively on UN, UO_2 and PuO_2 [294–298] According to a recent ATF-focused investigation (included U_3Si_2) by Johnson *et al*. [249], authors concluded that the oxidation of U_3Si_2 in air and water lead to formation of U_3O_8 and SiO. On further oxidation, SiO may be oxidized to SiO_2 which is relatively more stable compared to SiO.

There exist, however, limited studies aimed at unravelling the interactions of oxygen and water with U_3Si_2 surfaces. With the mechanism of early oxidation of U_3Si_2 surfaces yet to been established, this investigation is timely. Bo *et al.* [297] studied the adsorption and dissociation of H_2O on the (001) surface of uranium mononitride (UN) based on DFT+U calculations and *ab initio* thermodynamics. They also showed that the UN (001) surface reacts readily with water at ambient

temperature which leads to oxidation of the UN material. It was suggested that the water molecule dissociates into OH and H species via three pathways with small energy barriers. More recently, Tegner *et al.* [298] studied the adsorption of H_2O on (111), (110) and (100) surfaces of UO_2 and PuO_2, using DFT+U. They found a mix of molecular and dissociative water adsorption on (111) surface, while full dissociation is dominant on the (110) and (100) surfaces. In this paper, we experimentally establish the oxidation of U_3Si_2 in the presence of oxygen and have provided an atomistic insight into the mechanisms of the early oxidation of U_3Si_2 surfaces using Hubbard-corrected density-functional theory (DFT+U) calculations of the reactions of O_2 with the (110), (001) and (111)surfaces, considering both molecular and dissociative adsorption.

7.4. Experimental setup and Computational methodology

7.4.1 Characterization of U_3Si_2 samples: experimentation

The as-received U_3Si_2 sample was produced by arc melting of pure U metal and Si in an Argon environment at Los Alamos National Laboratory. The method of preparation, phase identification and micrographs are documented in a previous study [13]. The sample was oxidized by exposing the as-received sample to synthetic air (80% Nitrogen and 20% oxygen) at a flow rate of 100 standard cubic centimeters per minutes (sscm) at a heating rate of 10 ^oC/min to 1000 ^oC and held there for an hour for isothermal oxidation. The sample was then cooled at 20 ^oC/min. The oxidized sample was transferred into a capillary tube and sealed at both end in a glove box using paraffin wax before transfer to the Raman sample stage while the sample used for XRD phase ID was sealed with Kapton tape before mounting on XRD sample stage.

The as-received and oxidized matrices were then characterized by means of spectrochemical and surface microscopy. Raman spectroscopy was deployed in studying the functional chemistry between these samples using a Renishaw Raman InVia reflex microscope (Renishaw, UK). The Raman spectroscopic measurements for respective samples were conducted varying the acquisition time for improved signal-to-noise ratio. A 100% laser power was attenuated for each trial to avoid sample damage or change of phase; this was conducted at 16 complete scans by means of a 514 nm laser. A Bruker D8 Discover XRD Diffractometer operating with a Cr K (α) radiation was also used in probing their diffraction patterns with a Cr K (α) radiation source. Most XRD use Cu–K (α) as a radiation source, however the choice here is based on the equipment available in our laboratory. For both samples, the XRD spectra were collected between 10 to 100^o

and analyzed using Philips X'Pert software. Surface analysis of these powders was conducted using SEM (Hitachi SU6600 scanning electron microscope, Japan) at a 30 kV acceleration voltage.

7.4.2. Computational details

The first-principles calculations were performed within the plane-wave pseudo-potential DFT technique [109,110], as implemented in Quantum ESPRESSO code [143]. The exchange-correlation functional potential is described by the generalized gradient approximation (GGA) in the *Wu-Cohen* (GGA-WC) formulation [127]. All our calculations use the norm-conserving *Wu-Cohen* (WC) pseudopotentials where these potentials treat $6d^1\ 5f^3\ 7s^1$ as valence electrons for U and $3s^2\ 3p^6$ as valence electrons for Si.

Due to the onsite Coulomb repulsion among the localized U 5*f* electrons, we used the Hubbard (DFT+U) approximation to account for the strong electronic correlation effect [264]. We have employed and effective value (U_{eff}) of 1.5 eV as a recently first-principles study of U-Si system by Noordhoek *et al.* [64] show that the effect of metastable state in U_3Si_2 is quite small due to the fact that the enthalpy difference for a GGA+U calculations with $U_{eff} = 1.5$ eV for U_3Si_2 with and without the U-ramping method [299] is about 0.01 eV/atom. Other methods such as quasi-annealing [300] and occupation matrix control [301] have been employed by other investigators to tackle the metastable states difficulty associated with uranium oxides but are beyond the scope of the present study.

The Kohn-Sham one-electron states were expanded in a plane wave basis set up to 120 Ry while the Fermi surface effects were treated by the smearing technique of Methfessel-Paxton [230], using a smearing parameter of 0.02 Ry (0.27 eV). An energy threshold defining self-consistency of the electron density was set to 10^{-8} eV and a beta mixing factor of 0.3. Brillouin zone integration was done using $7 \times 7 \times 10$ and $5 \times 5 \times 1$ Monkhorst-Pack [143] k-point grids (centred at the Γ point) for the bulk U_3Si_2 and the surface models, respectively. Structural relaxation was carried out to minimize the energy using the conjugate gradient method within the Broyden-Fletcher-Goldfarb-Shanno (BFGS) algorithm [266], until the magnitude of the residual Hell-Feyman force on each relaxed atom reached 0.01 eV $Å^{-1}$. Visualization and analysis of the structures were perfomed using the VESTA program [231,232].

The bulk U_3Si_2 was modelled in the tetragonal structure as shown in Fig. 6.1 in the non-magnetic state as reported by Remischnig *et al.* [252]. An earlier DFT (GGA/PBE) calculation performed by Noordhoek *et al.* predicted a ferromagnetic phase [64], but here and in our previous study, we realized that using local density approximation (LDA) and generalized gradient approximation (GGA/WC) predict that the binding energy of U_3Si_2 with non-magnetic ordering is 1.13 eV (LDA) and 1.19 eV (GGA/WC) more stable than the ferromagnetic phase in agreement with experimental observation [252] and our earlier calculations [262] using CASTEP code and the same functional [263].

In order to narrow down the number of surfaces, we considered surfaces based on (i) surface compactness, (ii) Non polar surfaces, and (iii) surfaces where the ion coordination loss by creating the surface is minimized. Similar approaches have been adopted in the previous study of tetragonal ZrO_2 [302]. The different surface structures were created from the fully optimized bulk structure in order to eliminate the presence of fictitious forces during surface relaxation. Surfaces were created using the METADISE code [180], which not only considers periodicity in the plane direction but also provides the different atomic layer stacking resulting in a zero dipole moment perpendicular to the surface plane, as required for reliable and realistic surface calculations. METADISE code also considers condtion (i) and (iii) during surface cleavage. Surfaces which needs reconstruction are not considered in this work.

For each surface, 3 atomic layers with 30 atoms in each simulation cell were considered thick enough for surface energy calculations after testing convergence with 2, 3 and 4 atomic layers respectively. However, due to the thickness of the slabs in (112) and (102), 5 atomic layers with 50 atoms each were found to be sufficient to obtain converged surface energies for (112) and (102) slabs. A vacuum of size 15 Å was introduced to the surface models in the z-direction and found to be large enough to avoid any spurious interactions between the slabs. This was chosen after considering a vacuum of 10 and 12 Å respectively. The relative stabilities of the U_3Si_2 surfaces were determined using equation 3.69. The calculated unrelaxed and relaxed surface energies of the different low-Miller index U_3Si_2 surfaces are presented in Table 7.2.

The (001), (110) and (111) surfaces were modelled by slabs constructed as a 3-layer 2×1 supercell with 60 atoms per simulation cell. This choice was considered reasonable for this work after testing with 3-layer 2×2 slab containing 120 atoms and given the computational resources available. We

considered several unique geometric orientations for oxygen molecule adsorption for each surface in this work. The oxygen molecule was modelled in the spin triplet state for all the cases and was introduced to the surfaces in a vertical (end-on) or horizontal (side-on) orientation. The charge transfer between the O_2−U_3Si_2 systems was characterized using the Bader topological method [240].

7.5. Results and discussion

7.5.1. Bulk properties of U_3Si_2

U_3Si_2 is a tetragonal structure with space group of *P4/mbm* (127) and has ten atoms in the conventional unit cell (Fig. 6.1). From experimental measurement, the lattice parameters are $a = b = 7.33$ Å, c = 3.98 Å, $^{c}/_{a} = 0.543$; $\alpha = \beta = \gamma = 90$ [252]. There are two symmetrically distinct U sites occupying the 2*a* and 4*h* Wyckoff positions and the Si occupies the 4*g* site. The above reported experimental structural parameters were used as starting point for our DFT calculations.

Table 7.1 presents the calculated lattice parameters of U_3Si_2, with the DFT and the Hubbard-corrected DFT+U schemes. The calculated lattice parameters (*a*, *c*) and unit cell volumes (*v*) differ to various degree compared to previously reported theoretical data [63, 64]. The GGA result is comparable to previous GGA prediction [63] except that there is an underestimation of ~3% in the *c*. Whereas, our GGA with U=1.5 eV underestimate *a* and *c* by ~4% and ~3% respectively when compared to work by Noordhoek [64] where similar U value is used. In comparison to Wang *et al* [63] with U= 4.0 eV, our lattice *a* is overestimated by ~2% while *c* is underestimated by ~1%. Since a U value of 1.5 eV is used in this work, we compared our result with experimental data for U=1.5 eV. There is overall good agreement with an overestimation of ~1% in *a* while *c* is comparable. The *v* is underestimated by ~4% in comparison to the experimental data [252]. The difference between our result and previous DFT + U data might be due to the fact that a projected augmented wave (PAW) potential is used in previous studies while a GGA-WC pseudopotential is used here.

The electronic structure of U_3Si_2 was determined through analyses of the band structure and the projected density of states (PDOS) as shown in Fig. 7.1. It is evident from both the band structure and PDOS that U_3Si_2 is metallic with the energy band crossing the Fermi level. It can be seen in

the PDOS that the conduction band is composed of significant hybridization of the uranium 5*f* states with the silicon 2*p* states. The U atoms act as the charge carriers and the 5*f* electrons as conduction electrons as observed in the region around the Fermi energy which is predominantly the uranium *f* electrons. This is typical of the U-Si compounds as shown in the DFT calculations by Zhang *et al*. [290].

Table 7.1. Optimized structural parameters of U_3Si_2 with U_{eff} =1.5 eV using GGA/WC pseudopotential.

	This work			Literature		
	GGA+U			GGA+U [63,64]		
	GGA	U= 1.5 (4.0) eV	Expt.[252]	GGA [63]	U= 4.0 eV	U= 1.5 eV
a (Å)	7.17	7.21 (7.48)	7.3151	7.14	7.32	7.479
b (Å)	7.17	7.21 (7.48)	7.3151	7.14	7.32	7.479
c (Å)	3.79	3.86 (3.87)	3.8925	3.89	3.92	3.975
V($Å^3$)	194.94	200.66(216.53)	208.29	198.31	210.04	222.34

The nature of bonding is further elucidated qualitatively by electron density plot in Fig. 7.1b which shows the formation of covalent bond between adjacent Si atoms, while the U-Si atoms form ionic bond evidence by the lack of diffuse electron density between neighboring U-Si atoms.

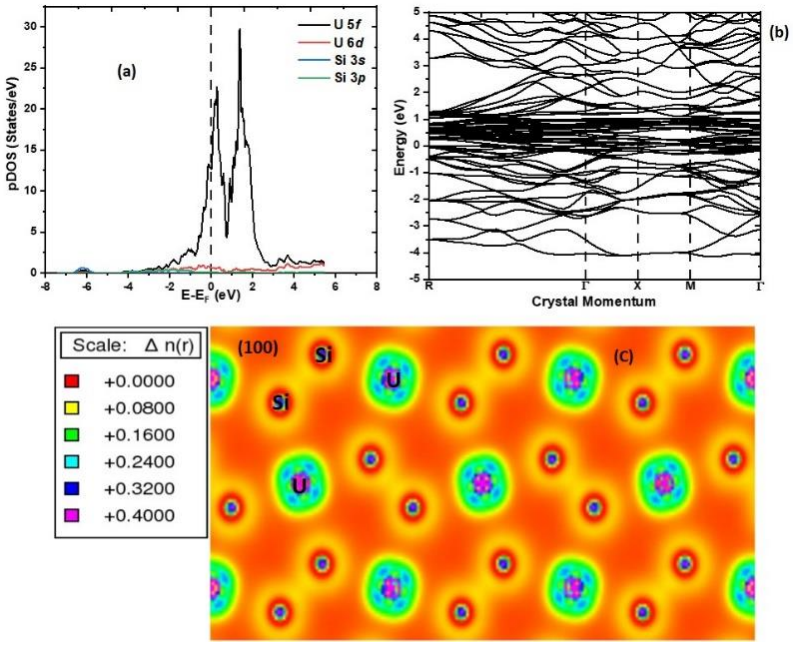

Fig. 7.1. (a) Partial density of state (b) Band structure and (c) Electron density map in the (100) of bulk U_3Si_2.

The result of band structure calculation along the highly symmetric points in the Brillouin zone (Fig. 7.1c) reveals several dispersive bands mainly from the U 5*f* cross the Fermi level, especially along the R–Γ direction. The Fermi energy is set at 0 eV as indicated by the horizontal line. There is also appreciable band overlap between valence and conduction states, which is responsible for the metallic nature of U_3Si_2 and the significant amount of electrons at the Fermi level, $N(E_F)$ implies that the high electronic contribution to the heat capacity and thermal conductivity of U_3Si_2 is mainly due to the U 5*f* state.

7.5.2. Evidence of Oxidation

7.5.2.1. Chemistry of samples and morphology

The Raman spectra of the pure and oxidized U_3Si_2 samples depicted in Fig. 7.2a were collected with the aid of ×5 and ×50 long-focus objectives designed for 785 nm lasers. Distinct peaks related to a possible *v*(USi) stretching vibration within U_3Si_2 can be observed at 1591 cm^{-1} while uranyl symmetric and antisymmetric stretching bands are represented at 827 and 479 cm^{-1} [303]. The Raman band at 459 cm^{-1} broadens, and this may be attributed to increased local disorder. These low intensity $v(UO_2)^{2+}$ type band could be linked with oxidative changes occurring within the bulk of the sample upon storage or exposure to the atmosphere. Similar vibration bands are also observed on the Raman spectrum of the oxidative product, and the difference in peak patterns between both two systems is suggestive of thermal oxidation [304]. The reported UO_2 must have been due to the formation of thin adsorbed oxide film on the sample during transfer from the custody of the University of Saskatchewan's radiation safety office (The radiation officer weighed sample in a fume cupboard).

Upon oxidation, new Raman peaks are formed between 800 and 1500 cm^{-1}. The bands around 1157 cm^{-1} are some of the defining Raman peaks characteristic of an oxidized sample. According to Rao *et al.* [305], this assignment is attributed to a second-order longitudinal optic (2LO) phonon, being an evidence of oxidation. Driscoll *et al.* [303] have also opined that low intensity Raman bands between 390 and 480 cm^{-1} are related to silicate antisymmetric bending vibrations.

To complement the results from Raman spectroscopy, we also conducted XRD studies of these samples. As displayed in Fig. 7.2b, the XRD patterns reveal some unique features and data fitting offered a reliable error estimation between both systems owing to their varying chemical environments. As expected of pure U_3Si_2, there are diffraction peaks for U_3Si_2 at (110), (111) and

(211) amongst others while the (102) correspond to the USi peak. The (311) peak is for UO_2 which must be due to exposure to air during the transfer at the radiation safety office, at the University of Saskatchewan. This is consistent with the reported Raman vibrational peak for UO_2. Hence the difference in the XRD data reported here and the previous work by Remischnig *et al.* [252].

The XRD pattern of the oxidized sample reveals some diffraction patterns due to the formation of oxide phases. According to Rousseau *et al.* [306], the observed asymmetric diffraction broadening peak at (200) is indicative of a higher oxide. The authors have reported tetragonal a phase associated with U_3O_7. Upon fitting with Rietveld refinement, Gracia *et al.* [307] have attributed the inability to reconcile some of the X-ray diffracted peaks to the preferential orientation and granulometry, and the arrangement of U_3Si_2 atoms. Specifically, the (200) and (311) peaks correspond to UO_2 while (702) and (880) are peaks which correspond to U_3O_8 and U_4O_9 respectively. The U_3Si_2 phase is not completely wiped out as evident by the (111) peak.

The surface analysis of the pure U_3Si_2 powders was also conducted using SEM, and Fig. 7.3 represents the microstructure and elemental composition of the compound. As observed, Fig. 7.3a is an uneven surface with intermittent grooves enriched with powdered amorphous granules of a secondary USi phase (see inset). From our experience, the development of this second phase as depicted in Fig. 7.3b is a consequence of choice powder metallurgy technique deployed in synthesis as discussed in the experimental methodology section. White *et al.* [13] have observed a similar trend upon synthesizing U_3Si_2 from pure U and Si; authors also reported significant Si loss due to arc melting-induced volatilization. The formation of new phases of secondary products is also promoted by the inability to control reaction conditions, not limited to temperature, during synthesis.

According to White *et al.* [15], this unique behavior could be further explained by monitoring the phase transformations at various temperatures as represented in a typical U-Si partial phase diagram in Okamoto's work [308]. For Garcia *et al.* [307], product matrix from common synthetic routes comprise of two crystalline regular phases (U_3Si_2 and USi) within the same sample with entirely different irradiation behaviors.

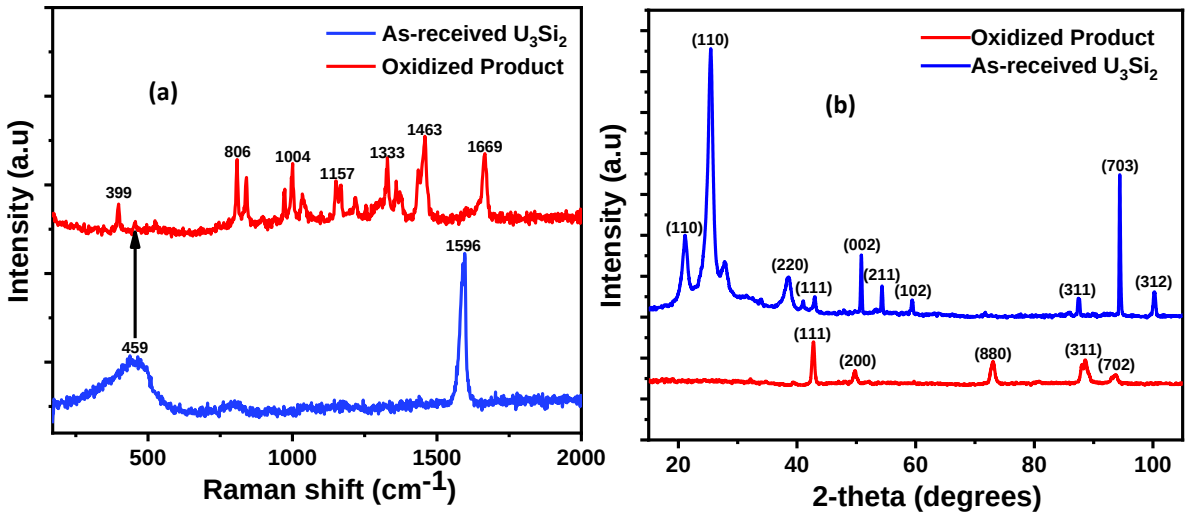

Fig. 7.2. Representative (a) Raman and (b) XRD spectra of pure U_3Si_2 and its oxidized form.

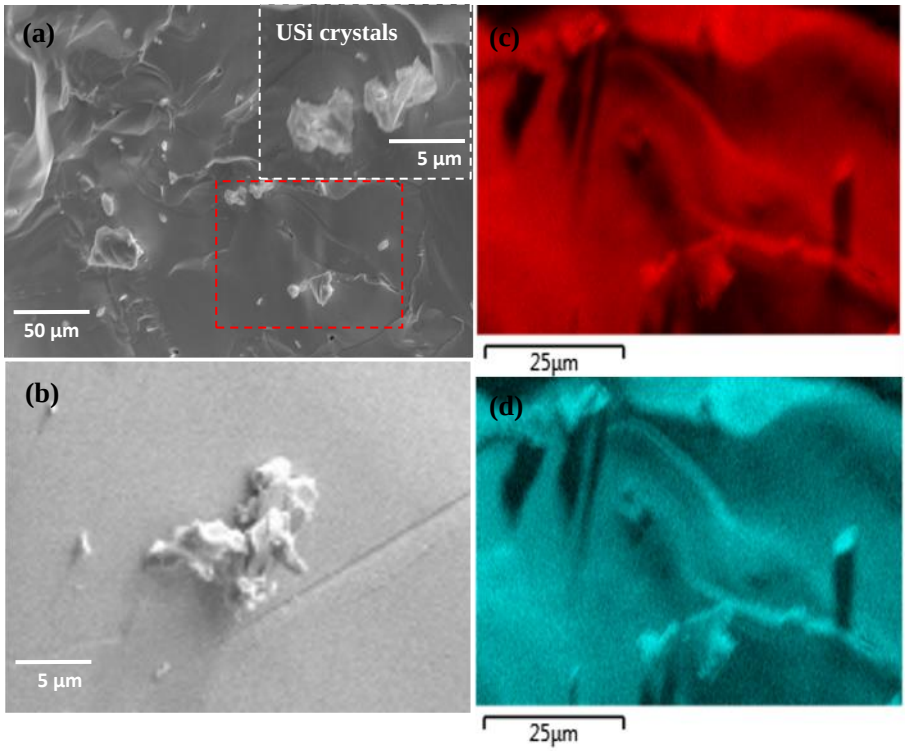

Fig. 7.3. SEM micrograph showing the pure U_3Si_2 sample obtained from the bright field imaging mode (a); the powdered granule develops a secondary USi phase as observed in the grains displayed in (a) inset as well as (b); the elemental U Mα1 (80%) and Si Kα1 (15%) maps from energy dispersive x-ray (EDX) are presented in (c) and (d), respectively. The area where EDX scan was taken is highlighted in red region on the SEM image (a).

7.5.3. *Ab initio* surface characterization

Prior to studying the adsorption and surface reaction of oxygen, we have characterized the structure and relative stabilities of the (001), (100), (110), (011), (101), (111), (102), and (112) surfaces which are commonly observed low crystallographic planes in tetragonal structures. It must be noted that (010) plane is not considered separately as it is equivalent to the (100) plane. Fig. 7.4 presents the optimized structures of the clean surfaces of U_3Si_2, whereas Table 7.2 summarizes the calculated surface energies of the surfaces. The surface energies of the clean (110), (100), (101), (001), (112), (111), (011) and (102) surfaces are calculated at 2.57, 2.76, 2.80, 2.82, 2.84, 2.97, 3.08, and 3.15 J/m^2 respectively, which implies that the order of decreasing stability of the U_3Si_2 surfaces is (110) > (100) > (101) > (001) > (112) > (111) > (011) > (102). Using the calculated surface energies, we constructed the thermodynamic crystal morphology of U_3Si_2.

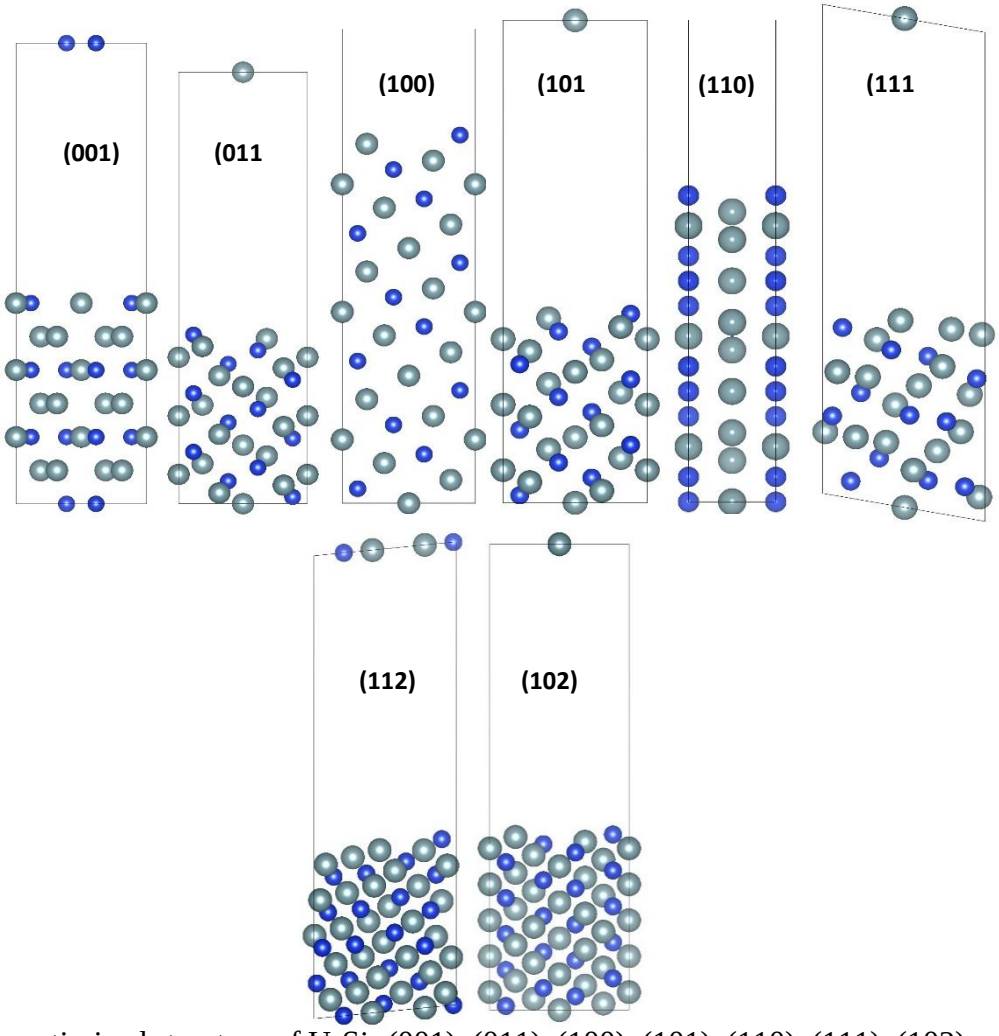

Fig. 7.4. The optimized structure of U_3Si_2 (001), (011), (100), (101), (110), (111), (102) and (112) surface slabs.

Table 7.2. Calculated surface energies of pristine (γ) U_3Si_2 low miller index surfaces.

Surface	(110)	(100)	(101)	(001)	(112)	(111)	(011)	(102)
γ (Jm^{-2})	2.57	2.76	2.80	2.82	2.84	2.97	3.19	3.08

The equilibrium morphologies of the U_3Si_2 crystal was constructed according to Wulff's theorem, which states that a polar plot of surface energy versus the orientation of normal vectors would give the crystal morphology based on the approach of Gibbs [308]. The calculated morphology of U_3Si_2 in Fig. 7.5 shows facets of clean U_3Si_2 crystal. It must be noted that because of the small difference in the surface energies of (101) and (001), they are expressed in the same facet of the morphology just like the (102) and (011).

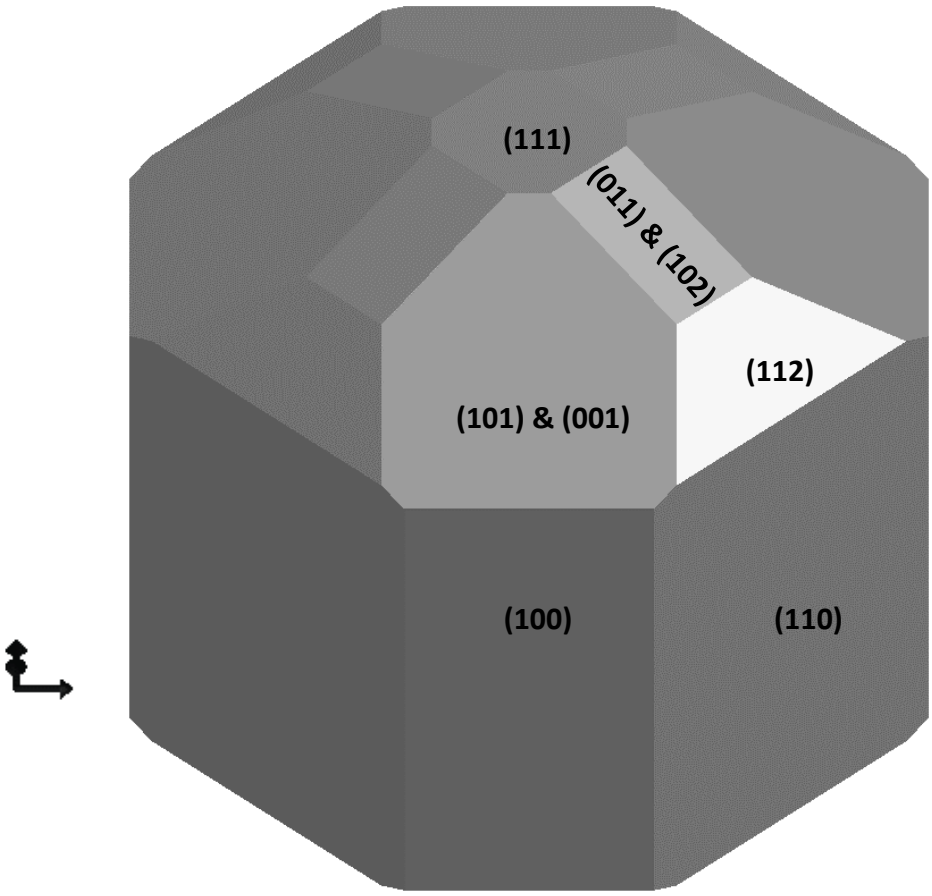

Fig. 7.5. Wulff construction of the equilibrium crystal morphology of U_3Si_2.

As commonly observed at materials surfaces, geometry relaxation of the U_3Si_2 surfaces slightly altered the positions of surface atoms and therefore their interlayer spacing, which is characterized using the relation:

$$\Delta d_{ij} = \frac{(d_{ij} - d_{bulk})}{d_{bulk}} \times 100\%, \quad (7.1)$$

where negative values imply inward relaxation (contraction), while positive values denote outward relaxation (expansion) of the interlayer spacing. When a crystal is cut to expose a surface, the charge density is redistributed at the surface such that the charge is moved from the regions directly above the atom cores to the regions between the atoms [309]. This accounts for the adjustments in the interlayer spacing perpendicular to the surface and there is no change in the periodicity parallel to the surface nor symmetry of the surface [310]. The extent of interlayer relaxation is small on the topmost layer of the (001), (011) and (111) surfaces compared to the (110), (100), (101), (102) and (112) surfaces as presented in Table 7.3.

Table 7.3. Surface relaxation of the unreconstructed clean surface of U_3Si_2.

d_{ij}/surface	(001)	(110)	(111)	(100)	(101)	(011)	(112)	(102)
d_{12}	+2.27	–24.90	–0.12	+16.90	+7.17	–2.99	+7.39	+4.65
d_{23}	+0.93	–0.52	–0.61	+15.85	+3.65	–1.03	+3.90	+2.28
d_{34}	+0.19	–0.08	–0.04	+10.31	+0.35	–0.77	+2.52	+3.51
d_{45}	–2.25	+22.20	–30.52	+9.59	+0.26	–0.52	+0.18	+2.40

7.5.4. Oxygen adsorption

The adsorption of oxygen molecule on the U_3Si_2 surfaces is an important starting step towards understanding its early oxidation mechanisms. The first interest of this study is therefore to determine the lowest-energy adsorption structures and modes of oxygen on some of the low-index U_3Si_2 (001), (110) and (111) surfaces, and to characterize the strength of their interaction and the extent of O-O bond elongation.

Different O_2 initial adsorption possibilities, including side-on and end-on configurations, have been subjected to geometry optimization until the residual forces on all atoms were ≤ 0.03 eV/Å. The adsorption energy (E_{ads}), which is a measure of the strength of the O_2–U_3Si_2 interactions, is calculated using equation 3.70. By the definition of E_{ads} in equation 3.70, a negative value of E_{ads} indicates an exothermic and stable adsorption, whereas a positive value indicates unstable adsorption.

7.5.4.1. Adsorption of molecular and dissociated oxygen on U_3Si_2 (001) surface

For the adsorption of molecular oxygen on the U_3Si_2 (001)-U-Si terminated surface, we have considered two adsorption modes; the end-on type, where O_2 vertically binds to the surface atom,

and a side-on type, where O_2 binds parallel to the surface atom. Fig. 7.6 presents the optimized adsorption structures of molecular and dissociative O_2 adsorption at various high symmetry sites on the U_3Si_2 (001)-U-Si terminated surface. The calculated adsorption energies, interatomic bond distances and average Bader charge are presented in Table 7.4. Generally, we found that the U sites are more active toward O_2 adsorption than the Si sites as reflected in the stronger adsorption energies calculated for the U sites.

For the adsorption of molecular oxygen on the U_3Si_2 (001) surface, the strongest and the most stable adsorption configuration is calculated for the side-on U-Si bridge (**M2**) adsorption with an adsorption energy of –3.80 eV, compared to –3.29 eV for the side-on top-U site (**M6**) adsorption and –3.52 eV for the head-on top-U site (**M4**) adsorption. In the lowest-energy molecular O_2 structure (**M2**), the Si-O and U-O bond lengths are calculated at 1.720 and 2.221 Å, respectively, whereas for the **M1** adsorption mode, the Si-O bonds are converged at 1.697 and 1.662 Å, respectively with energy of –2.86 eV. Given that bond distances are characteristics of a compound [311], suggests the formation of mixed oxides of uranium and silicon in the **M2** configuration since the bond distances are in close agreement with experimental and DFT predicted bond distance of 1.618 Å [312] for Si-O bonds in Si-O oxides and 1.989-2.12 Å [313–316] for U-O bonds in UO_2 and U_3O_8. This is consistent with Bader charge analyses which reveal a charge transfer from surface U and Si ions to the O atoms. Consequently, the O bonds become stretched compared to the free gas phase bond distance of 1.21 Å.

Formation of intermediate oxides starting with UO_2 which subsequently oxidizes to U_3O_7/U_4O_9 and terminates at U_3O_8 has been proposed recently by two independent work which is reflected in the range of U-O bond distances calculated in this study [249,250]. The unusual formation of Si-O bonds here are due to the difference in electronegativity of Si (1.887) and O (3.758) [317], hence O draws charges from Si as shown by the –1.73 e drawn by O species coupled with the unique topology (atomic arrangement) of the (001)-U-Si surface termination. A closer look at the (001)-U-Si surface showed that some of uranium atoms are ~2.8–2.9 Å lower in comparison to the Si atoms for a given atomic layer. This makes it possible for Si to react with O atoms.

It interesting to note that the formation of SiO_2 is desirable on U_3Si_2 surface as it forms a passivation layer that can prevent further oxidation. This reaction is thermodynamically unfavorable compared to UO_2 formation in bulk U_3Si_2 experimentally [250]. However, in our

calculation, Si-O bonds are formed in the **M1**, **M3** and **D2** configurations of the U_3Si_2 (001)-U-Si surface termination which corresponds to Si-O bond lengths in oxides of silicon [312].

Furthermore, orientation of the oxygen molecule also plays an important role in the formation of the mixed oxides. It is well known that the exposure of certain crystal planes play an important role in determining the surface dependent properties of materials. This understanding has led to the synthesis of high index (311) CuO_2 crystals with enhanced catalytic property in the oxidation of CO. Also, crystal and morphology controlled γ-Fe_2O_3 has been prepared with reactive (110) and (100) planes that favors catalytic reduction of NO with NH_3 [318–320].

In the molecular adsorption of oxygen at U sites, the adsorption energies for the side-on (**M6**) and head-on (**M4**) configurations are calculated at –3.29 eV and –3.52 eV, respectively which implied that the formation of UO_2 is more feasible compared to SiO_2 especially when the **M5** configuration is compared where the two Si-O bond are calculated at 1.829 and 1.932 Å with an adsorption energy of –1.97 eV. The two U-O bonds in the **M6** structure are 2.023 and 2.023 Å, whereas in the **M4** structure is calculated at 2.213 Å. This thermodynamically suggest the possibility formation of U-O type oxides on the (001) surface which has been established in previous work and support the results from XRD and Raman spectroscopy presented in this work.

The least stable molecular O_2 structure is calculated for the case in which the O_2 adsorbed at Si-Si Bridge sites (**M3**), which released adsorption energy of –0.50 eV, with the Si-O bond distance converged at 1.590 Å as shown in Table 7.4. In molecularly adsorbed O_2 at the U_3Si_2 (001) surface, we observe elongation of the O-O bond lengths (1.392−1.669 Å), which can be attributed to the significant charge gained by the O_2 molecule upon adsorption as shown in Table 7.4. The elongated O-O bonds in the adsorbed O_2, especially in the **M2** and **M6** structures, suggest that these molecular states are likely precursors for O_2 dissociation.

We have therefore determined the energetics of the dissociative adsorption of oxygen on the U_3Si_2 (001) surface as shown in Fig. 7.6 (**D1**−**D3**). The lowest-energy dissociative O_2 adsorption structure is obtained for case in which the dissociated O atoms are adsorbed at adjacent Si sites, with adsorption energy of –4.87 eV and the average Si-O bond distance at 1.629 Å. Similar adsorption energy (–4.63 eV) was calculated for the case in which one of the dissociated O atoms is adsorbed at Si site (Si-O =1.808 Å) and the other at U site (U-O =1.960 Å).

Compared to the lowest-energy molecular adsorption structure (**M1**), both dissociated **D1** and **D2** structures are thermodynamically more stable, suggesting that on the U_3Si_2 (001) surface, oxygen may exist preferentially in a dissociative state at Si sites. When the dissociated O atoms are adsorbed at distance U sites, the least dissociative adsorption energy of –1.39 eV was released. The weaker adsorption of the atomic oxygen species at the U sites compared to the Si sites, here suggest that the Si sites are active towards dissociated oxygen adsorption.

During the dissociative adsorption of O_2 at the U_3Si_2 (001) surface is characterized by significant charge transfer from the interacting surface species into the partially filled π^*_{2p} and unfilled σ^*_{2p} orbitals respectively as shown by the electronic density of states of the adsorbed oxygen compared to an isolated oxygen molecule. This is further discussed with supporting data in section 7.5.5 where oxygen molecule before and after adsorption on the surfaces is presented. This also corroborated by the partial density of states plot in Fig. 7.11 where there is hybridization of surface U 5*f* and O 2*p*. This is not surprising because, experimental work by Sooby-Wood *et al.* opined the possibility of an SiO_2 phase formation that is either too small to detect by SEM or as an amorphous phase undetectable by XRD [250].

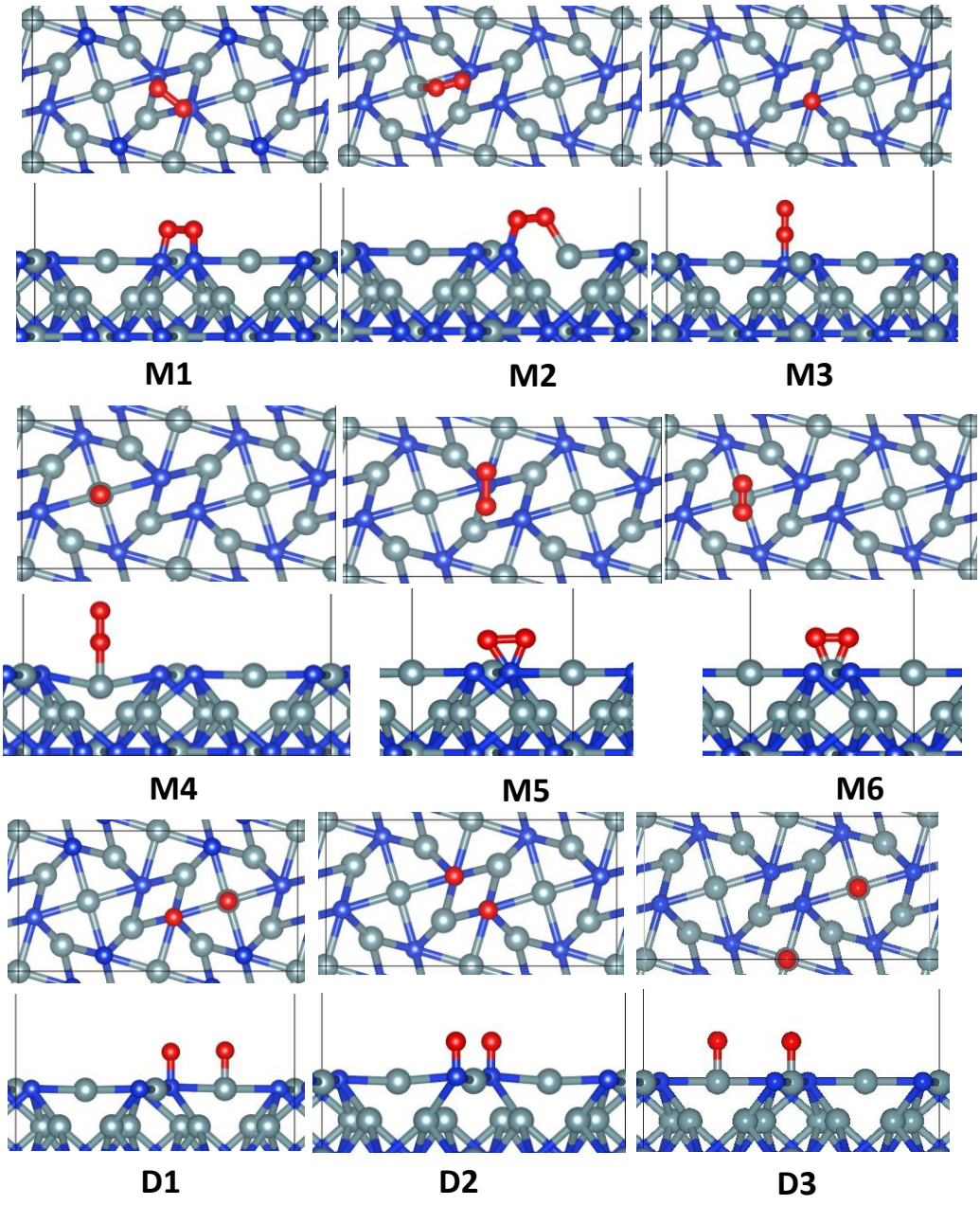

Fig. 7.6. Top and side views of the relaxed adsorption structures of molecular oxygen adsorbed at Si-bridge sites (**M1**), U-Si bridge sites (**M2**), head-on at top Si site (**M3**), head-on at top U site (**M4**), side-on at top-Si site (**M5**), and side-on at top-U site (**M6**); dissociated oxygen at adjacent top U-Si sites (**D1**), at adjacent top-Si sites (**D2**), and at adjacent top-U sites (**D3**) respectively, on U_3Si_2(001)-Si terminated surface. (Color scheme: U = grey, Si = blue, and O = red).

To ascertain whether the (001) surface will favor Si-O oxides formation over oxides of uranium irrespective of the termination, we have further investigated the adsorption properties of O_2 on an alternative surface model of the (001) which exposes only uranium atoms in the topmost layer as shown in Fig. 7.7. The molecular end-on (**M1**) and side-on (**M2**) configurations released

adsorption energies of –0.80 and –3.64 eV, respectively, whereas the dissociative adsorption at adjacent U ion sites (**D1**) released an adsorption energy of –4.56 eV, Table 7.4. When compared to similar adsorption configurations on the U-Si terminated (001) surface, we note that the side-on O_2 configuration is 0.35 eV more stable on the U-terminated (001) surface than on the U-Si-terminated surface (Fig. 7.6 (**M6**)). The dissociative adsorption mode is also found to be highly stable on U-terminated surface (–4.56 eV) compared to the U-Si-terminated surface (–1.37 eV), which suggest that the (001)-U termination is more reactive that the (001)-Si-U-termination.

The calculated U-O bond distances (Table 7.4) compare closely with previous experimental [313,315] and DFT [316] studies, which suggest the formation of oxides of uranium. When compared to the Si adsorption sites on the (001)-U-Si-terminated surface, we also found that both calculated molecular side-on O_2 configurations (Fig. 7.6 (**M1** & **M5**)) are less favored compared to O_2 side-on adsorption at U sites on both U-Si and U terminations.

Dissociative O_2 adsorption at Si sites on the U-Si termination is however, 0.31 eV more stable than at U sites on the U terminated surface. The thermodynamic favorability of molecular O_2 at the U sites and dissociative O_2 at Si sites suggests the possibility of a mixed oxide formation (oxides of uranium and silicon).

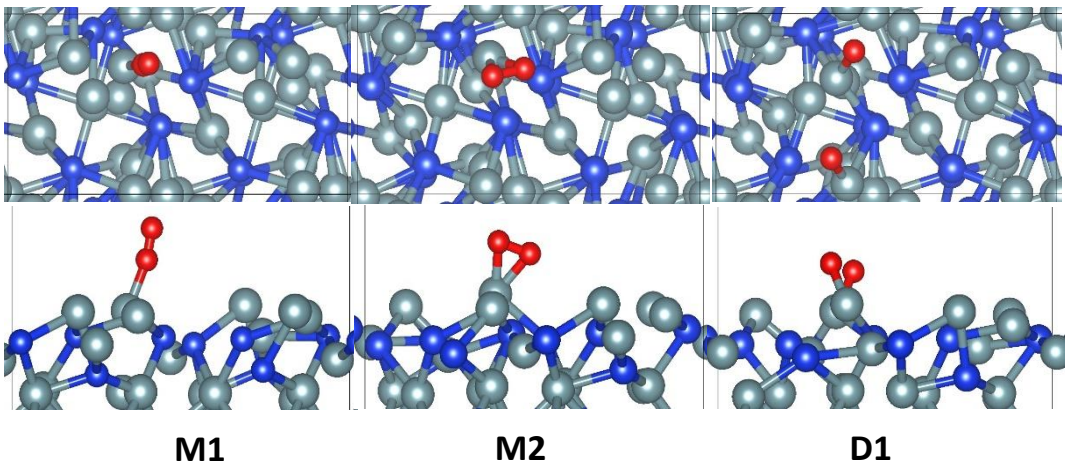

Fig. 7.7. Top and side views of the relaxed adsorption structures of molecular oxygen adsorbed at head-on at top U site (**M1**), and side-on at top-U site (**M2**); dissociated oxygen at adjacent top U-U sites (**D1**), on U_3Si_2(001)-U terminated surface. (Color scheme: U= grey, Si= blue, and O= red).

Table 7.4. Calculated adsorption energy (E_{ads}), relevant bond distance (d), of molecular (O_2) and dissociated (O--O) oxygen on the (001), (110) and (111) surfaces of U_3Si_2.

Surface	Adsorbate	Config.	E_{ads}/eV	d (O-O)/Å	d (Si-O1)/Å	d (Si-O2)/Å	d (U-O1)/Å	d (U-O2)/Å	Δq/e
(001)-U-Si termination	O_2	**M1**	–2.86	1.639	1.697	1.662			–1.00
		M2	–3.80	1.396	1.720		2.221	–	–2.49
		M3	–0.50	1.392	1.590		–	–	–1.62
		M4	–3.52	1.564	–	–	2.213	–	–1.48
		M5	–1.97	1.669	1.829	1.932		–	–0.85
		M6	–3.29	1.414	–	–	2.023	2.023	–2.02
	O--O	**D1**	–4.63	–	1.808	–	1.960	–	–1.60
		D2	–4.87	–	1.615	1.643	–	–	–2.18
		D3	–1.39	–	–	–	1.978	1.977	–0.75
(001)- U termination	O_2	**M1**	–0.80	1.294	–	–	2.226	–	–1.61
		M2	–3.64	1.446	–	–	2.243	2.224	–2.86
	O--O	**D1**	–4.56	–	–	–	2.126	2.080	–1.73
(110)- U-Si termination	O_2	**M1**	–2.26	1.508	2.152	2.105	–	–	–1.73
		M2	–2.36	1.662	–	–	2.310	2.356	–1.50
		M3	–0.35	1.290	1.612	–	–	–	–1.31
		M4	–0.68	1.500	–	–	2.691	–	–1.50
	O--O	**D1**	–3.53						–0.68
		D2	–3.37	–	1.517	1.542	–	–	–0.52
		D3	–3.73	–	–	–	2.404	2.313	–2.84
(111)- U termination	O_2	**M1**	–2.73	1.548	–	–	2.465	2.805	–2.14
	O--O	**D1**	–5.06	–	–	–	2.193	2.238	–1.25
		D2	–4.11	–			1.932	1.952	–2.10

7.5.4.2. Adsorption of molecular and dissociated oxygen on U_3Si_2 (110) surface

As with the U_3Si_2 (001) surface, we have also explored different adsorption sites and binding configurations for O_2 on the U_3Si_2 (110) surface in order to determine the lowest-energy adsorption structures. Fig. 7.8 depicts the lowest-energy adsorption configuration identified, whereas the calculated adsorption energies, the optimized bond distances and Bader charges for adsorbed species are reported in Table 4. Compared to the U_3Si_2 (001) surface, molecular oxygen adsorbed side-on at top-U site (**M2**) on the U_3Si_2 (110) surface is observed to bind 0.237 eV more strongly than the side-on adsorption at top-Si site (**M1**). This is consistent with the preferred formation of U-O compared to Si-O bond due to the ease of transfer of electrons from a metallic system to the oxygen molecule.

It is interesting to note that, when adsorbed at the U-bridge sites (**D3**), molecular oxygen spontaneously dissociates into atomic species, with an exothermic adsorption energy of –3.73 eV. The U-O interatomic bond distances are calculated at 2.404 and 2.313 Å, both of which are close to the U-O bond distance of 2.544 Å observed from experimental measurements in UO_2 [321]. A total of –2.84 e was transferred from the U to the dissociated O species. The adsorption energies of the head-on binding mode at top Si site (**M3**), and the side-on mode at top-U site (**M4**) are calculated at –0.352 and –0.677 eV respectively, with charge transfer of –1.50 e from the U atom and –1.31e from the Si atom, suggestive of stronger U-O bond than Si-O bond as has been observed experimentally [250].

At the U_3Si_2 (110) surface, the O-O bond of the adsorbed O_2 molecule becomes generally elongated ranging between 1.290–1.662 Å which on the average is similar to a peroxo (O_2^{-2}) species with bond length of 1.40–1.60 Å, suggesting the formation of peroxo-like (O_2^{-2}) precursor when molecular oxygen is adsorbed on the U_3Si_2 (110) surface. The peroxo is often referred to as a precursors for dissociation [322], hence the population of this state of oxygen accounts for the rapid dissociation of molecular oxygen on the (110) surface. The significant charge gained by the O_2 molecule upon adsorption, which is characterized by the peroxo (O_2^{-2}) account for the elongation of the O-O bond lengths reported here.

Dissociative adsorption of oxygen on the U_3Si_2 (110) is found to be highly exothermic for the two adsorption sites; at adjacent top U-Si sites (**D1**), and at adjacent top-Si sites (**D2**) respectively, with energies of -3.37 and -3.53 eV, respectively. This suggest that oxidation by dissociated oxygen species is generally more stable than molecular oxygen. Similar dissociation mechanism has been observed on a number of transition metal surfaces before their oxidation. Examples include Pt (111), Pd (111), Ni (111), Ag (110) and Cu (110) [323] as well as on actinide surfaces such as on actinide metal surfaces such as ϒ-U (100) [324], and Pu (100) [325].

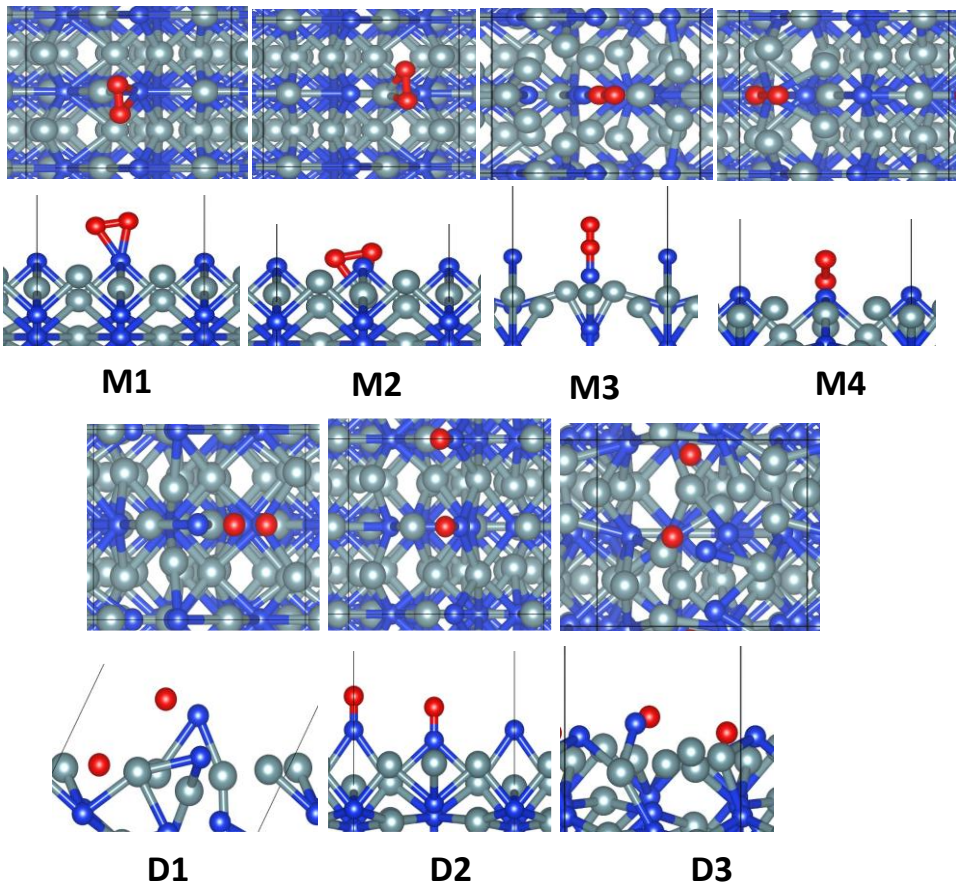

Fig. 7.8. Top and side views of the relaxed adsorption structures of molecular oxygen adsorbed side-on at top-Si site (**M1**), side-on at top-U site (**M2**), head-on at top Si site (**M3**), and side-on at top-U site (**M4**); dissociated oxygen at adjacent top U-Si sites (**D1**), at adjacent top-Si sites (**D2**), and at U-bridge sites (**D3**), respectively, on U_3Si_2(110)-U-Si terminated surface. (Color scheme: U = grey, Si = blue, and O = red).

7.5.4.3. Adsorption of molecular and dissociated oxygen on U_3Si_2 (111) surface

Again, we have explored several possible sites and modes of adsorption of O_2 on the U_3Si_2 (111) surface as shown in Fig. 7.9. Table 7.6 presents the calculated adsorption energies, bond lengths and charge transfers. Molecular adsorption of O_2 at top-U site in a side-on configuration (Fig. 7.9 (**M1**)), released an adsorption energy of –2.73 eV. The O-O bond is calculated at 1.548 Å compared to 1.214 Å for the gas phase oxygen molecule, indicating significant elongation upon adsorption. The dissociative adsorption structures of O_2 (Fig. 7.9 (**D1** and **D2)**) were calculated to be considerably more stable than the molecular adsorption structure Fig. 7.9 (**M1**). When dissociated at adjacent top U-sites (Fig. 7.9 (**D1**)), the adsorption energy is calculated at –4.12 eV, whereas when the dissociated species adsorb at distant U-sites (Fig. 7.9 (**D2**), the adsorption energy is -5.06 eV.

The dissociated O ions, which adsorb preferentially at top-U site (Fig. 7.9, **D1** and **D2**), draw a combined charge of –1.25 e and –2.10 e respectively from the interacting surface U ions, resulting in their significant oxidation, with the U ions becoming more positively charged compared to the bare U atoms. Similar adsorption features has been observed in the AnO_2 (An=U, Pu and Am) type oxides where An-O bonds are preferentially formed compared to An-OH when H_2O dissociates on the surfaces [295].

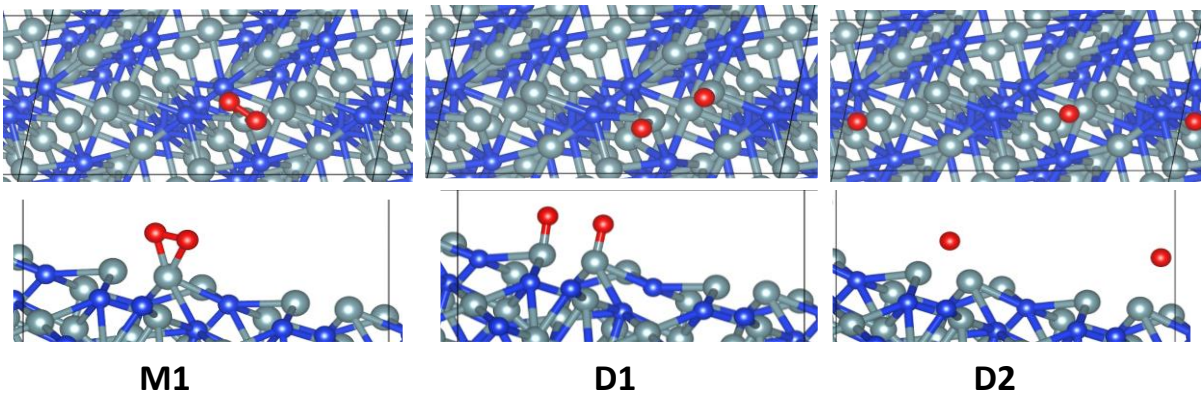

Fig. 7.9. Top and side views of the relaxed adsorption structures of molecular oxygen adsorbed side-on at top-U site (**M1**) dissociated oxygen at adjacent top U-Si sites (**D1**), side-on at top-Si site (**D2**); on U_3Si_2(111)- terminated surface. (Color scheme: U = grey, Si = blue, and O = red).

7.5.5. Electronic structures

Insight into the extent of oxidation of the U_3Si_2 surfaces was further explored by calculating and analyzing the density of states (DOS) projected on the oxygen, silicon and uranium atoms in the first layer of the U_3Si_2 surfaces. The density of states (DOS) of a structure indicates the number of states at each energy level which is available to be occupied and the DOS at the Fermi energy level (E_F) quantitatively gives the amount of electrons $N(E_F)$ available for bond formation in a reaction [326].

The PDOS of the clean U_3Si_2 (001), (110) and (111) surfaces (before O_2 adsorption), with projection on the U *f*-states and Si *p*-states are shown in Fig. 7.10. The U *f*-states significantly contribute to the DOS around the Fermi level of the three low-index surfaces studied, with only small contribution from the Si *p* states at the Fermi level. The contribution of the U *f*-states at the Fermi level increases in the order (110) < (001) < (111), which explains why more electrons were transferred from the (111) surface to the oxygen molecule compared to the (001) and (110) surfaces.

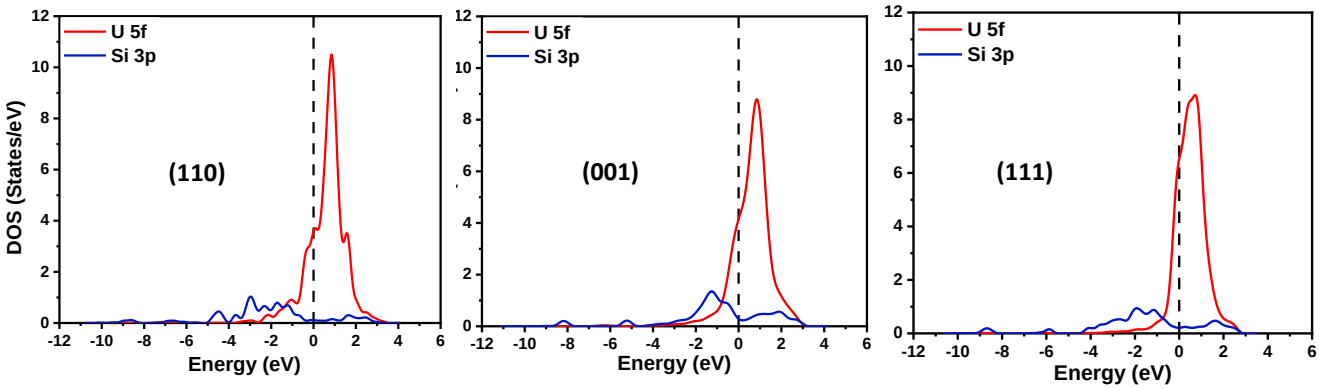

Fig. 7.10. Electron density of states of U_3Si_2 (110), U_3Si_2 (001) and U_3Si_2 (111) naked surfaces projected on the U-*f* and Si-*p* states. Electron density of the U-f states at the Fermi level for the different surface increases in the order (110) < (001) < (111).

For the U_3Si_2-O_2 surfaces, we have investigated the nature of their interactions with the oxygen molecule by analyzing the PDOS of the interacting U *f*-states and Si *p*-states as shown in Fig. 7.11. We observed hybridization between the U 5*f* and O 2*p* states, which is an indication of electron transfer from the interacting U ions to the adsorbed oxygen. This chemical change is confirmed by the electron transfer from the U species to the O ions as evident in the calculated Bader charges.

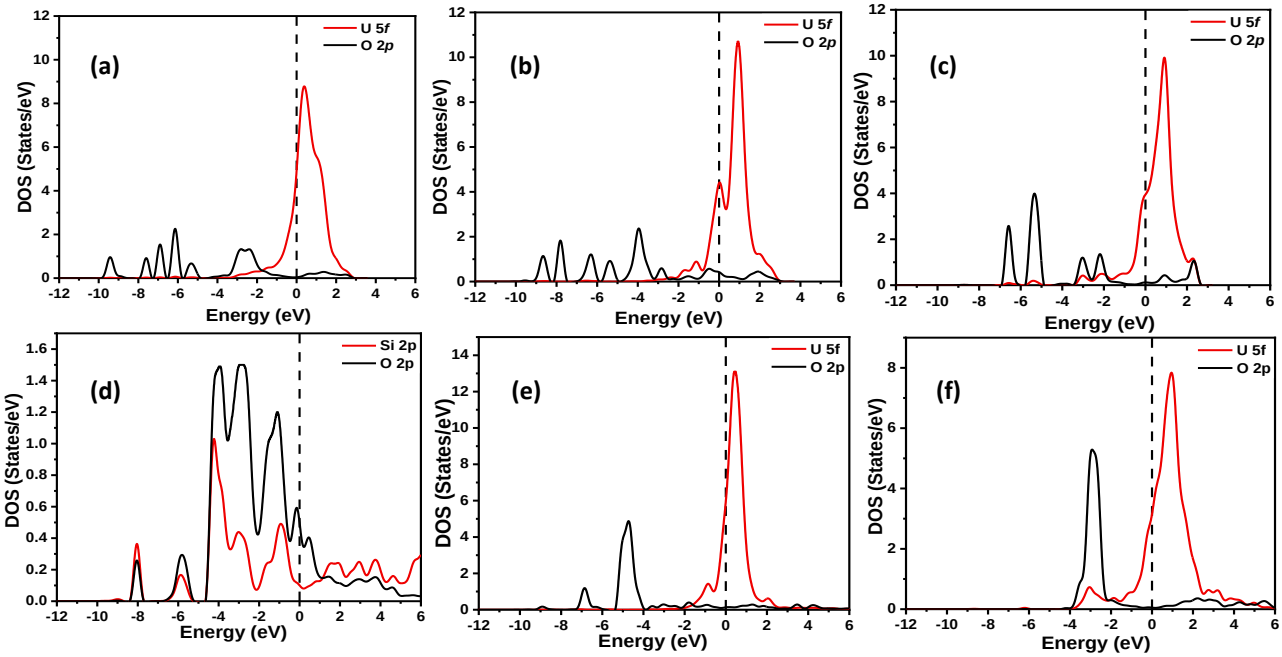

Fig. 7.11. Partial DOS projected on the interacting surface U *f*-states and O *p*-states for adsorbed molecular oxygen for (a) (001) (b) (110) and (c) (111) and adsorbed atomic oxygen for (d) (001) (e) (110) and (f) (111) surfaces respectively.

Even though electrons are transferred to the O 2*p* orbital as shown by Fig. 7.11, further analysis of the total DOS of the oxygen molecule in the adsorbed state at the various surface and compared to the gas phase molecule show specific orbital where electrons are transferred during the reactions (Fig. 7.12). The DOS for the gas-phase O_2 molecule is shown in Fig. 7.12a where the molecular orbitals are labelled as π_{2p}, σ_{2p} π^*_{2p} and σ^*_{2p} respectively, while those for the lowest-energy adsorption configurations at the O_2-U_3Si_2 (001), (110), and (111) interfaces are shown in Fig. 7.12 (b, c, and d) where the spin-polarized DOS projected onto the O-O bond has change considerably.

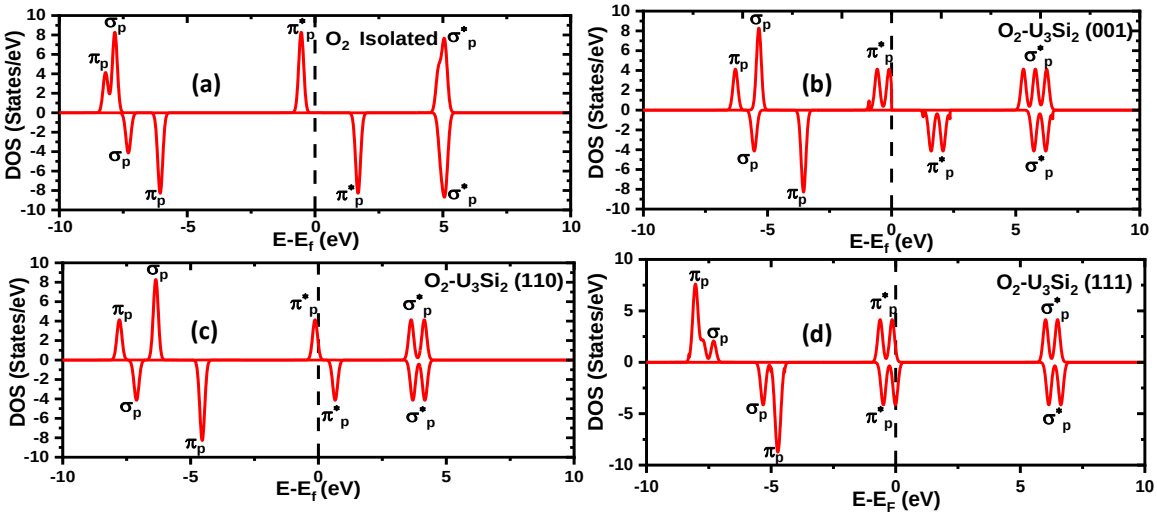

Fig. 7.12. DOS for O_2 in the (a) free state and adsorbed in the lowest-energy geometry at the oxygen-U_3Si_2 interfaces (b−d).

7.6. Summary and conclusions

We have performed experimental and Density Functional Theory investigations of the early oxidation of U_3Si_2 in the presence of adsorbed oxygen molecules. The chemical picture presented by the DFT calculation reveals the oxygen molecule interacts strongly with the U_3Si_2 surfaces, with the adsorption characterized by significant charge transfer from the interacting surfaces to the adsorbing oxygen molecule. The population of the partially filled π^*_{2p} and unfilled σ^*_{2p} orbitals resulted in the formation of a peroxo-like (O_2^{2-}) species with elongated O-O bonds on the U_3Si_2 surfaces. Generally, the U_3Si_2 surfaces are shown to be easily oxidized by dissociated oxygen molecules which imply that dissociation is a necessary step before the oxidation of U_3Si_2 and this is consistent with more stable exothermic energies calculated for dissociative compared to the molecular adsorption.

Experimental analyses of the oxidized U_3Si_2 samples have revealed the formation of higher oxides from Raman spectroscopy and XRD techniques. The low intensity $\nu(UO_2)^{2+}$ type bands observed for the pure sample could be linked with partial oxidative changes on the powder due to exposure to air. Its morphology reveals an uneven surface with intermittent grooves enriched with granules of a secondary USi phase.

Chapter 8

DFT+U study of the adsorption and dissociation of water on clean, defective and oxygen-covered U_3Si_2 (001), (110), and (111) surfaces

8.1. Overview of Chapter 8

In this chapter, the effects of single and multiple water molecules on the thermodynamic feasibility of U_3Si_2 oxidation process is investigated. The role of surface defects on the adsorption mechanism of water is also elucidated. Finally, the oxidized surfaces are analyzed for possible corrosion products that are formed during the oxidation of U_3Si_2 fuel.

This chapter is presented as manuscript #4 (E. Jossou, L. Malakkal, N.Y. Dzade, A. Claisse, B. Szpunar, J.A. Szpunar, DFT+U study of the adsorption and dissociation of water on clean, defective and oxygen-covered U_3Si_2 (001), (110), and (111) surfaces, Phys. Chem. C. (2019). My contributions to this paper include a review of relevant literature, design and carrying out of the required simulation, analysis of results and preparation of the manuscript. My supervisors; Prof. Jerzy Szpunar and Dr. Barbara Szpunar reviewed the paper before it was submitted for publication. To avoid repetition of information provided in Chapter 6 of this thesis, the crystal description of the U_3Si_2 have been removed from this chapter. The copyright permission to use the manuscript in this thesis was obtained from the publishers and it is provided in APPENDIX E. The manuscript was published in 2019 in *Journal of Physical Chemistry C*.

- E. Jossou, L. malakkal, N.Y. Dzade, A. Claisse, B. Szpunar, J.A. Szpunar, DFT+U study of the adsorption and dissociation of water on clean, defective and oxygen-covered U_3Si_2 (001), (110), and (111) surfaces, J. Phys. Chem. C. (2019). doi:10.1021/acs.jpcc.9b03076.

DFT+U study of the adsorption and dissociation of water on clean, defective and oxygen-covered U_3Si_2 (001), (110), and (111) surfaces

Ericmoore Jossou[1], Linu Malakkal[1], Nelson Y. Dzade[2], Antoine Claisse[3], Barbara Szpunar[4], Jerzy Szpunar[1]

[1]*Department of Mechanical Engineering, College of Engineering, University of Saskatchewan, 57 Campus Drive, Saskatoon, S7N 5A9, Saskatchewan,* Canada.

[2]*School of Chemistry, Cardiff University, Main Building, Park Place, Cardiff, CF10 3AT, UK.*
[3]*Westinghouse Electric Sweden AB, SE-721 63, Västerås, Sweden.*

[4]*Department of Physics and Engineering Physics, College of Art and Science, University of Saskatchewan, 116 Science Place, Saskatoon, S7N 5E2, Saskatchewan,* Canada.

8.2. Abstract

The interfacial interaction of U_3Si_2 with water leads to corrosion of nuclear fuels, which affects various processes in the nuclear fuel cycle. However, the mechanism and molecular-level insights into the early oxidation process of U_3Si_2 surfaces in the presence of water and oxygen and water is not fully understood. In this work, we present Hubbard-corrected Density Functional Theory (DFT+U) calculations of the adsorption behavior of water on the low Miller indices of pristine and defective surfaces as well as water dissociation and accompanied H_2 formation mechanisms. The adsorption strength decreases in the order U_3Si_2 (001) > U_3Si_2 (110) > U_3Si_2 (111) for both molecular and dissociative H_2O adsorption. Consistent with the superior reactivity, of the dissociated products, dissociative water adsorption is found to be more stable than molecular adsorption. We have also explored the adsorption of H_2O on oxygen-covered U_3Si_2 surface and showed that the pre-adsorbed oxygen could activate the OH bond and speed up the dissociation of H_2O. Generally, we found that during the adsorption of water on the oxygen-covered, defective surface, multiple water molecules are thermodynamically more stable on the surface than water monomer on pristine surfaces. Mix molecular and dissociative water adsorption modes are also noted to be stable on the (111) surface, whereas fully dissociative water adsorption is most stable on the (110) and (001) surfaces.

Keywords: *Uranium Silicide; Nuclear fuel; Oxidation; Surfaces; Density Functional Theory.*

8.3. Introduction

There is an increase interest in the development and use of advanced nuclear fuels such U_3Si_2 given the enhanced thermophysical properties as compared to traditional uranium dioxide fuel (UO_2) [13]. However, a key issue to deal with is the ease of oxidation of metallic nuclear fuels in the presence of water, oxygen or combination of both, which has required the synthesis of U_3Si_2 in controlled environment.

Significant number of earlier experimental works have assessed the behavior of U_3Si_2 in corrosion susceptible environments in comparison to other metallic and UO_2 fuels. Recently, Nelson *et al.* compared the oxidation behavior of U_3Si_2 to UO_2 and some other advanced fuel concepts (UN, U_3Si_5) following exposure to pressurized H_2O that is typical in light water reactors (LWRs) at temperatures ranging from 300 to 350 ^oC. Their results showed that both UN and U_3Si_5 rapidly pulverize in less than 50 h at 300 ^oC, while the behavior of U_3Si_2 was superior but still below the corrosion resistance of UO_2 fuel. It is worthy to mention that the mechanism of pulverization of U_3Si_2 might be due to spallation of UO_2 or due to internal hydriding [55,57]. Formation of $U_3Si_2H_{1.8}$ with volumetric increase has already been shown by experiment and DFT calculations [105].

In this work, we unraveled the detailed mechanism of the early oxidation of U_3Si_2 from an atomistic point of view, which is difficult to achieve experimentally. Earlier theoretical works have focused on the bulk properties of U_3Si_2 within the framework of DFT+U formalism and molecular dynamics technique [58,64,66,105,271,327]. For instance, Middleburgh *et al.* [105] investigated the defects evolution in U_3Si_2 and also proposed a phase diagram capable of predicting fuel behavior during burnup. Furthermore, Noordhoek *et al.* [64] studied the electronic, structural and elastic properties showing detailed bonding characteristics of U_3Si_2 by electron density of states which corroborate the work of Remschnig *et al.* [252] as regards the metallic nature of U_3Si_2.

Surface science provides fundamental insight into the chemistry and physics of corrosion in materials, but such experiments are expensive and require dedicated facilities especially in the study of an actinide containing compound. Hence, theoretical surface science provides an important alternative tool for investigating oxidation mechanisms in nuclear fuel materials. Bo *et*

al. [328] modelled the surface properties of the low index NpO_2 (111), (110), and (100) surfaces as well as the adsorption and dissociation behaviors of water on these surfaces by using DFT+U calculations in combination with *ab initio* atomistic thermodynamic simulations. Their results showed that water dissociation is enhanced by oxygen vacancy, while coverage of the water molecules play no significant role during molecular adsorption [329]. More recently, Wellington and co-worker [330] investigated the adsorption and dissociation of water on pristine and reduced UO_2 and PuO_2 surfaces using periodic electrostatic-embedded cluster method and Hubbard-corrected periodic condition implemented in DFT based code. Oxygen vacancies were shown to be easily formed on PuO_2 than UO_2, which is due to ease of Pu reduction in comparison to U metal ions. Their results also showed that dissociation is favored over molecular adsorption of water both on defect free and oxygen deficit surfaces of UO_2 and PuO_2.

Given the success of first-principles DFT+U calculations in the modelling surfaces, we recently studied the adsorption of molecular and dissociated O_2 on stoichiometric U_3Si_2 lower index surfaces [254]. To further our understanding of the underlying mechanism of oxidation, we have considered the synergetic effect of water and oxygen interaction with U_3Si_2 perfect surfaces. Real surfaces are never perfect and chemical processes often occur at defect sites.

In the present work, we have explored the effects of U and Si vacancies on the adsorption mechanisms of water and oxygen on the (001), (110) and (111) surfaces of U_3Si_2. Surface vacancies in UN, UO_2, PuO_2 and CeO_2 have been shown in previous studies to affect the oxidation behavior of such surfaces in the presence of oxidizing and hydriding agents [328–334]The fundamental aspects of oxygen and water adsorption, including the initial adsorption geometries, adsorption energies, structural parameters, and electronic properties, are presented. Our results reveal a chemical picture of the initial steps involved in the oxidation process of the U_3Si_2 surfaces in the presence of oxygen and water (considering both molecular and dissociative adsorption).

8.4. Computational details

The first-principles calculations were performed within the plane-wave pseudo-potential DFT technique [109,110], as implemented in Quantum ESPRESSO code [143]. The exchange-correlation functional potential was described by the generalized gradient approximation (GGA)

in the *Wu-Cohen* (GGA-WC) formulation [127]. All our calculations deployed the norm-conserving *Wu-Cohen* (WC) pseudopotentials (where these potentials treat $6d^1\ 5f^3\ 7s^1$ as valence electrons for U and $3s^2\ 3p^6$ as valence electrons for Si). Due to the onsite Coulomb repulsion among the localized U 5*f* electrons, we used the Hubbard (DFT+U) corection to account for the strong correlation effect [264]. We have used an effective U value of 1.5 eV, which has been shown to give an accurate description of the structural parameters and the electronic properties of U_3Si_2 [14].

The Kohn-Sham one-electron states were expanded in a plane wave basis set up to 120 Ry while the Fermi surface effects were treated by the smearing technique of Methfessel-Paxton [230], using a smearing parameter of 0.02 Ry (0.27 eV). An energy threshold defining self-consistency of the electron density was set to 10^{-8} eV and a beta mixing factor of 0.3. The Brillouin zone integration was done using $7 \times 7 \times 10$ and $5 \times 5 \times 1$ Monkhorst-Pack [143] k-point grids (centred at the Γ point) for the bulk U_3Si_2 and the surface models, respectively.

Structural relaxation was carried out to minimize the energy using the conjugate gradient method within the Broyden-Fletcher-Goldfarb-Shanno (BFGS) algorithm [266], until the magnitude of the residual Hell-Feyman force on each relaxed atom reached 0.01 eV $Å^{-1}$. Visualization and analysis of the structures were perfomed using the VESTA program [231,232].

The (001), (110) and (111) surfaces were considered for the oxygen and water adsorption calculations as they are possible growth facets of U_3Si_2 amongst others which were determined in Chapter 7 of this thesis. The different surface structures were created from fully optimized bulk tetragonal U_3Si_2 structure (Fig. 6.1) [6] in order to eliminate the presence of fictitious forces during surface relaxation using the METADISE code [180], which ensures the creation of surfaces with zero dipole moment perpendicular to the surface plane.

The (001), (110) and (111) surfaces were modelled by slabs constructed as 3-layer 2×1 supercell with 60 atoms per simulation cell based on previous work [254].A vacuum of 15 Å was introduced to the surface models in the *z*-direction, which is large enough to avoid any spurious interactions between periodic slabs. Bader population analysis was carried out on all adsorbate-substrate

systems in order to quantify any charge tranfers between the U_3Si_2 surface and O_2/H_2O species [240].

The vibrational frequencies analysis of the water molecule before and after adsorption were computed by using a density functional perturbation theory [335] which is implemented in QE code at gamma-point and a convergence threshold of 1.0×10^{-14} is imposed during the calculations.

8.5. Results and discussion

8.5.1. Defective surface models

8.5.1.1. Surface defects energies and stability

Defective surfaces (vacancies) were created by removing one Si/U atom at a time from the either the first or second layer (Fig. 8.1) in order to access their energetics or stability. The silicon vacancies are denoted as V_{Si} whereas the two considered uranium vacancy sites are denoted as V_{U1} and V_{U2} respectively, on the surface. V_{U1} and V_{U2} are assigned base on the coordination with nearest neighbor Si atoms. For instance, V_{U1} on the (110) surface is a uranium site which is coordinated to 4 nearest neighbor silicon while the V_{U2} is created at a uranium site coordinated to 2 nearest neighbor silicon.

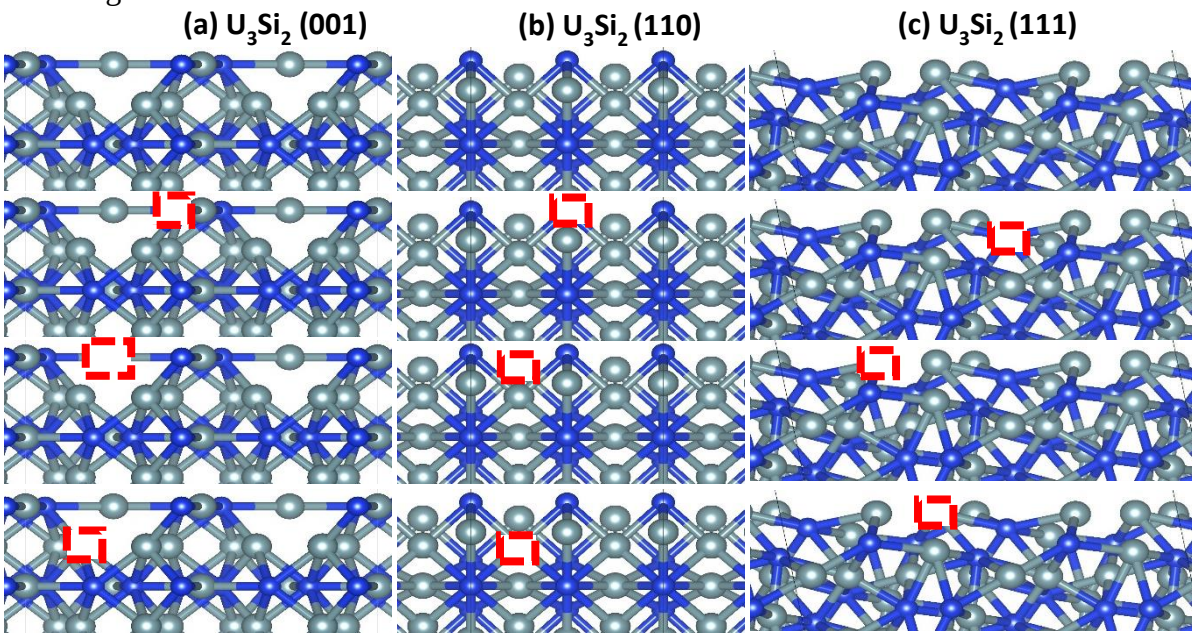

Fig. 8.1. Optimized surface geometry of the (a) U_3Si_2 (001) (b) U_3Si_2 (110) (c) U_3Si_2 (111) with Si, U2 and U1 surface vacancy represented by rectangular red box in the second, third and fourth rows respectively. (Color scheme: U=grey, Si=blue).

The method of Wellington *et al.* [330], was employed, which ensured that U and Si atoms are removed from the supercell, both from surface and subsurface layers are coordinated to neighboring atoms to avoid edge defects which do not capture nearest neighboring interaction [330]. The vacancy formation energy was calculated using equation 3.93. Where E^{N-1} is the energy of a surface slab with uranium or silicon vacancy, E^{N} is the energy of the relaxed stoichiometric slab of the same type and μ(X) is chemical potential for X= Si and U as the energy per atom in its fundamental diamond and orthorhombic structure respectively.

Presented in Table 8.1 are the calculated vacancy formation energies on the (001), (110) and (111) U_3Si_2 surfaces. We found higher Si vacancy formation for the (110) surface (2.62 eV) than for the (001) surface (0.16 eV), and (111) surface (1.54 eV) similar trend is observed in the subsurface Si vacancies formation. Clearly, Si vacancy on the (110) subsurface (2.62 eV) is close to the 2.48 eV calculated for bulk U_3Si_2 by Andersson *et al*. [135] This is not surprising, given that the (110) has the lowest surface energy and similar neighboring atom coordination. There are two U sites denoted here as U1 and U2 with vacancy defect formation energies of 1.64 and 2.65 eV respectively for the bulk [135], which is comparable to the value of 1.61 and 2.60 eV calculated in this thesis. Meanwhile, the vacancy formation energy for Si is calculated to be 2.52 eV, which is consistent with the value of 2.48 eV reported by Andersson *et al*. [135]. The first and second layer U vacancy energies were calculated as presented in Table 8.1. In some cases, it is easier to form a vacancy in the surface layer compared to the subsurface which might be due to difference in nearest neighbor atoms and the coordination numbers.

Table 8.1. Uranium and silicon vacancy formation energies (eV) of the (001), (110), and (111) Surfaces of U_3Si_2.

Surface	First Layer			Second Layer		
	V_{Si}	V_{U1}	V_{U2}	V_{Si}	V_{U1}	V_{U2}
(001)	0.16	1.72	1.87	1.74	2.13	2.88
(110)	2.62	3.18	2.41	1.62	2.03	2.61
(111)	1.54	3.81	3.70	2.44	1.46	3.10

The formation of Si and U vacancies resulted in a nonstoichiometric surface, which allows variation in the surface energies as the chemical potential, μ of Si and U change. The

thermodynamic stability of a given surface in general depends on the specific chemical environment. To determine the stability of the surfaces due to vacancies, we calculate the surface energy, γ, as a function of the Si and U chemical potential respectively. At zero temperature the surface energy of a crystal may be derived from a *N*-layer slab using equation 3.89.

Due to the surface vacancy defects, the surface energy depends on the specific thermodynamic conditions, *i.e.,* the reservoir with which the atoms of the compound are exchanged in a structural transition. Therefore, the chemical potential of the constituents enters the surface energy. The most stable surface structure is determined by the minimum of the free energy which at zero temperature is given by equation 8.1:

$$\gamma = \frac{1}{2A}\left[E_{surf} - \sum_i N_i \mu_i\right], \tag{8.1}$$

In the case of U_3Si_2, equation 8.1 can be expressed by equation 8.3 to account for the chemical potential μ of U and Si atoms:

$$\gamma = \frac{1}{2A}\left[E_{surf} - N_U \mu_U - N_{Si}\mu_{Si}\right], \tag{8.2}$$

The μ_U and μ_{Si} are bounded by a set of conditions. Assuming U and Si are in thermal equilibrium with U_3Si_2 crystal, it would imply that:

$$\mu_{U_3Si_2} = 3\mu_U + 2\mu_{Si}, \tag{8.3}$$

Furthermore, since there is no precipitation of $\alpha\text{-U}_{(solid)}$ and $Si_{(solid)}$ on the U_3Si_2 surface, the following conditions must also be fulfilled:

$$\mu_{Si}^{Si\ surf} \leq \mu_{Si}^{Si\ bulk}, \tag{8.4a}$$

$$\mu_U^{surf} \leq \mu_U^{bulk}, \tag{8.4b}$$

Also, the heat of formation of bulk U_3Si_2, ΔH_f (eVf.u.$^{-1}$), is defined as

$$\Delta H_f = 3\mu_U^{bulk} + 2\mu_{Si}^{bulk} - \mu_{U_3Si_2}^{bulk}, \tag{8.5}$$

Combining equations (8.3), (8.4a-b), and (8.5), we obtain a range for possible values of the Si chemical potential as follows:

$$\mu_{Si}^{(Si\ bulk)} - \frac{1}{2}\Delta H_{U_3Si_2} < \mu_{Si} < \mu_{Si}^{(Si\ bulk)}, \quad (8.6a)$$

$$\mu_{U}^{(U\ bulk)} - \frac{1}{3}\Delta H_{U_3Si_2} < \mu_{U} < \mu_{U}^{(U\ bulk)}, \quad (8.6b)$$

Combining equation (8.2) and (8.3), gives a surface energy as a function of μ_{Si}:

$$\gamma = \frac{1}{2A}\left[E_{surf} - \frac{1}{3}N_U E_{bulk} + \mu_{Si}\left(\frac{2}{3}N_U - N_{Si}\right)\right], \quad (8.7)$$

Similar to equation 8.7, the surface energy can also be expressed as a function μ_U:

$$\gamma = \frac{1}{2A}\left[E_{surf} - \frac{1}{2}N_{Si} E_{bulk} + \mu_{U}\left(\frac{3}{2}N_{Si} - N_U\right)\right], \quad (8.8)$$

At ambient temperature and pressure, E_{surf} can be taken as the total energy from DFT calculation neglecting contributions from configurational or vibrational entropies. In Fig. 8.2, we show the results of the calculated surface energies of the (001), (110), and (111) surfaces of U_3Si_2 as functions of the change in the silicon chemical potential μ_{Si}. Silicone poor environment corresponds to $\mu_{Si} = 0$ (Si in the FCC structure) and silicon rich environments corresponds to $\mu_{Si} = -7.46\ eV$ (Si_4 molecule). This is chosen in order to cover a wide range of μ_{Si} environment while making sure that the values considered fall within the range established by equation 8.6a. Similar approach has been used in the literature in the for study of FeS_2 and RuO_2 systems [336–338].

The lower limit which is the Si-poor environment is defined by the decomposition of the silicide into U and Si. Meanwhile the upper limit is the Si-rich state which corresponds to a situation where gas phase is so rich in silicone that they condensed on the substrate. In the case of stoichiometric surfaces considered in this work, the surface free energy is independent of μ_{Si} as expected since the coefficient of equation 8.4 containing μ_{Si} vanishes.

8.5.2. Adsorption of water molecule

The adsorption of water molecule on the U_3Si_2 surfaces is an important starting step towards understanding its early oxidation mechanisms. The first interest of this study is therefore to determine the lowest-energy adsorption structures and modes of water on the low-index U_3Si_2 (001), (110) and (111) surfaces, and to characterize the strength of their interaction and the extent

of O-H bond activation during dissociation process. Different H_2O initial adsorption possibilities, including H_w and O_w head-on configurations, have been subjected to geometry optimization until the residual forces on all atoms were ≤ 0.03 eV/Å.

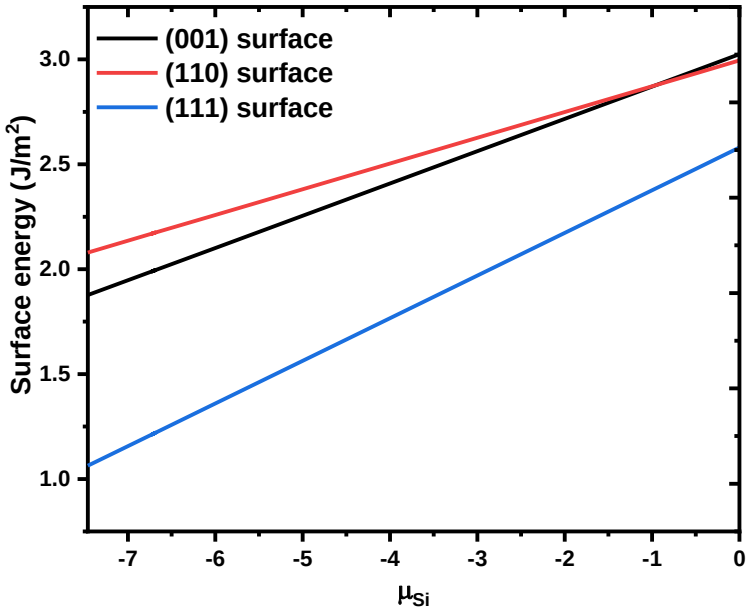

Fig. 8.2. Calculated surface energies of the (001), (110), and (111) surfaces of U_3Si_2 as functions of the change in silicon chemical potential μ_{Si}.

Prior to adsorption, we have calculated the reference energies, bond length, bond angle and vibrational frequencies of one free H_2O molecule compared them with earlier theoretical results and available experimental data. The values of the O-H bond and H-O-H angle of water are determined to be 0.970 Å and 104.5^o, respectively which are in good agreement with previous experimental and theoretical values [339,340]. The calculated scissoring bend, asymmetric and symmetric stretching vibrational frequencies are calculated to be 1555, 3523, and 3635 cm^{-1}, in close agreement with the experimental results (1596, 3652, and 3756 cm^{-1}) [341]. The adsorption energy (E_{ads}), which characterize the strength of water adsorption has been defined as the mean adsorption energy per molecule of H_2O-U_3Si_2 interaction using the equation 3.90. By this definition, a negative value of E_{ads} indicates an exothermic and stable adsorption, whereas a positive value indicates an endothermic and unstable adsorption.

8.5.2.1. Water adsorption and dissociation on clean U_3Si_2 (001)

For the adsorption of molecular water on the U_3Si_2 (001) surface, different adsorption sites and configurations were explored in order to determine the lowest-energy adsorption structures, as presented in Fig. 8.3. The calculated adsorption energies and the optimized interatomic bond distances are summarized in Table 8.2. The calculated lowest-energy water adsorption structure is presented in Fig. 8.3a, wherein the water molecule adsorbs through the O atom at U site (U-O = 2.56 Å), releasing an adsorption energy of –3.70 eV. The adsorption of water at Si site (O-Si =2.376 Å) released an adsorption energy of –3.11 eV.

When the water molecule is adsorbed with the hydrogen atoms pointing towards the surface Si site (Fig. 8.3b), it moved away perpendicularly from the surface during energy minimization until the closest H–Si distance was 3.044 Å. The adsorption energy of this configuration was calculated at –1.97 eV, while the α(H-O-H) bond-angle and O-H bonds are obtained at 102.32^o and 0.965/0.967 Å, respectively. Compared to the lowest-energy water adsorption on U_3Si_2 (001), Bo *et al* calculated an adsorption energies of –2.07 eV and –1.27 eV for the lowest-energy adsorption structures of water monomer on UN (001) and UO_2 (110), respectively, which suggest that U_3Si_2 (001) is more reactive towards water adsorption than both UN (001) and UO_2 (110) [342,343].

In all three adsorption modes, the O-H bond lengths were slightly elongated and the α(H-O-H) bonds bond angle were larger compared to the gas-phase free H_2O molecule in vacuum, suggesting that the O-H bonds are activated to some extent when water is adsorbed on the U_3Si_2 (001). In the lowest-energy O-U structure (Fig. 8.3a), the two O-H bonds are calculated at 0.975 and 0.996 Å compared to the gas phase molecule at 0.970 Å and is consistent with O-H bond stretching vibrational frequencies presented in Table 8.1, whereas the α(H-O-H) bonds bond angle is obtained at 107.6^o compared to the gas phase value of 104.5^o which is supported by the red shift in the bending vibrational frequencies in Table 8.2. The stretched O-H bond lengths is indicative of weaker O-H bonds, resulting from the π-antibonding occupation. The activated O-H bonds suggest that these molecular adsorption states are likely precursors for H_2O dissociation.

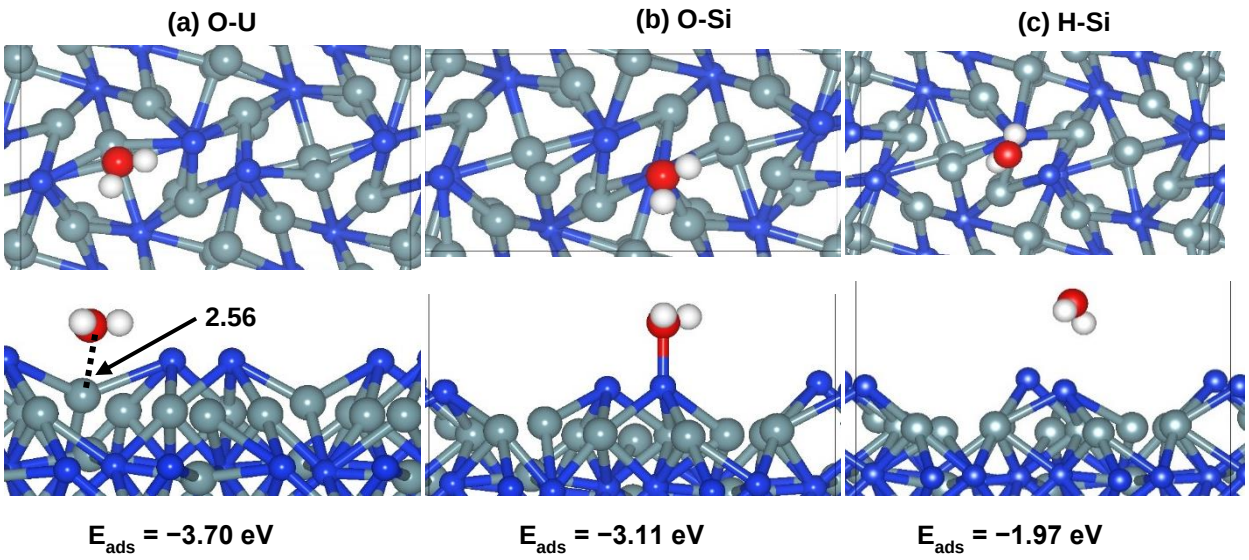

Fig. 8.3. Top and side views of the relaxed adsorption structures of molecular H_2O adsorbed at: (a) O-U (b) H-Si (c) O-Si. (Color scheme: U = grey, Si = blue, H = white and O = red).

Dissociative adsorption of H_2O on the clean U_3Si_2 (001) surface is found to be highly exothermic with adsorption energies of –6.81, –5.43 and –3.61 eV, respectively for the different configurations presented in Fig. 8.4 and Table 8.2. Consistent with their stronger adsorption, the collective amount of charge transfer gained by the dissociated H_2O species is larger than those of the molecular adsorbed water systems. Due its metallic nature, the U ions seems to donate more electrons than Si ions during bond formation.

The preference for dissociative over molecular adsorption of water can be attributed to the fact that the energy required to break an O-H bond requires less energy compare to the energy released in the formation of the Si-H and U-OH bonds on the U_3Si_2 (001) surface. In like manner, on several metals and oxide surfaces, the dissociative state of H_2O is thermodynamically more stable than the molecularly adsorbed state, for example, on Cu and Al_2O_3, because the breaking of an O-H bond is effectively balanced by the formation of a metal-O and another O-H bond with a surface oxygen [344,345].

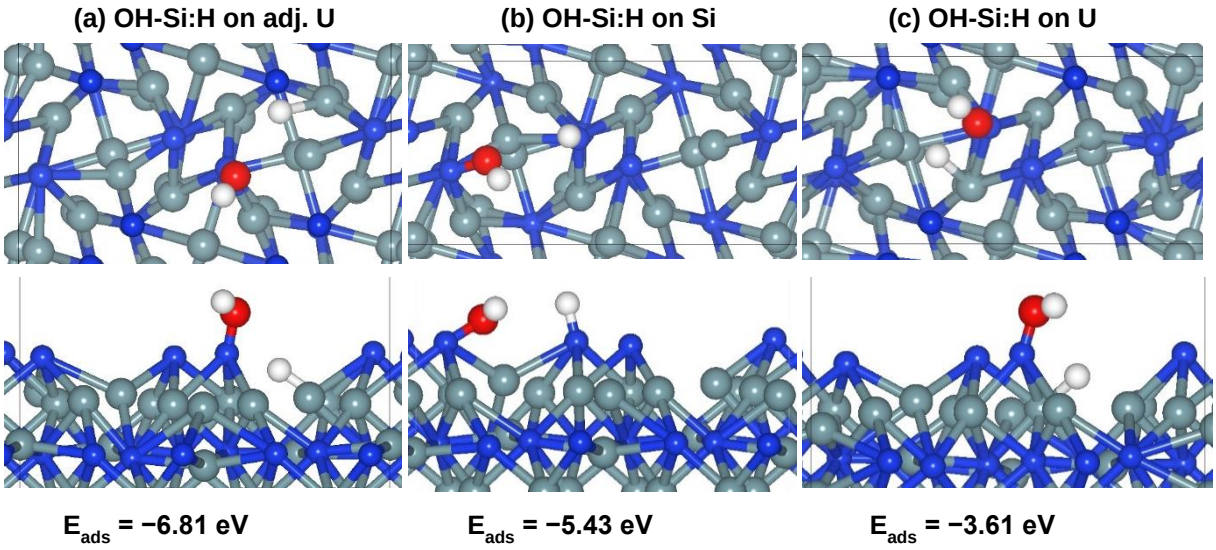

Fig. 8.4. Top and side views of the relaxed adsorption structures of dissociated water configuration with (a) OH-Si: H on adj. U (b) OH-Si: H on Si, and (c) OH-Si: H on U, on U_3Si_2 (001)-Si terminated surface. (Color scheme: U = grey, Si = blue, H= white and O = red).

8.5.2.2. Water adsorption and dissociation on clean U_3Si_2 (110)

As on the U_3Si_2 (001) surface, we have also explored different adsorption configuration of H_2O on (110) surface, including O adsorbed laterally at U or Si sites or H placed head-on Si sites. The optimized adsorption structures are shown in Fig. 8.5, whereas the energies of adsorption, geometric parameters and Bader charge transfer analyses are presented in Table 8.2.

The lowest-energy water adsorption configuration at the U_3Si_2 (110) was calculated to be O-Si structure (Fig. 8.5a), wherein the water molecule is adsorbed at Si site through the oxygen atom (O-Si = 2.120 Å), releasing an energy of −2.46 eV. In this structure, we observed elongation of the O-H bond calculated at 0.996 and 0.978 Å and broadening of the α(H-O-H) bond angle (107.3^o).

The next stable configuration is the O-U structure (Fig. 8.5b), which released an adsorption energy of −0.60 eV. The interacting O-U distance is calculated at 2.805 Å, and O-H bonds and α(H-O-H) bond angle are calculated at 0.985/1.005 Å and 104.0^o, respectively.

Table 8.2. Calculated adsorption energy (E_{ads}), relevant bond distance (d), vibrational frequencies, and variation of the total Bader charge of molecular (H_2O) and dissociated (OH + H) adsorbed on the (001), (110) and (111) surfaces of U_3Si_2.

Surface	Adsorbate	Config.	$E_{ads.}$ (eV)	d (O-H1) (Å)	d (O-H2) (Å)	d (Si-O) (Å)	d (U-O) (Å)	d (U-H) (Å)	d(Si-H) (Å)	α(HOH) (°)	ν_b (cm^{-1})	ν_s (cm^{-1})	ν_{as} (cm^{-1})	Δq (e–)
		H_2O	–	0.970	0.970	–	–	–	–	104.490	1555	3523	3635	–
(001)	H_2O	O-U	–3.70	0.975	0.996	–	2.622	–	–	107.642	1534	3390	3661	0.08
		O-Si	–3.11	0.994	0.976	2.376	2.562	–	–	105.399	1543	3553	3675	0.09
		H-Si	–1.97	0.975	0.977	–	–	–	–	102.323	1540	3767	3862	0.05
	OH+H	OH-Si: H on adj. U	–6.81	0.983	–	–	2.598	–	1.551	–				2.13
		OH-Si: H on Si	–5.43	0.971	–	1.741	2.618	–	1.501	–				1.21
		OH-Si: H on U	–3.61	0.965	–	1.644	–	2.119	–	–				1.17
(110)	H_2O	O-Si	–2.46	0.996	0.978	2.120	–	–	–	107.343	1532	3418	3673	0.15
		O-U	–0.60	0.985	1.005	–	–	–	–	104.041	1600	3326	3590	0.16
		H-Si	0.55	0.971	0.970	–	–	–	–	103.232	1601	3425	3571	0.05
	OH+H	OH-Si: H on U	–3.24	0.979	–	1.676	–	2.396	1.583	–				0.44
		OH-U: H on Si	–2.27	0.974	–		2.200		1.510	–				0.17
(111)	H_2O	O-U	–1.40	0.977	0.995	–	2.548	–	–	105.454	1543	3432	3690	0.19
		H-Si	–0.20	0.957	0.977	–	–	–	–	99.181	1575	3677	3948	0.05
		O-Si	1.02	0.977	0.982	–	–	–	–	102.205	1622	3584	3691	0.01
	OH+H	OH-U: H on Si	–3.30	0.971	–	–	2.194	–	1.697	–				2.18
		OH-Si: H on U	–1.21	0.969	–	1.702	–	2.181	–	–				0.34

Key: Config. denotes configuration

When the H atoms placed head-on Si (Fig. 8.5c), the adsorption process is found to be endothermic by 0.55 eV and an average O-H bond length is 0.971 Å and there is a preferential Si-O bond formation with interatomic distance of 1.932 Å after energy minimization. From Bader populations analysis, we found the adsorption process is characterized by charge transfer from the surface to the water molecule, with the water molecule gaining a change of 0.15, 0.16, 0.05 e– in the O-Si, O-U and H-Si configurations, respectively. We also observed that the change in the vibrational modes and bond strengths is related to the Bader transfer between the surface and the adsorbed water molecule (Table 8.1).

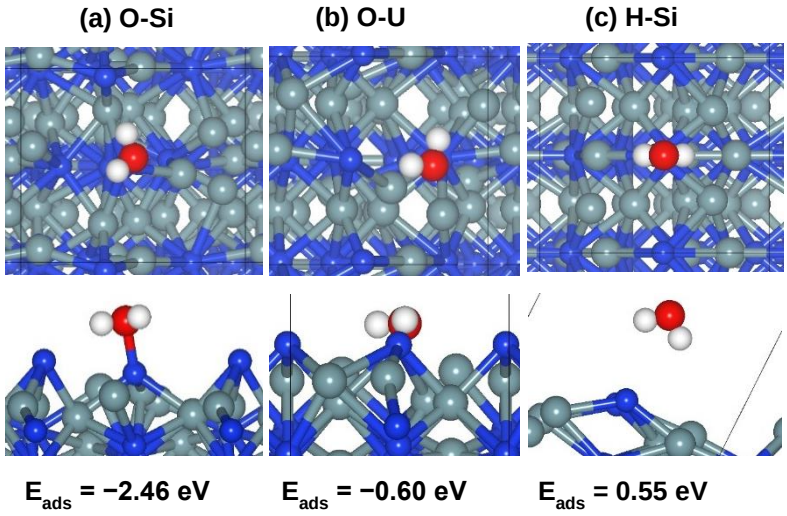

Fig. 8.5. Top and side views of the relaxed adsorption structures of molecular oxygen adsorbed at (a) O-Si (b) O-U (c) H-Si on U_3Si_2 (110) surface. (Color scheme: U = grey, Si = blue, H= white and O = red).

Compared to the molecular adsorption, dissociative water adsorption is found to have average adsorption energies of –3.24 and –2.27 eV for O_{OH} placed head-on Si and head-on U, respectively. For the dissociative adsorption through the H_{OH}, we initially placed an H_{OH} above the surface Si. After optimization, a Si-O bond was formed through the O_{OH} atom which means that dissociative adsorption through the H_{OH} is unstable. The dissociative adsorption structures are characterized by higher charge transfer from the surface to the dissociating species as evident by the calculated Bader charges of 0.44 and 0.17 e–. The charge transfer from the U_3Si_2 surface to the OH group is necessary condition for water to bind to the surface which is consistent with water dissociation on metal surfaces [346].

Furthermore, the above predicted adsorption energetics indicate that the dissociative adsorption of water is notably stronger than the molecular adsorption on the U_3Si_2 (110) surface. We also observe the formation of U-H with bond lengths of 2.396 and 2.275 Å in the dissociative configurations, which is required for the H^+ to achieve stability. In comparison to previous work, the U-H distances are 2.30–2.32 Å in α and β-UH_3 configurations [347]. The schematic representations of adsorption structures of dissociated water on the clean U_3Si_2 (110) surface are shown in Fig. 8.6.

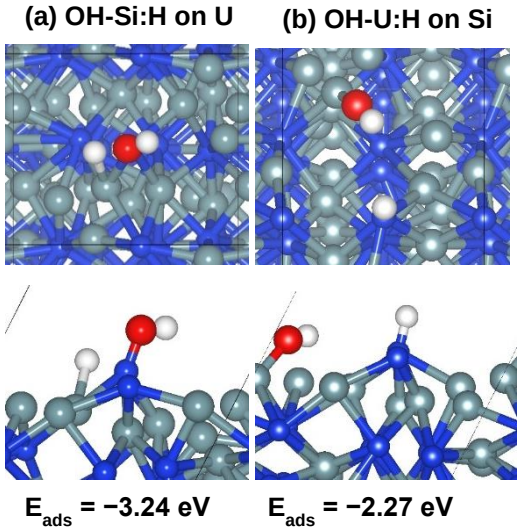

Fig. 8.6. Top and side views of the relaxed adsorption structures of dissociated H_2O at (a) OH-Si: H on U (b) OH-U: H on Si on U_3Si_2 (110) surface. (Color scheme: U = grey, Si = blue, H= white and O = red).

8.5.2.3. Water adsorption and dissociation on clean U_3Si_2 (111)

The images of the lowest energy adsorption structures obtained on the U_3Si_2 (111) surface are shown in Fig. 8.7a–c. Compared to the (001) and (110) surfaces, the water molecules are adsorbed least strongly on the (111) surface. The lowest energy adsorption structure on the U_3Si_2 (111) surface is calculated to be the O-U configuration (Fig. 8.7a), which released an adsorption energy of –1.40 eV. In this structure, the water molecule binds *via* the O atom lying laterally above the U atom at O-U distance of 2.548 Å, with the α(H-O-H) bond angle that slightly increased to 105.5° compared to the gas phase value of 104.5°. When the H_2O molecule is adsorbed with the H atoms pointing towards the surface Si atoms (Fig. 8.7b), an adsorption energy of –0.20 eV was released. The closest distance between H and Si/U sites

is calculated at 2.632/2.942 Å ruling out the formation silane and uranium hydrides. The O−H bond lengths are elongated within the range of 0.977 – 0.995 Å while the α(H-O-H) bond angle increased slightly by 0.964° as presented in Table 8.2. The adsorption of H_2O through O_w is unstable with an endothermic energy of 1.20 eV and tends to move further away from Si after optimization as shown in Fig. 8.7c.

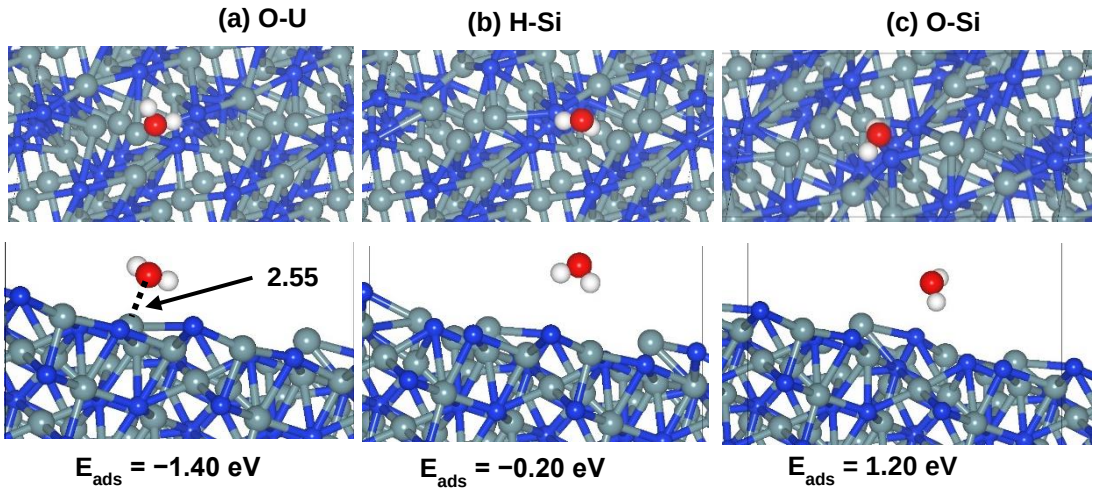

Fig. 8.7. Top and side views of the relaxed adsorption structures of molecular H_2O adsorbed at: (a) O-U site (b) H-Si site (c) O-Si site on U_3Si_2 (111) surface. (Color scheme: U = grey, Si = blue, H = white and O = red).

For dissociative adsorption of water on U_3Si_2 (111), the OH radical and one H atom are placed on the surface with two different adsorption modes as shown in Fig. 8.8a–b. In Fig. 8.8a, the OH^- forms a bond with a surface U atom while the H atom bonded to a neighboring Si atom. The formed U-O, Si-O and Si-H bond lengths are 2.655, 1.722 and 1.610 Å, respectively. The calculated adsorption energy for this configuration is –0.76 eV, whereas the adsorption of O_{OH} on U leads to the formation of U-O (2.194 Å) and Si-H (1.697 Å) bond after optimization requiring an energy of –3.30 eV. The larger adsorption energies, suggest preference for dissociative water adsorption over molecular adsorption on the U_3Si_2 (111) surface, which is consistent with previous studies of uranium bearing systems [343,348,349].

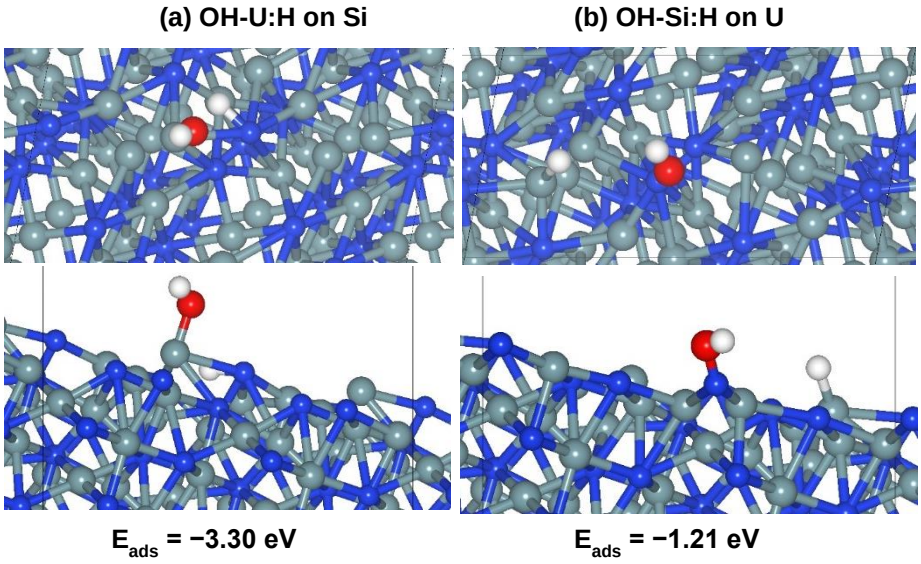

Fig. 8.8. Top and side views of the relaxed adsorption structures dissociated water configuration with (a) O-U: H, and (b) O-Si: H, on U_3Si_2 (111)-Si terminated surface. (Color scheme: U = grey, Si = blue, H= white and O = red).

8.5.3. Effects of surface coverage, oxygen-covered and surface vacancy on adsorption of water

8.5.3.1. Water adsorption at higher coverage

The effect of coverage on the adsorption properties of water on the U_3Si_2 surfaces were investigated by adsorbing up to four water molecules in a molecular, mixed, and partially dissociative modes. The optimized structures of the most stable adsorption modes are shown in Fig. 8.9, whereas the adsorption energies are reported in Table 8.3. We found no clear trends in the adsorption energies with increasing number of water molecules on the U_3Si_2 surfaces. On the (001) surface, the adsorption energies of one, two, three and four water molecules representing a coverage of 0.25, 0.50, 0.75, and 1.00 monolayer (ML) are –3.70, –2.83, –3.02, and –3.10 eV, respectively. At the (110) surface the adsorption energy increased from –2.46 eV for one water molecule to –3.23, –3.06, and –2.58 eV for two, three and four water molecules, respectively. A decreased in the adsorption energy is observed at the (111) surface with increasing number of water molecules; –3.30 for one water molecule compared to –1.42, –2.01, and –2.53 eV for the two, three and four water molecules, respectively.

Table 8.3. Adsorption energies (eV) per water molecule, mixed molecular and dissociated water on U_3Si_2 surfaces.

Adsorbate	(001)	(110)	(111)
1M	–3.70	–2.46	–3.30
2M	–2.83	–3.23	–1.42
3M	–3.02	–3.06	–2.01
4M	–3.10	–2.58	–2.53
1D + 3M	–3.25	–2.68	–2.69
2D + 2M	–3.26	–2.69	–2.65
3D + 1M	–4.12	–2.72	–2.48
4D	–3.54	–3.68	–3.45

Where M= H_2O and D=OH + H

Apart from the molecularly adsorbed water molecules, we have also explored mixed adsorption modes, where some of the water molecules are dissociated and some remained molecularly adsorbed. The scenario of fully dissociated modes, in which all the water molecules are dissociated at full coverage was also investigated. The optimized structures of the most stable adsorption states are shown in Fig. 8.9, and the adsorption energies are reported in Table 8.3. The mix adsorption modes of the molecular and dissociative water results in the formation different oxides, hydroxides and oxygen molecule on the U_3Si_2 surface depending on the ratio of the dissociative to molecularly adsorbed water as shown in Fig. 8.9 for the most stable adsorption energies. The remaining stable structures are reported in Appendix D (Figs. D.8.1 – D.8.3). For instance, on (001) surface, in the case of 75/25 mix adsorption, oxygen molecule was formed with a bond length of 0.99 Å directly on the Si surface with bond distance of 1.70 Å typical of SiO_2 formation. The strongest and most stable adsorption modes at the (001) surface is predicted for the 3D + 1M, which released an adsorption energy of –4.12 eV, compared to the 4D structures on the (110) and (111) surfaces which released adsorption energies of –3.68 and –3.45 eV, respectively.

Even though, U_3Si_2 is a metallic fuel, it is important to draw comparison between the silicide and urania which is the standard fuel for LWRs. Hence, it is interesting to note that studies by Bo *et al*. [343] on UO_2 and recent work by Wellington *et al*. [298] predicted the mixed 50/50 molecular/dissociative adsorption modes as the most stable adsorption configurations. The differences in the results can be attributed to differences in the crystallographic

arrangement of the two systems and their electronic structures, UO_2 is a of semiconductor with experimental band gap of 2.1 eV [350,351] whereas U_3Si_2 is metallic. Note, however, that the energy difference between the fully dissociative case and the fully molecular case is –0.44, –1.10 and –0.92 eV on the (001), (110) and (111) surfaces, respectively. The increase in adsorption energies in the dissociative configuration may be attributed to the formation of stronger intramolecular hydrogen bonds on the crowded surfaces compared to the purely molecular mode.

We have also carried out detailed analyses of the bond lengths for the molecular and dissociative adsorption of multiple water on the surfaces as shown in Table 8.4. We observed shorter hydrogen bond length for the Si-H compared to U-H on the U_3Si_2 (001), (110) and (111) surfaces which suggests stronger hydrogen bonding in Si-H when it is formed on the surface. There is also strong adsorption of molecular H_2O on the surface forming U-H_2O and Si-H_2O complexes with the exception of the (111) surface where formation of Si-H_2O is not observed.

Table 8.4. Selected interatomic distances (Å) for molecular and dissociative water on the U_3Si_2 (001), (110) and (111) surfaces at coverages from 0.5 to 1.0 monolayers (ML).

Bond type	(001) 0.5 – 1.0 ML (Å)	(110) 0.5 – 1.0 ML (Å)	(111) 0.5 – 1.0 ML (Å)
Si–O	1.70	N/A	N/A
Si–H	1.50 – 1.71	1.57 – 1.60	N/A
Si–OH	1.66 – 1.68	1.67 – 1.68	1.62 – 1.70
Si–H_2O	1.89 – 2.11	2.02 – 2.06	N/A
U–O	2.13	N/A	N/A
U–H	2.17 – 2.34	2.34 – 2.45	2.16 – 2.35
U–OH	N/A	2.31 – 2.78	2.48 – 2.71
U–H_2O	2.51 – 2.67	2.35 – 2.65	2.64 – 2.69

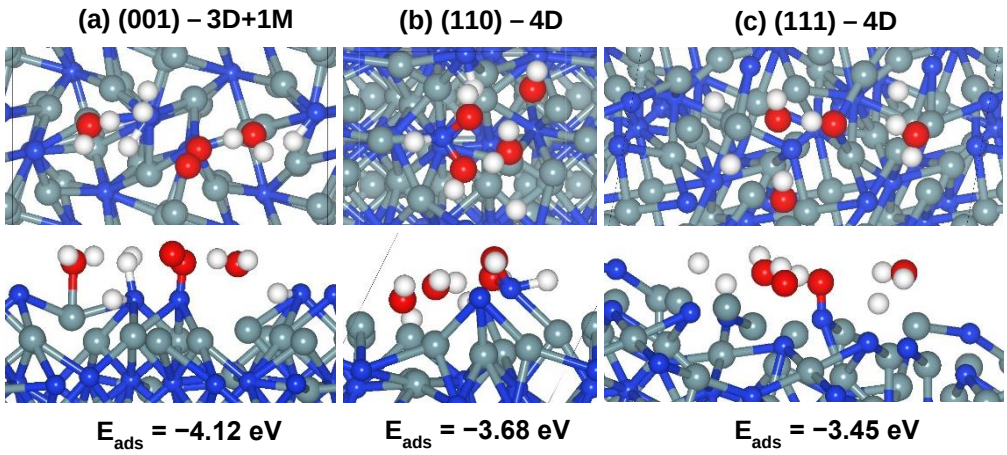

Fig. 8.9. Top and side view of the relaxed adsorption structures of mix (dissociative to molecular) 3:1 adsorption of H_2O on (a) (001) and full dissociative adsorption of H_2O on (b) (110) and (c) (111) U_3Si_2 surface. (Color scheme: U = grey, Si = blue, H= white and O = red).

8.5.3.2. Water adsorption and dissociation on O-covered U_3Si_2 (001), (110) and (111) surfaces

Pre-adsorbed oxygen atoms play an important role in the activation of O-H bond and further increase the rate of surface oxidation due to rapid water dissociation [352,353]. Hence, it is important to investigate the adsorption behavior of H_2O on oxygen-covered U_3Si_2 (001), (110) and (111) surfaces. Prior to investigating the adsorption of H_2O on oxygen-covered U_3Si_2 (001), (110) and (111) surfaces, we have systematically characterized the adsorption of atomic oxygen on the different U_3Si_2 surfaces in order to elucidate their surface oxide formation.

In our previous study [254] we have provided information regarding the mechanism of oxygen adsorption and dissociation on U_3Si_2 surface. The adsorption of atomic O is found to be energetically more favorable at U-sites than Si-sites on the (001), (110) and (111) U_3Si_2 surfaces (Table S4 and Figure S5). The adsorption energies at the U- and Si-site at calculated at –2.44 and –0.67 eV on the (001), –2.71 and –0.77 eV on the (110), and –2.85 and –0.81 eV on the (111) surface. Similar results were predicted for molecular O_2 at the different U_3Si_2 surfaces, which suggest that on normal U_3Si_2 surfaces, UO_2 formation is favored over SiO_2 [254].

Table 8.5. Calculated Adsorption Energy (E_{ads}) and Relevant Bond Distances for H_2O Co-adsorbed with Atomic Oxygen U_3Si_2 (001), U_3Si_2 (110) and U_3Si_2 (111) Surfaces.

Surface	adsorbate	Config.	E_{ads} (eV)	d (O_w-H1) (Å)	d (O_w-H2) (Å)	d (O-H2) (Å)	d (Si-O) (Å)	d (Si-OH) (Å)	d (U-O) (Å)	d (U-OH) (Å)	$\alpha(HOH)$ (º)	Δq (e–)
(001)	H_2O+O	H–U: O on U	–5.47	0.977	–	1.026	–	1.641	–	2.339	–	1.95
		O_w–Si: O on Si	–3.54	0.970	0.988	–	1.729	–	2.525	–	106.760	1.83
		O–Si: O on U	–3.49	0.975	–	0.953	–	1.680	–	2.525	–	1.79
		O_w–U: O on Si	–2.87	0.973	–	1.099	1.675	–	–	–	–	1.75
(110)	H_2O+O	O_w–U: O on U bridge	–7.41	0.975	0.975	–	2.763		2.268		105.523	1.21
		O_w–Si: O on U	–4.13	0.982	–	–	–	–	2.236	–	–	0.92
		H_w–Si: O on U	–3.67	0.978	–	1.154	–	–	–	1.80	–	
(111)	H_2O+O	O_w–Si: O on U	–1.39	0.979	–	1.006		1.710	–	2.145	–	1.67
		O_w–U: O on Si	–0.81	0.977	0.974	–	1.695		2.567	–	109.975	1.87
		H_w–Si: O on U	–0.27	0.974	–	–	–	–	2.021	–	–	

For the adsorption of water on O-U_3Si_2 (001) surface, various coadsorption structures were explored with the water adsorbed at neighbor or distant sites from the pre-adsorbed O atoms (Fig. 8.10). The coadsorption energies between the H_2O and O on the U_3Si_2 surface is calculated using equation 3.91.

In most cases, we found the water molecule co-adsorbed with oxygen dissociate to form OH ions due to the attractive force between the hydrogen atoms and pre-adsorbed O atoms. The most favorable co-adsorption mode on the (001) surface is predicted for the configuration in which water molecule is adsorbed at U site near O atom that is pre-adsorbed at U site. Due to strong attractive force between the two adsorbates, H_2O molecule spontaneously dissociate to form two hydroxyl species, releasing an adsorption energy of –5.47 eV (Table 8.5), which is consistent with water dissociation on oxygen covered metal surfaces [340,354]. The U-OH and Si-OH interaction bond lengths are calculated at 2.339 and 1.641Å, respectively. Consistent with the strong adsorption, the two OH species draws a combined charge of 1.95 e– from the interacting surface species. When the water molecule remained molecularly adsorbed at a Si site near a pre-adsorbed O atom (Fig. 8.11b), an adsorption energy of –3.54 eV is released.

It is important to point out that OH + OH adsorption is more stable on the surface compared to coadsorption of H_2O + O due to the fact hydroxyl ions which are negatively do not need to be activated like the water molecules before adsorption. Previous studies showed the hydrogen bonding interaction between hydroxyl groups may contribute to their stability on surfaces [355]. On the other hand, water needs to be activated by the O atom before strong interaction with the surface ions.

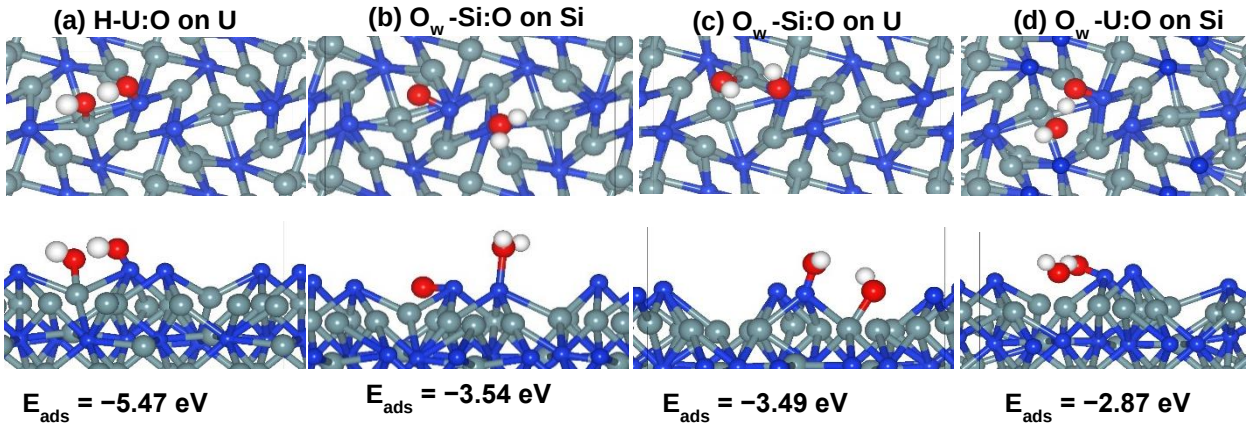

Fig. 8.10. Top and side views of the relaxed adsorption structures of molecular H_2O (a) H-U: O on U (b) O_w-Si: O on Si (c) O_w-Si: O on U and (d) O_w-U: O on Si U_3Si_2 (001) surface.

We have also investigated the adsorption and dissociation of water on the U_3Si_2 (110) surface in the presence of pre-adsorbed atomic oxygen. Three coadsorption modes have been explored with the H_2O and O coadsorbed at neighboring surface U and U-bridge sites. The optimized adsorption geometries are shown in Fig. 8.11a-c, while the coadsorption energies and the relevant optimized geometric parameters are summarized in Table 8.5.

When water is adsorbed with O_w head on Si and the pre-adsorbed O atom at nearest neighbor U-U bridge, the coadsorption energy is −7.41 eV, which is more negative than the sum of the separate adsorption energies (−5.17 eV) suggesting strong interaction evident by the stretching of the OH bonds and significant transfer of electrons (1.21 e−) from Si to the water molecule. It is clear that the oxygen atom has stronger affinity for the uranium forming a U-O-U complex with a bond angle of 97.65°. Hence, the water molecule preferred to bond with the surface Si atom rather than deprotonate to form hydroxyl ions as was observed on iron sulfide surfaces[340].

When water is coadsorbed with O head on a neighboring U site, the coadsorption energy is calculated to be −4.13 eV, which is less negative than the sum of the separate adsorption energies (−5.17 eV), suggesting that H_2O and O can be individually readily adsorbed on the top U site in preference to coadsorption. However, the coadsorption is quite negative to suggest the possibility of interaction between the two adsorbates, which gives rise to the dissociation of water due to the deprotonation resulting in the formation of silane, uranium oxide and hydroxyl species (Fig. 8.11b). In this case where H_w is placed on Si atom, we observed a repulsion between H and Si while the nearest O atom form a bond with one of the H_w leading to formation of hydroxyl ions as shown in Fig. 8.11c releasing energy of −2.67 eV.

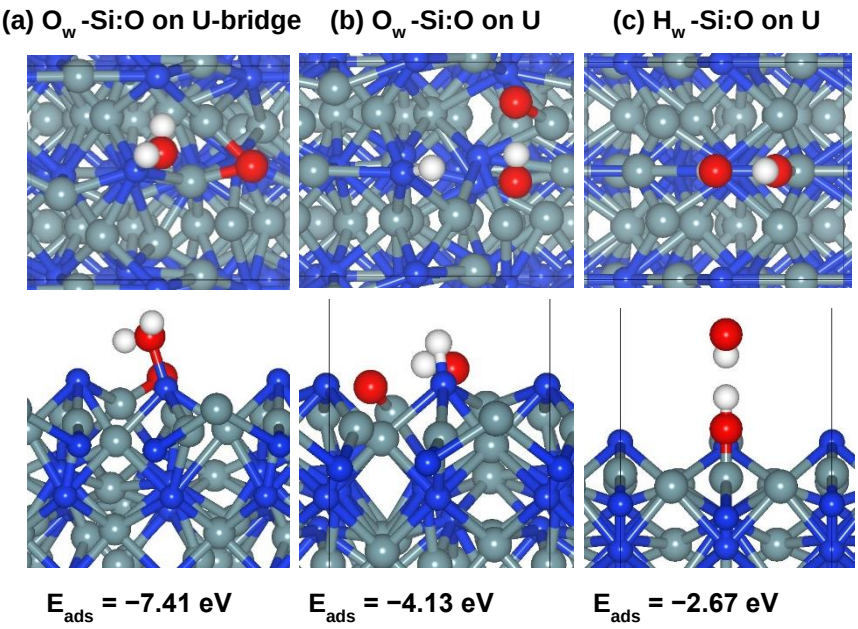

Fig. 8.11. Top and side views of the relaxed adsorption structures of molecular H_2O (a) O_w-Si: O on U-bridge (b) O_w-Si: O on U and (c) H_w-Si: O on U on U_3Si_2 (110) surface. (Color scheme: U = grey, Si = blue, H= white and O = red).

The most favorable coadsorbed configuration of the $(H_2O + O)/U_3Si_2$ system on the (111) surface is found to be the structure with the water molecule adsorbed on Si while one of the hydrogen atoms pointing toward the preadsorbed O atom on the top-U site (Fig. 8.12a) releasing an energy of −1.39 eV, which is less negative than the sum of the separate adsorption energies of −1.83 eV. This indicates that the adsorption of an oxygen atom separately is energetically more favorable than water. Therefore, when the oxygen is coadsorbed with the water molecule on the Si site, energy is needed to break the hydrogen bonding present in water. This makes the coadsorption energy slightly lower than when they were adsorbed separately. However, in the coadsorption case, dissociation of the water molecule leads to the formation of two Si-OH and U-OH configurations.

Whereas in the adsorption of the O atom on Si site (Fig. 8.12b) leads to the O atom preferentially forming a trihedral network with U and Si atoms, this is facilitated by drawing electrons from a metal surface that is easy compare to a Si atom while there stretching of the OH bonds (0.977 and 0.974 Å) with the O_w forming bond with the surface U atom.

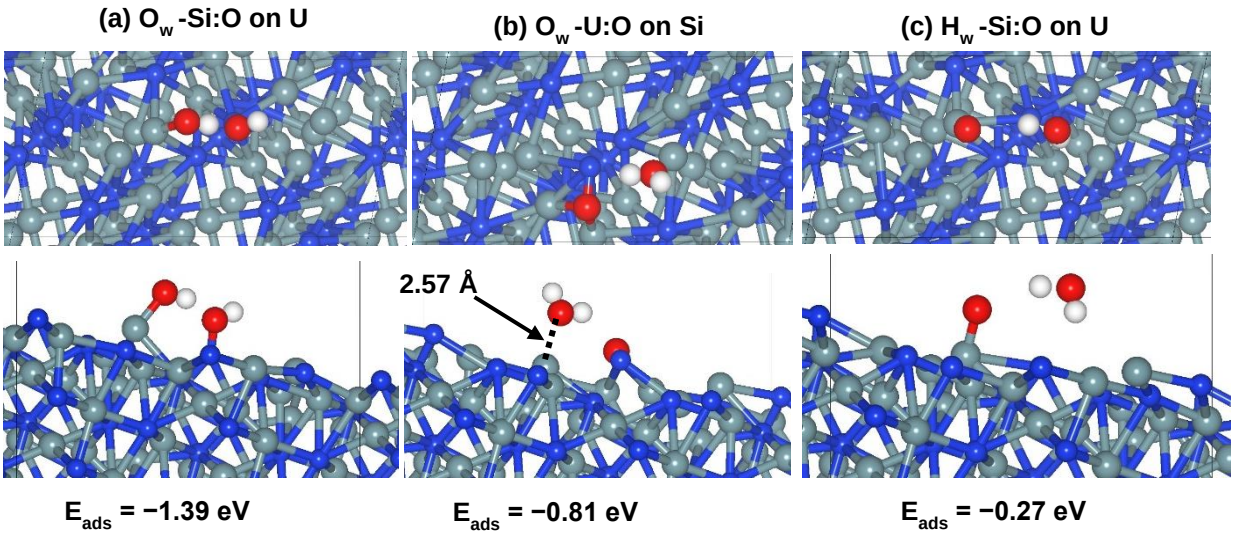

Fig. 8.12. Top and side views of the relaxed adsorption structures of molecular H_2O (a) O_w-U: O and (b) O_w-Si: O on U_3Si_2 (111) surface. (Color scheme: U = grey, Si = blue, H= white and O = red).

8.5.3.3. Water adsorption on defective (nonstoichiometric) surfaces

Considering that real surfaces are never perfect under reaction conditions and chemical processes often occur at defect sites, we have also investigated water adsorption at the defective surfaces containing one Si or U vacancies at the (001), (110) and (111) surfaces. The optimized structure of defective U_3Si_2 with H_2O are shown in Fig. 8.13 and the calculated adsorption energies and optimized geometry parameters are listed in Table 8.6. At the defective (001), (110) and (111) surfaces containing one Si vacancy site (Si–1), the adsorption energy of water monomer in the molecular state is calculated at –3.43, –3.18 and –2.92 eV, respectively. In (001) and (110) adsorption structures, there is a complete dissociation of water molecule which is consistent with the chemisorbed nature of water [332] while the OH bonds on the (111) surface stretches to 1.245 and 0.980 Å, respectively suggesting the instability of water molecule on nonstoichiometric surface. The computed bond distance of U-O (2.163 – 2.321 Å) and Si-O (1.536 – 1.892 Å) suggest the formation of UO_2 and SiO_2.

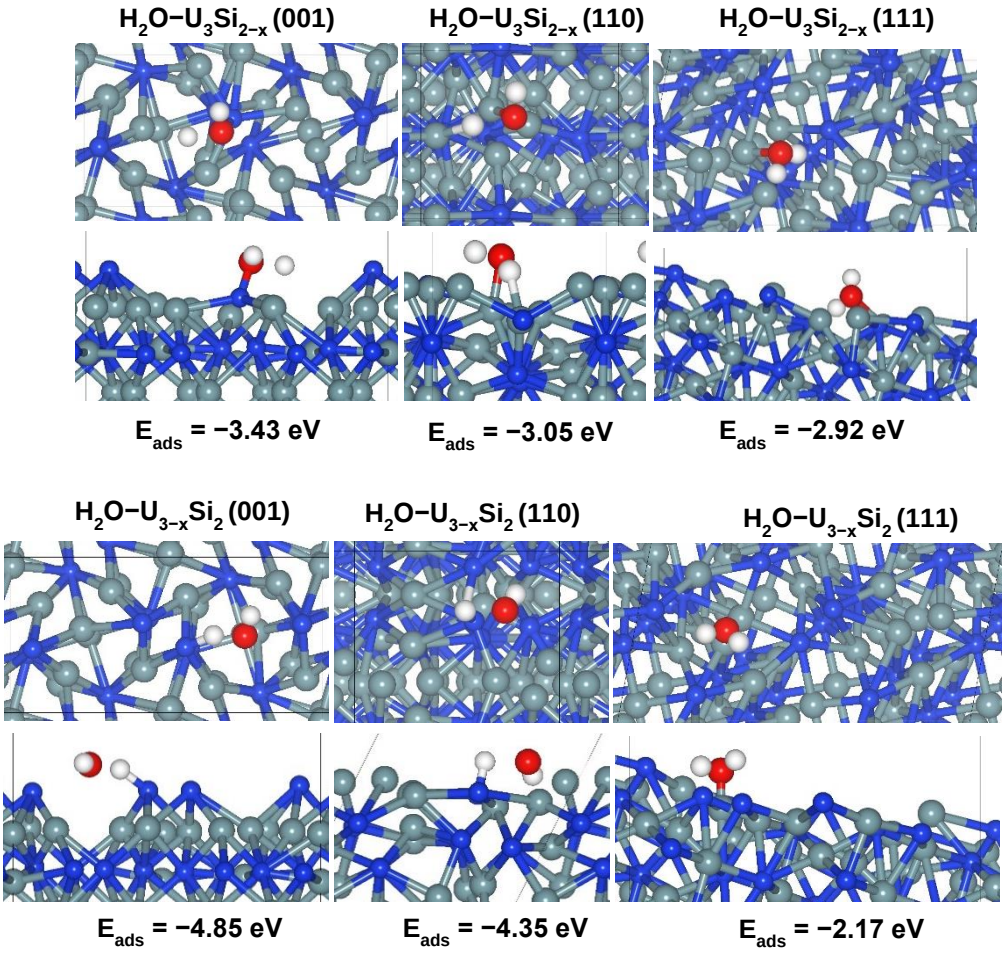

Fig. 8.13. Top and side views of the relaxed adsorption structures of Si and U vacancy assisted molecular H_2O adsorption (a) H_2O-U_3Si_{2-x} (001) (b) H_2O-U_3Si_{2-x} (110) (c) H_2O–U_3Si_{2-x} (111) (d) H_2O-$U_{3-x}Si_2$ (001) (e) H_2O-$U_{3-x}Si_2$ (110) (f) H_2O-$U_{3-x}Si_2$ (111) surface. (Color scheme: U = grey, Si = blue, H= white and O = red).

At the surfaces containing one U vacancy site (U–1), the dissociative adsorption of H_2O on the defective $U_{3-x}Si_2$ (110) is found to be highly exothermic (E_{ads} = –5.84 eV), which suggests that the defective $U_{3-x}Si_2$ (001) favors dissociative H_2O adsorption rather than molecular adsorption, similar to the findings on the defective $U_{3-x}Si_2$ (001) and (111) surfaces. Bader population analysis reveals that a significant amount of charge (~1.32 e–) was transferred to the dissociated water species from the interacting surface species. This is not surprising, since vacancies result in the formation of dangling bonds (reactive sites) due to the availability of electrons for transfer to water molecules on the surface.

Table 8.6. Adsorption Energies (eV) of water molecule on nonstoichiometric U_3Si_2 (001), (110) and (111) surfaces.

Adsorption site	(001)	(110)	(111)
Si vacancy	–3.43	–3.18	–2.92
U1 vacancy	–4.85	–4.35	–2.17
U2 vacancy	–5.84	–4.22	–3.54

8.5.4. Electronic structure and bonding mechanism

Fundamental understanding of the nature of interactions between the H_2O molecule and the U_3Si_2 surfaces and any adsorption induced changes in the electronic structures of the U_3Si_2 were gained through projected density of states (PDOS) analysis (Fig. 8.14).

The empty (filled) electronic states near the Fermi level can accept (donate) more electrons to enhance the reduction (oxidation) reactions. We observed various degree of shifts in the PDOS indicative of change in electronic structure due to electron transfer from U and Si ions to the water molecules leading to OH bond elongation; a step before deprotonation of water molecule. The charge gained by the H_2O molecule in the different adsorption complexes is calculated to be in the range of 0.05−0.11 e− at the water-U_3Si_2 (001) surface, 0.04−0.05 e− at the water-U_3Si_2 (111) surface, and 0.15−0.25 e− at the water-U_3Si_2 (110) surface (Tables 8.3).

We further analyze the total DOS of the isolated water molecule in the adsorbed state at the various surface and compared to the gas phase molecule (Fig. 8.15). The DOS for the gas-phase H_2O molecule is shown in Fig. 8.15a where the molecular orbitals (MOs) are labelled as 2a1, 1b2, 3a1 and 1b1 respectively, while those for the lowest-energy adsorption configurations at the water-U_3Si_2 (001), (110), and (111) interfaces are shown in Fig. 8.15 (b, c, and d), respectively.

Due to the strong water-U_3Si_2 hybridization, electron transfer from the interacting surface U *f*-states, we observed a shift of the 3a1 and 1b1 MOs around the Fermi level of water adsorbed at the (001) and (111) surfaces. At the water-U_3Si_2 (110) interface, we observe a splitting of the 1b1 MO, coupled with a shift toward lower energy levels (Fig. 8.15d), which signifies stabilization of the water molecule via physiosorption.

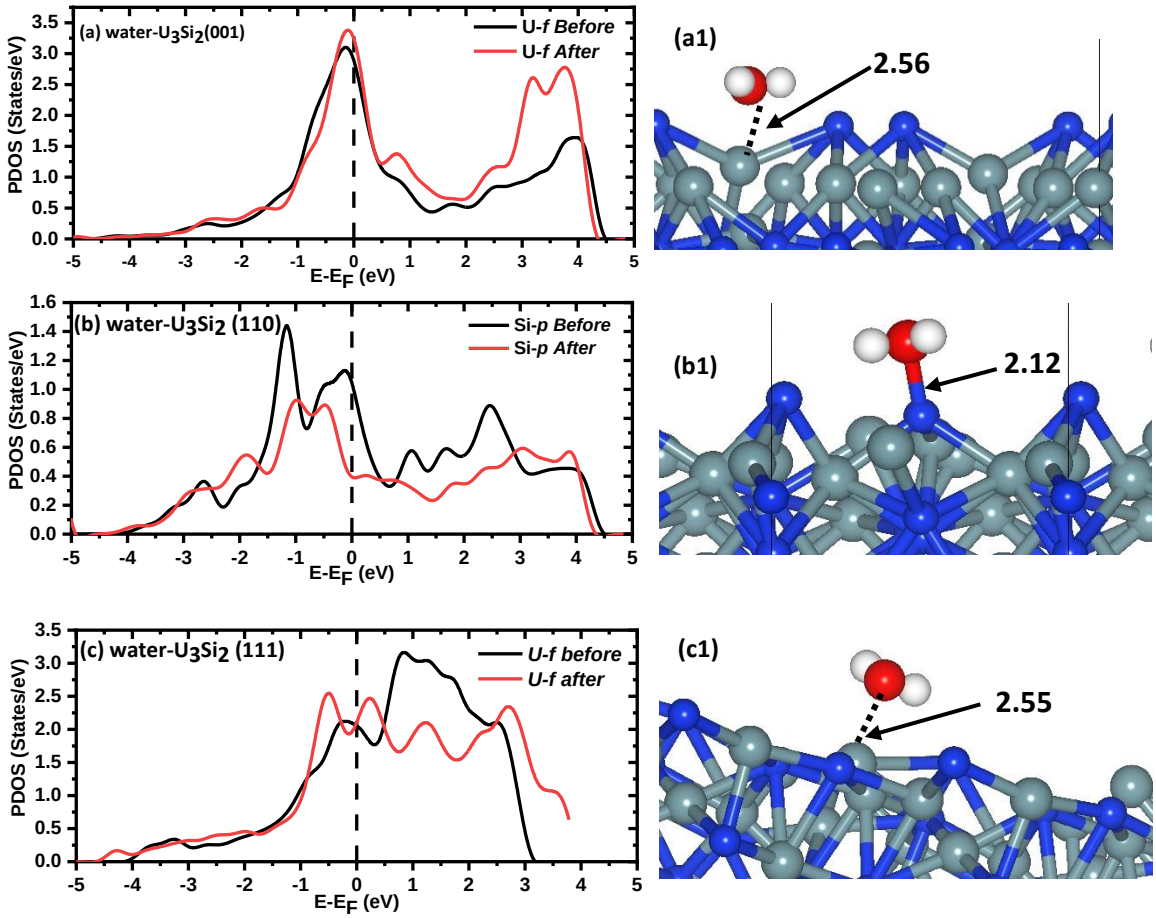

Fig. 8.14. (Right) PDOS for the interacting surface U *f*-states before and after the adsorption of H_2O at the (a) water-U_3Si_2 (001) and (b) for interacting surface Si *p*-states at the water-U_3Si_2 (110) interface, and for the interacting surface U *f*-states before and after the adsorption of H_2O at the (c) water-U_3Si_2 (111) interface. (Left) the corresponding optimized water-U_3Si_2 interfaces with U-O and Si-O bond lengths.

The reactivity of the surface is influenced largely by the ease of electron transfer between surface and adsorbate. Previous, work by Hammer *et al.* showed that the electronic states of the valence band of the surface plays a key role during surface-adsorbate interaction due to the hybridization energy between the bonding and anti-bonding adsorbate states and the metal valence-bands [356].

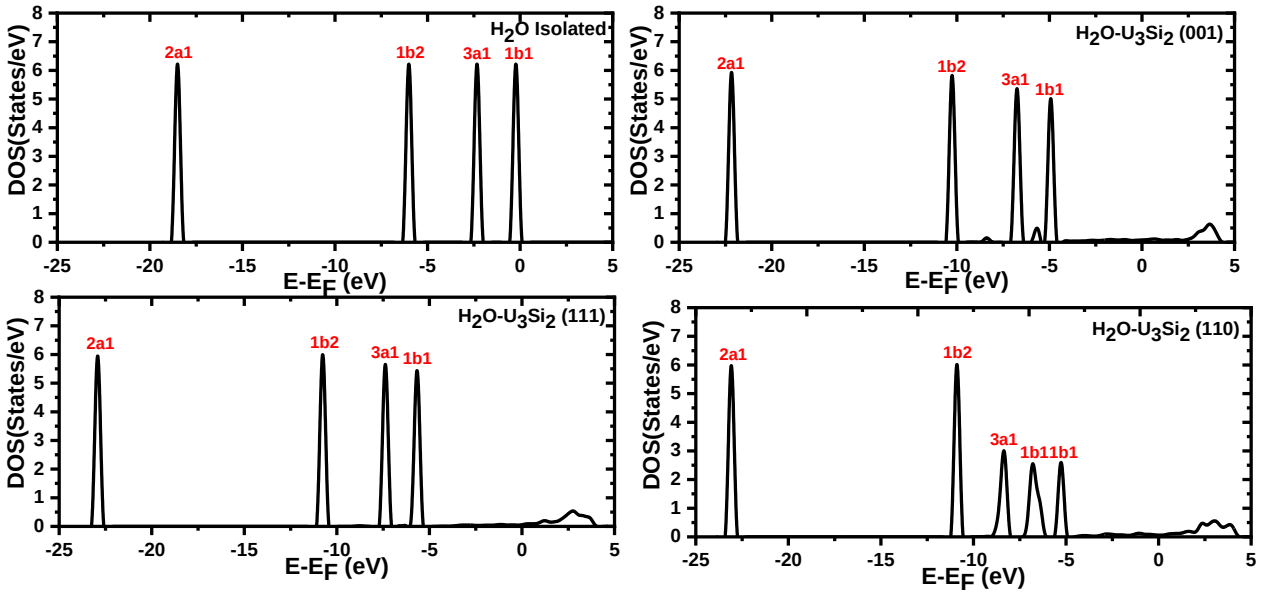

Fig. 8.15. DOS for H_2O in the (a) free state and adsorbed in the lowest-energy geometry at the water-U_3Si_2 interfaces (b−d).

As the pre-adsorbed oxygen species enhance the O-H bond activation to dissociate, a necessary step for the formation of surface oxides, we have also characterized the electronic structures of the O_2-U_3Si_2 surfaces and show that the U atoms to which atomic oxygen is bound become more positive (1.12, 1.20, and 1.61 e− on the (001), (110) and (111) surfaces, respectively) compared to the clean surface U charge of +0.98 e− (001), 0.96 e− (110) and 1.01e− (111), which from the qU^{4+}/qU^{6+} ratio is enough to suggest that they have been oxidized from U^{4+} to U^{6+}.. (See Appendix D, Table D.8.4 and Figure D.8.5 for full details of O-U_3Si_2 in terms of bond lengths and charge transfer).

We further investigated the nature of the interaction of the bonding between surface U and atomic oxygen by analyzing the partial DOS of the interacting surface U *f*-states and O p-state, as shown in Fig. 8.16. We observe strong hybridization between the interacting U *f*-states and O p-state which is due to charge transfer from surface U ions into the adsorbed oxygen π orbital, in good agreement with previous studies of oxygen adsorption on metal surfaces [357].

The work function gives a picture of the nature of such electronic interactions, hence we have calculated the work function of the clean and adsorbate containing U_3Si_2 surfaces to characterize the level of difficulty for an electron transferring from the surface to the vacuum.

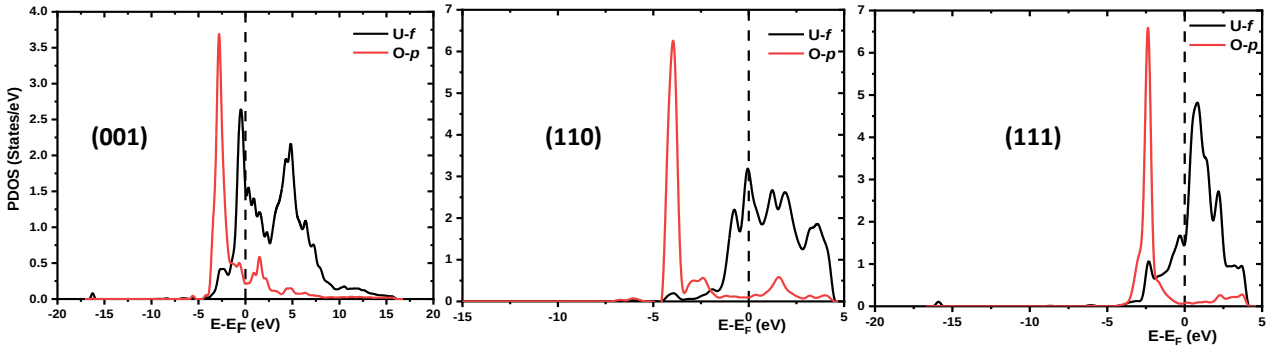

Fig. 8.16. Partial DOS projected on the interacting surface U *f*-states and O *p*-states for adsorbed atomic oxygen on top-U site on (a) (001) (b) (110), (c) (111) surfaces.

The work function is the minimum energy needed to remove an electron from the bulk of a material through a surface to a point outside the material and can be written as:

$$\Phi = V_{vacuum} - E_{Fermi} \tag{8.9}$$

The potential in the vacuum region (V_{vacuum}) and the Fermi energy (E_{Fermi}) were derived from the same calculation. In practice, this is the energy required at 0 K to remove an electron from the Fermi level of the material to the vacuum potential. We determined the work function of the clean surface and further probe the effect of oxygen on the electronic states of the surface and oxygen assisted dissociation of H_2O.

The work function depends on the crystallographic direction as shown by the results in Table 8.7. The anisotropic nature of the work function comes from the crystallographic arrangement of the surface planes which determines the spreading of the electronic charge into the vacuum [358]. Furthermore, the adsorption acts to smoothen the surface electric charge distribution which lowers the work function. The work function is such that $\Phi_{(H_2O+O)} < \Phi_{(H_2O)} < \Phi_{dry}$ due to partial transfer of electron charge from the substrate to the adsorbate and the resulting adsorption-induced surface dipoles (Table 8.7) [359].

Table 8.7. Calculated work functions of the dry (Φ_{dry}), hydrated (Φ_{H_2O}) and coadsorbed H_2O + O (Φ_{H_2O+O}) U_3Si_2 surfaces.

Surface	Φ_{dry} (eV)	Φ_{H_2O} (eV)	Φ_{H_2O+O} (eV)
(001)	3.09	3.05	2.86
(110)	1.89	1.48	1.21
(111)	2.86	2.30	1.96

8.6. Summary and conclusions

We have investigated the adsorption and dissociation reactions of H_2O on the clean oxygen-covered and defective U_3Si_2 (001), (110) and (100) surfaces using density functional theory calculations. The adsorption energetics and characteristics of molecular water adsorption were compared with full dissociative and a mixed (molecular and dissociative) adsorption modes on the U_3Si_2 surfaces. We showed, from our calculations that the major interactions between the adsorbing water molecules and the U_3Si_2 surfaces occur through oxygen and the surface U or Si site.

Compared to the clean surfaces, pre-adsorbed O atoms are shown to enhance the activation the O–H bonds of water and their subsequent dissociation reactions to form surface hydroxyl species, which are driven by significant charge transfer from the surface to the adsorbing species. We demonstrated that surface vacancy defects enhance the adsorption and dissociation of H_2O compared to a stoichiometric defect free surfaces. The molecular-level insights derived from this work provide fundamental understanding of the adsorption processes and mechanisms of the early stage of oxidation of U_3Si_2 in the presence of oxygen and water, and might open new avenues for the rational design of oxidation resistance fuels for nuclear reactors.

Chapter 9

Summary, conclusions, original contribution, and future work

9.1. Overview of Chapter 9

The results presented within this thesis have elucidated the atomic scale behaviors of UB_2 and U_3Si_2 fuels. The prediction of inherent thermophysical properties of UB_2 and U_3Si_2 have also been vividly explained. The behavior of UB_2 fuel in the presence of some fission products as well as the effect of oxidizing environments on U_3Si_2 have also been investigated. The results in this work will serve as a baseline for future investigations under reactor conditions. A brief summary will be given of the key conclusions reached in each chapter's results. Following that, some of the future works will be highlighted in detail.

9.2. Summary and conclusion

9.2.1. Thermophysical properties

Due to the importance of the thermophysical properties of nuclear fuel materials, we started by predicting the thermal and thermodynamic properties of UB_2 and U_3Si_2 across a wide range of temperatures typical of a nuclear reactor. Heat capacity is one of the key properties affecting fuel temperature distribution, and it determines the amount of energy stored in a system. The combination of these parameters play an important role in reactor dynamics and the performance of the reactor systems during transient conditions.

Therefore, in Chapter 5 the DFT technique was used to investigate the structural properties, electronic structure, and thermophysical properties of UB_2. The dynamic and structural stabilities were elucidated from the phonon dispersion relation and elastic constants results. The Poisson's ratio and B/G ratio were computed to show the ionic and ductile natures of UB_2 fuel. Electronic structure calculations showed a metallic behavior which accounts for the *el–el* scattering in the system. The *el–el* interaction coupled with *el–ph* scattering is responsible for the electronic contribution to thermal conductivity, which increased with temperature. The anisotropic nature of the thermal conductivity of UB_2 was calculated by taking the ratio of $\boldsymbol{k_z/k_x}$ as a function of temperature. This has implication for the even dissipation of heat in nuclear reactors.

Furthermore, a systematic study of the anisotropic, temperature-dependent thermophysical properties of U_3Si_2 was carried out using MEAM interatomic potential and first principles

calculations. The values of the thermal expansion coefficient, bulk modulus, and heat capacities at different temperatures were obtained from the equilibrated structure of U_3Si_2. These results are in good agreement with experimental measurements. A comparison of the calculated molar heat capacity with experimental data also shows reasonable agreement with the experiments. Due to the anisotropy in lattice expansion at different temperatures, we established a directional dependence in the linear thermal expansion coefficient, which has also been experimentally observed. The calculated data was validated by comparing the results with available experimental data. This confirms the fidelity of the MEAM potential, which is necessary before further use of the potential.

In addition, temperature dependent values of k_{ph} for U_3Si_2 was also calculated using both the EMD and the NEMD methods. Both techniques were also used for predictions of the directional dependence of k_{ph} in U_3Si_2. It is important to note here that the use of NEMD for anisotropic prediction is computationally challenging as two sets of calculations are required to compute the values of k_{ph} in the *x* and *z* directions. However, the use of EMD is sometimes difficult especially when a converged value of the HCACF is not achievable due to divergence. This behavior has been observed in disordered materials. Overall, both methods are complementary. However, the use of either technique should be guided by the nature of the materials to be studied.

In conclusion, the anisotropic thermophysical properties of U_3Si_2 and UB_2 make them potential ATFs, because metallic thermal conduction observed in both systems increases linearly with temperature. Besides, the calculated anisotropic thermophysical properties can be used as inputs in mesoscale and continuum models to predict the microstructural evolution of the fuel pellets under variable temperature and irradiation conditions to understand how the thermal gradient at the centerline of the fuel pellet evolves during normal operation and under accident conditions.

9.2.2. Radiation behavior

The presence of solid fission products, such as Zr, cause noticeable radial fuel swelling. It remains soluble within the fuel indefinitely [31] while gaseous FPs, such as the noble gases Xe, He, and Kr, contribute to swelling when they coalesce at grain boundaries. This event results in the formation of connected intergranular networks that extend to the pellet surfaces [32]. When this occurs, gaseous fission products can escape the fuel pellets, consequently increasing the internal pressure of the fuel rod.

To access and quantify such behavior in ATFs, the incorporation and solutions energies of Zr and Xe in UB_2 are investigated using DFT. It is worthy to note that Zr is more soluble in UB_2 than Xe while U vacancy is the most stable solution site in comparison to the B vacancy and interstitial sites. The partial density of state of the defective fuel matrix was calculated and, unlike UO_2 that transitions from semiconducting to metallic, UB_2 maintains its metallic properties with increasing FP concentrations. The same holds true for the point defects considered in this work.

The effect of Zr and Xe FPs on the structural properties of UB_2 was investigated by increasing the concentration of the FPs at different solution sites. As the concentration of Zr increased, there is a contraction in the volume of UB_2, while the increase in Xe results in swelling of the fuel matrix. This suggests that FP accumulation will ultimately lead to fuel pellet cracking, especially as the fuel ages in the reactor.

The results obtained here provide a fundamental understanding of point defects stability and the diffusion behaviors of FPs in UB_2 at an atomic level. Also, as this material is expected to accumulate defects quite readily in radiation environments, the volume change and anisotropic behavior must be considered when designing UB_2 as a standalone or composite fuel. For instance, samples should be sintered with sufficient porosity to accommodate swelling without imparting a significant outwards hoop strain on a cladding material. If used during sintering to improve the thermal properties of UO_2 fuel, it should be in small quantities in order for the swelling to be simply accommodated for by careful consideration of the fuel–cladding gap size.

9.2.3. Oxidation behavior

Due to the metallic nature of the proposed ATF fuels, experimental and DFT investigations of the early oxidation of U_3Si_2 in the presence of adsorbed oxygen molecules are significant. It is important to note that the oxygen molecule interacts strongly with the U_3Si_2 surfaces, with the adsorption characterized by significant charge transfer from the interacting surfaces to the adsorbing oxygen molecule. The donation of electrons into the partially filled π_{2p}^{*} orbital resulted in the formation of elongated O-O bonds which are precursors for dissociation of O_2 on the U_3Si_2 surfaces. Hence, the U_3Si_2 surfaces are shown to be easily oxidized by dissociated oxygen molecules which implies that dissociation is a necessary step before the oxidation of U_3Si_2. This is consistent with the more stable exothermic energies calculated for dissociative processes compared to the molecular adsorption.

Experimental analysis of the oxidized U_3Si_2 samples suggest the formation of higher oxides using Raman spectroscopy and XRD techniques, and this is consistent with the corrosion products formed on U_3Si_2 surfaces as observed in the DFT calculations. The low intensity of the T_{2g} Raman peak is typical of fluorite UO_2 structure, which appeared on the surface layer of the U_3Si_2 samples as a result of exposure to oxygen. The presence of the USi secondary phase is due to the incomplete reaction between uranium and silicon during sample preparation using a powder metallurgy technique. This suggest that U_3Si_2 manufacturing and handling must be done in a controlled environment. This will impact the cost of fuel production as the currently used UO_2 fuel does not require such an elaborate manufacturing environment.

To further improve our understanding, the adsorption and dissociation reactions of H_2O on the clean oxygen-covered and defective U_3Si_2 (001), (110), and (100) surfaces was investigated using DFT calculations. The adsorption energetics and characteristics of molecular water adsorption were compared with full dissociative and mixed adsorption modes on the U_3Si_2 surfaces.

It is clear from the DFT calculations that the major interactions between the adsorbing water molecules and the U_3Si_2 surfaces occur through oxygen on the surface U or Si site. Compared to the clean surfaces, pre-adsorbed O atoms are shown to enhance the activation the O-H bonds of water and their subsequent dissociation reactions to form surface hydroxyl species, which are driven by significant charge transfer from the surface to the adsorbing species. Results also showed that surface defects stabilize the adsorption and dissociation of H_2O compared to a stoichiometric surfaces.

The atomic-level insights from this work provide fundamental understanding of the adsorption mechanisms of the oxidation of U_3Si_2 in the presence of oxygen and water, and might open new avenues for the rational design of oxidation resistance and accident tolerant fuel for nuclear reactors. Overall, the work presented in this section of the thesis suggest that the oxidation of U_3Si_2 fuel pellet can be improved by developing preparation methods that favor the formation of a preferred surface orientation.

9.3. Original contribution

The following are original contributions that can be drawn from the research findings obtained in this study:

I. The thermophysical properties of UB_2 and U_3Si_2 were calculated using atomic scale methods to complement experimental efforts. The contributions from phonon-phonon scattering and electron-electron scattering were determined for the first time. Even though experimental data is available for the thermal conductivity of U_3Si_2, this work established the anisotropic nature of the thermal properties which is difficult to derive from experiment.

II. The calculated point defects and fission products accumulation affect the volume change and secondary phase formation in UB_2. The formation ZrB_2 and Zr as secondary phases in UB_2 was predicted for the first time. This has implication for the microstructural evolution of UB_2 under radiation as well as the thermophysical properties.

III. The oxidation behavior of U_3Si_2 in an oxygen environment indicate that U_3Si_2 fuel could oxidized due to formation of oxides of uranium on the (001)-U termination, (110) and (111) surfaces based on the bond lengths analysis Bader charge transfer. This is consistent with experimental observation. However, there is formation of Si-O bonds in some of the configurations explored in the (001)-U-Si termination. This has potential for protection of U_3Si_2 surfaces due to the possibility of Si-O type oxides acting as passivating layer. This conclusion is based on the Bader charge analysis which show the transfer of electrons from the surface uranium or silicon atoms to the interacting oxygen molecule or atoms. Further bond length analysis also supports the transfer of charge to the oxygen based on the bond elongation after adsorption.

9.4. Future work

9.4.1. Pellet-cladding interaction

Despite the progress described in this thesis, there remains substantial work in investigating the thermophysical properties, oxidation, and irradiation performance of the analyzed fuels in order to ensure their compatibility with next-generation cladding materials such as SiC and FeCrAl among others. Therefore, work is ongoing to understand the process of Pellet-Cladding Interaction (PCI) as it is of concern in U_3Si_2-SiC system. It is well known that PCI is associated with Stress Corrosion Cracking (SCC) when aggressive FPs, generated in the fuel pellets, interact with the inner surface of the fuel cladding material [360]. Over time, the cladding is additionally subject to increasing concentrations of stress, from either mechanical contact with the swollen cracked fuel

pellets, or from the building pressure of gaseous FPs. These processes are well understood in Zircalloy-UO_2 systems. Due to the lack of data on U_3Si_2-SiC fuel-cladding systems, DFT and MD simulations can provide fundamental insights into the migration processes and the electronic structure at the interface. The advantages of using DFT include the ability to study the effects of FPs on the volume change, diffusivity of elements, and mechanical properties of U_3Si_2-SiC as a function of temperature.

9.4.2. Phonon and magnetic properties of some actinide compounds for ATF using neutron diffraction scattering

A neutron scattering measurement of phonon density of states will complement and provide additional information to validate theoretical prediction. There is ongoing work to measure phonon density of states for U_3Si_2 (both pristine and oxidized), UO_3, and U_3O_8 at 300 K. Using either the C5 or N5 triple axis spectrometers with PG002 monochromator and analyzer crystals, at each temperature we will perform energy scans up to 10 THz at several momentum transfers in order to clearly identify phonon excitations and obtain the phonon density of states. We will perform the measurements in a fixed final energy mode and will employ both E_f =3.35 and E_f =7.37 THz respectively in order to obtain a large coverage of energy-momentum transfers. The results will be compared with our models to further gain insight on the validity of the theoretical calculations and to examine the behavior of thermal properties in the reactor environment.

In addition, the diffraction patterns as a function of temperature will be measured in order to identify the presence of any possible magnetic order in pristine U_3Si_2. Initially, the patterns will be measured at high and low temperatures. If the results exhibit a change beyond the expected temperature dependence due to the change in atomic spacing and lattice vibrations, then further temperature dependence search will be investigated for any possible magnetic phase transition. This measurement will resolve any conflicting results regarding magnetic properties of this material from theoretical calculations and experimental measurements.

9.4.3. Thermophysical properties of $(U_xAm_{1-x})O_2$ MOX Fuel

Uranium dioxide is the standard fuel in today's Light Water Reactors. It is subjected to extreme conditions such as high radiation dosage and temperature. This leads to generation of minor actinides (MAs) oxides such as AmO_2, CmO_2, and NpO_2 during reactor operation. Due to the large

yield, long half-life, and high radioactivity of the MAs, it is important to develop technologies for their reuse, just like PuO_2 and ThO_2 oxides. In comparison to $(U_xPu_{1-x})O_2$, $(U_xTh_{1-x})O_2$, and $(U_xNp_{1-x})O_2$ MOX, there is limited studies on $(U_xAm_{1-x})O_2$ fuel [361–365]. One of the most promising techniques for the reuse of MAs is to add MA elements into the MOX fuel, which can serve as fuel for fast breeder reactors and/or transmutation reactors [366]. The use of MA based MOX fuel is dependent on thorough understanding of its thermophysical properties needed for prediction of in-pile fuel behavior when used in parametrization of performance codes.

In recent time, Bellino *et al.* [367] determined the thermophysical properties of $(Np_xPu_{1-x})O_2$ MOX fuel using molecular dynamics, while Cooper *et al.* [364] calculated the thermal conductivity of $(U_xTh_{1-x})O_2$ and $(U_xPu_{1-x})O_2$. They reported that the thermal conductivity of MOX fuel is independent of solid solution composition at high temperature, however there is a very limited work on thermophysical properties of MA based MOX fuel [368–371]. Given the success of the empirical potential developed by Cooper *et al.* [363,364,367,372–374] in reproducing the thermophysical properties of actinide oxides such as AnO_2 where An=Ce, U, Th, Pu, Np, Cm, and Am. We decided to use the same potential to study the thermophysical properties of $(U_xAm_{1-x})O_2$ MOX fuel (where x=0.00, 0.25, 0.50, 0.75, and 1.00) from 300 to 3200 K with emphasis on the calculation of lattice constants, linear coefficient of thermal expansion, enthalpy, heat capacity at constant pressure, elastic constants, and the thermal conductivity. Furthermore, the effect of porosity on the thermal conductivity is reported given that ~5% porosity is often present as a result of the pores formed during sintering [375].

The focus on thermal expansion is due to the importance of fuel pellet–cladding interaction, which has been studied for UO_2, ThO_2, NpO_2, and MOX fuels [363,367,371,376,377]. Thermal conductivity plays a major role in efficient heat dissipation and might even delay the onset of accidents when properly tuned. There is a significant body of work to determine thermal conductivity by experiments and theoretical calculations. For example, Li *et al*. [378] used partial ionic model of Born-Mayer-Huggins interatomic potential to predict small degradation in thermal conductivity due to mix cation lattice of $(U_{0.7-x}Pu_{0.3}Am_x)O_2$ which has been observed independently by Cooper *et al.* in $(Pu_xTh_{1-x})O_2$ and $(U_xTh_{1-x})O_2$ [364]. Ma *et al*. [361] showed that oxygen vacancies have significant effect on the thermal conductivity of $(U_{0.75}Pu_{0.25})O_{2-y}$. They noted that when oxygen vacancies exist the influence of plutonium concentration on the thermal

conductivity is so small that it can be ignored. The elastic properties in fuel materials play a significant role in the mechanical properties of fuel during irradiation and directly determines the phonon group velocities, which are important parameters that govern thermal properties of materials. Recently, Rahman *et al*. [379] compared the thermomechanical properties of $(U_xTh_{1-x})O_2$, $(U_xPu_{1-x})O_2$, and $(Pu_xTh_{1-x})O_2$ for x=0.3 and 0.5 using MD simulation in the temperature range of 300 to 1500 K. They reported the effect of porosity and fission gas on the degradation of elastic properties of ThO_2 [274].

References

[1] S.J. Zinkle, K.A. Terrani, J.C. Gehin, L.J. Ott, L.L. Snead, Accident tolerant fuels for LWRs: A perspective, J. Nucl. Mater. 448 (2014) 374–379.

[2] M. Chollet, R.C. Belin, J.-C. Richaud, M. Reynaud, F. Adenot, High-Temperature X-ray Diffraction Study of Uranium–Neptunium Mixed Oxides, Inorg. Chem. 52 (2013) 2519–2525.

[3] B.J. Lewis, B. Szpunar, F.C. Iglesias, Fuel oxidation and thermal conductivity model for operating defective fuel rods, J. Nucl. Mater. 306 (2002) 30–43.

[4] H. Stehle, Performance of oxide nuclear fuel in water-cooled power reactors, J. Nucl. Mater. 153 (1988) 3–15.

[5] J. Noirot, L. Desgranges, J. Lamontagne, Detailed characterisations of high burn-up structures in oxide fuels, J. Nucl. Mater. 372 (2008) 318–339.

[6] X.-M. Bai, M.R. Tonks, Y. Zhang, J.D. Hales, Multiscale modeling of thermal conductivity of high burnup structures in UO_2 fuels, J. Nucl. Mater. 470 (2016) 208–215.

[7] H. Kim, M.H. Kim, M. Kaviany, Lattice thermal conductivity of UO_2 using ab-initio and classical molecular dynamics, J. Appl. Phys. 115 (2014) 123510.

[8] H.-G. Kim, J.-H. Yang, W.-J. Kim, Y.-H. Koo, Development Status of Accident-tolerant Fuel for Light Water Reactors in Korea, Nucl. Eng. Technol. 48 (2016) 1–15.

[9] L.J. Ott, K.R. Robb, D. Wang, Preliminary assessment of accident-tolerant fuels on LWR performance during normal operation and under DB and BDB accident conditions, J. Nucl. Mater. 448 (2014) 520–533.

[10] R.C. Birtcher, J.W. Richardson, M.H. Mueller, Amorphization of U_3Si_2 by ion or neutron irradiation, J. Nucl. Mater. 230 (1996) 158–163.

[11] H. E. Flotow, D. W. Osborne, P. A. G. O'Hare, J. L. Settle, F. C. Mrazek, W. N. Hubbard, Uranium Diboride: Preparation, Enthalpy of Formation at 298.15 K, Heat Capacity from 1 to 350 K, and Some Derived Thermodynamic Properties, J. Chem. Phys. 51, 583 (1969).

[12] K.D. Johnson, J. Wallenius, M. Jolkkonen, A. Claisse, Spark plasma sintering and porosity

studies of uranium nitride, J. Nucl. Mater. 473 (2016) 13–17.

[13] J.T. White, A.T. Nelson, J.T. Dunwoody, D.D. Byler, D.J. Safarik, K.J. McClellan, Thermophysical properties of U_3Si_2 to 1773K, J. Nucl. Mater. 464 (2015) 275–280.

[14] J.T. White, A.T. Nelson, D.D. Byler, J.A. Valdez, K.J. McClellan, Thermophysical properties of U_3Si to 1150K, J. Nucl. Mater. 452 (2014) 304–310.

[15] J.T. White, A.T. Nelson, D.D. Byler, D.J. Safarik, J.T. Dunwoody, K.J. McClellan, Thermophysical properties of U_3Si_5 to 1773K, J. Nucl. Mater. 456 (2015) 442–448.

[16] J.T. White, A.T. Nelson, J.T. Dunwoody, D.D. Byler, K.J. McClellan, Thermophysical properties of USi to 1673 K, J. Nucl. Mater. 471 (2016) 129–135.

[17] U. Pierre, The First Nuclear Industry: Radioisotopes, State and Society, presented at Université Pierre et Marie Curie February 2017, 1–57.

[18] J.S. Carlton, R. Smart, V. Jenkins, The nuclear propulsion of merchant ships: Aspects of engineering, science and technology, 4177 (2014).

[19] C. Nandi, D. Jain, V. Grover, R. Dawar, S. Kaity, A. Prakash, A.K. Tyagi, $Zr_{0.70}[Y_{1-x}Nd_x]_{0.30}O_{1.85}$ as a potential candidate for inert matrix fuel: Structural and thermo-physical property investigations, J. Nucl. Mater. 510 (2018) 178–186.

[20] T.Y. Karlsson, G.L. Fredrickson, T.-S. Yoo, D. Vaden, M.N. Patterson, V. Utgikar, Thermal analysis of projected molten salt compositions during FFTF and EBR-II used nuclear fuel processing, J. Nucl. Mater. 520 (2019) 87–95.

[21] A. Einstein, Ist die Trägheit eines Körpers von seinem Energieinhalt abhängig, Ann. Phys. 323 (1905) 639–641.

[22] N. Bohr, J.A. Wheeler, The Mechanism of Nuclear Fission, Phys. Rev. 56 (1939) 426–450.

[23] J.J. Kraushaar, R.A. Ristinen, (1993) "Energy and problems of a technical society", John Wiley and Sons Inc., New York.

[24] T.H. Osgood, Physics in 1939, J. Appl. Phys. 11 (1940) 2–17.

[25] J. Bruno, R.C. Ewing, Spent Nuclear Fuel, Elements. 2 (2006) 343–349.

[26] R.W. Grimes, C.R.A. Catlow, The stability of fission products in uranium dioxide, Phi. Trans. R. Soc. Lon. A (1991) 609–634.

[27] A. Marks, Physics of Uranium and Nuclear Energy- World Nuclear Association, (2014) 1-9.

[28] S.M. Goldberg, R. Rosner, Nuclear Reactors: Generation to Generation.

[29] A Technology Roadmap for Generation IV Nuclear Energy Systems.

[30] F. Tocino, S. Szenknect, A. Mesbah, N. Clavier, N. Dacheux, Dissolution of uranium mixed oxides: The role of oxygen vacancies vs the redox reactions, Prog. Nucl. Energy. 72 (2014) 101–106.

[31] W.D. Magwood, H. Paillere, Looking ahead at reactor development, Prog. Nucl. Energy. 102 (2018) 58–67.

[32] G. Locatelli, M. Mancini, N. Todeschini, Generation IV nuclear reactors: Current status and future prospects, Energy Policy. 61 (2013) 1503–1520.

[33] Nuclear Reactor Types: An environment and energy factfile provided by the IEE, 2005.

[34] Preparing the Future through Innovative Nuclear Technology: Outlook for Generation IV Technologies, 2018 Report.

[35] S.C. Chetal, V. Balasubramaniyan, P. Chellapandi, P. Mohanakrishnan, P. Puthiyavinayagam, C.P. Pillai, S. Raghupathy, T.K. Shanmugham, C.S. Pillai, The design of the Prototype Fast Breeder Reactor, Nucl. Eng. Des. 236 (2006) 852–860.

[36] H. Okamoto, O-U (Oxygen-Uranium), J. Phase Equilibria Diffus. 28 (2007) 497.

[37] L. Leibowitz, R.A. Blomquist, A.D. Pelton, Thermodynamics of the uranium-zirconium system, J. Nucl. Mater. 167 (1989) 76–81.

[38] C. Guéneau, M. Baichi, D. Labroche, C. Chatillon, B. Sundman, Thermodynamic assessment of the uranium–oxygen system, J. Nucl. Mater. 304 (2002) 161–175.

[39] A. Aitkaliyeva, J.W. Madden, C.A. Papesch, J.I. Cole, TEM identification of subsurface phases in ternary U-Pu-Zr fuel, J. Nucl. Mater. 473 (2016) 75–82.

[40] J.K. Fink, Thermophysical properties of uranium dioxide, J. Nucl. Mater. 279 (2000) 1–18.

[41] https://www.world-nuclear.org/information-library/current-and-future-generation/nuclear-power-in-the-world-today.aspx

[42] R.J.M. Konings, T. Wiss, O. Beneš, Predicting material release during a nuclear reactor accident, Nat. Publ. Gr. 14 (2015) 247–252.

[43] J.A. Turnbull, R.M. Cornell, The re-solution of fission-gas atoms from bubbles during the irradiation of UO_2 at an elevated temperature, J. Nucl. Mater. 41 (1971) 156–160.

[44] S. Kashibe, K. Une, K. Nogita, Formation and growth of intragranular fission gas bubbles in UO_2 fuels with burnup of 6–83 GWd/t, J. Nucl. Mater. 206 (1993) 22–34.

[45] T. Cardinaels, K. Govers, B. Vos, S. Van den Berghe, M. Verwerft, L. de Tollenaere, G. Maier, C. Delafoy, Chromia doped UO_2 fuel: Investigation of the lattice parameter, J. Nucl. Mater. 424 (2012) 252–260.

[46] J. Braun, C. Guéneau, T. Alpettaz, C. Sauder, E. Brackx, R. Domenger, S. Gossé, F. Balbaud-Célérier, Chemical compatibility between UO_2 fuel and SiC cladding for LWRs. Application to ATF (Accident-Tolerant Fuels), J. Nucl. Mater. 487 (2017) 380–395.

[47] D. Chandramouli, S.T. Revankar, Development of Thermal Models and Analysis of UO_2 - BeO Fuel during a Loss of Coolant Accident, Int. J. Nucl. Ener. 2014 (2014) 1–9.

[48] Y. Che, G. Pastore, J. Hales, K. Shirvan, Modeling of Cr_2O_3-doped UO_2 as a near-term accident tolerant fuel for LWRs using the BISON code, Nucl. Eng. Des. 337 (2018) 271–278.

[49] J. Arborelius, K. Backman, L. Hallstadius, M. Limbäck, J. Nilsson, B. Rebensdorff, G. Zhou, K. Kitano, R. Löfström, G. Rönnberg, Advanced doped UO_2 pellets in LWR applications, J. Nucl. Sci. Technol. 43 (2006) 967–976.

[50] D. Shepherd, A review of Accident Tolerant Fuel (ATF) concepts, (2018).

[51] Nuclear Energy Agency, state-of-the-Art Report on Light Water Reactor Accident-Tolerant Fuels, (2018).

[52] D. Kim, K.S. Kim, D.S. Kim, J.S. Oh, J.H. Kim, J.H. Yang, Y. Koo, Development status of

microcell UO_2 pellet for accident-tolerant fuel, Nucl. Eng. Technol. 50 (2018) 253–258.

[53] Y. Miao, K.A. Gamble, D. Andersson, B. Ye, Z. Mei, G. Hofman, A.M. Yacout, Gaseous swelling of U_3Si_2 during steady-state LWR operation: A rate theory investigation, Nucl. Eng. Des. 322 (2017) 336–344.

[54] T. Yao, B. Gong, L. He, Y. Miao, J.M. Harp, M. Tonks, J. Lian, In-situ TEM study of the ion irradiation behavior of U_3Si_2 and U_3Si_5, J. Nucl. Mater. 511 (2018) 56–63.

[55] E. Sooby-Wood, J.T. White, C.J. Grote, A.T. Nelson, U_3Si_2 behavior in H_2O: Part I, flowing steam and the effect of hydrogen, J. Nucl. Mater. 501 (2018) 404–412.

[56] Y. Miao, J. Harp, K. Mo, Y. Soo, S. Zhu, A.M. Yacout, Microstructure investigations of U_3Si_2 implanted by high-energy Xe ions at 600 ^oC, J. Nucl. Mater. 503 (2018) 314–322.

[57] A.T. Nelson, A. Migdisov, E. Sooby-Wood, C.J. Grote, U_3Si_2 behavior in H_2O environments: Part II , pressurized water with controlled redox chemistry, J. Nucl. Mater. 500 (2018) 81–91.

[58] D.J. Antonio, K. Shrestha, J.M. Harp, C.A. Adkins, Y. Zhang, J. Carmack, K. Gofryk, Thermal and transport properties of U_3Si_2, J. Nucl. Mater. 508 (2018) 154–158.

[59] D. Adorno, A. Benarosch, S. Middleburgh, K.D. Johnson, Spark plasma sintering and microstructural analysis of pure and Mo doped U_3Si_2 pellets, J. Nucl. Mater. 496 (2017) 234–241.

[60] J. Turner, J. Buckley, G. Phillips, T.J. Abram, The use of gadolinium as a burnable poison within U_3Si_2 fuel pellets, J. Nucl. Mater. 509 (2018) 204–211.

[61] C. Sven, T. Lixona, J. Taylor, Crystal Structure Evolution of U-Si Nuclear Fuel Phases as a Function of Temperature, LA-UR-18-28584 (2018).

[62] E.G. Obbard, K.D. Johnson, P.A. Burr, D.A. Lopes, D.J. Gregg, K.-D. Liss, G. Griffiths, N. Scales, S.C. Middleburgh, Anisotropy in the thermal expansion of uranium silicide measured by neutron diffraction, J. Nucl. Mater. 508 (2018) 516–520.

[63] T. Wang, N. Qiu, X. Wen, Y. Tian, J. He, K. Luo, X. Zha, Y. Zhou, Q. Huang, J. Lang, S. Du, First-principles investigations on the electronic structures of U_3Si_2, J. Nucl. Mater.

469 (2016) 194–199.

[64] M.J. Noordhoek, T.M. Besmann, D. Andersson, S.C. Middleburgh, A. Chernatynskiy, Phase equilibria in the U-Si system from first-principles calculations, J. Nucl. Mater. 479 (2016) 216–223.

[65] K. McClellan, FY2015 Ceramic Fuels Development Annual Highlights, Technical Report, Los Alamos, NM, USA, (2015).

[66] S.C. Middleburgh, R.W. Grimes, E.J. Lahoda, C.R. Stanek, D.A. Andersson, Non-stoichiometry in U_3Si_2, J. Nucl. Mater. 482 (2016) 300–305.

[67] D.A. Andersson, X.-Y. Liu, B. Beeler, S.C. Middleburgh, A. Claisse, C.R. Stanek, Density functional theory calculations of self- and Xe diffusion in U_3Si_2, J. Nucl. Mater. 515 (2019) 312–325.

[68] D.A. Lopes, V. Kocevski, T.L. Wilson, E.E. Moore, T.M. Besmann, Stability of U_5Si_4 phase in U-Si system : Crystal structure prediction and phonon properties using fi rst-principles calculations, J. Nucl. Mater. 510 (2018) 331–336.

[69] B. Beeler, M. Baskes, D. Andersson, M.W.D. Cooper, Y. Zhang, A modified Embedded-Atom Method interatomic potential for uranium-silicide, J. Nucl. Mater. 495 (2017) 267–276.

[70] S.F. Matar, J. Etourneau, The electronic structures of uranium borides from local spin density functional calculations, Int. J. Inorg. Mater. 2 (2000) 43–51.

[71] E. Jossou, D. Oladimeji, L. Malakkal, S. Middleburgh, B. Szpunar, J. Szpunar, First-principles study of defects and fission product behavior in uranium diboride, J. Nucl. Mater. 494 (2017) 147–156.

[72] P.A. Burr, E. Kardoulaki, R. Holmes, S.C. Middleburgh, Defect evolution in burnable absorber candidate material: Uranium diboride, UB_2, J. Nucl. Mater. 513 (2019) 45–55.

[73] H. Guo, J. Wang, D. Chen, W. Tian, S. Cao, Boro/carbothermal reduction synthesis of uranium tetraboride and its oxidation behavior in dry air, (2019) 1049–1056.

[74] Y. Miao, J. Harp, K. Mo, S. Bhattacharya, P. Baldo, A.M. Yacout, Short Communication

on “In-situ TEM ion irradiation investigations on U_3Si_2 at LWR temperatures,” J. Nucl. Mater. 484 (2017) 168–173.

[75] Y. Miao, K. Mo, A. Yacout, J. Harp, Simulated Fission Gas Behavior in Silicide Fuel at LWR Conditions, Annual Report from Argonne National Laboratory, 2016.

[76] Y. He, P. Chen, Y. Wu, G.H. Su, W. Tian, S. Qiu, Preliminary evaluation of U_3Si_2 - FeCrAl fuel performance in light water reactors through a multi-physics coupled way, J. Nucl. Mater. 328 (2018) 27–35.

[77] L. He, J.M. Harp, R.E. Hoggan, A.R. Wagner, Microstructure studies of interdiffusion behavior of U_3Si_2/Zircaloy-4 at 800 and 1000 ^oC, J. Nucl. Mater. 486 (2017) 274–282.

[78] R.E. Hoggan, L. He, J.M. Harp, Interdiffusion behavior of U_3Si_2 with FeCrAl via diffusion couple studies, J. Nucl. Mater. 502 (2018) 356–369.

[79] K.A. Gamble, J.D. Hales, K.A. Gamble, J.D. Hales, Preliminary Modeling of Accident Tolerant Fuel Concepts under Accident Conditions, Top Fuel Conference, (2016).

[80] Y. Miao, K.A. Gamble, D. Andersson, Z. Mei, A.M. Yacout, Rate theory scenarios study on fi ssion gas behavior of U_3Si_2 under LOCA conditions in LWRs, Nucl. Eng. Des. 326 (2018) 371–382.

[81] R. Liu, W. Zhou, J. Cai, Multiphysics modeling of accident tolerant fuel-cladding U_3Si_2-FeCrAl performance in a light water reactor, Nucl. Eng. Des. 330 (2018) 106–116.

[82] Y. He, K. Shirvan, Y. Wu, G.H. Su, Fuel performance optimization of U_3Si_2-SiC design during normal , power ramp and RIA conditions, J. Nucl. Engr. & Des. 353 (2019) 110276.

[83] Y. Miao, J. Harp, K. Mo, S. Zhu, T. Yao, J. Lian, A.M. Yacout, Bubble morphology in U_3Si_2 implanted by high-energy Xe ions at 300 ^oC, J. Nucl. Mater. 495 (2017) 146–153.

[84] K. Terrani, D. Wang, L. Ott, and R. Montgomery, The effect of fuel thermal conductivity on the behavior of LWR cores during loss-of-coolant accidents, J. Nucl. Mater. 448 (2014) 512-519.

[85] W. Zhou, W. Zhou, Annals of Nuclear Energy Enhanced thermal conductivity accident

tolerant fuels for improved reactor safety – A comprehensive review, Ann. Nucl. Energy. 119 (2018) 66–86.

[86] G. Youinou, R.S. Sen, Enhanced Accident Tolerant Fuels for LWRs – A Preliminary Systems Analysis, Technical Report, Idaho, USA, 2013.

[87] C. Ronchi, M. Sheindlin, M. Musella, G.J. Hyland, Thermal conductivity of uranium dioxide up to 2900 K from simultaneous measurement of the heat capacity and thermal diffusivity, J. Appl. Phys. 85 (1998) 776–789.

[88] S.L. Hayes, J.K. Thomas, K.L. Peddicord, Material property correlations for uranium mononitride: III. Transport properties, J. Nucl. Mater. 171 (1990) 289–299.

[89] T.K. Huber, H. Breitkreutz, D.E. Burkes, A.J. Casella, A.M. Casella, S. Elgeti, C. Reiter, A.B. Robinson, F.N. Smith, D.M. Wachs, W. Petry, Thermal conductivity of fresh and irradiated U-Mo fuels, J. Nucl. Mater. 503 (2018) 304–313.

[90] P. Bowning, Thermodynamic properties of uranium dioxide: A study of the experimental enthalpy and specific heat, Journal of Nuclear Materials, vol. 98, pp. 345-356, 1981.

[91] S.L. Hayes, J.K. Thomas, K.L. Peddicord, Material property correlations for uranium mononitride, J. Nucl. Mater. 171 (1990) 300–318.

[92] S. Chiba, T. Wakabayashi, Y. Tachi, N. Takaki, A. Terashima, Method to Reduce Long-lived Fission Products by Nuclear Transmutations with Fast Spectrum Reactors, Sci. Rep. (2017) 1–10.

[93] M.G. Marquez, A.M. Ougouag, B. Petrovic, Annals of Nuclear Energy Model for radiation damage-induced grain subdivision and its influence in U_3Si_2 fuel swelling, Ann. Nucl. Energy. (2017).

[94] T. Barani, G. Pastore, D. Pizzocri, D.A. Andersson, C. Matthews, A. Alfonsi, K.A. Gamble, P. Van Uffelen, L. Luzzi, J.D. Hales, Multiscale modeling of fi ssion gas behavior in U_3Si_2 under LWR conditions, J. Nucl. Mater. 522 (2019) 97–110.

[95] A. V Gelis, P. Kozak, A.T. Breshears, M.A. Brown, L. Cari, E.L. Campbell, G.B. Hall, T.G. Levitskaia, V.E. Holfeltz, G.J. Lumetta, Closing the Nuclear Fuel Cycle with a

Simplified Minor Actinide Lanthanide Separation Process (ALSEP) and Additive Manufacturing, (2019) 1–11.

[96] L. Rodríguez-Penalonga, B.Y.M. Soria, A Review of the Nuclear Fuel Cycle Strategies and the Spent Nuclear Fuel Management Technologies, Energies (2017), 10, 1235.

[97] A. Carolin, A. Benarosch, G. El, M. Jonsson, Radiation induced dissolution of U_3Si_2 - A potential accident tolerant fuel, J. Nucl. Mater. 517 (2019) 263–267.

[98] C.M. Lousada, M. Trummer, M. Jonsson, Reactivity of H_2O_2 towards different UO_2 - based materials : The relative impact of radiolysis products revisited, 434 (2013) 434–439.

[99] T. Yan, D. Xie, Z. Chen, R. Yang, K. Zhu, C. Jiang, C. Ma, J. Liu, X. Wang, K. Liu, L. Luo, Q. Pan, Initial oxidation of U_3Si_2 studied by in-situ XPS analysis, J. Nucl. Mater. 520 (2019) 2–6.

[100] E. Sooby-Wood, J.T. White, A.T. Nelson, The effect of aluminum additions on the oxidation resistance of U_3Si_2, J. Nucl. Mater. 489 (2017) 84–90.

[101] A. Kolomiets, L. Havela, A. Llobet, H. Nakotte, K. Kothapalli, Journal of Alloys an d Compounds Impact of hydrogen absorption on crystal structure and magnetic properties of geometrically frustrated Nd_2Ni_2In, J. Alloy. Compd. 566 (2013) 22–30.

[102] O. Barrera, D. Bombac, Y. Chen, T.D. Daff, P. Gong, D. Haley, Understanding and mitigating hydrogen embrittlement of steels: A review of experimental , modelling and design progress from atomistic to continuum, J. Mater. Sci. 53 (2018) 6251–6290.

[103] O. Courty, A.T. Motta, J.D. Hales, Modeling and simulation of hydrogen behavior in Zircaloy-4 fuel cladding, J. Nucl. Mater. 452 (2014) 311–320.

[104] K. Miliyanchuk, L. Havela, S. Ma, Hydrogen absorption in U_3Si_2 and its impact on electronic properties, 487 (2017) 418–423.

[105] S.C. Middleburgh, A. Claisse, D.A. Andersson, R.W. Grimes, P. Olsson, S. Ma, Solution of hydrogen in accident tolerant fuel candidate material: U_3Si_2, J. Nucl. Mater. 501 (2018) 234–237.

[106] D.S. Sholl and J.A. Steckel, *Density Functional Theory: A Practical Introduction* (Wiley,

Hoboken, New Jersey, 2009).

[107] R. Lesar, *Introduction to Computational Materials Science: Fundamental to Applications* (Cambridge University Press, New York, 2013).

[108] K. Lejaeghere, V. Van Speybroeck, G. Van Oost, S. Cottenier, Error Estimates for Solid-State Density-Functional Theory Predictions: An Overview by Means of the Ground-State Elemental Crystals, Crit. Rev. Solid State Mater. Sci. 39 (2014) 1–24.

[109] P. Hohenberg, W. Kohn, Inhomogeneous Electron Gas, Phys. Rev. 136 (1964) B864--B871.

[110] W. Kohn, L.J. Sham, Self-Consistent Equations Including Exchange and Correlation Effects, Phys. Rev. 140 (1965) A1133--A1138.

[111] M. Born, R. Oppenheimer, Zur Quantentheorie der Molekeln, Ann. Phys. 389 (1927) 457–484.

[112] K. Burke, Perspective on density functional theory, J. Chem. Phys. 136 (2012) 150901.

[113] A.D. Becke, Perspective: Fifty years of density-functional theory in chemical physics, J. Chem. Phys. 140 (2014) 18A301.

[114] N.Q. Su, X. Xu, Development of New Density Functional Approximations, Annu. Rev. Phys. Chem. 68 (2017) 155–182.

[115] R.O. Jones, Density functional theory: Its origins, rise to prominence, and future, Rev. Mod. Phys. 87 (2015) 897–923.

[116] E.S. Kryachko, E. V Ludeña, Density functional theory: Foundations reviewed, Phys. Rep. 544 (2014) 123–239.

[117] R.M. Martin, *Electronic structure: Basic theory and practical methods* (Cambridge University Press, UK, 2004).

[118] J.P. Perdew, K. Burke, M. Ernzerhof, Generalized Gradient Approximation Made Simple, Phys. Rev. Lett. 77 (1996) 3865–3868.

[119] D.C. Langreth, J.P. Perdew, Theory of nonuniform electronic systems. I. Analysis of the

gradient approximation and a generalization that works, Phys. Rev. B. 21 (1980) 5469–5493.

[120] D.C. Langreth, M.J. Mehl, Beyond the local-density approximation in calculations of ground-state electronic properties, Phys. Rev. B. 28 (1983) 1809–1834.

[121] J.P. Perdew, W. Yue, Accurate and simple density functional for the electronic exchange energy: Generalized gradient approximation, Phys. Rev. B. 33 (1986) 8800–8802.

[122] K. Burke, J.P. Perdew, Y. Wang, Derivation of a Generalized Gradient Approximation: The PW91 Density Functional BT - Electronic Density Functional Theory: Recent Progress and New Directions, in: J.F. Dobson, G. Vignale, M.P. Das (Eds.), Springer US, Boston, MA, 1998: pp. 81–111.

[123] A.D. Becke, Density-functional exchange-energy approximation with correct asymptotic behavior, Phys. Rev. A. 38 (1988) 3098–3100.

[124] C. Lee, W. Yang, R.G. Parr, Development of the Colle-Salvetti correlation-energy formula into a functional of the electron density, Phys. Rev. B. 37 (1988) 785–789.

[125] J.P. Perdew, K. Burke, M. Ernzerhof, Perdew, Burke, and Ernzerhof Reply:, Phys. Rev. Lett. 80 (1998) 891.

[126] J.P. Perdew, A. Ruzsinszky, G.I. Csonka, O.A. Vydrov, G.E. Scuseria, L.A. Constantin, X. Zhou, K. Burke, Restoring the Density-Gradient Expansion for Exchange in Solids and Surfaces, Phys. Rev. Lett. 100 (2008) 136406.

[127] Z. Wu, R.E. Cohen, More accurate generalized gradient approximation for solids, Phys. Rev. B. 73 (2006) 235116.

[128] A.D. Becke, Density-functional thermochemistry. III. The role of exact exchange, J. Chem. Phys. 98 (1993) 5648–5652.

[129] N.A.W. Holzwarth, G.E. Matthews, R.B. Dunning, A.R. Tackett, Y. Zeng, Comparison of the projector augmented-wave, pseudopotential, and linearized augmented-plane-wave formalisms for density-functional calculations of solids, Phys. Rev. B. 55 (1997) 2005–2017.

[130] K. Parlinski, Z.Q. Li, Y. Kawazoe, Ab initio calculations of phonons in $LiNbO_3$, Phys. Rev. B. 61 (2000) 272–278.

[131] Q. Li, B. Wang, C.H. Woo, H. Wang, R. Wang, First-principles study on the formation energies of intrinsic defects in $LiNbO_3$, J. Phys. Chem. Solids. 68 (2007) 1336–1340.

[132] D.R. Hamann, M. Schluter, C. Chiang, Norm-conseving pseudopotentials,Phys. Rev. Lett. 43, 20 (1979) 20–23.

[133] https://commons.wikimedia.org/wiki/File:Sketch_Pseudopotentials.png.

[134] A.I. Liechtenstein, V.I. Anisimov, J. Zaanen, Density-functional theory and strong interactions: Orbital ordering in Mott-Hubbard insulators, Phys. Rev. B. 52 (1995) 5467–5471.

[135] A.D. Andersson, Density functional theory calculations of defect and fission gas properties in U-Si fuels, Technical Report (2016).

[136] S.L. Dudarev, G.A. Botton, S.Y. Savrasov, C.J. Humphreys, A.P. Sutton, Electron-energy-loss spectra and the structural stability of nickel oxide: An LSDA+U study, Phys. Rev. B. 57 (1998) 1505–1509.

[137] M. Cococcioni, The LDA + U Approach: A Simple Hubbard Correction for Correlated Ground States, Technical Report (2012).

[138] M.T. Czyżfiyk, G.A. Sawatzky, Local-density functional and on-site correlations: The electronic structure of La_2CuO_4 and $LaCuO_3$, Phys. Rev. B. 49 (1994) 14211–14228.

[139] A.G. Petukhov, I.I. Mazin, L. Chioncel, A.I. Lichtenstein, Correlated metals and the LDA + U method, Phys. Rev. B. 67 (2003) 153106.

[140] V.I. Anisimov, F. Aryasetiawan, A.I. Lichtenstein, First-principles calculations of the electronic structure and spectra of strongly correlated systems: the LDA + U method, J. Phys. Condens. Matter. 9 (1997) 767–808.

[141] M. Cococcioni, S. de Gironcoli, Linear response approach to the calculation of the effective interaction parameters in the LDA + U method, Phys. Rev. B. 71 (2005) 35105.

[142] F. Aryasetiawan, K. Karlsson, O. Jepsen, U. Schönberger, Calculations of Hubbard U

from first-principles, Phys. Rev. B. 74 (2006) 125106.

[143] P. Giannozzi, S. Baroni, N. Bonini, M. Calandra, R. Car, C. Cavazzoni, D. Ceresoli, G.L. Chiarotti, M. Cococcioni, I. Dabo, A.D. Corso, S. de Gironcoli, S. Fabris, G. Fratesi, R. Gebauer, U. Gerstmann, C. Gougoussis, A. Kokalj, M. Lazzeri, L. Martin-Samos, N. Marzari, F. Mauri, R. Mazzarello, S. Paolini, A. Pasquarello, L. Paulatto, C. Sbraccia, S. Scandolo, G. Sclauzero, A.P. Seitsonen, A. Smogunov, P. Umari, R.M. Wentzcovitch, QUANTUM ESPRESSO: a modular and open-source software project for quantum simulations of materials, J. Phys. Condens. Matter. 21 (2009) 395502.

[144] M.P. Allen and D.J. Tildesley, *Computer Simulation of Liquids* (Oxford University Press, Oxford, 1987).

[145] M.E. Tuckerman, *Statistical Mechanics: Theory and Molecular Simulation* (Oxford University Press, Oxford, 2009).

[146] T. Wiss, H. Matzke, C. Trautmann, Radiation damage in UO_2 by swift heavy ions, Inst. & Methods in Phys. Res., 122 (1997) 583–588.

[147] D. Wolf, P. Keblinski, S.R. Phillpot, J. Eggebrecht, Exact method for the simulation of Coulombic systems by spherically truncated, pairwise r−1 summation, J. Chem. Phys. 110 (1999) 8254–8282.

[148] S.M. Foiles, M.I. Baskes, M.S. Daw, Embedded-atom-method functions for the fcc metals Cu, Ag, Au, Ni, Pd, Pt, and their alloys, Phys. Rev. B. 33 (1986) 7983–7991.

[149] M.I. Baskes, Modified embedded-atom potentials for cubic materials and impurities, Phys. Rev. B. 46 (1992) 2727–2742.

[150] Y.-M. Kim, B.-J. Lee, M.I. Baskes, Modified embedded-atom method interatomic potentials for Ti and Zr, Phys. Rev. B. 74 (2006) 14101.

[151] J.M. Ziman, Electrons and Phonons: The Theory of Transport Phenomena in Solids, Oxford University Press, Oxford, 2001.

[152] G.K.H. Madsen, D.J. Singh, BoltzTraP. A code for calculating band-structure dependent quantities, Comput. Phys. Commun. 175 (2006) 67–71.

[153] R. Peierls, Zur kinetischen Theorie der Wärmeleitung in Kristallen, Ann. Phys. 395 (1929) 1055–1101.

[154] A.A. Joshi, A. Majumdar, Transient ballistic and diffusive phonon heat transport in thin films, J. Appl. Phys. 74 (1993) 31–39.

[155] G. Chen, Thermal conductivity and ballistic-phonon transport in the cross-plane direction of superlattices, Phys. Rev. B. 57 (1998) 14958–14973.

[156] S.V.J. Narumanchi, J.Y. Murthy, C.H. Amon, Submicron Heat Transport Model in Silicon Accounting for Phonon Dispersion and Polarization, J. Heat Transfer. 126 (2005) 946–955.

[157] M. Omini, A. Sparavigna, An Iterative Approach to the Phonon Boltzmann Equation in the Theory of An iterative approach to the phonon Boltzmann equation in the theory of thermal conductivity, Physica B 212 (1995) 101-112.

[158] W. Li, J. Carrete, N. A. Katcho, N. Mingo, ShengBTE: A solver of the Boltzmann transport equation for phonons, Comput. Phys. Commun. 185 (2014) 1747–1758.

[159] A. Ward, D.A. Broido, D.A. Stewart, G. Deinzer, Ab initio theory of the lattice thermal conductivity in diamond, Phys. Rev. B. 80 (2009) 125203.

[160] A. Ward, D.A. Broido, Intrinsic phonon relaxation times from first-principles studies of the thermal conductivities of Si and Ge, Phys. Rev. B. 81 (2010) 85205.

[161] R. Kubo, Statistical-Mechanical Theory of Irreversible Processes. I. General Theory and Simple Applications to Magnetic and Conduction Problems, J. Phys. Soc. Japan. 12 (1957) 570–586.

[162] M.S. Green, Markoff Random Processes and the Statistical Mechanics of Time-Dependent Phenomena, J. Chem. Phys. 20, 1281 (1952).

[163] A.J.H. McCaughey, M. Kaviany, Introduction, phonon transport in molecular dynamics simulations: formulation and thermal conductivity prediction, Advances heat Transfer 39 (2006) 169–255.

[164] Z. Liang, A. Jain, A.J.H. Mcgaughey, P. Keblinski, Molecular simulations and lattice

dynamics determination of Stillinger-Weber GaN thermal conductivity, J. Appl. Phys. 125104 (2015) 1–5.

[165] K. Termentzidis, O. Pokropyvnyy, M. Woda, S. Xiong, Y. Chumakov, P. Cortona, S. Volz, Large thermal conductivity decrease in point defective Bi_2Te_3 bulk materials and superlattices, J. Appl. Phys. 113 (2013) 13506.

[166] P.K. Schelling, S.R. Phillpot, P. Keblinski, Comparison of atomic-level simulation methods for computing thermal conductivity, Phys. Rev. B. 65 (2002) 1–12.

[167] P.T. Jochym, K. Parlinski, M. Sternik, TiC lattice dynamics from ab initio calculations, Eur. Phys. J. B. 10 (1999) 9–13.

[168] P.T. Jochym, K. Parlinski, Ab initio lattice dynamics and elastic constants of ZrC, Eur. Phys. J. B. 15 (2000) 265–268.

[169] M. Born, On the stability of crystal lattices, Math. Proc. Cambridge Philos. Soc. 36 (1940) 160–172.

[170] W. Voigt, Lehrbuch der Kristallphysik, 1966.

[171] A. Reuss, Berechnung der Fließgrenze von Mischkristallen auf Grund der Plastizitätsbedingung für Einkristalle, ZAMM - J. Appl. Math. Mech. / Zeitschrift Für Angew. Math. Und Mech. 9 (1929) 49–58.

[172] R. Hill, The Elastic Behaviour of a Crystalline Aggregate, Proc. Phys. Soc. Sect. A. 65 (1952) 349.

[173] S.I. Ranganathan, M. Ostoja-Starzewski, Universal Elastic Anisotropy Index, Phys. Rev. Lett. 101 (2008) 55504.

[174] W.R. Buessem, Conference Report-International Symposium On Anisotropy In Single-Crystal Refractory Compounds, Mater. Res. Bull., 1967: p. 969.

[175] O.L. Anderson, A simplified method for calculating the debye temperature from elastic constants, J. Phys. Chem. Solids. 24 (1963) 909–917.

[176] A.G. Every, Determination of the elastic constants of anisotropic solids, NDT E Int. 27 (1994) 3–10.

[177] W. Martiessen and H. Warlimont, Springer Handbook of Condensed Matter and Materials Data, Springer, NY (2205).

[178] H.Y. Xiao, Y. Zhang, W.J. Weber, Thermodynamic properties of $Ce_xTh_{1-x}O_2$ solid solution from first-principles calculations, Acta Mater. 61 (2012) 467–476.

[179] F.D. Murnaghan, The Compressibility of Media under Extreme Pressures., Proc. Natl. Acad. Sci. U. S. A. 30 (1944) 244–247.

[180] G.W. Watson, E.T. Kelsey, N.H. de Leeuw, D.J. Harris, S.C. Parker, Atomistic simulation of dislocations, surfaces and interfaces in MgO, J. Chem. Soc., Faraday Trans. 92 (1996) 433–438.

[181] P.W. Tasker, The stability of ionic crystal surfaces, J. Phys. C Solid State Phys. 12 (1979) 4977–4984.

[182] I. Chorkendorff, J.W. Niemantsverdriet, Concepts of Modern Catalysis and Kinetics, Weinheim: Wiley–VCH, (2003).

[183] F. Bruneval, J.-P. Crocombette, Ab initio formation volume of charged defects, Phys. Rev. B. 86 (2012) 140103.

[184] L.H. Ortega, B.J. Blamer, J.A. Evans, S.M. McDeavitt, Development of an accident-tolerant fuel composite from uranium mononitride (UN) and uranium sesquisilicide (U_3Si_2) with increased uranium loading, J. Nucl. Mater. 471 (2016) 116–121.

[185] J.P. Dancausse, E. Gering, S. Heathman, U. Benedict, L. Gerward, S. Staun Olsen, F. Hulliger, Compression study of uranium borides UB_2, UB_4 and UB_{12} by synchrotron X-ray diffraction, J. Alloys Compd. 189 (1992) 205–208.

[186] X.L. Chen, Q.Y. Tu, M. He, L. Dai, L. Wu, The bond ionicity of MB_2 (M = Mg, Ti, V, Cr, Mn , Zr, Hf, Ta, Al and Y), J. Phys: Condens. Matter. 13 (2001) L723.

[187] S. Baroni, P. Giannozzi, A. Testa, Green-Function Approach to Linear Response in Solids, Phys. Rev. Lett. 58 (1987) 1861–1864.

[188] L. Malakkal, B. Szpunar, J.C. Zuniga, R.K. Siripurapu, J.A. Szpunar, First principles calculation of thermo-mechanical properties of thoria using Quantum ESPRESSO, Int. J.

Comput. Mater. Sci. Eng. (2016) 1650008.

[189] R.M. Hazen, L.W. Finger, High-pressure and high-temperature crystal chemistry of beryllium oxide, J. Appl. Phys. 59 (1986) 3728–3733.

[190] G.K.H. Madsen, P. Blaha, K. Schwarz, E. Sjöstedt, L. Nordström, Efficient linearization of the augmented plane-wave method, Phys. Rev. B. 64 (2001) 195134.

[191] P. Blaha, K. Schwarz, G.K.H. Madsen, D. Kvasnicka, J. Luitz, WIEN2k, an Augmented Plane Wave Plus Local Orbitals Program for Calculating Crystal Properties, Vienna University of Technology, Vienna, 2001.

[192] K.O. Obodo, N. Chetty, First principles LDA + U and GGA + U study of protactinium and protactinium oxides: dependence on the effective U parameter, J. Phys. Condens. Matter. 25 (2013) 145603.

[193] S.C. Middleburgh, D.C. Parfitt, P.R. Blair, R.W. Grimes, Atomic Scale Modeling of Point Defects in Zirconium Diboride, J. Am. Ceram. Soc. 94 (2011) 2225–2229.

[194] B. Dorado, M. Freyss, G. Martin, GGA + U study of the incorporation of iodine in uranium dioxide, Eur. Phys. J. B. 69 (2009) 203–209.

[195] J.H. Lan, Z.C. Zhao, Q. Wu, Y.L. Zhao, Z.F. Chai, W.Q. Shi, First-principles DFT + U modeling of defect behaviors in anti-ferromagnetic uranium mononitride, J. Appl. Phys. 114 (2013).

[196] G. Beckman, R. Kiessling, Thermal Expansion Coefficients for Uranium Boride and β-Uranium Silicide, Nature. (1956) 1341.

[197] S.F. Pugh, XCII. Relations between the elastic moduli and the plastic properties of polycrystalline pure metals, London, Edinburgh, Dublin Philos. Mag. J. Sci. 45 (1954) 823–843.

[198] G.N. Greaves, A.L. Greer, R.S. Lakes, T. Rouxel, Poisson's ratio and modern materials, Nature Mater. 10 (2011) 823–838.

[199] Y.L. Hao, S.J. Li, B.B. Sun, M.L. Sui, R. Yang, Ductile Titanium Alloy with Low Poisson's Ratio, Phys. Rev. Lett. 98 (2007) 216405.

[200] M.E. Fine, L.D. Brown, H.L. Marcus, Elastic constants versus melting temperature in metals, Scr. Metall. 18 (1984) 951–956.

[201] X. Sha, R.E. Cohen, First-principles thermoelasticity of bcc iron under pressure, Phys. Rev. B. 74 (2006) 214111.

[202] Z. Wang, F. Wang, L. Wang, Y. Jia, Q. Sun, First-principles study of negative thermal expansion in zinc oxide, J. Appl. Phys. 114 (2013) 63508.

[203] A. Jain, A.J.H. McGaughey, Thermal transport by phonons and electrons in aluminum, silver, and gold from first principles, Phys. Rev. B. 93 (2016) 81206.

[204] S. Goumri-Said, M.B. Kanoun, Ab-initio investigations of the electronic properties of bulk wurtzite Beryllia and its derived nanofilms, Phys. Lett. A. 374 (2010) 3977–3981.

[205] H. Gzyl, Integration of the boltzmann equation in the relaxation time approximation, J. Stat. Phys. 29 (1982) 617–622.

[206] J. Callaway, Model for lattice Thermal Conductivity at Low Temperatures, Phys. Rev. 113 (1959) 1046–1051.

[207] G.A. Slack, S.B. Austerman, Thermal Conductivity of BeO Single Crystals, J. Appl. Phys. 42 (1971) 4713–4717.

[208] H. Peng, N. Kioussis, D.A. Stewart, Anisotropic lattice thermal conductivity in chiral tellurium from first principles, Appl. Phys. Lett. 107 (2015) 251904.

[209] H. Shao, X. Tan, G.-Q. Liu, J. Jiang, H. Jiang, A first-principles study on the phonon transport in layered BiCuOSe, Sci. Rep. 6 (2016) 21035.

[210] J.L. Snelgrove, G.L. Hofman, C.L. Trybus, T.C. Wiencek, "Development of Very-High-Density Fuels by the Reduced Enrichment for Research and Test Reactors (RERTR) program, Presented at the 19th International Meeting on Reduced Enrichment for RERTR, (1996).

[211] A. Jelea, M. Colbert, F. Ribeiro, G. Tréglia, R.J.M. Pellenq, An atomistic modelling of the porosity impact on UO_2 matrix macroscopic properties, J. Nucl. Mater. 415 (2011) 210–216.

[212] S.C. Middleburgh, P.A. Burr, D.J.M. King, L. Edwards, G.R. Lumpkin, R.W. Grimes, Structural stability and fission product behaviour in U_3Si, J. Nucl. Mater. 466 (2015) 1–6.

[213] Y. Miao, J. Harp, K. Mo, S. Bhattacharya, P. Baldo, A.M. Yacout, In-situ TEM ion irradiation investigations on U_3Si_2 at LWR temperatures, J. Nucl. Mater. 484 (2017) 168–173.

[214] V. V. Rondinella, T. Wiss, The high burn-up structure in nuclear fuel, Mater. Today. 13 (2010) 24–32.

[215] B.J. Jaques, J. Watkins, J.R. Croteau, G.A. Alanko, B. Tyburska-Püschel, M. Meyer, P. Xu, E.J. Lahoda, D.P. Butt, Synthesis and sintering of UN-UO_2 fuel composites, J. Nucl. Mater. 466 (2015) 745–754.

[216] M.R. Tonks, X.Y. Liu, D. Andersson, D. Perez, A. Chernatynskiy, G. Pastore, C.R. Stanek, R. Williamson, Development of a multiscale thermal conductivity model for fission gas in UO_2, J. Nucl. Mater. 469 (2016) 89–98.

[217] B. Dorado, D.A. Andersson, C.R. Stanek, M. Bertolus, B.P. Uberuaga, G. Martin, M. Freyss, P. Garcia, First-principles calculations of uranium diffusion in uranium dioxide, Phys. Rev. B - Condens. Matter Mater. Phys. 86 (2012).

[218] M. Freyss, First-principles study of uranium carbide: Accommodation of point defects and of helium, xenon, and oxygen impurities, Phys. Rev. B - Condens. Matter Mater. Phys. 81 (2010).

[219] D. Pérez Daroca, A.M. Llois, H.O. Mosca, A first-principles study of He, Xe, Kr and O incorporation in thorium carbide, J. Nucl. Mater. 460 (2015) 216–220.

[220] J.H. Lan, L. Wang, S. Li, L.Y. Yuan, Y.X. Feng, W. Sun, Y.L. Zhao, Z.F. Chai, W.Q. Shi, First principles modeling of zirconium solution in bulk UO_2, J. Appl. Phys. 113 (2013).

[221] M.W.D. Cooper, S.C. Middleburgh, R.W. Grimes, Swelling due to the partition of soluble fission products between the grey phase and uranium dioxide, Prog. Nucl. Energy. 72 (2014) 33–37.

[222] P.A. Burr, S.C. Middleburgh, R. Holmes, DFT study of UB_2 for use in nuclear power

applications, Journal Nuclear Materials Conference, Le Corum, Montpellier, France 7–10 November 2016.

[223] Y.J. Zhang, J.H. Lan, T. Bo, C.Z. Wang, Z.F. Chai, W.Q. Shi, First-principles study of barium and zirconium stability in uranium mononitride nuclear fuels, J. Phys. Chem. C. 118 (2014) 14579–14585.

[224] A.K. Rajagopal, J. Callaway, Inhomogeneous electron gas, Phys. Rev. B. 7 (1973) 1912–1919.

[225] D. Vanderbilt, Soft self-consistent pseudopotentials in a generalized eigenvalue formalism, Phys. Rev. B. 41 (1990) 7892–7895.

[226] V.I. Anisimov, F. Aryasetiawan, A.I. Lichtenstein, First-Principles Calculations of the Electronic Structure and Spectra of Strongly Correlated Systems: the LDA + U Method, J. Phys. Condens. Matter. 9 (1997) 767.

[227] E. Jossou, L. Malakkal, B. Szpunar, D. Oladimeji, J.A. Szpunar, A first principles study of the electronic structure, elastic and thermal properties of UB_2, J. Nucl. Mater. 490 (2017) 41–48.

[228] J.D. Pack, H.J. Monkhorst, "special points for Brillouin-zone integrations"-a reply, Phys. Rev. B. 16 (1977) 1748–1749.

[229] R.P. Feynman, Forces in molecules, Phys. Rev. 56 (1939) 340–343.

[230] M. Methfessel, A.T. Paxton, High-precision sampling for Brillouin-zone integration in metals, Phys. Rev. B. 40 (1989) 3616–3621.

[231] K. Momma, F. Izumi, VESTA3 for three-dimensional visualization of crystal, volumetric and morphology data, J. Appl. Crystallogr. 44 (2011) 1272–1276.

[232] K. Momma, F. Izumi, VESTA: a three-dimensional visualization system for electronic and structural analysis, J. Appl. Crystallogr. 41 (2008) 653–658.

[233] A. Kokalj, Computer graphics and graphical user interfaces as tools in simulations of matter at the atomic scale, Comput. Mater. Sci. 28 (2003) 155–168.

[234] G. Mills, H. Jönsson, Quantum and thermal effects in H_2 dissociative adsorption:

Evaluation of free energy barriers in multidimensional quantum systems, Phys. Rev. Lett. 72 (1994) 1124–1127.

[235] G. Henkelman, B.P. Uberuaga, H. Jónsson, Climbing image nudged elastic band method for finding saddle points and minimum energy paths, J. Chem. Phys. 113 (2000) 9901–9904.

[236] G.E. Grechnev, A.V. Fedorchenko, A.V. Logosha, A.S. Panfilov, I.V. Svechkarev, V.B. Filippov, A.B. Lyashchenko, A.V. Evdokimova, Electronic structure and magnetic properties of transition metal diborides, J. Alloys Compd. 481 (2009) 75–80.

[237] S. Otani, T. Aizawa, N. Kieda, Solid solution ranges of zirconium diboride with other refractory diborides: HfB_2, TiB_2, TaB_2, NbB_2, VB_2 and CrB_2, J. Alloys Compd. 475 (2009) 273–275.

[238] D. Pérez Daroca, S. Jaroszewicz, A.M. Llois, H.O. Mosca, First-principles study of point defects in thorium carbide, J. Nucl. Mater. 454 (2014) 217–222.

[239] M. Topsakal, R.M. Wentzcovitch, Accurate projected augmented wave (PAW) datasets for rare-earth elements (RE=La–Lu), Comput. Mater. Sci. 95 (2014) 263–270.

[240] R.F.W. Bader, Atoms in molecules, Acc. Chem. Res. 18 (1985) 9–15.

[241] J.P. Crocombette, Ab initio energetics of some fission products (Kr, I, Cs, Sr and He) in uranium dioxide, J. Nucl. Mater. 305 (2002) 29–36.

[242] Y.J. Zhang, J.H. Lan, C.Z. Wang, Q.Y. Wu, T. Bo, Z.F. Chai, W.Q. Shi, Theoretical investigation on incorporation and diffusion properties of Xe in uranium mononitride, J. Phys. Chem. C. 119 (2015) 5783–5789.

[243] G. Brillant, A. Pasturel, Study of Ba and Zr stability in $UO_{2\pm x}$ by density functional calculations, Phys. Rev. B - Condens. Matter Mater. Phys. 77 (2008) 1–9.

[244] T. Xiao-Feng, L. Chong-Sheng, Z. Zheng-He, G. Tao, Molecular dynamics simulation of collective behaviour of Xe in UO_2, Chinese Phys. B. 19 (2010) 57102.

[245] S.C. Middleburgh, R.W. Grimes, K.H. Desai, P.R. Blair, L. Hallstadius, K. Backman, P. Van Uffelen, Swelling due to fission products and additives dissolved within the uranium

dioxide lattice, J. Nucl. Mater. 427 (2012) 359–363.

[246] R. Gomer, Diffusion of adsorbates on metal surfaces, Rep. Prog. Phys. 53 (1990) 917–1002.

[247] M. Mantina, Y. Wang, L.Q. Chen, Z.K. Liu, C. Wolverton, First principles impurity diffusion coefficients, Acta Mater. 57 (2009) 4102–4108.

[248] I. Charit, Accident Tolerant Nuclear Fuels and Cladding Materials, JOM. 70 (2018) 173–175.

[249] K. Johnson, V. Ström, J. Wallenius, D.A. Lopes, Oxidation of accident tolerant fuel candidates, J. Nucl. Sci. Technol. 54 (2017) 280–286.

[250] E. Sooby-Wood, J.T. White, A.T. Nelson, Oxidation behavior of U-Si compounds in air from 25 to 1000 ^{o}C, J. Nucl. Mater. 484 (2017) 245–257.

[251] W.H. Zachariasen, Crystal chemical studies of the 5f-series of elements. VIII. Crystal structure studies of uranium silicides and of $CeSi_2$, $NpSi_2$ and $PuSi_2$, Acta Crystallogr. 2 (1949) 94.

[252] K. Remschnig, T. Le Bihan, H. Noël, P. Rogl, Structural chemistry and magnetic behavior of binary uranium silicides, J. Solid State Chem. 97 (1992) 391–399.

[253] Y.S. Kim, G.L. Hofman, J. Rest, A.B. Robinson, Temperature and dose dependence of fission-gas-bubble swelling in U_3Si_2, J. Nucl. Mater. 389 (2009) 443–449.

[254] E. Jossou, U. Eduok, N.Y. Dzade, B. Szpunar, J.A. Szpunar, Oxidation behaviour of U_3Si_2: An experimental and first principles investigation, Phys. Chem. Chem. Phys. 20 (2018) 4708–4720.

[255] M.R. Tonks, X.-Y. Liu, D. Andersson, D. Perez, A. Chernatynskiy, G. Pastore, C.R. Stanek, R. Williamson, Development of a multiscale thermal conductivity model for fission gas in UO_2, J. Nucl. Mater. 469 (2016) 89–98.

[256] S. Plimpton, Fast Parallel Algorithms for Short-Range Molecular Dynamics, J. Comput. Phys. 117 (1995) 1–19.

[257] M.I. Baskes, J.S. Nelson, A.F. Wright, Semiempirical modified embedded-atom potentials

for silicon and germanium, Phys. Rev. B. 40 (1989) 6085–6100.

[258] D.T. Morelli, G.A. Slack, High Lattice Thermal Conductivity Solids BT- High Thermal Conductivity Materials, in: S.L. Shindé, J.S. Goela (Eds.), Springer New York, New York, NY, 2006: pp. 37–68.

[259] D.P. Sellan, E.S. Landry, J.E. Turney, A.J.H. McGaughey, C.H. Amon, Size effects in molecular dynamics thermal conductivity predictions, Phys. Rev. B. 81 (2010) 214305.

[260] F. Müller-Plathe, A simple nonequilibrium molecular dynamics method for calculating the thermal conductivity, J. Chem. Phys. 106 (1997) 6082–6085.

[261] M.J.R. and B.S. and J.A. Szpunar, The induced anisotropy in thermal conductivity of thorium dioxide and cerium dioxide, Mater. Res. Express. 4 (2017) 75512.

[262] B. Szpunar, L. Malakkal, E. Jossou, J.A. Szpunar, in: X. Liu, Z. Liu, K. Brinkman, S. Das, S. Dryepondt, J.W. Fergus, Z. Guo, M. Han, J.A. Hawk, T. Horita, P. Hosemann, J. Li, E. Olivetti, A. Pandey, R.B. Rebak, I. Roy, C. Shang, J. Zhang (Eds.), First principles investigations of alternative nuclear fuels BT - energy materials, Springer International Publishing, Cham, 2017, pp. 367-376.

[263] S. J. Clark, M. D. Segall, C. J. Pickard, P. J. Hasnip, M. I. J. Probert, K. Refson, M. C. Payne, First principles methods using CASTEP, Zeitschrift f¨ur Krist. 220 (2005) 567–570.

[264] A.I. Liechtenstein, V.I. Anisimov, J. Zaanen, Density-functional theory and strong interactions: Orbital ordering in Mott-Hubbard insulators, Phys. Rev. B. 52 (1995) R5467--R5470.

[265] H.J. Monkhorst, J.D. Pack, Special points for Brillouin-zone integrations, Phys. Rev. B. 13 (1976) 5188–5192.

[266] J.D. Head, M.C. Zerner, A Broyden—Fletcher—Goldfarb—Shanno optimization procedure for molecular geometries, Chem. Phys. Lett. 122 (1985) 264–270.

[267] L.D. Loch, G.B. Engle, M.J. Snyder, W.H. Duckworth, Surveying of Refractory Uranium Compounds, Tech. Rep. BMI-1124, Battelle Memorial Institute, August 1956.

[268] H. Shimizu, The Properties and Irradiation Behavior of U_3Si_2, Tech. Rep. NAASR-10621, Atomics International, July 1965.

[269] K.M. Taylor, C.H. McMurtry, Synthesis and Fabrication of Refractory Uranium Compounds, Tech. Rep. ORO-400, Carborundum Company, February 1961.

[270] Nuclear Materials Characterization Brochure, NETZSCH Instruments North America, LLC.

[271] D. Chattaraj, C. Majumder, Structural, electronic, elastic, vibrational and thermodynamic properties of U_3Si_2: A comprehensive study using DFT, J. Alloys Compd. 732 (2018) 160–166.

[272] J.T. White, A.T. Nelson, J.T. Dunwoody, D.J. Safarik, K.J. Mcclellan, Corrigendum to "Thermophysical properties of U_3Si_2 to 1773 K" [J . Nucl . Mater . 464 (2015) 275-280], J. Nucl. Mater. 484 (2017) 386–387.

[273] O. Knacke, O. Kubaschewski, K. Hesselmann, Tables, Thermo. Prop. Inorg. Subst. (1991) 1-2541.

[274] M.J. Rahman, B. Szpunar, J.A. Szpunar, Effect of fission generated defects and porosity on thermo-mechanical properties of thorium dioxide, J. Nucl. Mater. 510 (2018) 19–26.

[275] U. Carvajal-Nunez, T.A. Saleh, J.T. White, B. Maiorov, A.T. Nelson, Determination of elastic properties of polycrystalline U_3Si_2 using resonant ultrasound spectroscopy, J. Nucl. Mater. 498 (2018) 438–444.

[276] Z. Wu, E. Zhao, H. Xiang, X. Hao, X. Liu, J. Meng, Crystal structures and elastic properties of superhard IrN_2 and IrN_3 from first principles, Phys. Rev. B. 76 (2007) 54115.

[277] M.A. Ghebouli, B. Ghebouli, M. Fatmi, First-principles calculations on structural, elastic, electronic, optical and thermal properties of $CsPbCl_3$ perovskite, Phys. B Condens. Matter. 406 (2011) 1837–1843.

[278] Z. Zhang, E.J. Maginn, A comparison of methods for melting point calculation using molecular dynamics simulations, J. Chem. Phys., 136 144116 (2012).

[279] M.J. Mehl, B.M. Klein, D.A. Papaconstantopoulos, First principles calculations of elastic

properties of metals, Intermetallic Compounds: Principles and Practice, J. H. Westbrook and R. L. Fleischer, eds., John Wiley and Sons (London, 1994).

[280] B. Szpunar, L. Malakkal, E. Jossou, J.A. Szpunar, First Principles Investigations of Alternative Nuclear Fuels BT - Energy Materials 2017, in: X. Liu, Z. Liu, K. Brinkman, S. Das, S. Dryepondt, J.W. Fergus, Z. Guo, M. Han, J.A. Hawk, T. Horita, P. Hosemann, J. Li, E. Olivetti, A. Pandey, R.B. Rebak, I. Roy, C. Shang, J. Zhang (Eds.), Springer International Publishing, Cham, 2017: pp. 367–376.

[281] A. Berche, C. Rado, O. Rapaud, C. Guéneau, J. Rogez, Thermodynamic study of the U–Si system, J. Nucl. Mater. 389 (2009) 101–107.

[282] B. Beeler, M. Baskes, D. Andersson, M.W.D. Cooper, A modified Embedded-Atom Method interatomic potential for, J. Nucl. Mater. 495 (2017) 267–276.

[283] P.K. Schelling, S.R. Phillpot, P. Keblinski, Comparison of atomic-level simulation methods for computing thermal conductivity, Phys. Rev. B. 65 (2002) 144306.

[284] J.E. Turney, E.S. Landry, A.J.H. McGaughey, C.H. Amon, Predicting phonon properties and thermal conductivity from anharmonic lattice dynamics calculations and molecular dynamics simulations, Phys. Rev. B. 79 (2009) 64301.

[285] H. Peng, N. Kioussis, D.A. Stewart, H. Peng, N. Kioussis, D.A. Stewart, Anisotropic lattice thermal conductivity in chiral tellurium from first principles Anisotropic lattice thermal conductivity in chiral tellurium from first principles, Appl. Phys. Lett. 107, 251904 (2015).

[286] A.H. Wilson, The theory of metals, Cambridge Uni. Press, Cambridge, England, 1953.

[287] K. Srinivasu, B. Modak, T.K. Ghanty, Electronic structure and thermophysical properties of U_3Si_2: A systematic first principle study, J. Nucl. Mater. 510 (2018) 360–365.

[288] T. Miyadai, H. Mori, T. Oguchi, Y. Tazuke, H. Amitsuka, T. Kuwai, Y. Miyako, Magnetic and electrical properties of the U-Si system (part II), J. Magn. Magn. Mater. 104–107 (1992) 47–48.

[289] J.I. Ranasinghe, E. Jossou, L. Malakkal, B. Szpunar, J.A. Szpunar, Study on Radial

Temperature Distribution of Aluminum Dispersed Nuclear Fuels: U_3O_8-Al, U_3Si_2-Al, and UN-Al, J. Nucl. Eng. Radiat. Sci. 4 (2018) 31020–31027.

[290] Y. Zhang, A.D.R. Andersson, A thermal conductivity model for USi compounds, United States, 2017.

[291] S. Zhou, R. Jacobs, W. Xie, E. Tea, C. Hin, D. Morgan, Combined *ab initio* and empirical model of the thermal conductivity of uranium, uranium-zirconium, and uranium-molybdenum, Phys. Rev. Mater. 2 (2018) 83401.

[292] E.S. Landry, M.I. Hussein, A.J.H. McGaughey, Complex superlattice unit cell designs for reduced thermal conductivity, Phys. Rev. B. 77 (2008) 184302.

[293] J.-S. Wang, B. Li, Intriguing Heat Conduction of a Chain with Transverse Motions, Phys. Rev. Lett. 92 (2004) 74302.

[294] J.P.W. Wellington, A. Kerridge, J. Austin, N. Kaltsoyannis, Electronic structure of bulk AnO_2 (An = U, Np, Pu) and water adsorption on the (111) and (110) surfaces of UO_2 and PuO_2 from hybrid density functional theory within the periodic electrostatic embedded cluster method, J. Nucl. Mater. 482 (2016) 124–134.

[295] T. Bo, J.-H. Lan, Y.-L. Zhao, Y.-J. Zhang, C.-H. He, Z.-F. Chai, W.-Q. Shi, First-principles study of water adsorption and dissociation on the UO_2 (111), (110) and (100) surfaces, J. Nucl. Mater. 454 (2014) 446–454.

[296] G. Jomard, F. Bottin, G. Geneste, Water adsorption and dissociation on the PuO_2 (110) surface, J. Nucl. Mater. 451 (2014) 28–34.

[297] T. Bo, J.-H. Lan, Y.-J. Zhang, Y.-L. Zhao, C.-H. He, Z.-F. Chai, W.-Q. Shi, Adsorption and dissociation of H_2O on the (001) surface of uranium mononitride: energetics and mechanism from first-principles investigation, Phys. Chem. Chem. Phys. 18 (2016) 13255–13266.

[298] B.E. Tegner, M. Molinari, A. Kerridge, S.C. Parker, N. Kaltsoyannis, Water Adsorption on AnO_2 {111}, {110}, and {100} Surfaces (An = U and Pu): A Density Functional Theory + U Study, J. Phys. Chem. C. 121 (2017) 1675–1682.

[299] B. Meredig, A. Thompson, H.A. Hansen, C. Wolverton, A. Van De Walle, Method for locating low-energy solutions within DFT+U, Phys. Rev. B - Condens. Matter Mater. Phys. 82 (2010) 2–6.

[300] H.Y. Geng, Y. Chen, Y. Kaneta, M. Kinoshita, Q. Wu, Interplay of defect cluster and the stability of xenon in uranium dioxide from density functional calculations, Phys. Rev. B. 82 (2010) 94106.

[301] B. Dorado, B. Amadon, M. Freyss, M. Bertolus, DFT + U, Phys. Rev. B. 79 (2009) 235125.

[302] A. Christensen, E.A. Carter, First-principles study of the surfaces of zirconia, Phys. Rev. B. 58 (1998) 8050–8064.

[303] R.J.P. Driscoll, D. Wolverson, J.M. Mitchels, J.M. Skelton, S.C. Parker, M. Molinari, I. Khan, D. Geeson, G.C. Allen, A Raman spectroscopic study of uranyl minerals from Cornwall, UK, RSC Adv. 4 (2014) 59137–59149.

[304] L. Desgranges, G. Baldinozzi, P. Simon, G. Guimbretière, Raman spectrum of U_4O_9: A new interpretation of damage lines in UO_2, J. Raman Spectrosc. 2012, 43, 455–458.

[305] R. Rao, R.K. Bhagat, N.P. Salke, A. Kumar, Raman Spectroscopic Investigation of Thorium Dioxide–Uranium Dioxide (ThO_2–UO_2) Fuel Materials, Appl. Spectrosc. 68 (2014) 44–48.

[306] G. Rousseau, L. Desgranges, F. Charlot, N. Millot, J.C. Nièpce, M. Pijolat, F. Valdivieso, G. Baldinozzi, J.F. Bérar, A detailed study of UO_2 to U_3O_8 oxidation phases and the associated rate-limiting steps, J. Nucl. Mater. 355 (2006) 10–20.

[307] R. H. L. Garcia, A. M. Saliba-Silva, E. F. U. Carvalho, N. B. Lima, R. U. Ichikawa and L. G. Martinez, Characterization of uranium silicide powder using XRD INAC, 2013: International Nuclear Atlantic Conference, Brazil.

[308] ASM International, Alloy Phase Diagrams (ASM Handbook), 1998.

[309] R. Smoluchowski, Anisotropy of the Electronic Work Function of Metals, Phys. Rev. 60 (1941) 661–674.

[310] U. Landman, R.N. Hill, M. Mostoller, Lattice relaxation at metal surfaces: An electrostatic model, Phys. Rev. B. 21 (1980) 448–457.

[311] D.R. Lide, Handbook of Chemistry and Physics, 82nd ed.; CRC Press: Boca Raton, Fl, 2001.

[312] G.E. Brown, G.V. Gibbs, Oxygen coordination and Si-O bond, J. Am. Min., 54 (1969) 1528–1539

[313] F. Garrido, A.C. Hannon, R.M. Ibberson, L. Nowicki, B.T.M. Willis, Neutron diffraction studies of U_4O_9: Comparison with EXAFS results, Inorg. Chem. 45 (2006) 8408–8413.

[314] G.C. Allen, P.A. Tempest, J.W. Tyler, Coordination model for the defect structure of hyperstoichiometric UO_{2+x} and U_4O_9, Nature. 295 (1982) 48–49.

[315] S.D. Conradson, B.D. Begg, D.L. Clark, C. Den Auwer, M. Ding, P.K. Dorhout, F.J. Espinosa-Faller, P.L. Gordon, R.G. Haire, N.J. Hess, R.F. Hess, D.W. Keogh, G.H. Lander, D. Manara, L.A. Morales, M.P. Neu, P. Paviet-Hartmann, J. Rebizant, V. V. Rondinella, W. Runde, C.D. Tait, D.K. Veirs, P.M. Villella, F. Wastin, Charge distribution and local structure and speciation in the UO_{2+x} and PuO_{2+x} binary oxides for $x \leq 0.25$, J. Solid State Chem. 178 (2005) 521–535.

[316] F.N. Skomurski, J.W. Wang, R.C. Ewing, U. Becker, Charge distribution and oxygen diffusion in hyperstoichiometric uranium dioxide UO_{2+x} ($x \leqslant 0.25$), J. Nucl. Mater. 434 (2013) 422–433.

[317] K. Li, D. Xue, Estimation of electronegativity values of elements in different valence states, J. Phys. Chem. A. 110 (2006) 11332–11337.

[318] M. Leng, M. Liu, Y. Zhang, Z. Wang, C. Yu, X. Yang, H. Zhang, C. Wang, Polyhedral 50-Facet Cu_2O Microcrystals Partially Enclosed by {311} High-Index Planes: Synthesis and Enhanced Catalytic CO Oxidation Activity, J. Am. Chem. Soc. 132 (2010) 17084–17087.

[319] D. Su, S. Dou, G. Wang, Single Crystalline Co_3O_4 Nanocrystals Exposed with Different Crystal Planes for Li-O_2 Batteries, Sci. Rep. 4 (2014) 5767.

[320] X. Mou, B. Zhang, Y. Li, L. Yao, X. Wei, D.S. Su, W. Shen, Rod-Shaped Fe_2O_3 as an Efficient Catalyst for the Selective Reduction of Nitrogen Oxide by Ammonia, Angew. Chemie Int. Ed. 51 (2012) 2989–2993.

[321] M. Magnuson, S.M. Butorin, L. Werme, J. Nordgren, K.E. Ivanov, J.-H. Guo, D.K. Shuh, Uranium oxides investigated by X-ray absorption and emission spectroscopies, Appl. Surf. Sci. 252 (2006) 5615–5618.

[322] D. Yu, G.S. Hwang, T.A. Kirichenko, S.K. Banerjee, Structure and diffusion of excess Si atoms in UO_2, Phys. Rev. B. 72 (2005) 205204.

[323] M. Yan, Z.-Q. Huang, Y. Zhang, C.-R. Chang, Trends in water-promoted oxygen dissociation on the transition metal surfaces from first principles, Phys. Chem. Chem. Phys. 19 (2017) 2364–2371.

[324] M.N. Huda, A.K. Ray, Density functional study of O_2 adsorption on (100) surface of γ-uranium, Int. J. Quantum Chem. 102 (2005) 98–105.

[325] M.N. Huda, A.K. Ray, A density functional study of molecular oxygen adsorption and reaction barrier on Pu (100) surface , Eur. Phys. J. B. 43 (2005) 131–141.

[326] D.-K. Ko, C.B. Murray, Probing the Fermi Energy Level and the Density of States Distribution in PbTe Nanocrystal (Quantum Dot) Solids by Temperature-Dependent Thermopower Measurements, ACS Nano. 5 (2011) 4810–4817.

[327] B. Beeler, M. Baskes, D. Andersson, M.W.D. Cooper, Y. Zhang, Molecular dynamics investigation of grain boundaries and surfaces in U_3Si_2, J. Nucl. Mater. 514 (2019) 290–298.

[328] T. Bo, J. Lan, Y. Zhao, Y. Zhang, C. He, Z. Chai, W. Shi, Surface Science Surface properties of NpO_2 and water reacting with stoichiometric and atomistic thermodynamics, Surf. Sci. 644 (2016) 153–164.

[329] T. Bo, J.-H. Lan, Y.-L. Zhao, Y.-J. Zhang, C.-H. He, Z.-F. Chai, W.-Q. Shi, Surface properties of NpO_2 and water reacting with stoichiometric and reduced NpO_2 (111), (110), and (100) surfaces from ab initio atomistic thermodynamics, Surf. Sci. 644 (2016) 153–164.

[330] J.P.W. Wellington, B.E. Tegner, J. Collard, A. Kerridge, N. Kaltsoyannis, Oxygen Vacancy Formation and Water Adsorption on Reduced AnO_2{111}, {110}, and {100} Surfaces (An = U, Pu): A Computational Study, J. Phys. Chem. C. 122 (2018) 7149–7165.

[331] M. Molinari, S.C. Parker, D.C. Sayle, M.S. Islam, Water Adsorption and Its Effect on the Stability of Low Index Stoichiometric and Reduced Surfaces of Ceria, J. Phys. Chem. C. (2012), 116, 12, 7073-7078.

[332] T. Bo, J.-H. Lan, C.-Z. Wang, Y.-L. Zhao, C.-H. He, Y.-J. Zhang, Z.-F. Chai, W.-Q. Shi, First-Principles Study of Water Reaction and H_2 Formation on UO_2 (111) and (110) Single Crystal Surfaces, J. Phys. Chem. C. 118 (2014) 21935–21944.

[333] J. Fan, C. Li, J. Zhao, Y. Shan, H. Xu, The Enhancement of Surface Reactivity on CeO_2 (111) Mediated by Subsurface Oxygen Vacancies, J. Phys. Chem. C. (2016), 120, 49, 27917-27924.

[334] Y. Zhukovskii, D. Bocharov, D. Gryaznov, E. Kotomin, First Principles Simulations on Surface Properties and Oxidation of Nitride Nuclear Fuels. Advances in Nuclear Fuel, IntechOpen, edited by S.T. Revankar (2012).

[335] S. Baroni, S. de Gironcoli, A. Dal Corso, P. Giannozzi, Phonons and related crystal properties from density-functional perturbation theory, Rev. Mod. Phys. 73 (2001) 515–562.

[336] K. Reuter, M. Scheffler, Composition , structure , and stability of RuO_2 (110) as a function of oxygen pressure, Phys. Rev. B. 65 (2001) 1–11.

[337] Y.N. Zhang, J. Hu, M. Law, R.Q. Wu, Effect of surface stoichiometry on the band gap of the pyrite FeS_2 (100) surface, Phys. Rev. B. 85 (2012) 1–5.

[338] A.S. Barnard, S.P. Russo, Modelling nanoscale FeS_2 formation in sulfur rich conditions, J. Mater. Chem., (2009) 3389–3394.

[339] W.M. Hyanes, D.R. Lide, T.J. Bruno, Handbook of Chemistry and Physics, 97th ed.; CRC Press: Boca Raton, Fl, 2016-2017.

[340] N.Y. Dzade, A. Roldan, N.H. de Leeuw, DFT-D2 Study of the Adsorption and

Dissociation of Water on Clean and Oxygen-Covered {001} and {011} Surfaces of Mackinawite (FeS), J. Phys. Chem. C. 120 (2016) 21441–21450.

[341] G. Herzberg, Molecular Spectra and Moleculsr Structure. II. Infrared and Raman Spectra of Polyatomic Molecules; Lancaster Press: New York, 1946; p 365.

[342] T. Bo, J. Lan, Y. Zhang, Y. Zhao, C. He, Z. Chai, W. Shi, surface of uranium mononitride: energetics and, Phys. Chem. Chem. Phys. 18 (2016) 13255–13266.

[343] T. Bo, J. Lan, Y. Zhao, Y. Zhang, C. He, Z. Chai, W. Shi, First-principles study of water adsorption and dissociation on the UO_2, J. Nucl. Mater. 454 (2014) 446–454.

[344] V. Shapovalov, T.N. Truong, Ab Initio Study of Water Adsorption on α-Al_2O_3 (0001) Crystal Surface, J. Phys. Chem. B. 104 (2000) 9859–9863.

[345] Z. Pang, S. Duerrbeck, C. Kha, E. Bertel, G.A. Somorjai, M. Salmeron, Adsorption and Reactions of Water on Oxygen-Precovered Cu (110), J. Phys. Chem. C. 120 (2016) 9218–9222.

[346] L. Chen, J. Lu, P. Liu, L. Gao, Y. Liu, F. Xiong, S. Qiu, X. Qiu, Y. Guo, X. Chen, Dissociation and Charge Transfer of H_2O on Cu (110) Probed in Real Time Using Ion Scattering Spectroscopy, Langmuir. 32 (2016) 12047–12055.

[347] C.D. Taylor, T. Lookman, R.S. Lillard, Ab initio calculations of the uranium – hydrogen system : Thermodynamics , hydrogen saturation of α-U and phase-transformation to UH_3, Acta Mater. 58 (2010) 1045–1055.

[348] T. Bo, J.-H. Lan, Y.-J. Zhang, Y.-L. Zhao, C.-H. He, Z.-F. Chai, W.-Q. Shi, Adsorption and dissociation of H_2O on the (001) surface of uranium mononitride: energetics and mechanism from first-principles investigation, Phys. Chem. Chem. Phys. 18 (2016) 13255–13266.

[349] X. Tian, H. Wang, H. Xiao, T. Gao, Adsorption of water on UO_2 (111) surface: Density functional theory calculations, Comput. Mater. Sci. 91 (2014) 364–371.

[350] J. Schoenes, Optical properties and electronic structure of UO_2, J. Appl. Phys. 49 (1978) 1463–1465.

[351] J. Wang, R.C. Ewing, U. Becker, Electronic structure and stability of hyperstoichiometric UO_{2+x} under pressure, Phys. Rev. B. 88 (2013) 24109.

[352] M.A. Henderson, The interaction of water with solid surfaces: fundamental aspects revisited, Surf. Sci. Rep. 46 (2002) 1–308.

[353] C. Ammon, A. Bayer, H.-P. Steinrück, G. Held, Low-temperature partial dissociation of water on Cu(110), Chem. Phys. Lett. 377 (2003) 163–169.

[354] Z. Jiang, T. Fang, Dissociation mechanism of H_2O on clean and oxygen-covered Cu (111) surfaces : A theoretical study, Vaccum. 128 (2016) 252–258.

[355] H. Wang, H. Zhang, J.U.N. Liu, D. Xue, H. Liang, X. Xia, Hydroxyl Group Adsorption on GaN (0001) Surface: First Principles and XPS Studies, J. of Elect. Mater., 48 (2019) 2430–2437.

[356] J. Li, S. Zhu, H. Li, E.E. Oguzie, Y. Li, F. Wang, Bonding Nature of Monomeric H_2O on Pd: Orbital Cooperation and Competition, (2009) 1931–1938.

[357] T. Akbay, A. Staykov, J. Druce, H. Tellez, T. Ishihara, J.A. Kilner, The interaction of molecular oxygen on LaO terminated surfaces of La_2NiO_4, J. Mater. Chem. A, 2016, 4, 13113–13124.

[358] C. Fall, Ab initio study of the work functions of elemental metal crystals, thesis work published by EPFL, Lausanne, (1999).

[359] W. Zhang, L. Liu, L. Wan, L. Liu, L. Cao, F. Xu, J. Zhao, Z. Wu, Electronic structures of bare and terephthalic acid adsorbed TiO_2(110)-(1×2) reconstructed surfaces: origin and reactivity of the band gap states, Phys. Chem. Chem. Phys. 17 (2015) 20144–20153.

[360] B. Cox, Pellet-clad interaction (PCI) failures of zirconium alloy fuel cladding — A review, J. Nucl. Mater. 172 (1990) 249–292.

[361] J. Ma, J. Zheng, M. Wan, J. Du, J. Yang, G. Jiang, Molecular dynamical study of physical properties of $(U_{0.75}Pu_{0.25})O_{2-x}$, J. Nucl. Mater. 452 (2014) 230–234.

[362] S. Nichenko, D. Staicu, Molecular Dynamics study of the mixed oxide fuel thermal conductivity, J. Nucl. Mater. 439 (2013) 93–98.

[363] M.W.D. Cooper, S.T. Murphy, M.J.D. Rushton, R.W. Grimes, Thermophysical properties and oxygen transport in the $(U_x,Pu_{1-x})O_2$ lattice, J. Nucl. Mater. 461 (2015) 206–214.

[364] M.W.D. Cooper, S.C. Middleburgh, R.W. Grimes, Modelling the thermal conductivity of $(U_xTh_{1-x})O_2$ and $(U_xPu_{1-x})O_2$, J. Nucl. Mater. 466 (2015) 29–35.

[365] P.S. Ghosh, N. Kuganathan, C.O.T. Galvin, A. Arya, G.K. Dey, B.K. Dutta, R.W. Grimes, Melting behavior of $(Th,U)O_2$ and $(Th,Pu)O_2$ mixed oxides, J. Nucl. Mater. 479 (2016) 112–122.

[366] T. Wakabayashi, Transmutation characteristics of MA and LLFP in a fast reactor, Prog. Nucl. Energy. 40 (2002) 457–463.

[367] P.A. Bellino, H.O. Mosca, S. Jaroszewicz, Evaluation of thermophysical properties of $(Np,Pu)O_2$ using molecular dynamics simulations, J. Alloys Compd. 695 (2017) 944–951.

[368] O.S. Vălu, D. Staicu, O. Beneš, R.J.M. Konings, P. Lajarge, Heat capacity, thermal conductivity and thermal diffusivity of uranium–americium mixed oxides, J. Alloys Compd. 614 (2014) 144–150.

[369] O. Bene, O.S. V, E. Colineau, J. Griveau, R.J.M. Konings, The low-temperature heat capacity of $(U_{1-y}Am_y)O_2$ for y =0.08 and, J. Nucl. Mater. 507 (2018) 126–134.

[370] J. Zappey, F. Lebreton, P.M. Martin, C. Gu, O.S. V, High temperature heat capacity of (U , Am)$O_{2\pm x}$, J. Nucl. Mater. 494 (2017) 95–102.

[371] T. Matsumoto, T. Arima, Y. Inagaki, K. Idemitsu, M. Kato, K. Morimoto, M. Ogasawara, Thermal conductivity measurement of $(Pu_{1-x}Am_x)O_2$ (x=0.028, 0.072), J. Alloys Compd. 629 (2015) 92–97.

[372] M.J. Qin, M.W.D. Cooper, E.Y. Kuo, M.J.D. Rushton, R.W. Grimes, G.R. Lumpkin, S.C. Middleburgh, Thermal conductivity and energetic recoils in UO_2 using a many-body potential model, J. Phys. Condens. Matter. 26 (2014) 495401.

[373] M.W.D. Cooper, M.J.D. Rushton, R.W. Grimes, A many-body potential approach to modelling the thermomechanical properties of actinide oxides, J. Phys. Condens. Matter. 26 (2014) 105401.

[374] M.W.D. Cooper, C.R. Stanek, J.A. Turnbull, B.P. Uberuaga, D.A. Andersson, Simulation of radiation driven fission gas diffusion in UO_2, ThO_2 and PuO_2, J. Nucl. Mater. 481 (2016) 125–133.

[375] S. Nichenko, D. Staicu, Thermal conductivity of porous UO_2: Molecular Dynamics study, J. Nucl. Mater. 454 (2014) 315–322.

[376] J.-J. Ma, J.-G. Du, M.-J. Wan, G. Jiang, Molecular dynamics study on thermal properties of ThO_2 doped with U and Pu in high temperature range, J. Alloys Compd. 627 (2015) 476–482.

[377] W. Li, J. Ma, J. Du, G. Jiang, Molecular dynamics study of thermal conductivities of $(U_{0.7-x}Pu_{0.3}Am_x)O_2$, J. Nucl. Mater. 480 (2016) 47–51.

[378] H. Xiao, C. Long, X. Tian, H. Chen, Effect of thorium addition on the thermophysical properties of uranium dioxide: Atomistic simulations, Mater. Des. 96 (2016) 335–340.

[379] M.J. Rahman, B. Szpunar, J.A. Szpunar, Comparison of thermomechanical properties of $(U_x,Th_{1-x})O_2$, $(U_x,Pu_{1-x})O_2$ and $(Pu_x,Th_{1-x})O_2$ systems, J. Nucl. Mater. 513 (2019) 8–15.

APPENDIX A

This supporting document contains the plot of Hubbard U fitting to lattice parameter used in Chapter 4 of this thesis.

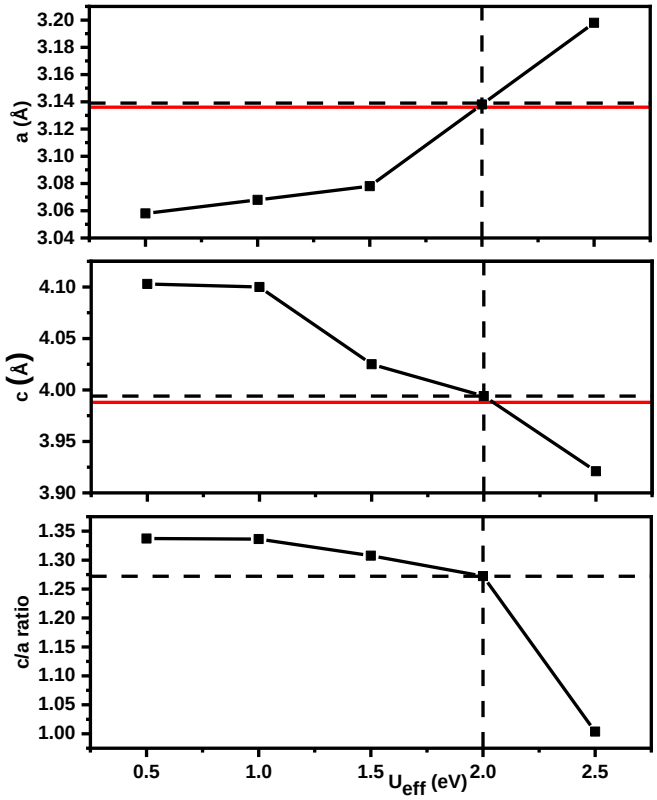

Fig. A.4.1. Lattice parameters of UB_2 as a function of +U for nonmagnetic state. The red solid line represents experimental lattice parameter. A more recent fitting by Burr *et al*. [72] puts the U value at 1.8 eV to 3.2 eV.

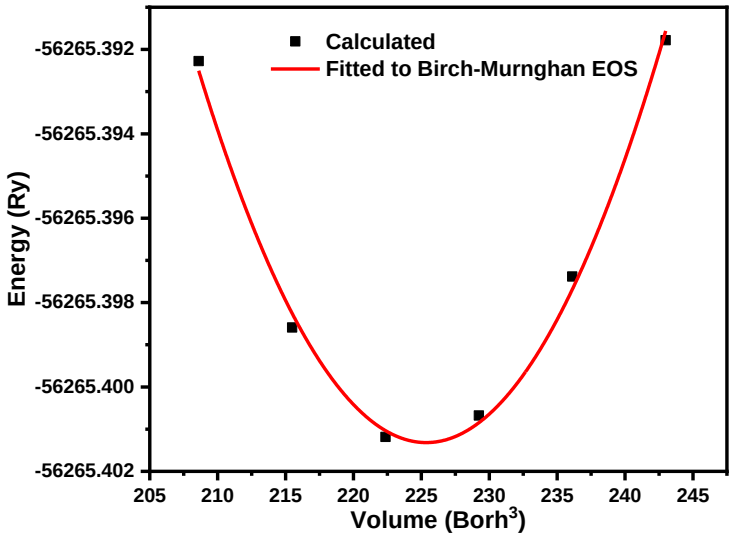

Fig. A.4.2. The calculated total energy versus cell volume and the fitted parameters to the Birch–Murnaghan equation of state (EOS).

APPENDIX B

Table B.5.1. The incorporation energy and solution energy per atom of Zr and Xe in UB_2 at different concentration. Statistical analysis of the median, average, minimum is presented here.

	Zr		Xe	
Conc.	E^{inc}	E^{sol}	E^{inc}	E^{sol}
3.70	–14.48	–6.19	4.21	13.17
7.41	–13.65	–4.68	3.27	12.24
11.11	–13.72	–4.83	4.07	11.96
14.81	–13.05	–4.27	2.99	11.77
Median	–13.69	–4.76	3.17	12.10
Average	–13.73	–4.99	3.39	12.28
Minimum	–14.48	–6.19	2.99	11.77

APPENDIX C

This supporting document contains the detailed information on the Convergence test on Heat Current AutoCorrelation Function (HCACF) with respect to the supercell size, Lattice thermal expansion coefficient (LTEC) and heat capacity at constant pressure (C_p) fitting technique.

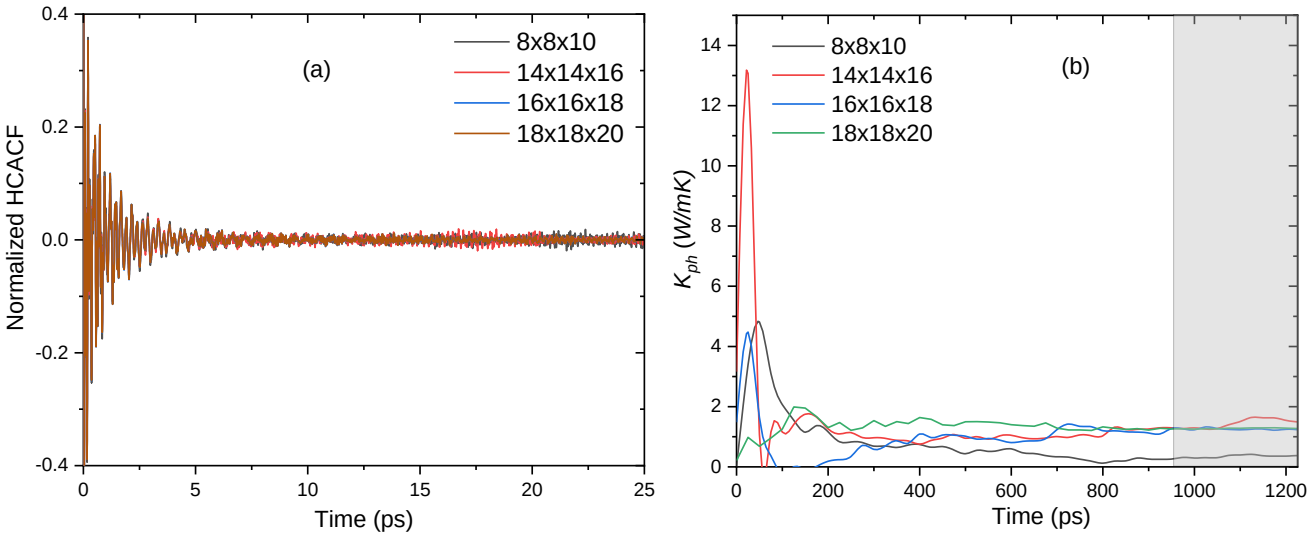

Fig. C.6.1. (a) Convergence of HCACF with respect to supercell size (b) The dependence of k_{ph} on collection time t in ps calculated for cell sizes of $8 \times 8 \times 10$, $14 \times 14 \times 16$, $16 \times 16 \times 18$ and $18 \times 18 \times 20$.

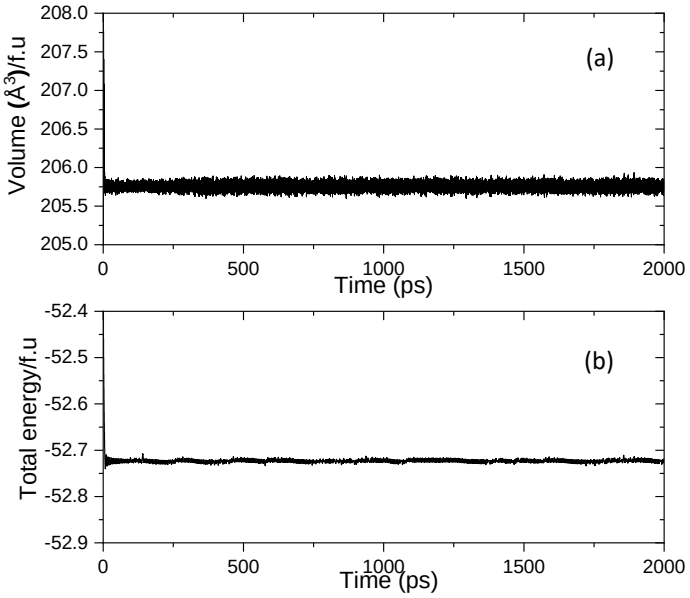

Fig. C.6.2. (a) Convergence of (a) Volume per formula unit (b) Total energy per formula unit.

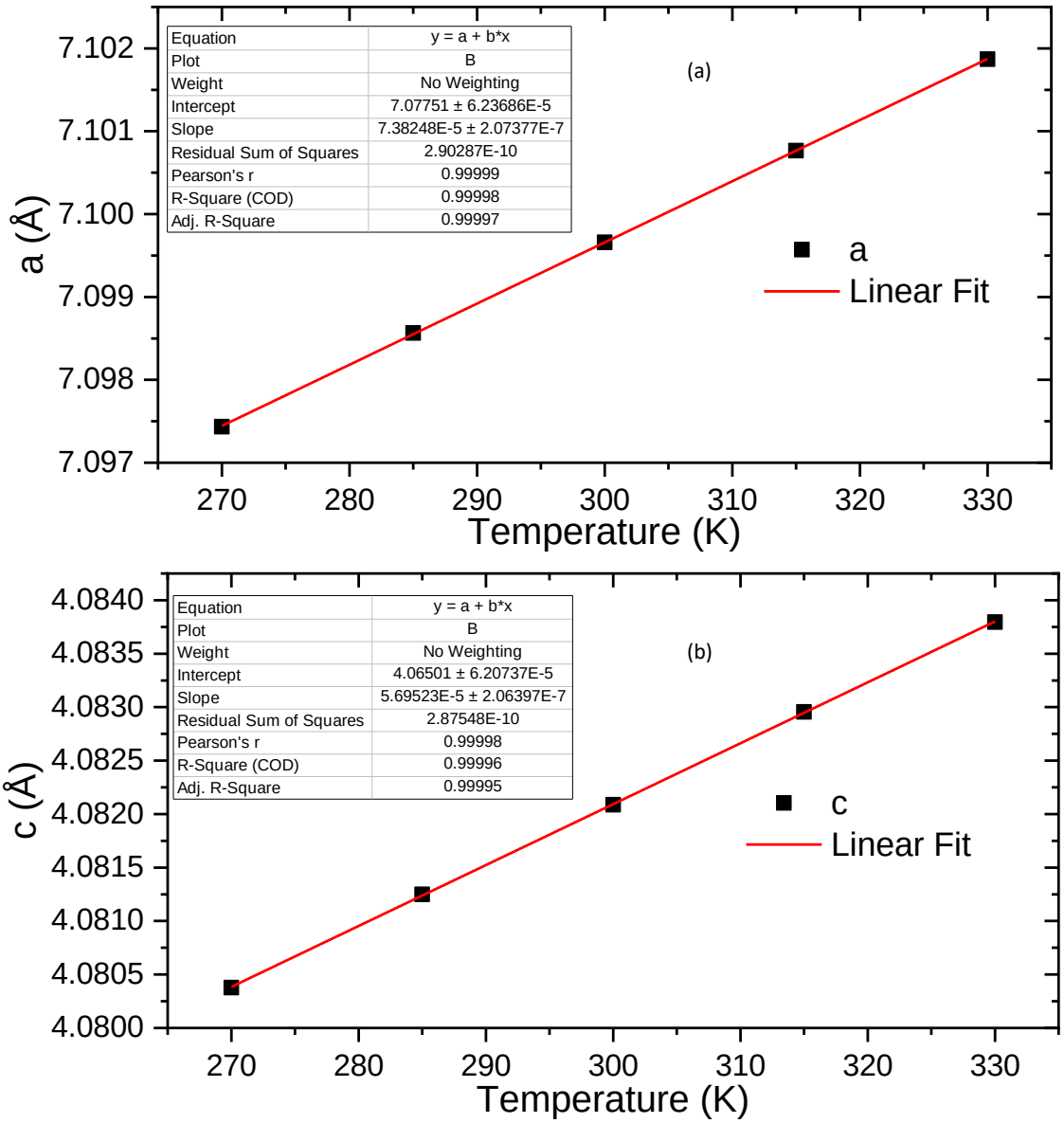

Fig. C.6.3. (a) – (b) Calculation of $\frac{\partial L}{\partial T}$ by fitting a straight line to the lattice parameter at specific temperature and the points within 15 K on either side. L= a or c in Å.

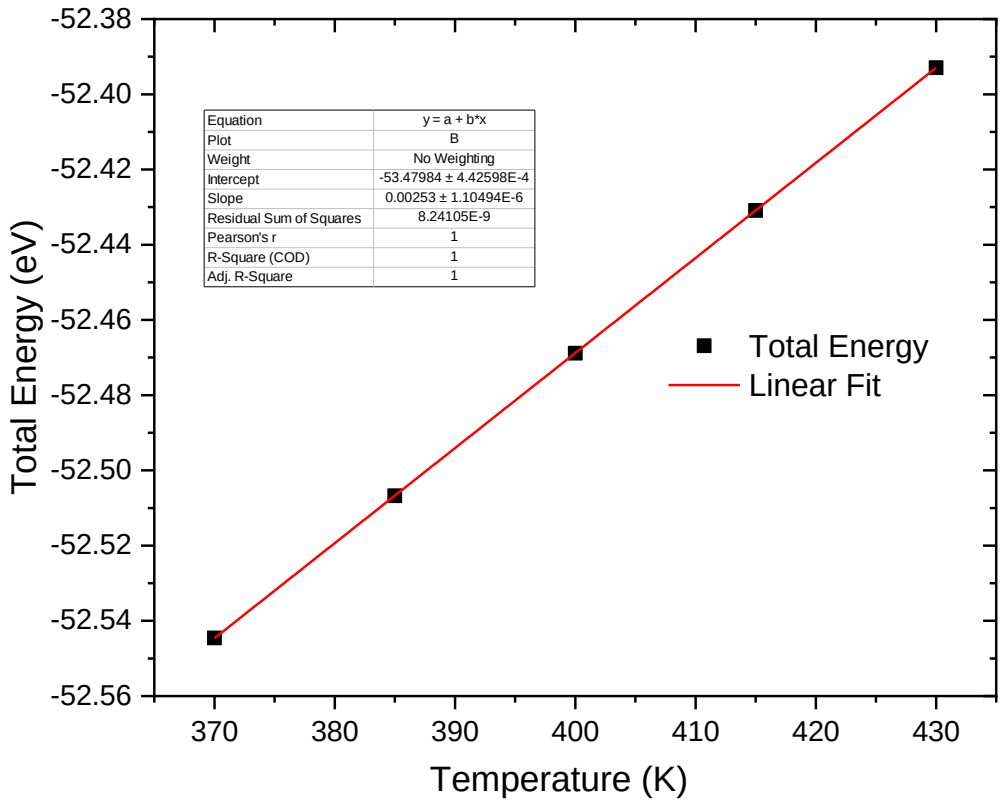

Fig. C.6.4. Calculation of $\left(\frac{\partial H}{\partial T}\right)_p$ by fitting a straight line to the total energy (eV) at specific temperature and the points within 15 K on either side.

APPENDIX D

This supporting material contains the detailed information on all mix mode water adsorption configurations and adsorption energies on stoichiometric U_3Si_2 (001), (110) and (111) surfaces respectively.

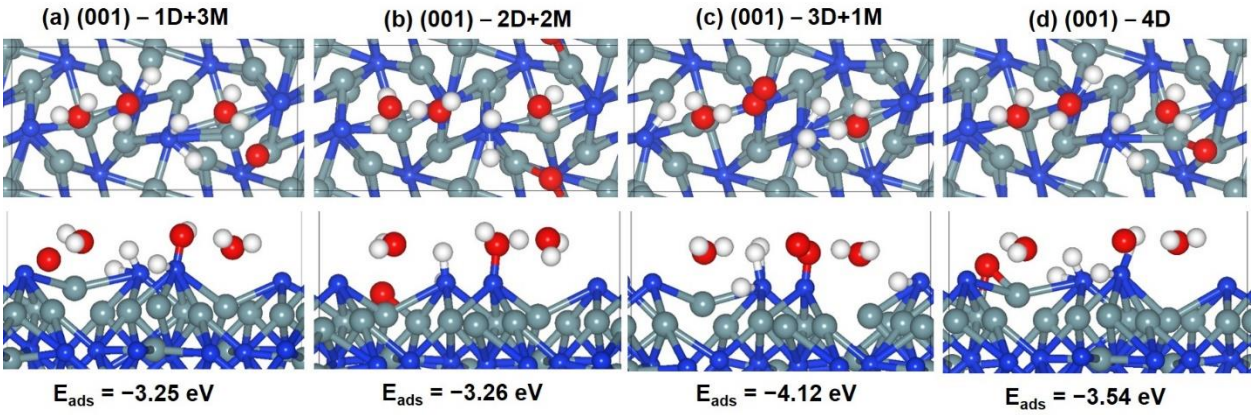

Fig. D.8.1. Top and side view of the relaxed adsorption structures of mix mode (dissociative to molecular) adsorption of (a) 1D + 3M (b) 2M + 2D (c) 3D + 1M (d) 4D H_2O on (001) U_3Si_2 surface. (Color scheme: U = grey, Si = blue, H= white, O = red, D= Dissociated water and M= Water molecule).

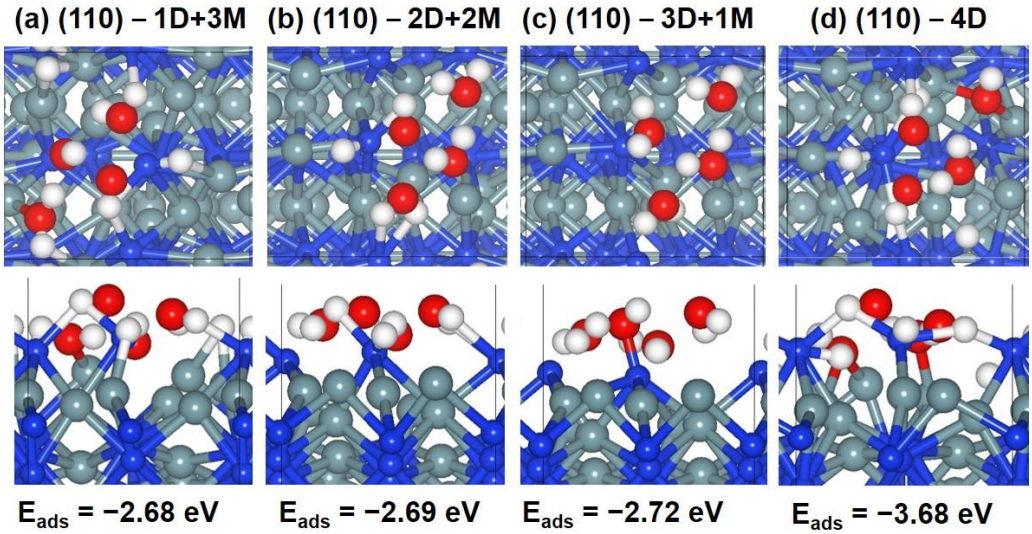

Fig. D.8.2. Top and side view of the relaxed adsorption structures of mix mode (dissociative to molecular) adsorption of (a) 1D + 3M (b) 2M + 2D (c) 3D + 1M (d) 4D H_2O on (110) U_3Si_2 surface. (Color scheme: U = grey, Si = blue, H= white, O = red, D= Dissociated water and M= Water molecule).

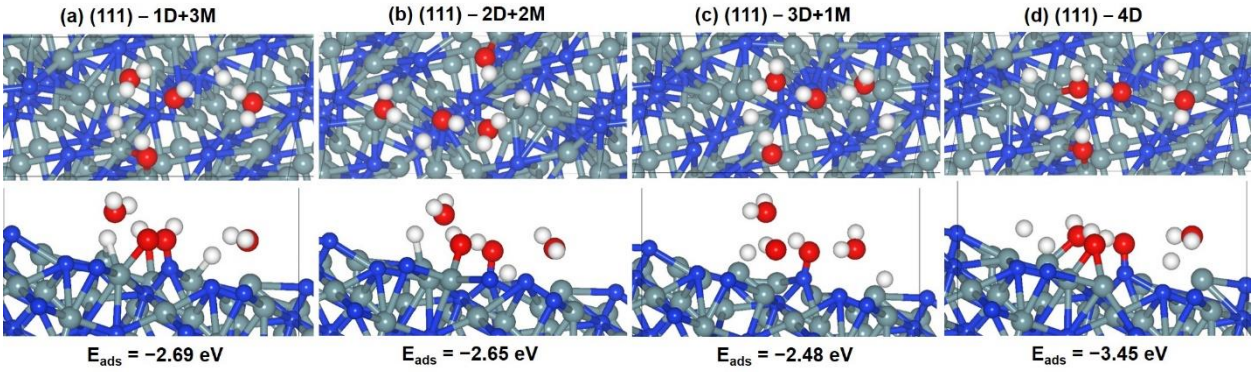

Fig. D.8.3. Top and side view of the relaxed adsorption structures of mix mode (dissociative to molecular) adsorption of (a) 1D + 3M (b) 2M + 2D (c) 3D + 1M (d) 4D H_2O on (111) U_3Si_2 surface. (Color scheme: U = grey, Si = blue, H= white, O = red, D= Dissociated water and M= Water molecule).

Table S8.1. Calculated Adsorption Energy ($E_{ads.}$), Relevant Bond Lengths (d) of atomic (O) Oxygen on (001), (110) and (111) U_3Si_2 surfaces.

Adsorbate	Surface	Config.	$E_{ads.}$ (eV)	d(U–O) (Å)	d(Si–O) (Å)	Δq (e–)
O	(001)	O on U	–2.44	1.981	–	1.06
		O on Si	–0.67	–	2.079	0.15
	(110)	O on U	–2.71	1.999	–	0.76
		O on Si	–0.77	–	1.626	0.10
	(111)	O on U	–2.85	2.060	–	1.01
		O on Si	–0.81	–	2.130	0.14

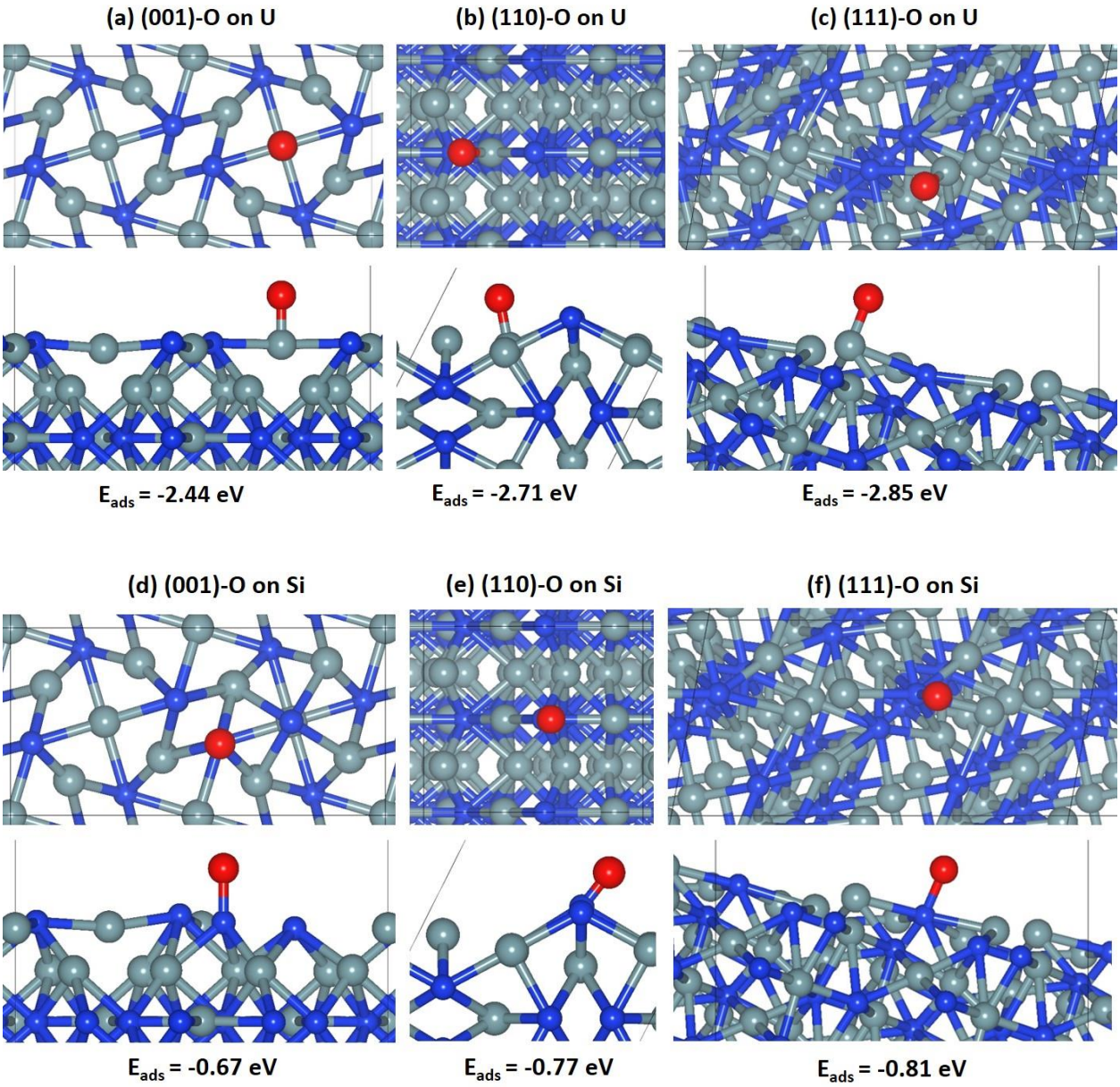

Fig. D.8.4. Top and side view of the relaxed adsorption structures of atomic adsorption on top U-sites on (a) (001) (b) (110) (c) (111) and adsorption on top Si-sites (d) (001) (e) (110) (f) (111) U_3Si_2 surface. (Color scheme: U = grey, Si = blue, H= white, O = red).

APPENDIX E

COPYRIGHT PERMISSIONS

For previously published manuscripts that form a part of a thesis, written permission from the publisher (copyright holder) is required by the College of Graduate and Postdoctoral Studies (CGPS). This appendix includes the copyright permissions from the publishers for the manuscripts that were published or are under review and used in the thesis.

Copyright Permission for Manuscript #1 Used in Chapter 4

Title: A first principles study of the electronic structure, elastic and thermal properties of UB2

Author: Ericmoore Jossou,Linu Malakkal,Barbara Szpunar,Dotun Oladimeji,Jerzy A. Szpunar

Publication: Journal of Nuclear Materials

Publisher: Elsevier

Date: July 2017

Please note that, as the author of this Elsevier article, you retain the right to include it in a thesis or dissertation, provided it is not published commercially. Permission is not required, but please ensure that you reference the journal as the original source. For more information on this and on your other retained rights, please visit: https://www.elsevier.com/about/our-business/policies/copyright#Author-rights

BACK CLOSE WINDOW

Copyright Permission for Manuscript #2 Used in Chapter 5

Copyright Clearance Center RightsLink® Home Account Info Help

Title: First-principles study of defects and fission product behavior in uranium diboride

Author: Ericmoore Jossou,Dotun Oladimeji,Linu Malakkal,Simon Middleburgh,Barbara Szpunar,Jerzy Szpunar

Publication: Journal of Nuclear Materials

Publisher: Elsevier

Date: October 2017

Logged in as:

Ericmoore Jossou

University of Saskatchewan

Account #:

3001455283

LOGOUT

Please note that, as the author of this Elsevier article, you retain the right to include it in a thesis or dissertation, provided it is not published commercially. Permission is not required, but please ensure that you reference the journal as the original source. For more information on this and on your other retained rights, please visit: https://www.elsevier.com/about/our-business/policies/copyright#Author-rights

BACK CLOSE WINDOW

Copyright Permission for Manuscript #3 Used in Chapter 6

Copyright Clearance Center RightsLink® Home Account Info Help

Title: Anisotropic thermophysical properties of U3Si2 fuel: An atomic scale study

Author: Ericmoore Jossou,Md Jahidur Rahman,Dotun Oladimeji,Benjamin Beeler,Barbara Szpunar,Jerzy Szpunar

Publication: Journal of Nuclear Materials

Publisher: Elsevier

Date: 1 August 2019

Logged in as:

Ericmoore Jossou

University of Saskatchewan

Account #:

3001455283

LOGOUT

Copyright Permission for Manuscript #4 Used in Chapter 7

Copyright Clearance Center RightsLink®

Account Info | Help

Title:	Physical chemistry chemical physics
Article ID:	1463-9084
Publication:	Publication1
Publisher:	CCC Republication
Date:	Jan 1, 1999

Logged in as:
Ericmoore Jossou
University of Saskatchewan
Account #:
3001455283
LOGOUT

Order Completed

Thank you for your order.

This Agreement between Ericmoore E Jossou ("You") and Royal Society of Chemistry ("Royal Society of Chemistry") consists of your order details and the terms and conditions provided by Royal Society of Chemistry and Copyright Clearance Center.

License number	Reference confirmation email for license number
License date	May, 20 2019
Licensed content publisher	Royal Society of Chemistry
Licensed content title	Physical chemistry chemical physics
Licensed content date	Jan 1, 1999
Type of use	Thesis/Dissertation
Requestor type	Academic institution
Format	Electronic
Portion	chapter/article
The requesting person/organization	Ericmoore Jossou
Title or numeric reference of the portion(s)	Figure 1,2,3,4,5,6,7,8,9,10,11,12
Title of the article or chapter the portion is from	Oxidation behaviour of U3Si2: an experimental and first principles investigation
Editor of portion(s)	N/A
Author of portion(s)	N/A
Volume of serial or monograph	N/A
Page range of portion	
Publication date of portion	2018
Rights for	Main product
Duration of use	Current edition and up to 5 years
Creation of copies for the disabled	no
With minor editing privileges	no
For distribution to	United States and Canada
In the following language(s)	Original language of publication
With incidental promotional use	no
Lifetime unit quantity of new product	Up to 499
Title	ATOMIC SCALE SIMULATION OF ACCIDENT TOLERANT FUEL MATERIALS FOR FUTURE NUCLEAR REACTORS
Institution name	University of Saskatchewan

Expected presentation date	Jul 2019
Requestor Location	University of Saskatchewan 57 Campus Drive Saskatoon, SK S7N 5A9 Canada Attn: University of Saskatchewan
Billing Type	Invoice
Billing address	University of Saskatchewan 57 Campus Drive Saskatoon, SK S7N 5A9 Canada Attn: University of Saskatchewan
Total (may include CCC user fee)	0.00 USD
Total	0.00 USD

CLOSE WINDOW

Copyright Permission for Manuscript #5 Used in Chapter 8

Title:	DFT U Study of the Adsorption and Dissociation of Water on Clean, Defective and Oxygen-Covered U3Si2 (001), (110), and (111) Surfaces
Author:	Ericmoore Elijah Jossou, Linu Malakkal, Nelson Y. Dzade, et al
Publication:	The Journal of Physical Chemistry C
Publisher:	American Chemical Society
Date:	Jul 1, 2019

PERMISSION/LICENSE IS GRANTED FOR YOUR ORDER AT NO CHARGE

This type of permission/license, instead of the standard Terms & Conditions, is sent to you because no fee is being charged for your order. Please note the following:

- Permission is granted for your request in both print and electronic formats, and translations.
- If figures and/or tables were requested, they may be adapted or used in part.
- Please print this page for your records and send a copy of it to your publisher/graduate school.
- Appropriate credit for the requested material should be given as follows: "Reprinted (adapted) with permission from (COMPLETE REFERENCE CITATION). Copyright (YEAR) American Chemical Society." Insert appropriate information in place of the capitalized words.
- One-time permission is granted only for the use specified in your request. No additional uses are granted (such as derivative works or other editions). For any other uses, please submit a new request.

BACK CLOSE WINDOW

Copyright Permission for Fig. 2.7, 2.8, 2.9, and 3.4

SPRINGER NATURE LICENSE
TERMS AND CONDITIONS

May 25, 2019

This Agreement between University of Saskatchewan -- Ericmoore Jossou ("You") and Springer Nature ("Springer Nature") consists of your license details and the terms and conditions provided by Springer Nature and Copyright Clearance Center.

License Number	4595760308326
License date	May 25, 2019
Licensed Content Publisher	Springer Nature
Licensed Content Publication	Nature Materials
Licensed Content Title	Predicting material release during a nuclear reactor accident
Licensed Content Author	Rudy J. M. Konings, Thierry Wiss, Ondřej Beneš
Licensed Content Date	Feb 20, 2015
Licensed Content Volume	14
Licensed Content Issue	3
Type of Use	Thesis/Dissertation
Requestor type	academic/university or research institute
Format	electronic
Portion	figures/tables/illustrations
Number of figures/tables/illustrations	1
High-res required	no
Will you be translating?	no
Circulation/distribution	<501
Author of this Springer Nature content	no
Title	ATOMIC SCALE SIMULATION OF ACCIDENT TOLERANT FUEL MATERIALS FOR FUTURE NUCLEAR REACTORS
Institution name	University of Saskatchewan
Expected presentation date	Jul 2019
Portions	Figure 2
Requestor Location	University of Saskatchewan 57 Campus Drive Saskatoon, SK S7N 5A9 Canada Attn: University of Saskatchewan
Total	0.00 CAD

Terms and Conditions

Springer Nature Terms and Conditions for RightsLink Permissions

Springer Nature Customer Service Centre GmbH (the Licensor) hereby grants you a non-exclusive, world-wide licence to reproduce the material and for the purpose and

requirements specified in the attached copy of your order form, and for no other use, subject to the conditions below:

1. The Licensor warrants that it has, to the best of its knowledge, the rights to license reuse of this material. However, you should ensure that the material you are requesting is original to the Licensor and does not carry the copyright of another entity (as credited in the published version).

   If the credit line on any part of the material you have requested indicates that it was reprinted or adapted with permission from another source, then you should also seek permission from that source to reuse the material.

2. Where **print only** permission has been granted for a fee, separate permission must be obtained for any additional electronic re-use.

3. Permission granted **free of charge** for material in print is also usually granted for any electronic version of that work, provided that the material is incidental to your work as a whole and that the electronic version is essentially equivalent to, or substitutes for, the print version.

4. A licence for 'post on a website' is valid for 12 months from the licence date. This licence does not cover use of full text articles on websites.

5. Where **'reuse in a dissertation/thesis'** has been selected the following terms apply: Print rights of the final author's accepted manuscript (for clarity, NOT the published version) for up to 100 copies, electronic rights for use only on a personal website or institutional repository as defined by the Sherpa guideline (www.sherpa.ac.uk/romeo/).

6. Permission granted for books and journals is granted for the lifetime of the first edition and does not apply to second and subsequent editions (except where the first edition permission was granted free of charge or for signatories to the STM Permissions Guidelines http://www.stm-assoc.org/copyright-legal-affairs/permissions/permissions-guidelines/), and does not apply for editions in other languages unless additional translation rights have been granted separately in the licence.

7. Rights for additional components such as custom editions and derivatives require additional permission and may be subject to an additional fee. Please apply to Journalpermissions@springernature.com/bookpermissions@springernature.com for these rights.

8. The Licensor's permission must be acknowledged next to the licensed material in print. In electronic form, this acknowledgement must be visible at the same time as the figures/tables/illustrations or abstract, and must be hyperlinked to the journal/book's homepage. Our required acknowledgement format is in the Appendix below.

9. Use of the material for incidental promotional use, minor editing privileges (this does not include cropping, adapting, omitting material or any other changes that affect the meaning, intention or moral rights of the author) and copies for the disabled are permitted under this licence.

10. Minor adaptations of single figures (changes of format, colour and style) do not require the Licensor's approval. However, the adaptation should be credited as shown in Appendix below.

Appendix — Acknowledgements:

For Journal Content:
Reprinted by permission from [**the Licensor**]: [**Journal Publisher** (e.g. Nature/Springer/Palgrave)] [**JOURNAL NAME**] [**REFERENCE CITATION** (Article name, Author(s) Name), [**COPYRIGHT**] (year of publication)

For **Advance Online Publication papers:**
Reprinted by permission from [**the Licensor**]: [**Journal Publisher** (e.g. Nature/Springer/Palgrave)] [**JOURNAL NAME**] [**REFERENCE CITATION** (Article name, Author(s) Name), [**COPYRIGHT**] (year of publication), advance online publication, day month year (doi: 10.1038/sj.[JOURNAL ACRONYM].)

For Adaptations/Translations:
Adapted/Translated by permission from [**the Licensor**]: [**Journal Publisher** (e.g. Nature/Springer/Palgrave)] [**JOURNAL NAME**] [**REFERENCE CITATION** (Article name, Author(s) Name), [**COPYRIGHT**] (year of publication)

Note: For any republication from the British Journal of Cancer, the following credit line style applies:

Reprinted/adapted/translated by permission from [**the Licensor**]: on behalf of Cancer Research UK: : [**Journal Publisher** (e.g. Nature/Springer/Palgrave)] [**JOURNAL NAME**] [**REFERENCE CITATION** (Article name, Author(s) Name), [**COPYRIGHT**] (year of publication)

For **Advance Online Publication** papers:
Reprinted by permission from The [**the Licensor**]: on behalf of Cancer Research UK: [**Journal Publisher** (e.g. Nature/Springer/Palgrave)] [**JOURNAL NAME**] [**REFERENCE CITATION** (Article name, Author(s) Name), [**COPYRIGHT**] (year of publication), advance online publication, day month year (doi: 10.1038/sj.[JOURNAL ACRONYM])

For Book content:
Reprinted/adapted by permission from [**the Licensor**]: [**Book Publisher** (e.g. Palgrave Macmillan, Springer etc) [**Book Title**] by [**Book author**(s)] [**COPYRIGHT**] (year of publication)

Other Conditions:

Version 1.1

Title:	Post-irradiation examinations of UO 2 composites as part of the Accident Tolerant Fuels Campaign
Author:	F. Cappia,J.M. Harp,K. McCoy
Publication:	Journal of Nuclear Materials
Publisher:	Elsevier
Date:	15 April 2019

Order Completed

Thank you for your order.

This Agreement between University of Saskatchewan -- Ericmoore Jossou ("You") and Elsevier ("Elsevier") consists of your license details and the terms and conditions provided by Elsevier and Copyright Clearance Center.

Your confirmation email will contain your order number for future reference.

printable details

License Number	4601970046074
License date	Jun 04, 2019
Licensed Content Publisher	Elsevier
Licensed Content Publication	Journal of Nuclear Materials
Licensed Content Title	Post-irradiation examinations of UO 2 composites as part of the Accident Tolerant Fuels Campaign
Licensed Content Author	F. Cappia,J.M. Harp,K. McCoy
Licensed Content Date	Apr 15, 2019
Licensed Content Volume	517
Licensed Content Issue	n/a
Licensed Content Pages	9
Type of Use	reuse in a thesis/dissertation
Portion	Fig.s/tables/illustrations

Number of Fig.s/tables/illustrations	4
Format	print
Are you the author of this Elsevier article?	No
Will you be translating?	No
Original Fig. numbers	Fig. 4
Title of your thesis/dissertation	ATOMIC SCALE SIMULATION OF ACCIDENT TOLERANT FUEL MATERIALS FOR FUTURE NUCLEAR REACTORS
Publisher of new work	University of Saskatchewan
Expected completion date	Jul 2019
Estimated size (number of pages)	1
Requestor Location	University of Saskatchewan 57 Campus Drive Saskatoon, SK S7N 5A9 Canada Attn: University of Saskatchewan
Publisher Tax ID	GB 494 6272 12
Total	0.00 CAD

ORDER MORE CLOSE WINDOW

Title:	KAERI's Development of LWR Accident-Tolerant Fuel
Author:	Yang-Hyun Koo, , Jae-Ho Yang, et al
Publication:	Nuclear Technology
Publisher:	Taylor & Francis
Date:	May 1, 2014

Rights managed by Taylor & Francis

Thesis/Dissertation Reuse Request

Taylor & Francis is pleased to offer reuses of its content for a thesis or dissertation free of charge contingent on resubmission of permission request if work is published.

BACK CLOSE WINDOW

American Physical Society Reuse and Permissions License

18-May-2019

This license agreement between the American Physical Society ("APS") and Ericmoore Jossou ("You") consists of your license details and the terms and conditions provided by the American Physical Society and SciPris.

Licensed Content Information

License Number:	**RNP/19/MAY/014965**
License date:	18-May-2019
DOI:	10.1103/PhysRevB.65.144306
Title:	Comparison of atomic-level simulation methods for computing thermal conductivity
Author:	Patrick K. Schelling, Simon R. Phillpot, and Pawel Keblinski
Publication:	Physical Review B
Publisher:	American Physical Society
Cost:	USD $ 0.00

Request Details

Does your reuse require significant modifications: No

Specify intended distribution locations:	Worldwide
Reuse Category:	Reuse in a thesis/dissertation
Requestor Type:	Student
Items for Reuse:	Figures/Tables
Number of Figure/Tables:	6
Figure/Tables Details:	System size dependence of 1/k on 1/Lz . Data are shown for Si at T 5500 K and T 51000 K and for diamond at T 51000 K. We note that the rate of change of 1/k with 1/Lz for Si appears to be only slightly
Format for Reuse:	Electronic

Information about New Publication:

University/Publisher:	University of Saskatchewan
Title of dissertation/thesis:	ATOMIC SCALE SIMULATION OF ACCIDENT TOLERANT FUEL MATERIALS FOR FUTURE NUCLEAR REACTORS
Author(s):	Ericmoore Elijah Jossou
Expected completion date:	Jul. 2019

License Requestor Information

Name:	Ericmoore Jossou
Affiliation:	Individual
Email Id:	ericmoore.jossou@usask.ca
Country:	Canada

American Physical Society
Reuse and Permissions License

TERMS AND CONDITIONS

The American Physical Society (APS) is pleased to grant the Requestor of this license a non-exclusive, non-transferable permission, limited to Electronic format, provided all criteria outlined below are followed.

1. You must also obtain permission from at least one of the lead authors for each separate work, if you haven't done so already. The author's name and affiliation can be found on the first page of the published Article.
2. For electronic format permissions, Requestor agrees to provide a hyperlink from the reprinted APS material using the source material's DOI on the web page where the work appears. The hyperlink should use the standard DOI resolution URL, http://dx.doi.org/{DOI}. The hyperlink may be embedded in the copyright credit line.
3. For print format permissions, Requestor agrees to print the required copyright credit line on the first page where the material appears: "Reprinted (abstract/excerpt/figure) with permission from [(FULL REFERENCE CITATION) as follows: Author's Names, APS Journal Title, Volume Number, Page Number and Year of Publication.] Copyright (YEAR) by the American Physical Society."
4. Permission granted in this license is for a one-time use and does not include permission for any future editions, updates, databases, formats or other matters. Permission must be sought for any additional use.
5. Use of the material does not and must not imply any endorsement by APS.
6. APS does not imply, purport or intend to grant permission to reuse materials to which it does not hold copyright. It is the requestor's sole responsibility to ensure the licensed material is original to APS and does not contain the copyright of another entity, and that the copyright notice of the figure, photograph, cover or table does not indicate it was reprinted by APS with permission from another source.
7. The permission granted herein is personal to the Requestor for the use specified and is not transferable or assignable without express written permission of APS. This license may not be amended except in writing by APS.
8. You may not alter, edit or modify the material in any manner.
9. You may translate the materials only when translation rights have been granted.
10. APS is not responsible for any errors or omissions due to translation.
11. You may not use the material for promotional, sales, advertising or marketing purposes.
12. The foregoing license shall not take effect unless and until APS or its agent, Aptara, receives payment in full in accordance with Aptara Billing and Payment Terms and Conditions, which are incorporated herein by reference.
13. Should the terms of this license be violated at any time, APS or Aptara may revoke the license with no refund to you and seek relief to the fullest extent of the laws of the USA. Official written notice will be made using the contact information provided with the permission request. Failure to receive such notice will not nullify revocation of the permission.
14. APS reserves all rights not specifically granted herein.
15. This document, including the Aptara Billing and Payment Terms and Conditions, shall be the entire agreement between the parties relating to the subject matter hereof.

APPENDIX F

All the results presented in this thesis are stored in the computer Canada clusters (cedar.computecanada.ca) with descriptions for future reference. The input and outputs of the calculations are described on a project basis such that each chapter is put a folder as a project with a readme file and descriptions. The location of all results is provided.

1. Results used in chapter 4 are stored on cedar.computecanada.ca

/project/6001430/ejossou/PhD-Projects-2015-2019/Chapter4

2. Results used in chapter 5 are stored on cedar.computecanada.ca

/project/6001430/ejossou/PhD-Projects-2015-2019/Chapter5

3. Results used in chapter 6 are stored on cedar.computecanada.ca

/project/6001430/ejossou/PhD-Projects-2015-2019/Chapter6

4. Results used in chapter 7 are stored on cedar.computecanada.ca

/project/6001430/ejossou/PhD-Projects-2015-2019/Chapter7

5. Results used in chapter 8 are stored on cedar.computecanada.ca

/project/6001430/ejossou/PhD-Projects-2015-2019/Chapter8